

ON THE POTENTIAL OF MAX PHASES FOR NUCLEAR APPLICATIONS

A Thesis

Submitted to the Faculty

Of

Drexel University

By

DARIN JOSEPH TALLMAN

In partial fulfillment of the

requirements for the degree

of

DOCTOR OF PHILOSOPHY

JUNE 2015



ProQuest Number: 3728860

All rights reserved

INFORMATION TO ALL USERS

The quality of this reproduction is dependent upon the quality of the copy submitted.

In the unlikely event that the author did not send a complete manuscript and there are missing pages, these will be noted. Also, if material had to be removed, a note will indicate the deletion.



ProQuest 3728860

Published by ProQuest LLC (2015). Copyright of the Dissertation is held by the Author.

All rights reserved.

This work is protected against unauthorized copying under Title 17, United States Code  
Microform Edition © ProQuest LLC.

ProQuest LLC.  
789 East Eisenhower Parkway  
P.O. Box 1346  
Ann Arbor, MI 48106 - 1346

©2015

Darin J. Tallman

All Rights Reserved.

## DEDICATIONS

This thesis is dedicated to my parents for instilling in me a yearning for knowledge and understanding, which drove me to pursue my interests in science and materials engineering. I also dedicate this work to my soon-to-be wife Erin, for had she not provided me with endless love and support, and not to mention countless hours of proofreading, I would never have been able to accomplish this feat.

## ACKNOWLEDGEMENTS

There are so many people to thank for allowing me to complete this work, and I am very glad to have the opportunity to express my gratitude.

Most importantly, an immense thank you to my thesis advisor, Prof. Michel W. Barsoum. I truly appreciate all of the support and encouragement you have given me over these few long years as we struggled with exploring irradiation of materials together. Thanks for the discussions we had, many of which were aided by a pint or two, to try and understand how irradiation was affecting our MAX phases, You have given me many opportunities to grow and learn in my academic career, and have always shown your respect and confidence in me to get the job done, as I was forging my own path for most of my projects. Thank you for your guidance over the years, and the freedom to make my own mistakes to better learn from them. Cheers.

I am also indebted to my collaborators at Savannah River National Laboratory and Idaho National Laboratory, two fantastic teams of researchers with incredible capability for handling irradiation work. A big thank you goes to Liz Hoffman for being a vital committee member, as well as leading the research efforts at SRNL. I also must thank Brenda Garcia-Diaz for continuing the research of MAX phases at SRNL and for keeping work on track even through all the red tape. Also, thanks to Robert Sindelar for the intriguing discussions and aid with direction of the projects. I would also like to thank the experimental staff who assisted me in all facets of my work at SRNL, Mike Tosten, Avery Reddick, Greg Creech, Dave Missimer, Michael Martinez and many others. I am also thankful to Liz for offering me two summer internships during my PhD career to work at SRNL in preparation for the irradiation work. Many thanks to Jose Cortes for letting me stay in his spare bedroom during my trips there.

A huge thank you goes out to Joanna Taylor and her team at the Center for Advanced Energy Studies at Idaho National Laboratory, including Jatu Burns, Dr. Yaquiao Wu, Kristi Moser-McIntire, and Bryan Forsmann, for wonderful assistance with performing radiological experiments and training for FIB/TEM work on my irradiated samples. I would also like to sincerely thank my good friend Dr. Lingfeng He for his expert assistance with TEM investigations of the MAX phases. I am proud to call him my friend and I look forward to many future collaborations. A major thank you goes to Collin Knight, Karen Wright, and Brandon Miller of the Materials and Fuels Complex at INL for their excellent assistance with radiological sample handling and preparation. Without them, I would never have been able to explore my samples after irradiation. I also wish to thank Jeff Benson and Jim Cole of INL for their leadership and guidance with conducting the PIE work at INL over the last few years.

I would also like to thank the rest of my committee members. Prof. Roger Doherty, your time and discussions have been invaluable for understanding how the MAX phases work, and how to make sense of the defects we observed. Prof. Antonios Kontsos, you always kept me grounded, and looking at the bigger picture, and for that I thank you, and feel my thesis is stronger due to your influences and suggestions. Prof. Garritt Tucker, your enthusiasm and immense interest for my research results were very welcome, and I am very hopeful for amazing experiments to come as a result of our collaborative efforts. Prof. Steven May, I am grateful for your guidance and encouragement throughout thesis work

I am deeply obliged to the incredible, accomplished, amiable, and supportive members of the MAX phase research group. I would not have wanted to work with any other research group. Our group has been a family to me, more close in friendship than I ever expected in a work environment. Everyone has been so helpful and encouraging, always willing to assist at a moment's notice for everyone's research. Prof. Barsoum chose his students well,

picking the brightest, friendliest crew, with top notch character and humility. Many thanks to all current and past members whom I've been fortunate enough to share time with in the MAX phase group: Dr. Babak Anasori, Dr. Nina J. Lane, Dr. Michael Naugib, Dr. Mohamed Shamma, Dr. Ivy Yang, Dr. Jian Yang, Limei Pan, Dr. Chunfeng Hu, Dr. Chao Li, John Lloyd, Ismail Albayrak, Charles B. Spencer, Jr., Joseph Halim, Mike Ghidiu, Grady Bentzel, Justin Griggs, Sankalp Kota, Derya Kapusuz, and Matthias Agne- you have all kept me sane and focused, and have made Drexel a wonderful place to work.

Dr. El'ad Caspi, I am thankful that I got to know you during your time here at Drexel, and I am very grateful for your guidance and knowledge in teaching me the ways of Rietveld refinement. I am glad we were able to collaborate on this work, and working with you has been an honor.

Thanks to the amazing faculty in the Materials Science and Engineering department at Drexel University. I appreciate the support and advice of Prof. Caroline Schauer, Prof. Antonis Zavaliangos, Dr. Richard Knight, and Prof. Michelle Marcolongo. A huge thank you goes to the amazing MSE staff, especially Sarit Kunz, Keiko Nakazawa, Yenneeka Long, Dorilona Rose, and Leslie Anastasio, for working countless miracles in scheduling and stipend disbursement and for encouraging such a great work environment in our small department.

A sincere thank you goes out to my incredible friends at Drexel, many of whom have become dear friends and colleagues, especially Katie Van Aken, Dr. Jake McDonough, Dr. Kristy A. Jost, and Matthew Hartshorne. May our paths cross again, and your lives be full of amazing science and discovery.

Of course, I am forever grateful to my family. Without the love and support of my parents, I would not be the man I am today. You always encouraged me to reach higher and explore the unknown, and I owe my passion for science to you. My brothers and sister have taught

me to be humble, and to enjoy all facets of life, not letting my work overtake my existence. I am ceaselessly thankful for your support, encouragement, and unconditional love.

And thank you, the reader, for taking time to peruse this thesis. Perhaps you might take some tidbit of knowledge from my work, and for that I am thankful for the opportunity to share it with you.

Darin Joseph Tallman  
September 2015



## TABLE OF CONTENTS

Dedications .....	ii
Acknowledgements.....	iii
Table of Tables.....	xi
Table of Figures .....	xiii
Abstract .....	xxi
1. Introduction.....	1
1.1. Overview.....	1
1.2. Scope .....	4
1.3. Outline.....	6
2. Literature Review.....	8
2.1. Nuclear Reactor Technologies .....	8
2.2. Irradiation Effects in Reactor Materials.....	12
2.3. MAX Phases.....	19
2.4. Conclusions .....	27
3. Materials and Methods.....	29
3.1. MAX Phase Fabrication .....	29
3.2. Metallography.....	36
3.3. X-ray Diffraction .....	39
3.4. Neutron Irradiation Experiments .....	40
3.5. Transmission Electron Microscopy.....	49

3.6.	Room Temperature Resistivity of Irradiated MAX phases .....	53
3.7.	Thermal Diffusivity, Non-irradiated.....	54
3.8.	Diffusion Bonding, Non-irradiated .....	54
3.9.	Helium Permeability.....	56
4.	Irradiated Structures and Phase Stability.....	59
4.1.	Diffraction Origins and Theory .....	60
4.2.	X-ray Diffraction Results: MITR Samples .....	65
4.3.	Theoretical Defective Structures.....	81
4.4.	Conclusions .....	88
5.	Irradiation Induced Defects.....	90
5.1.	Transmission Electron Microscopy, TEM.....	90
5.2.	TEM Results: MITR Samples.....	91
5.3.	TEM Results: ATR Samples .....	102
5.4.	Comparison with Ion Irradiation Studies .....	105
5.5.	Benefits of the A-layer in MAX Phase Structure .....	106
5.6.	Conclusions .....	107
6.	Effect of Irradiation on Properties .....	110
6.1.	Macroscopic Structure Post-irradiation .....	110
6.2.	Room Temperature Electrical Resistivity of Irradiated MAX Phases .....	114
6.3.	Thermal Conductivity of the MAX Phases .....	119
6.4.	Nanoindentation: Mechanical Properties of $Ti_3SiC_2$ and $Ti_2AlC$ .....	123
6.5.	Neutron Activation .....	129

6.6.	Conclusions .....	131
7.	Interaction with Reactor Components.....	133
7.1.	Reactivity with Zircaloy-4 Fuel Cladding.....	133
7.2.	Helium Permeability.....	149
7.3.	Conclusions .....	155
8.	General conclusions and perspectives.....	157
8.1.	Principle Discoveries.....	157
8.2.	Future Work .....	162
	References .....	165
A1	A Critical Review of the Oxidation of $Ti_2AlC$ , $Ti_3AlC_2$ and $Cr_2AlC$ in Air.....	176
A1.1	Introduction.....	177
A1.2	Literature Survey.....	177
A1.2.1	$Ti_2AlC$ .....	179
A1.2.2	$Ti_3AlC_2$ .....	180
A1.2.3	$Cr_2AlC$ .....	180
A1.3	Parabolic, Cubic or Power law Kinetics.....	182
A1.3.1	$Ti_2AlC$ and $Ti_3AlC_2$ .....	183
A1.3.2	Crack Healing.....	189
A1.3.3	$Cr_2AlC$ .....	192
A1.3.4	Implications of the presence of $Cr_7C_3$ layer after the oxidation of $Cr_2AlC$ .....	195
A1.4	Comparison to FeCrAl alloys .....	197
A1.5	Modelling of the Oxidation Kinetics.....	198

A1.6	Summary and Conclusions.....	200
	Acknowledgements.....	201
A2	Tensile Creep of $Ti_2AlC$ in Air in the 1000-1150 °C Temperature Range .....	202
A2.1	Manuscript.....	203
8.3.	Acknowledgments .....	212
Vita	.....	213
	Education.....	213
	Research and Collaborative Projects.....	213
	Honors and Awards.....	213
	Presentations.....	213
	Publications.....	213

## TABLE OF TABLES

Table 3.1 Metallographic procedure used for polishing MAX phases within this thesis.....	37
Table 3.2 Irradiation temperature and dose designators. ....	42
Table 3.3 Irradiation condition labels for each reactor experiment.....	42
Table 3.4 Irradiation exposure parameters for the MITR experiments. ....	43
Table 3.5 Nominal irradiation exposure parameters for the ATR experiments.....	45
Table 3.6 Focus ion beam milling procedure for MAX phase thin foils for TEM observation. .....	50
Table 4.1 Irradiation-induced structural and compositional changes in MITR irradiated MAX phases.....	75
Table 6.1 Room temperature resistivity of MAX Phases before and after MITR irradiations. .....	115
Table 6.2 Thermal conductivity $\kappa_{th}$ of various MAX phases as measured by laser flash analysis.....	120
Table 6.3 Calculated thermal $\kappa_e$ from RT $\rho$ using the Wiedmann-Franz law.....	123
Table 6.4 Young's modulus and hardness as determined from Berkovich nanoindentation*. .....	127
Table 7.1 Summary of phase compositions and their thicknesses, in $\mu\text{m}$ , across the $\text{Ti}_3\text{SiC}_2/\text{Zr-4}$ diffusion couples - starting with $\text{Ti}_3\text{SiC}_2$ - as a function of time and temperature. The last column lists the total thickness of the reaction layer and is the one plotted in Fig. 7.6. ....	138
Table 7.2 Summary of phase compositions and their thicknesses, in $\mu\text{m}$ , across the $\text{Ti}_2\text{AlC}/\text{Zr-4}$ diffusion couples - starting with $\text{Ti}_2\text{AlC}$ - as a function of time and temperature. The last column lists the total thickness of the reaction layer and is the one plotted in Fig. 7.6. ....	142

Table 7.3 Permeability of $Ti_2AlC$ , $Ti_3AlC_2$ and $Ti_3SiC_2$ at 850°C and 950°C.....	153
Table 7.4 Equivalent Darcy's permeability coefficient of $Ti_2AlC$ , $Ti_3AlC_2$ and $Ti_3SiC_2$ at 850°C and 950°C. ....	153
Table A1.1 Summary of $k_c$ ( $kg^3m^{-6}s^{-1}$ ) values for the oxidation of $Ti_2AlC$ , $Ti_3AlC_2$ and $Cr_2AlC$ .....	188

## TABLE OF FIGURES

Figure 2.1 Outlet temperatures and expected production processes for the proposed Gen IV reactor designs.....	9
Figure 2.2 TRISO fuel particle cross section showing layers of PyC and SiC for UO <sub>2</sub> fuel kernel containment. ....	10
Figure 2.3 Difference in damage morphology, displacement efficiency, and average recoil energy for 1 MeV particles of different type incident on nickel [16].....	13
Figure 2.4 Schematic of neutron knock-on damage in a crystalline solid.....	13
Figure 2.5 Formation of a dislocation loop.....	15
Figure 2.6 Summary of the microstructural development in cubic SiC during neutron and self ion irradiation. The resultant defect types depend upon irradiation dose, as well as temperature [14]. ....	17
Figure 2.7 a) Optical SEM micrograph of a SiC/Pd diffusion couple annealed at 1000°C for 10 hours.....	19
Figure 2.8 Unit cells of a) M <sub>2</sub> AX, b) M <sub>3</sub> AX <sub>2</sub> , and c) M <sub>4</sub> AX <sub>3</sub> phases reproduced from Ref. [25]. ....	20
Figure 2.9 Elements of the periodic table known to react to form the various MAX phases. ....	21
Figure 3.1. a) Uniaxial hot press, HP, used to produce MAX phase samples and, b) graphite dies used for producing MAX same. ....	30
Figure 3.2 Hot pressed blank of Ti <sub>3</sub> SiC <sub>2</sub> , with miniature tensile bars machined from a similar blank.....	33
Figure 3.3 Sample geometries for MITR and ATR irradiation studies. ....	33
Figure 3.4 Representative optical micrographs of a) Ti <sub>2</sub> AlC , b) Ti <sub>3</sub> AlC <sub>2</sub> , c) Ti <sub>2</sub> AlN, d) FG-Ti <sub>3</sub> SiC <sub>2</sub> , and e) CG-Ti <sub>3</sub> SiC <sub>2</sub> microstructures after etching with a solution of hydrofluoric acid,	

nitric acid, and water. The MAX phase samples were fully dense and predominately single phase, with randomly aligned plate like grains, which are vibrantly colored after etching. TiC appears as bright white grains, denoted by white arrows. ....	38
Figure 3.5 Normalized flux per unit lethargy of typical PWR and of in-core sample assembly, ICSA, configurations of a) ICSA thimble with aluminum dummy element (standard), b) 3mm H <sub>2</sub> O annulus introduced outside ICSA thimble. Note that the MAX phase irradiation took place with an approximately 1-mm water gap with the spectrum corresponding to curve (a). Flux per unit lethargy is equal to the flux divided by the natural log of the total energy range of the neutrons. ....	43
Figure 3.6 Representative capsule locations in the ATR loading positions. ....	46
Figure 3.7 Specimen loading configuration for the ATR irradiation capsules. Samples of each type were arranged in stainless steel holders and loaded vertically into the capsule tube. ....	47
Figure 3.8 Fixture configurations for tensile (top), TEM (middle) and resistivity (bottom) samples ....	48
Figure 3.9 a) Quanta 3D FEG focused ion beam used to prepare TEM foils and b) FEI TF30-FEG STwin STEM used to characterize the pristine and irradiated samples. ....	51
Figure 3.10 Schematic representation of the different diffraction conditions used in diffraction-contrast imaging: a) 2-beam dynamical, b) 2-beam kinematical, and c) weak-beam. In each case the Ewald sphere is sketched on the left-hand side, and a schematic diffraction pattern (DP) showing the position of the relevant Kikuchi lines on the right-hand side. The curvature of the Ewald sphere is exaggerated for clarity. The open circle represents the objective aperture [76]. ....	52
Figure 3.11 Schematic of the diffusion couple loading assembly that was in turn placed in the hot press. ....	55
Figure 3.12 a) Small furnace and b) sample chamber used for permeability testing. ....	57
Figure 4.1 Schematic of Bragg's law. ....	62



Figure 4.2 Rietveld analysis of XRD pattern of FG-Ti <sub>3</sub> SiC <sub>2</sub> .....	67
Figure 4.3 Rietveld analysis of XRD data of CG-Ti <sub>3</sub> SiC <sub>2</sub> . ....	69
Figure 4.4 Rietveld analysis of XRD patterns of Ti <sub>3</sub> AlC <sub>2</sub> . ....	71
Figure 4.5 Rietveld analysis of XRD patterns of Ti <sub>2</sub> AlC.....	73
Figure 4.6 Rietveld analysis of XRD pattern of Ti <sub>2</sub> AlN.....	76
Figure 4.7 Rietveld analysis of XRD patterns of M-D2-T2 samples of FG-Ti <sub>3</sub> SiC <sub>2</sub> and Ti <sub>2</sub> AlC .....	77
Figure 4.8 Lattice parameters of MAX phases as a function of irradiation temperature.....	80
Figure 4.9 Possible interstitial sites in the M <sub>3</sub> AX <sub>2</sub> structure include A: I <sub>pri</sub> , B: I <sub>hex</sub> , C: I <sub>tet</sub> , and D: I <sub>oct</sub> [79].....	82
Figure 4.10 Schematic of the lowest energy C interstitial arrangement showing the nearest neighbor bonds to the Si atoms within the basal layer and to the Ti atoms in the z-direction [82].....	84
Figure 4.11 ( <b>1010</b> ) view of M <sub>3</sub> AX <sub>2</sub> structure a) pristine, b) after irradiation at low temperatures (350 °C), and c) after irradiation at higher (700 °C) temperatures. Region I shows coherent interstitial loops; region II shows M atom antisite layers. Combinations of the two types of defects in a single layer are also possible. The unit cell is shown by the dotted line in a. ....	86
Figure 5.1 Representative TEM micrographs of unirradiated FG-Ti <sub>3</sub> SiC <sub>2</sub> and Ti <sub>2</sub> AlC. ....	92
Figure 5.2 Representative brightfield TEM micrographs of FG-Ti <sub>3</sub> SiC <sub>2</sub> after T2 irradiations. ....	93
Figure 5.3 Representative brightfield TEM micrographs of Ti <sub>2</sub> AlC after T2 irradiations.....	95
Figure 5.4 Representative brightfield TEM micrographs of FG-Ti <sub>3</sub> SiC <sub>2</sub> irradiated to M-D1-T4.....	96
Figure 5.5 Representative TEM micrographs of Ti <sub>2</sub> AlC irradiated to M-D1-T4.....	98
Figure 5.6 TEM microraphs detailing stacking faults in FG-Ti <sub>3</sub> SiC <sub>2</sub> and Ti <sub>2</sub> AlC .....	100

Figure 5.7 a) Brightfield TEM micrograph of a grain boundary found in FG-Ti <sub>3</sub> SiC <sub>2</sub> :M-D1-T4. The jagged features imply irradiation induced growth has occurred along the a-direction.	
b) Representative TEM micrograph of preexisting TiC particle found in the FG-Ti <sub>3</sub> SiC <sub>2</sub> :M-D1-T2 sample showing extensive microstructural damage compared to the relatively clean surrounding Ti <sub>3</sub> SiC <sub>2</sub> matrix. Representative TEM micrograph of Al <sub>2</sub> O <sub>3</sub> impurity particles observed in Ti <sub>2</sub> AlC samples irradiated to, c) M-D1-T2 and, d) M-D2-T2. Density of irradiation induced defects is larger in (d) than in (c) and in both cases, significantly higher than the defects in the surrounding Ti <sub>2</sub> AlC.	101
Figure 5.8 Brightfield TEM micrographs of Ti <sub>3</sub> SiC <sub>2</sub> irradiated at ATR at T3	103
Figure 5.9 TEM micrographs of Ti <sub>3</sub> SiC <sub>2</sub> :A-D5-T3	105
Figure 6.1 SEM micrographs of FG-Ti <sub>3</sub> SiC <sub>2</sub> a) pristine, and irradiated to, b) M-D1-T2, c) M-D1-T4, and d) M-D2-T2, and Ti <sub>2</sub> AlC e) pristine, and irradiated to f) M-D1-T2, g) M-D1-T4, and h) M-D2-T2.	112
Figure 6.2 a) Composite TEM micrographs of the Ti <sub>2</sub> AlC lift-out irradiated to M-D1-T2.	113
Figure 6.3 RT resistivity as a function of irradiation temperature for M-D1 samples.	116
Figure 6.4 RT resistivity as a function of irradiation dose of M-T2 samples.	118
Figure 6.5 Thermal conductivities of various MAX phases as a function of temperature.	121
Figure 6.6 Schematic illustration of indentation load-displacement data [104, 105].	124
Figure 6.7 Typical load-displacement curves of indentations in FG-Ti <sub>3</sub> SiC <sub>2</sub> :M-D1-T4 to various depths.	127
Figure 6.8 Effect of irradiation temperature on nanoindentation hardness of FG-Ti <sub>3</sub> SiC <sub>2</sub> and Ti <sub>2</sub> AlC.	128
Figure 7.1 Typical backscattered electron SEM micrographs of Ti <sub>3</sub> SiC <sub>2</sub> /Zr-4 diffusion couples	137
Figure 7.2 Typical backscattered electron SEM micrographs of Ti <sub>2</sub> AlC /Zr-4 diffusion couples	140

Figure 7.3 Typical composition profiles determined by EDX line scans of the $\text{Ti}_3\text{SiC}_2/\text{Zr-4}$ interfaces.....	144
Figure 7.4 Typical composition profiles determined by EDX line scans of the $\text{Ti}_2\text{AlC} / \text{Zr-4}$ interfaces.....	145
Figure 7.5 Typical backscattered electron SEM micrographs of etched diffusion couples ..	146
Figure 7.6 Total diffusion distance ( $x$ ) vs. $t^{1/2}$ for diffusion couples.....	147
Figure 7.7 Apparent diffusivity, $k'$ , of He in $\text{Ti}_3\text{SiC}_2$ , $\text{Ti}_3\text{AlC}_2$ , and $\text{Ti}_2\text{AlC}$ compared to Alumina [128]. .....	154
Figure A1.1 a) Oxidation of the $\text{Ti}_{n+1}\text{AlX}_n$ phases results in the formation of a rutile based solid solution with approximate chemistry of $(\text{Ti}_{1-y}\text{Al}_y)\text{O}_{2-y/2}$ , where $y \approx 0.05$ and alumina, $\text{Al}_2\text{O}_3$ . b) At longer times, kinetic demixing results in the formation of layers of $\text{TiO}_2$ , $\text{Al}_2\text{O}_3$ and pores [39]. c) SEM micrograph of $\text{Ti}_2\text{AlC}$ oxidized in air at 1200 °C for 2873 h showing a $\approx 21 \mu\text{m}$ thick, coherent and fully dense $\text{Al}_2\text{O}_3$ layer which conforms to the corners of the sample. ....	178
Figure A1.2 SEM micrograph of a) cross-sectioned $\text{Cr}_2\text{AlC}$ sample oxidized at 1200 °C. The outer layer is a Cr-containing $\text{Al}_2\text{O}_3$ and the inner layer is $\text{Cr}_7\text{C}_3$ ; b) of sample oxidized at 1100 °C for 35 h clearly showing $\text{Cr}_2\text{O}_3$ nodules (Gupta, unpublished results). This is the only MAX phase to show the formation of a carbide layer beneath the oxide layers formed during oxidation. ....	181
Figure A1.3 a) Replotted results from the 2003 Wang and Zhou papers on the oxidation of $\text{Ti}_3\text{AlC}_2$ and $\text{Ti}_2\text{AlC}$ [41, 42] showing a linear fit when $(\Delta w/A)^3$ is plotted vs. $t$ . Least squares fit of the 1300 °C plot results in an $R^2$ value of 0.998, compared to 0.98 for the parabolic fit reported in the original articles. The compounds and graphs are color coded for clarity. b) Oxide scale thickness ( $x$ ) versus time for $\text{Ti}_2\text{AlC}$ held at 1200 °C for >2800 h. A power fit of the results shown yields a time exponent of 0.36, viz. cubic kinetics. Dashed line shows the $\Delta x$ based on a parabolic rate constant fitted to the first 100 h of oxidation. ....	184

Figure A1.4 a) Magnitude of compressive residual stress within the  $\text{Al}_2\text{O}_3$  scale determined from luminescence-shifts as a function of time of isothermal oxidation at 1000, 1200 and 1400 °C [132]. The residual stresses are compressive, a function of time and temperature, and of the order of 500 MPa which is considered low [132]. b) Oxidation kinetics of  $\text{Ti}_2\text{AlC}$  are compared with other more established/commercial oxidation resistant alloys. Note that if the very first oxidation cycle is omitted from the  $\text{Ti}_2\text{AlC}$  results, its oxidation kinetics are comparable to PM2000 [132].

186

Figure A1.5 After oxidation at 1100 °C in air for 2 h, crack healing of  $\text{Ti}_3\text{AlC}_2$  is seen via SEM micrographs a) showing the formation of primarily  $\alpha\text{-Al}_2\text{O}_3$ , as well as some rutile  $\text{TiO}_2$ ; Energy dispersive x-ray spectroscopy (EDS) element maps of the crack region show concentrations of b) Ti, c) Al, and d) O as the alumina forms in the crack. A schematic of the process is shown in e [45].

190

Figure A1.6 Images of fracture and crack-healing in  $\text{Ti}_2\text{AlC}$ ; (a) Crack path after four cycles of healing at 1200 °C for 2 h, and subsequent fracture. (b) Crack path after seven cycles of healing, and subsequent fracture. The red arrows indicate the location of remnant crack parts. (c) OM image of a crack fractured eight times before annealing in air at 1200 °C for 100 h showing the complete filling of the crack. (d) Enlarged OM image taken from (c). Two opposite fracture surfaces were covered by the same  $\text{Al}_2\text{O}_3$  layer (black) and the gap between the two surfaces was fully filled by a mixture of  $\text{Al}_2\text{O}_3$  (black) and  $\text{TiO}_2$  (white particles). (e) SEM image of the healed-damage zone obtained using electron backscatter diffraction [125].

192

Figure A1.7 a) Re-plots of the results of Lin et al. [136] together with two power fits (solid lines), assuming cubic kinetics (dotted lines) and the parabolic rate constants reported by Lin *et al.* (dashed lines) are shown. Cubic power fits result in time exponents of 0.34 and 0.25 for 1200 °C and 1300 °C, respectively. b) The same exercise in a) - carried out on data by Lee *et al.* [139] - results in power fits shown by the solid lines with time exponent values of 0.24,

0.46 and 0.18 at 700 °C, 800 °C and 1000 °C, respectively. With the possible exception of 800 °C, the oxidation kinetics of Cr <sub>2</sub> AlC are certainly not parabolic, and in most cases even better than cubic.....	193
Figure A1.8 Arrhenian plot of cubic rate constants for Al <sub>2</sub> O <sub>3</sub> -forming MAX phases, Ti <sub>2</sub> AlC, Ti <sub>3</sub> AlC <sub>2</sub> and Cr <sub>2</sub> AlC listed in Table A1.1.....	195
Figure A1.9 SEM micrographs of the fracture surface of Ti <sub>2</sub> AlC after a) 25 h and b) 2873 h at 1200 °C in air. The oxide scale is seen to increase in grain size linearly towards the MAX phase interface.....	198
Figure A1.10 a) Oxide scale grain coarsening kinetics plotted with a power law fit. b) A least squares fit of d <sup>m</sup> vs. t results in a straight line, where the intercept is equal to d <sub>0</sub> <sup>m</sup> . At 0.93 μm, d <sub>0</sub> is sufficiently small to assume that at long times it can be ignored in Eq. A1.19 [155]. .....	200
Figure A2.1 a) OM micrographs of as-received microstructure are compared to b) SEM micrographs of the grip section post creep, showing minimal difference in grain size. c) plots the effect of time, <i>t</i> , and $\sigma$ on the minimum tensile strains, $\epsilon_{min}$ , at 1050 °C for step loads of. Inset in Fig. 1c shows a typical strain vs. time plot for a sample that was loaded to a load corresponding to a stress of 30 MPa at 1050 °C. ....	207
Figure A2.2 a) Ln-ln plot of $\epsilon_{min}$ vs. stress as a function of T; b) Arrhenius plots of min. strain rate as a function of stress; c) Ln-ln plot of min. strain rate vs. stress assuming Q of 362 kJ/mol for Ti <sub>2</sub> AlC compared to Ti <sub>3</sub> SiC <sub>2</sub> [56, 164]. Results of bilinear regression as a function of stress and temperature are shown as lines in each plot, the slopes of which reveal Q, n and $\sigma$ for the creep power law (Eq. A2.2).....	208
Figure A2.3 Composite OM micrographs showing cross-sections of step loaded Ti <sub>2</sub> AlC at a) 1100°C loaded at 10-20-30 MPa for 55h to a final strain of 27% and b) 1150°C loaded at 5-10-15-20 MPa for 86h to a final strain of 26%. Samples do not exhibit necking, and insets show the formation of protective Al <sub>2</sub> O <sub>3</sub> for each sample.....	209

Figure A2.4 SEM micrograph of, a) fracture surface of  $Ti_2AlC$  sample held at 1100 °C and 30 MPa for 3 h to a final strain of 16%. The distinctive layered structure can be seen, as well as stepped grain boundaries. Kinks (referred by black arrows) are readily apparent at the fracture surface. Ruptured grains stick out of the fracture plane. A difference in grain size between b) grip section and c) fracture surface can be seen.....211

## ABSTRACT

---

### **On the Potential of MAX Phases for Nuclear Applications**

Darin J. Tallman

Advisor: Michel W. Barsoum, PhD

Materials within nuclear reactors experience some of the harshest environments currently known to man, including long term operation in extreme temperatures, corrosive media, and fast neutron fluences with up to 100 displacements per atom, dpa. In order to improve the efficiency and safety of current and future reactors, new materials are required to meet these harsh demands. The  $M_{n+1}AX_n$  phases, a growing family of ternary nano-layered ceramics, possess a desirable combination of metallic and ceramic properties. They are composed of an early transition metal (M), a group 13-16 element (A), and carbon and/or nitrogen (X). The MAX phases are being proposed for use in such extreme environments because of their unique combination of high fracture toughness values and thermal conductivities, machinability, oxidation resistance, and ion irradiation damage tolerance. Previous ion irradiation studies have shown that  $Ti_3SiC_2$  and  $Ti_3AlC_2$  resist irradiation damage, maintaining crystallinity up to 50 dpa.

The aim of this work was to explore the effect of neutron irradiation, up to 9 dpa and at temperatures of 100 to 1000 °C, on select MAX phases for the first time. The MAX phases  $Ti_3SiC_2$ ,  $Ti_3AlC_2$ ,  $Ti_2AlC$ , and  $Ti_2AlN$  were synthesized, and irradiated in test reactors that simulate in-pile conditions of nuclear reactors. X-ray diffraction, XRD, pattern refinements of samples revealed a distortion of the crystal lattice after low temperature irradiation, which was not observed after high temperature irradiations. Additionally, the XRD results indicated that  $Ti_3AlC_2$  and  $Ti_2AlN$  dissociated after relatively low neutron doses. This led us to focus on  $Ti_3SiC_2$  and  $Ti_2AlC$ .

For the first time, dislocation loops were observed in  $\text{Ti}_3\text{SiC}_2$  and  $\text{Ti}_2\text{AlC}$  as a result of neutron irradiation. At  $1 \times 10^{23}$  loops/ $\text{m}^3$ , the loop density in  $\text{Ti}_2\text{AlC}$  after irradiation to 0.1 dpa at  $700^\circ\text{C}$  was 1.5 orders of magnitude greater than that observed in  $\text{Ti}_3\text{SiC}_2$ , at  $3 \times 10^{21}$  loops/ $\text{m}^3$ . The  $\text{Ti}_2\text{AlC}$  composition appeared more prone to microcracking than  $\text{Ti}_3\text{SiC}_2$ . Additionally, exceptionally large denuded zones, up to  $1 \mu\text{m}$  in width after 9 dpa irradiations at  $500^\circ\text{C}$ , were observed in  $\text{Ti}_3\text{SiC}_2$ , indicating that point defects readily diffuse to the grain boundaries. Denuded zones of this width, to our knowledge, have never been observed. In comparison,  $\text{TiC}$  impurity particles were highly damaged with various dislocation loops and defect clusters after irradiation. It is thus apparent that the A-layer, interleaved between MX blocks in the MAX phase nanolayered structure, readily accommodates and/or annihilates point defects, providing significant irradiation damage tolerance.

Comparison of defect densities, post-irradiation microstructure, and electrical resistivity showed  $\text{Ti}_3\text{SiC}_2$  to have the highest irradiation tolerance. Diffusion bonding of MAX phases to Zircaloy-4 was studied in the  $1100$  to  $1300^\circ\text{C}$  temperature range. The out diffusion of the A-group element into Zircaloy-4 formed Zr-intermetallic compounds that were roughly an order of magnitude thicker in  $\text{Ti}_2\text{AlC}$  than  $\text{Ti}_3\text{SiC}_2$ . Helium permeability results suggest that the MAX phases behave similarly to other sintered ceramics. Based on the totality of our results,  $\text{Ti}_3\text{SiC}_2$  remains a promising candidate for high temperature nuclear applications, and warrants future exploration. This work provides the foundation for understanding the response of the MAX phases to neutron irradiation, and can now be used to finely tune ion irradiation studies to accurately simulate reactor conditions.



# 1. INTRODUCTION

---

The impetus for the research and analysis included in this thesis was to explore new fuel cladding and structural materials for aging or future nuclear reactors. The priority for fuel cladding applications is the ability to withstand extreme environments during normal operation and accident conditions. With this in mind, this thesis investigates the MAX phases, a family of thermodynamically stable nanolaminated ceramics, for their potential use in fission reactors. This chapter introduces the main topics covered within and provides a summary of the scope of this work. Additionally, an outline of how the chapters are structured is provided.

## 1.1. Overview

---

The world population, currently around 7 billion, is expected to grow to 10 billion people by 2050. To meet the ever increasing demand for energy required for fostering quality of life and socio-economic opportunity, access to affordable, sustainable power is necessary in the immediate future. Increasing energy production by way of the historically dominant sources, e.g. oil, coal, natural gas, is not a forward-thinking option due to the adverse environmental effects associated with fossil fuel consumption. In order to mitigate long-term consequences due to global climate change, a shift away from the world's current energy production mix toward cleaner and more efficient energy is undeniably essential. Nuclear energy, which produces no greenhouse gases, has the potential to take the burden off the fossil fuel crisis while other sustainable energy technologies continue to be refined.

In order for nuclear power to become a prevalent energy source worldwide, improvements in reactor designs are necessary. As of 2015, over 400 nuclear power reactors are operating in 31 countries, with a combined output over 380 GWe. In 2014, 11% of the world's electricity was produced by these nuclear plants. As existing reactors age, they are being granted license renewals extending their original 25-40 year lifetimes for an additional 20 years of operation. While the aged reactors comply with regulation requirements for extension, the reactor designs are of the older generation III, Gen III, type, i.e. light water reactors, LWR, with outlet temperatures around 300 °C. Several nations have come together, in the International Forum for Nuclear Power (IFNP), to create a roadmap for designing and implementing next generation nuclear power plants. The generation IV, Gen IV, reactors are designed to have improved burnup potential, increased energy efficiency, operate at higher temperatures, and feature inherent safety protocols in the event of accidents.

In addition to developing new reactor designs, advancements in materials are needed to improve the safety factor of fuel cladding in current reactors. This is been a subject of study. Efforts are being made to address safety and security failings in the current fleet of LWR in commission throughout the world. Loss-of-cooling accident, LOCA, conditions present severe challenges for materials development, requiring high temperature stability, oxidation resistance, and radiation tolerance.

Materials innovation is similarly required to meet the demands proposed for Gen IV reactors. The most demanding applications in the nuclear system include the fuel matrix and cladding materials. Here, being installed in direct contact with uranium fuels, materials must withstand temperatures in excess of 1000 °C, constant contact with corrosive coolant media, and a fast flux irradiation at high fluences ( $> 100$  dpa) throughout the lifetime of the fuel rod. As the operating temperatures and irradiation dose increase with emerging designs,

conventional steels and metals are unable to adequately perform in high temperature applications. Ceramics, notably silicon carbide, have been investigated for decades in anticipation of the potential they have for these applications. Extensive work has explored the neutron irradiation response in these materials, the robustness of which is highly dependent on processing and purity. While SiC is able to withstand very high temperatures, it remains brittle at high temperatures and is prone to oxidation in the event of an accident. Coolant loss could lead to exposure to high temperature steam or oxygen in the atmosphere. As development of next generation reactors progresses, materials selection for these extreme applications becomes the focus of major research investigations.

This thesis explores a family of materials, known as the MAX phases, that has shown potential for nuclear applications. These materials, numbering over 60 compositions, share a nanolaminated hexagonal crystal structure composed of MX ceramic blocks interleaved with pure metal A-layers. These materials demonstrate an extraordinary combination of properties, both metallic and ceramic in nature. The combination of thermal conductivity, high fracture toughness, high stiffness, and high temperature stability with good oxidation resistance, while also being lightweight, high damping, and readily machinable, make these materials ideal candidates for nuclear reactor applications.

In recent years, irradiation studies using heavy ions have shown that several MAX phases possess irradiation damage tolerance. However, while ion studies provide a sufficient preliminary glimpse into the material behavior, neutron irradiation is required to fully comprehend the nature of the radiation response in these materials. Neutron irradiation impacts material properties over a large scale, from atomic level point defects, to macroscopic structural changes and mechanical behavior. Thankfully, a wide range of experimental tools is available to evaluate the effect of neutron irradiation on material properties. Rietveld refinement of x-ray diffraction, XRD, experiments provide atomic,

lattice, and compositional information, while transmission electron microscopy, TEM, and scanning electron microscopy, SEM, are used to image irradiation induced defects within the microstructure. Additional experiments to probe electrical and thermal conductivity, along with nanoindentation are all assessed as a function of irradiation dose to ascertain the effect of irradiation on specific properties.

In this thesis, these experimental tools are utilized to investigate, for the first time, the neutron irradiation of the MAX phases to develop a knowledge base of neutron response for potential use in nuclear applications.

## 1.2. Scope

---

XRD pattern refinements and TEM investigations are the majority contributors of experimental results in this exploration of irradiation defects and defect structure in neutron-irradiated MAX phases. Analysis of the XRD patterns using Rietveld refinement provides information about the lattice structure, atomic positions, and microstrain which describes disorder and distortion induced by neutrons. Refinement is completed by comparing experimental results with a theoretical pattern generated from predicted phases and structures. Compositional changes due to irradiation can be evaluated. TEM investigations, including various tilting experiments, selected area electron diffraction, SAED, and brightfield and darkfield imaging are conducted to understand the size, density, nature and location of specific irradiation induced defects. SEM is used visualize the macroscopic changes in the irradiated materials. Irradiation induced changes in electrical resistivity, thermal conductivity, hardness, and modulus were correlated to the defects revealed by TEM and XRD experiments. Diffusion bonding of several MAX phases with Zircaloy-4 was used

to ascertain the chemical compatibility with the fuel cladding material for use in current reactor designs. Additionally, as helium, He, generation from decay products leads to void formation, as well as He being a potential coolant gas for several Gen IV designs, the He permeability in several MAX phases was evaluated at high temperatures.

Using previously reported density functional theory, DFT, calculations for point defects in the MAX phases, in combination with the irradiation results herein, models for the defective lattice structures that accommodate irradiation defects are proposed.

Counter to DFT predictions, the results herein suggest that  $\text{Ti}_3\text{SiC}_2$  possesses greater irradiation damage resistance compared with  $\text{Ti}_2\text{AlC}$ . It is proposed that irradiation at low temperatures results in interacting point defects, which lead to a distorted lattice by increasing the bond lengths in the c-direction, and reduce them in the a-direction. At higher temperatures, point defects are seen to agglomerate into coherent dislocation loops that, as confirmed by TEM, lie within the basal planes. It is postulated that the resultant interstitial and substitutional defects form dislocation loops between the A-layer and closest M-layer in the MAX phase structure.  $\text{Ti}_3\text{SiC}_2$  exhibits large denuded zones,  $\sim 300$  nm wide, at doses as low as 0.1 dpa at 700 °C.  $\text{Ti}_2\text{AlC}$  exhibits detrimental microcracking, observed extensively after low temperature irradiations, that leads to degradation in electrical conductivity structural stability. Similar results have not been previously reported in literature, and this work presents a new perspective on how the MAX phases accommodate irradiation defects. In totality,  $\text{Ti}_3\text{SiC}_2$  remains a potential candidate for further study.

### 1.3. Outline

---

This thesis is divided into two main parts, with additional sections in the appendices:

**Part I** (Chapters 2-3) includes background on nuclear reactor designs and fundamentals of particle irradiation, an overview of the MAX phases and their properties that show promise for nuclear applications. Additionally, the experimental methods are described, including sample fabrication, experimental set-up, and data analysis.

**Part II** (Chapters 4-8) provides and discusses the results and major findings obtained by me and my collaborators, most of which have been published in Refs [1-7]:

- Chapter 4 presents the theory of Rietveld refinement of XRD patterns, and includes results from XRD of pristine and irradiated  $\text{Ti}_3\text{SiC}_2$ ,  $\text{Ti}_3\text{AlC}_2$ ,  $\text{Ti}_2\text{AlC}$ , and  $\text{Ti}_2\text{AlN}$ . Also presented are proposed irradiated lattice structure that were developed to explain the results observed after low and high temperature irradiation.
- Chapter 5 focuses on irradiation induced defects, as investigated by TEM experiments, including black spots, dislocation loops, and defects within stacking faults and impurity phase particles. The nature of the dislocation loops in  $\text{Ti}_3\text{SiC}_2$  and  $\text{Ti}_2\text{AlC}$  are discussed.
- Chapter 6 explores the effect of neutron irradiation on physical and mechanical properties of MAX phases, including electrical resistivity, thermal conductivity, hardness, modulus and radioactivity.
- Chapter 7 presents results on the interaction of MAX phases with certain reactor components. Diffusion bonding of  $\text{Ti}_3\text{SiC}_2$  and  $\text{Ti}_2\text{AlC}$  with Zircaloy-4 is studied in an effort to determine the efficacy of using MAX phases as a fuel cladding barrier coating in existing nuclear reactor designs. The permeability of He in  $\text{Ti}_3\text{SiC}_2$ ,

$Ti_3AlC_2$ , and  $TiAlC$  is explored as it both a fission gas product and a potential Gen IV coolant medium.

- Chapter 8 summarizes the principal findings of this work and discusses future directions for going beyond the research in this thesis.

**Appendices A and B** provide additional results and experimentation that lie outside of the scope of this thesis, published in Refs [4, 5]:

- Appendix A explores a critical review of high temperature and long term oxidation of Al-containing MAX phases, and how the presence of Al is critical in providing extraordinary oxidation resistance.
- Appendix B presents results on the high temperature creep of  $Ti_{n+1}AlC_n$  ( $n=1,2$ ).

## 2. LITERATURE REVIEW

---

The following chapter provides relevant information about nuclear reactors, the MAX phases, and their applicability for use in reactor designs. A general overview of requirements for next generation nuclear reactors is presented, followed by the fundamentals of irradiation interaction with materials. An overview of the MAX phases is then summarized, specifically detailing the properties which make these ceramics advantageous candidates for existing and future reactor applications. Finally, a literature review of recent irradiation studies of the MAX phases and theoretical modelling is presented.

### 2.1. Nuclear Reactor Technologies

---

In order to meet the growing demands for future power consumption, nuclear energy might be relied upon to generate a larger share of the world's electricity. Current reactors are aging, many of the oldest nearing 40 years in use. New reactor designs are being developed to incorporate higher operating temperatures, passive safety features, and improved energy efficiency with the ability to burnup minor actinides and other fissionable material that is disposed of as waste material in existing reactors. Future Gen IV nuclear reactors will require materials that safely function at conditions beyond those of current nuclear plants. New plant designs are incorporating higher temperature coolants, resulting in higher power generation efficiency [8-11]. Materials in these environments must be able to withstand extreme temperatures, elevated irradiation doses, and resist chemical attack from corrosive coolants.



### 2.1.1. Next Generation Reactors

The six leading reactor designs under consideration in the GEN IV study are the Very High Temperature Reactor (VHTR), the Lead-cooled Fast Reactor (LFR), the Sodium-cooled Fast Reactor (SFR), the Molten Salt-cooled Reactor (MSR), the Gas-cooled Fast Reactor (GFR), and the Super Critical Water-cooled Reactor (SCWR) [8, 10]. These designs meet the criteria for Gen IV reactors: efficiency, sustainability, passive safety, high temperature process heat, and technical feasibility. However, the performance demands for materials in each of these reactors are extreme, and few materials available at present can meet the challenge. Gen IV reactors will operate at sustained temperatures of 500 – 1000°C, depending on the reactor type (Figure 2.1). They are designed to generate fast neutrons with neutron energies > 0.1 MeV compared to the 1 eV thermal neutrons in current light water reactors (LWR) [10]. Future reactors will be able to fission a larger range of fuel materials, and ultimately be more efficient in removing minor actinides from the waste products by burning them during the fuel cycle.

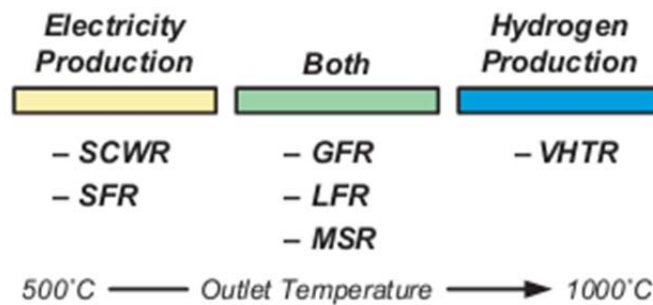


Figure 2.1 Outlet temperatures and expected production processes for the proposed Gen IV reactor designs.

To improve the efficiency of the Gen IV reactors, new fuel designs have been developed. Currently, tri-structural-isotropic, commonly referred to as TRISO, fuel pellets are being

considered for the VHTR and GFR designs (Figure 2.2). These fuel assemblies consist of small  $\text{UO}_2$  kernels surrounded by several layers of pyrolytic carbon, PyC, and chemical vapor deposition, CVD, SiC cladding [8, 12, 13]:

- Porous PyC buffer layer to allow volume for gas evolution and kernel swelling.
- Inner, dense PyC layer to retain fission gases and act as diffusion barrier for metallic fission products
- Dense CVD SiC as the primary fission product barrier and structural load-bearing layer
- Outer, dense PyC to contain fission gases and provide compressive stress on SiC during irradiation due to shrinkage.

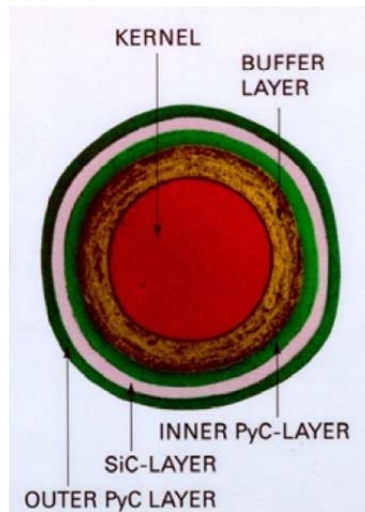


Figure 2.2 TRISO fuel particle cross section showing layers of PyC and SiC for  $\text{UO}_2$  fuel kernel containment.

TRISO fuel pellets made of SiC are able to reach temperatures of  $1600^\circ\text{C}$  before failure, and have been shown to provide containment of fission products [12, 14]. A drawback to SiC is that it is a brittle ceramic, even at higher temperatures. This causes concern in regard to

loss-of-coolant accident (LOCA) conditions, where elevated temperatures and core impacts can lead to fuel cladding failure. Additionally, SiC is vulnerable to palladium attack and silver diffusion, two reaction products that can form in sufficient quantities over the lifetime of fuel assemblies to lead to cladding degradation through interaction.

### 2.1.2. Material Requirements for Gen IV Reactors

Robust materials are critical to meet evolving reactor and fuel designs, which require materials to function in extreme environments of elevated temperatures, corrosive media, and high radiation fluences over an expected lifetime of greater than 60 years [11, 15]. Possibly the most crucial component of the reactor is the fuel cladding. The fuel cladding must be able to contain the fuel and radioactive fission products while simultaneously transferring the intense nuclear heat generated by fuel to the coolant. Cladding material candidates must possess optimal thermal conductivity, corrosion resistance, compatibility with fuel compositions, and ease of manufacturing. Fuel components must reliably operate for several years in their high dose environment, likely reaching  $>100$  dpa, while regularly exposed to high temperatures and mechanical stresses.

Select next generation reactor models are designed to use exotic coolants, such as molten sodium, molten Pb-Bi eutectic, or high temperature helium, He. As higher melting point coolant media, these allow for increased process temperatures, improving the efficiency of the reactors. New fuel cladding materials will need to demonstrate chemical compatibility with these various coolants. To that end, the He permeability of select MAX phases is discussed in Chapter 7.

## 2.2. Irradiation Effects in Reactor Materials

---

As part of this thesis, structural defects induced by neutron irradiation were studied. The following fundamentals are relevant to understanding how neutrons interact with atoms in a crystal lattice. This section presents the fundamentals of particle irradiation, and how radiation damage occurs and evolves within material systems.

### 2.2.1. Irradiation Fundamentals

Irradiation of materials can lead to significant material damage and distortion. Regardless of the type of irradiating particle, possible interactions include: no interaction, scattering, ionization of lattice members, or knock-on damage. The depth of damage varies based on the type of irradiation particles, such as electrons, heavy ions, or neutrons. Neutrons result in the largest interaction volume (Figure 2.3). Experiments in this thesis illustrate the effect of knock-on damage caused by neutron irradiation from nuclear fuels. Knock-on damage is caused when a high energy particle impacts the nucleus of a lattice atom. The energy transferred is sufficient to remove this atom from its site, sending it pummeling through the surrounding atoms. The displaced primary knock-on atom, PKA, can travel several unit cells before losing enough energy to stop. Each subsequently impacted atom is deemed a secondary knock-on atom, SKA. The procession of collisions is known as a cascade event (Figure 2.4), where many atoms are displaced from their lattice positions, generating numerous interstitial and vacancy point defects, also known as Frenkel pairs.

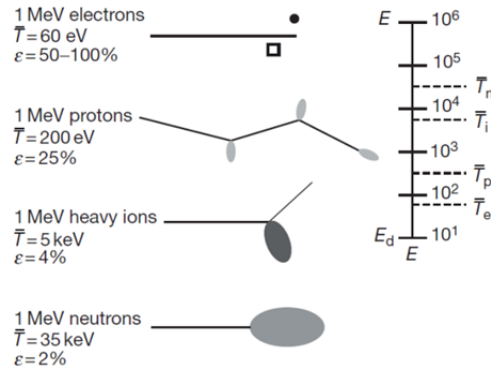


Figure 2.3 Difference in damage morphology, displacement efficiency, and average recoil energy for 1 MeV particles of different type incident on nickel [16].

The cascade is also accompanied by a thermal spike, due to the large amount of heat generated by the friction of the collisions. With this localized heating, the majority of the Frenkel pairs formed during the cascade event recombine and annihilate, leaving a few surviving point defects [17]. Over time, with continuous bombardment of irradiation, the surviving point defects accumulate, resulting in irradiation damage.

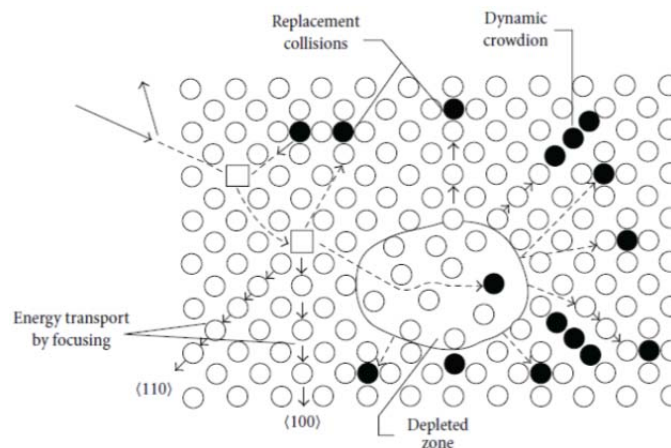


Figure 2.4 Schematic of neutron knock-on damage in a crystalline solid.

The primary knock-on atom further displaces subsequent atoms from their lattice positions, resulting in a depleted zone surrounded by various point defects. After a short time ( $\sim$ ps), localized thermal annealing from the friction of displaced atoms results in the recovery of these defects, leaving only a few Frenkel pairs in the lattice after relaxation. [17].

The Kinchin-Pease model was developed to calculate the rate of atomic displacement due to irradiation damage. Taking the energy of the neutron to be  $E_n$ , a specific threshold energy is required in order to permanently displace an atom from its lattice, known as the displacement energy,  $E_d$ , with a value of  $\sim 25\text{eV}$ . An atom will only become displaced and become a primary knock-on atom, PKA, when the energy transferred,  $T$ , is greater than  $E_d$ . This model assumes that the cascade event caused by subsequent PKA collisions is a sequence of two-body elastic collisions, and ignores energy loss to the lattice. If the flux,  $\phi(E_n)$ , of neutrons with energy  $E_n$  is the number of neutrons impacting a unit area per second, then the rate of atomic displacements,  $R$ , is given by [17]:

$$R = \frac{\#displacements}{cm^3s} = N \int_{E_{min}}^{E_{max}} \sigma_d(E_n) \phi(E_n) dE_n, \quad (1)$$

where  $N$  is the number density of target atoms,  $E_{min}$  is the minimum energy of the neutron,  $E_{max}$  is the maximum, and  $\sigma_d(E_n)$  is the energy dependent displacement cross-section, given by [17]:

$$\sigma_d(E_n) = \int_{T_{min}}^{T_{max}} \sigma(E_n) \nu(T) dT. \quad (2)$$

$T_{min}$  and  $T_{max}$  are the minimum and maximum energy transferred to the lattice atom, respectively,  $\sigma(E_n)$  is the collision cross-section of a neutron of energy  $E_n$  that results in a transfer of energy  $T$  to the struck atom, and  $\nu(T)$  is the number of displacements per primary knock-on atom. Dividing  $R$  by  $N$  gives the rate of displacements per atom, dpa/s. Knowing the length irradiation exposure, the total dpa dose level can be determined. These equations work equally well with other irradiation particles, allow for comparison of irradiation results through calculating respective dpa.

### 2.2.2. Effect of Irradiation on Materials

The types of defects that form due to irradiation depend on the irradiation temperature and fluence dose. As previously mentioned, point defects form after the initial cascade events. The density of point defects increases as a function of dose, due to the increased frequency of cascade events. Additionally, as interstitial mobility is generally higher than vacancy mobility, interstitials tend to separate from vacancies and the defects that do not recombine tend to agglomerate with like species. At lower irradiation temperatures, these defects coalesce locally to form defect clusters, also called black spots as observed in TEM. These defect clusters lead to the degradation of material properties, discussed in detail in the following sections [17]. With increasing irradiation temperature, interstitials and vacancies become more mobile, leading to a higher recombination rate after cascade events, and less residual damage. Defect sinks, such as grain boundaries and free surfaces, attract point defects from within grains, resulting in denuded zones adjacent to the sinks.

Defect clusters tend to coarsen with further annealing and irradiation. Depending on the nature of the defect cluster, a platelet of interstitials or vacancies can collect and collapse into a dislocation loop (Figure 2.5) [18]. Irradiation-induced dislocation loops impede dislocation motion and result in reduced ductility, increased hardness, and embrittlement.

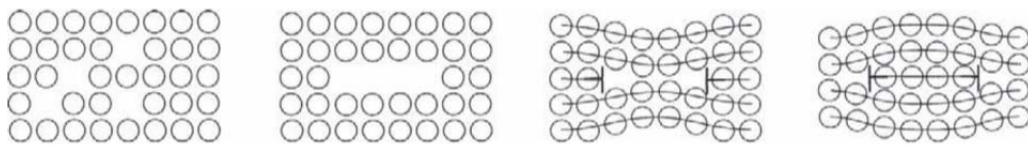


**Figure 2.5** Formation of a dislocation loop.

a) Schematic of a crystal with non-equilibrium vacancy concentration. b) Vacancies collect on a close-packed plane and c) collapse forming an edge dislocation. d) Schematic of a loop formed by a platelet of self-interstitial atoms [18].

Dislocation loops form coherently within the lattice, and can grow by (i) Ostwald Ripening by diffusion of point defects between loops and (ii) by addition of additional point defects generated by continued irradiation. At further increased irradiation temperatures, the increased mobility of vacancies leads to the formation of voids and bubbles. Structural materials exposed to irradiation face several threats to material performance, including radiation hardening and embrittlement, phase instabilities, irradiation creep, volumetric swelling from void formation, and high temperature helium embrittlement [11].

SiC is a leading candidate for Gen IV fuel cladding applications, and as such, it is important for comparison to consider the effect of irradiation on this material. Below 150 °C, at doses as low as 0.01 dpa, SiC experiences significant swelling and amorphization due to irradiation damage. Above that critical temperature, the Si and C defect mobilities increase, allowing for recombination of defects and structural recovery. The effect of irradiation temperature and fluence on defect types observed in SiC reveals several distinct defect regimes Figure 2.6.



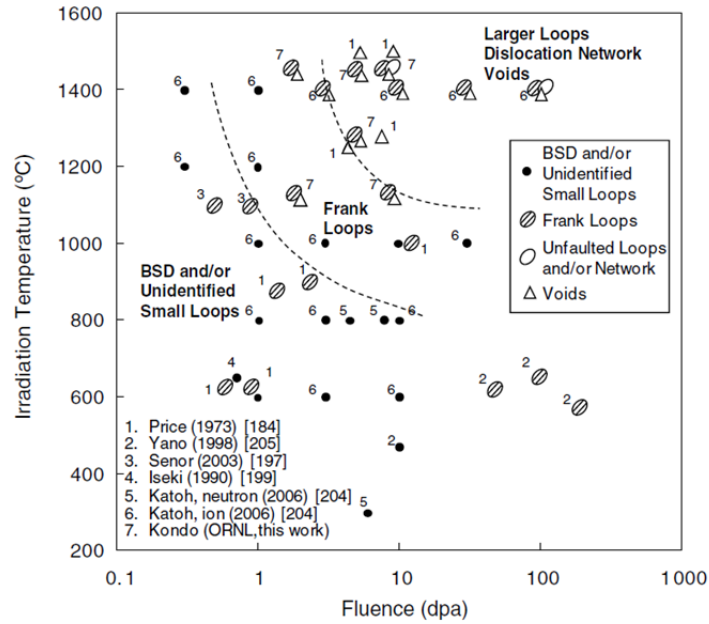


Figure 2.6 Summary of the microstructural development in cubic SiC during neutron and self ion irradiation. The resultant defect types depend upon irradiation dose, as well as temperature [14].

At fluences between 0.1 and 10 dpa, below 1000 °C, black spots and defect clusters dominate. Dislocation loops are more common above 1000 °C, as defect clusters coarsen and form interstitial and vacancy loop structures. Thermal annealing of irradiated samples results in fewer but larger loops, as they coalesce and grow. At irradiation at temperatures above 1200 °C and fluences of >10 dpa, vacancy diffusion takes over, leading to the formation of voids within the microstructure. Voids negatively affect the material properties by causing embrittlement due to dislocation pinning, decreasing thermal and electrical conductivity due to an increase in scattering. They also cause swelling. In addition, radiation can induce amorphization, which will reduce conductivity. A major drawback for SiC is its reduction in thermal conductivity under irradiation, which significantly impacts its ability to draw heat energy away from the fuel pellets [14]. Point defects scatter electrical and phonon transport, reducing electrical and thermal conductivity in irradiated samples.

### 2.2.3. Chemical Compatibility with Reactor Components

In addition to irradiation damage, materials within the reactor core can interact negatively with surrounding coolants, fuel materials, and fission products. In current LWRs, the coolant is high pressure or boiling water operating at  $\sim 300^{\circ}\text{C}$  and 7-15 MPa pressures. In comparison, the Gen IV reactors will use a coolants such as molten sodium, lead-bismuth, molten salts, and high temperature helium, He, gas to achieve operating temperatures of 500-1000 $^{\circ}\text{C}$ . Molten lead-bismuth and sodium can be quite corrosive, depending on levels of dissolved oxygen [8, 19].

Fuel interaction with the cladding is also significant, as the fuel itself swells during the fuel cycle. Conventional cladding, such as HT-9 and Zircaloy-4 for LWR fuel rods, behaves poorly under uranium diffusion conditions [20, 21]. A diffusion barrier is necessary to prevent local diffusion and cracking of the fuel cladding.

Fission products are also a major concern and fuel cladding must be able to contain large internal pressures generated by swelling fuel, and the release of fission gases [15]. Known issues with TRISO fuel operations include de-bonding [14], cracking in the SiC layer during fuel swelling [22], and Pd attack [12, 23, 24]. SiC used in TRISO fuel pellets reacts negatively with palladium, a commonly generated fission product [12, 23, 24]. Palladium readily forms  $\text{PdSi}_2$  from the surrounding SiC, causing the formation of microcracks and ultimately leading to containment failure for the fuel particles (Figure 2.7) [12, 23, 24].

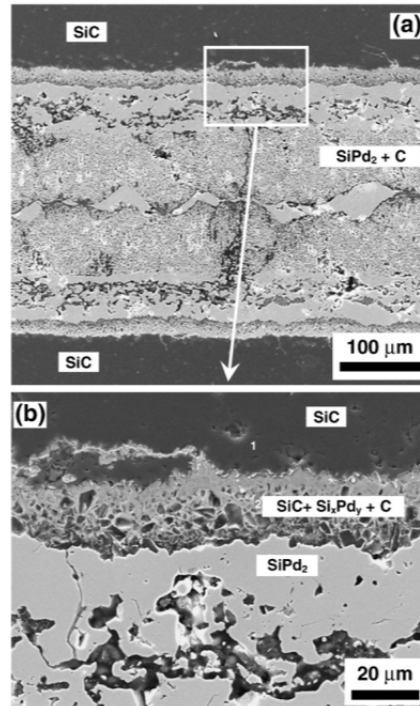


Figure 2.7 a) Optical SEM micrograph of a SiC/Pd diffusion couple annealed at 1000°C for 10 hours showing the significant SiC degradation that occurs in the presence of Pd, with b) higher magnification of region in the white box [24].

### 2.3. MAX Phases

---

This section describes the MAX phases, including their origins, structure, and notable material properties that make them potential candidates for fuel cladding and structural components for nuclear reactors.

#### 2.3.1. Structure and Discovery

The  $M_{n+1}AX_n$ , or MAX, phases are a class of layered, machinable, ternary carbides and/or nitrides where  $n = 1, 2, \text{ or } 3$ , M is an early transition metal, A is an A-group (groups 13-16) element, and X is C and/or N. Common to each structure of various  $n$  values, near-close-packed M layers are interleaved with layers of pure group-A element with the X atoms filling

all octahedral sites between the M atoms (Figure 2.8a–c). The MX layer is composed of edge sharing  $M_6X$  octahedra with a structure identical to that of rock salt [25]. The number of M layers separating A layers in each structure is dependent on the value of  $n$ ; two layers in  $M_2AX$ , three in  $M_3AX_2$ , etc. The nanolaminated structures of these MAX phases give rise to the unique combination of metallic and ceramic properties that make them such remarkable materials.

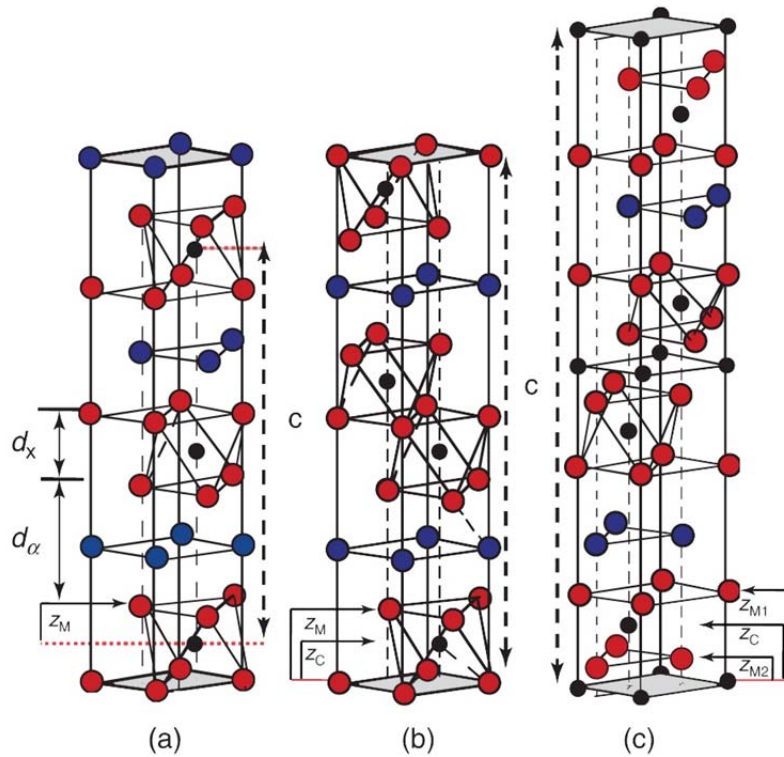


Figure 2.8 Unit cells of a)  $M_2AX$ , b)  $M_3AX_2$ , and c)  $M_4AX_3$  phases reproduced from Ref. [25]. The  $c$  parameters are depicted by vertical dashed lines.  $d_x$  denotes the thickness, from atom center to atom center, of the  $M_{n+1}X_n$  layers;  $d_a$  that of the A layers. Also shown are the various  $z$  heights for M and C atoms.

The MAX phases were first discovered in the 1960s by Nowotny and his group. He reviewed the syntheses of a large number of carbides and nitrides, a group of which were known then as the Hägg phases, which possessed the  $M_2AX$  structure [26]. For nearly 40 years, there were few published works exploring phase pure compositions that would later

become known as the MAX phases. However, in 1996, Barsoum *et al.* fabricated fully dense, single phase  $\text{Ti}_3\text{SiC}_2$  samples via reactive hot pressing, becoming the first group to characterize the phase in bulk form, revealing the combination of properties this family possesses [27]. In the recent decades, over 60 phases have been identified, which have been the subject of extensive research efforts, as they have suggested great potential in a wide range of applications. These phases represent a new class of solids described as thermodynamically stable nanolaminates, and the remarkable properties they display are due to their layered structure.

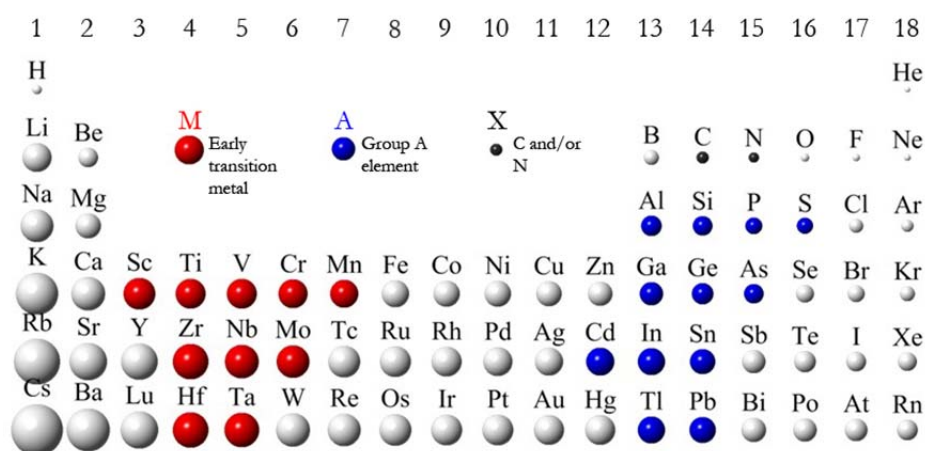


Figure 2.9 Elements of the periodic table known to react to form the various MAX phases.

### 2.3.2. Ideal Properties for Irradiation Environments

MAX phases are considered in this work for their potential suitability for the demanding performance needed in nuclear environments. Applications might include use as structural elements, fuel matrix components, or fuel cladding and coating material with anticipated superlative performance due to their high temperature capabilities, high damage tolerance,

chemical resistance, and versatile manufacturing techniques [25, 28-33]. The MAX phases exhibit a unique combination of properties, both metallic and ceramic in nature. For example, some of them exhibit relatively high fracture toughness values (8-12 MPa $\sqrt{m}$ ) and are elastically stiff like their binary carbide and nitride counterparts, and yet they are readily machinable, lightweight, and relatively soft [25, 28-33]. The MAX phases also undergo plastic-to-brittle transitions at high temperatures, and the materials can withstand high compressive stresses at room temperatures, RT [28, 33].

MAX phases also have elevated temperature characteristics that can provide significant benefits for new fuel and reactor designs. The following is a list of MAX phase attributes that are of particular interest in mitigating fuel design issues and improving fuel performance and reliability:

#### **Tailored Composition Choices for Individual Applications**

Properties can be tailored to the application by the choice of specific elements as components in a MAX phase. For example, for thermal reactor neutron economy, a low absorption cross section MAX phase, mainly composed of zirconium, silicon, and carbon, could be used. This would have a neutron absorption cross-section of about 60% of standard Zircaloy-4 on a per volume basis. Another example, for a diffusion barrier to prevent fuel cladding chemical interaction with the fuel, the MAX phase can be based on vanadium which has shown resistance to fuel diffusion [21].

#### **Thermal Conductivity at High Temperatures**

For nuclear fuel, the ability to transfer heat energy from the fuel pellet into the coolant is a prime consideration both for normal and accident operations. Degradation of thermal conductivity with exposure can be a performance margin concern. Since MAX phases have a semi-metallic crystal structure, it is expected to resist conductivity degradation with

irradiation and retain the desired higher levels of thermal conductivity better than SiC. A high conductivity will result in a cooler fuel centerline operation which extrapolates to higher fuel burn-up capability.

### **Elevated Temperature Transient (LOCA Type) Resistance**

With the Gen III fuels being operated at increased burn-up levels, the issues with high temperature transient responses are becoming more critical. The current metallic cladding alloys are challenged with the high temperature exposure to retain adequate ductility and a coolable fuel configuration at the transient temperatures of around 1200 °C, experienced during a loss of coolant accident, LOCA [34-36]. MAX phases have characteristics that provide a significant temperature resistance margin to eliminate these concerns. Based on the high resistance to oxidation of some MAX phase compounds at temperatures near 1300 °C [4, 37-48], it is likely that a MAX phase, such as  $Ti_3SiC_2$  or  $Ti_2AlC$ , chosen for fuel cladding would be able to resist the transient temperature without significant degradation. Another related issue is the hydriding effects in the metal cladding during oxidation and the resultant effects on clad ductility [34-36, 49]. With increased oxidation resistance of MAX phases, it is expected that hydrogen generation issue would be significantly reduced compared to the current Zirconium alloys

### **Hermetically Sealable**

For applications involving fuel cladding, it is of prime importance that the cladding be sealable to retain the fission products generated in the fuel and to prevent fuel-coolant contact and interaction. The current metal alloy claddings are weldable and provide a reliable barrier between the coolant and the fuel pellets. Ceramic based cladding designs such as SiC have a significant challenge to develop a productionized clad sealing system. Unlike most ceramics, MAX phases have the ability to be induction heated and have shown the ability to bond with a variety of materials [6, 50-54]. Induction heating of a MAX phase

carbide tube and end plug has the potential to provide the needed hermetic seal with a process amenable for use in a commercial production line. The ability to form a bonded joint with induction heating is also an advantage in structural component applications.

### **Machinability**

MAX phase compounds can be machined using conventional techniques, as simple as a hacksaw. This characteristic provides a significant advantage for applications as high temperature fuel structural support components, which might require complex shapes.

### **Ductility**

Another desirable characteristic of the MAX phase is that some ductility exists at the high transient temperatures [5, 30, 55-59]. This characteristic offers advantages, for example, as a fuel pellet coating that will accommodate fuel swelling without cracking. Compared to SiC, the MAX phases could provide strain margins and improved toughness for protection against clad breaches and cracks during the transient.

### **Dimensional Stability**

Dimensional stability, when discussed in terms of nuclear fuels, primarily refers to the absence of significant dimensional distortions of the material in the presence of a high radiation flux, in addition to the normal thermal expansion distortions. While it is necessary to obtain irradiation data on specific MAX phases, initial evaluations using ion irradiation tests indicate that MAX phases should retain good dimensional stability under high temperature irradiation. Regarding dimensional changes with elevated temperatures, MAX phases have thermal expansion coefficients, TEC, ranging from  $\approx 5-15 \times 10^{-6}/\text{K}$ , about twice that of SiC. For some applications higher TECs may have an advantage in accommodating swelling strains during operation, and for bonding to other fuel cladding materials.



It is the combination of the above properties that have garnered attention for the MAX phases' possible use in reactor applications, both in current and next generation designs. As interest in these materials for nuclear applications has grown over the past several years, irradiation studies have explored the effect of heavy ion and helium irradiation on several MAX phase compositions. Initial irradiation studies are discussed below.

### 2.3.3. Ion Irradiation Studies

Many recent studies have explored the damage tolerance and amorphization resistance of several MAX phases irradiated with heavy ions [22, 60-69]. In 2009, Nappé *et al.* explored the effect of 90 MeV Xe ions on  $\text{Ti}_3\text{SiC}_2$ , showing surface layer amorphization of the  $\text{Ti}_3\text{SiC}_2$  and impurity phases, as well as, selective grain boundary sputtering due to nuclear interactions [60]. Liu *et al.* characterized Al-doped  $\text{Ti}_3\text{SiC}_2$ , irradiated to a maximum dose of 3.25 dpa with high energy Kr and Xe ions, via X-ray diffraction, XRD, and nanoindentation showing an expansion of the c-lattice parameter, c-LP, and irradiation induced hardness increase that could be annealed out at 800 °C [64, 65]. They also reported the possible existence of a  $\beta$ - $\text{Ti}_3\text{SiC}_2$  phase to explain the presence of new peaks found in the post-irradiated XRD patterns [65].

Soon after, Le Flem *et al.* reported on selected area electron diffraction, SAED, patterns using transmission electron microscopy, TEM, of  $\text{Ti}_3(\text{Si,Al})\text{C}_2$  irradiated with 92 MeV Xe ions up to 6.67 dpa, which further confirmed this MAX phases' resistance to amorphization [66]. With increasing dose, diffraction peaks were found to disappear due to lattice disturbances. In 2010, Bugnet *et al.* explored the effect of 100 keV  $\text{Ar}^{2+}$  ion irradiation on multilayered  $(\text{Ti,Al})\text{N}/\text{Ti}_2\text{AlN}_x$  nitrogen-deficient thin films, reporting that the multilayered structure was preserved up to a dose of 12 dpa, likely due to nitrogen vacancies acting as sinks for interstitial point defects [69].

Along the same lines, Whittle *et al.* reported that  $\text{Ti}_3\text{AlC}_2$  and  $\text{Ti}_3\text{SiC}_2$  possess very high resistance to amorphization, even up to 25 dpa, irradiated with 1 MeV  $\text{Kr}^{2+}$  and 1 MeV  $\text{Xe}^{2+}$  [22]. Nappé *et al.* reported that nuclear collisions with 4 MeV Au ions, up to a dose of 4.3 dpa, resulted in a 2.2% swelling in  $\text{Ti}_3\text{SiC}_2$  [61]. Also in 2011, Nappé *et al.* investigated the structural changes of  $\text{Ti}_3\text{SiC}_2$  under a variety of ions and energies, concluding that  $\text{Ti}_3\text{SiC}_2$  is not sensitive to electrical interactions, and confirmed that nuclear collisions lead to an increase in c-LP and a decrease in the a lattice parameter, a-LP, and a concomitant increase in lattice microstrains [63]. In 2012, Zhang *et al.* reported that a TiC and/or 3C-SiC (cubic  $\beta$ ) nanocrystalline phase formed under 2 MeV  $\text{I}^{2+}$  irradiation of  $\text{Ti}_3\text{SiC}_2$ , though the material did not fully decompose, even up to 10.3 dpa [68]. In 2013, Le Flem reported on a saturation in irradiation damage at 3.2 dpa via hardness measurements and cell volume expansion due to defect formation under 92 MeV Xe ions in  $\text{Ti}_3\text{SiC}_2$  [67].

It is important to note, that in contrast to neutrons, which pass through the bulk, the penetration depth of heavy ion and helium, He, irradiation is limited to the surface, and He atoms tend to accumulate and form bubbles inside the material after momentum transfer. This has been illustrated by Xiao *et al.* via *ab initio* methods, showing the He most energetically favors Al-site interstitials in  $\text{Ti}_3\text{AlC}_2$  [70]. More recently, Wang *et al.* irradiated  $\text{Ti}_3\text{AlC}_2$  samples with 50 keV He ions with fluences ranging from  $8 \times 10^{16} \text{ cm}^{-2}$  to  $1 \times 10^{18} \text{ cm}^{-2}$ , resulting in the formation of spherical He bubbles, string-like bubbles and faulting zones [71]. Grazing incidence XRD analysis and SAED confirmed significant structural disorder without amorphization, even up to 52 dpa.

Patel *et al.* irradiated  $\text{Ti}_3\text{AlC}_2$  samples with 200 keV He ions to a maximum dose of 5.5 dpa at 500 °C, and showed, by careful analysis of XRD patterns, that the  $\text{Ti}_3\text{AlC}_2$  structure was maintained, but with an increased c-LP and a decreased a-LP, together with a highly disordered Al layer [3]. If He bubbles exist, they were  $< 1 \text{ nm}$  in diameter and did not

agglomerate as observed by Wang *et al.* at RT [71]. Very recently, Yang *et al.* reported on the structural transitions of  $\text{Ti}_3\text{AlC}_2$  irradiated with 50 keV He ions over a wide fluence range. While no amorphization was detected up to 31 dpa, antisite defects readily destroyed the nanolamellar  $\text{Ti}_3\text{AlC}_2$  structure, and a transition to  $\beta\text{-Ti}_3\text{AlC}_2$  was observed above 2.61 dpa.

In addition to heavy ion and He irradiation studies, Hoffman *et al.* have shown that neutron activation of  $\text{Ti}_3\text{SiC}_2$ ,  $\text{Ti}_3\text{AlC}_2$ , and  $\text{Ti}_2\text{AlC}$  compare well to SiC and are three orders of magnitude lower than Inconel alloy 617. SiC and Inconel 617 are two candidate materials for use in next generation reactors [2].

The general conclusions from these irradiation studies are that the MAX phases show tolerance to irradiation damage and amorphization, remaining crystalline even up to 52 dpa. Additionally, in all cases the irradiation resulted in an expansion in the c-lattice parameter, and a reduction in the a-lattice parameter, along with increased microstrains. Further, disruption of the layered MAX phase structure has been observed as well as the formation of a  $\beta$ -MAX phase polymorph after irradiation. In none of the ion irradiation studies to date has there been any mention or evidence of irradiation-induced dislocation loops. Also lacking from literature are any reports of neutron irradiation of MAX phases.

## 2.4. Conclusions

Nuclear power remains a viable production source in the near-term and future. In order to meet demands for growing energy consumption, nuclear power should be considered to provide a larger share of energy production. To improve their safety and performance, current and next generation nuclear reactors require advanced materials capable of withstanding the extreme environments imposed on fuel cladding and structural elements. The MAX phases possess a remarkable combination of properties that are desirable for in-core applications. Preliminary irradiation studies show that several MAX phase compositions are resistant to irradiation damage. For use in nuclear reactors, however, a full

understanding of the irradiation response to neutrons is necessary. This thesis investigates the first ever neutron irradiation of bulk MAX phases as a first step for generating a fundamental knowledge base of the neutron irradiation response.

### 3. MATERIALS AND METHODS

---

This chapter summarizes the experimental techniques and methods used within this thesis. All MAX phase samples used in this thesis were made in house at Drexel University. This allowed for control of sample compositions and part geometries. Here, a summary of preparation procedures for each set of samples is provided. The neutron irradiation conditions for both test reactors (MITR and INL ATR) are described in detail. Post-irradiation experiments, including X-ray diffraction, focused ion beam, transmission electron microscopy, resistivity measurements, thermal diffusivity, and nanoindentation are also described. Procedures for the diffusion couple and permeability experiments on non-irradiated samples are described as well.

#### 3.1. MAX Phase Fabrication

---

Hot pressing, HP, of elemental or pre-made powders yielded large blanks of predominately single-phase samples, which were then machined into test geometries for a wide range of experiments. In general, large batches of each MAX phase were produced so that multiple experiments could be conducted on the same sample batch. As noted above, all samples were prepared in house at Drexel University.

Specifically for this thesis, randomly oriented samples of  $\text{Ti}_3\text{SiC}_2$ ,  $\text{Ti}_3\text{AlC}_2$ ,  $\text{Ti}_2\text{AlC}$ ,  $\text{Ti}_2\text{AlN}$ ,  $\text{Cr}_2\text{AlC}$ ,  $(\text{Nb}_{0.5}\text{Zr}_{0.5})_2\text{AlC}$ ,  $(\text{Nb}_{0.75}\text{Zr}_{0.25})_2\text{AlC}$ ,  $(\text{Nb}_{0.75}\text{Zr}_{0.25})_2\text{AlC}$ , and  $(\text{Ti}_{0.75}\text{Zr}_{0.25})_2\text{AlC}$  were made via HP (Figure 3.1a). A graphite die (ISO-63, Toyo Tanyo, Troutdale, OR, USA) with an oblong rectangular shape was used, measuring 70 mm long  $\times$  25 mm wide, with rounded

ends (Figure 3.1b). The thickness of the blank could be controlled by adjusting the amount of powder mixture added, and was usually limited to  $\sim 350$  g of powder. After HPing, samples were usually  $\sim 40$  mm thick.



Figure 3.1. a) Uniaxial hot press, HP, used to produce MAX phase samples and, b) graphite dies used for producing MAX same.

### 3.1.1. Irradiation Specimens: MITR, Massachusetts Institute of Technology

Samples of  $\text{Ti}_3\text{SiC}_2$ ,  $\text{Ti}_3\text{AlC}_2$ ,  $\text{Ti}_2\text{AlC}$ , and  $\text{Ti}_2\text{AlN}$  were produced for irradiation at MITR. Samples of  $\text{Ti}_2\text{SC}$  were also produced, but resulted in abnormally high activation after irradiation, and were subsequently dropped from the characterization plans. Samples of chemical vapor deposition, CVD, cubic phase SiC (also called  $\beta$ -SiC) for TEM and resistivity experiments were purchased from Dow Chemical as a reference for comparison. In this case, due to time constraints out of our control, these samples were not characterized after irradiation. This is not a great loss, however, since as discussed in this thesis, the influence of neutrons on SiC is fairly well documented.

**$\text{Ti}_2\text{AlC}$ :** Samples of  $\text{Ti}_2\text{AlC}$  were prepared by pouring pre-reacted  $\text{Ti}_2\text{AlC}$  powders (Kanthal, Hallstahammar, Sweden) into graphite dies, which were loaded into a vacuum hot press and

hot pressed, HPed, at 1300 °C for 4 h under a load corresponding to a stress of  $\sim 40$  MPa and a vacuum of  $10^{-1}$  Pa.

**Ti<sub>3</sub>AlC<sub>2</sub>:** The Ti<sub>3</sub>AlC<sub>2</sub> samples were fabricated by ball milling stoichiometric mixtures of pre-reacted Ti<sub>2</sub>AlC and TiC powders (Alfa Aesar, Ward Hill, MA, USA) for 24 h. The latter were, in turn, HPed at 1400 °C for 4 h under a load corresponding to a stress of  $\sim 40$  MPa and a vacuum of  $10^{-1}$  Pa.

**Ti<sub>2</sub>AlN:** The Ti<sub>2</sub>AlN samples were fabricated by milling stoichiometric mixtures of Ti and AlN powders (Alfa Aesar, Ward Hill, MA, USA) as above, and then HPed them at 1300 °C for 4 h under a load corresponding to a stress of  $\sim 40$  MPa and a vacuum of  $10^{-1}$  Pa.

**Ti<sub>3</sub>SiC<sub>2</sub>:** Fine-grained samples of Ti<sub>3</sub>SiC<sub>2</sub>, henceforth referred to as FG-Ti<sub>3</sub>SiC<sub>2</sub>, were prepared by ball milling stoichiometric mixtures of Ti (99.9%, -325 mesh, Alfa Aesar, Ward Hill, MA, USA), Si (99.5%, -325 mesh, Alfa Aesar, Ward Hill, MA, USA), and C powders (99.9%, Alfa Aesar, Ward Hill, MA, USA) for 24 h, which were then HPed at 1450 °C for 6 h under a load corresponding to a stress of  $\sim 40$  MPa and a vacuum of  $10^{-1}$  Pa. Coarse-grained Ti<sub>3</sub>SiC<sub>2</sub>, henceforth referred to as CG-Ti<sub>3</sub>SiC<sub>2</sub>, were prepared from elemental mixtures as above, and HPed at 1500 °C for 4 h, followed by an anneal at 1600 °C for 8 h in an argon atmosphere in order to grow the grains.

**Ti<sub>2</sub>SC:** Samples of Ti<sub>2</sub>SC were prepared by pouring pre-reacted Ti<sub>2</sub>SC powders (Kanthal, Hallstahammar, Sweden) into graphite dies, which were loaded into a vacuum hot press and hot pressed, HPed, at 1500 °C for 4 h under a load corresponding to a stress of  $\sim 40$  MPa and a vacuum of  $10^{-1}$  Pa.

### 3.1.2. Irradiation Specimens: ATR, Idaho National Laboratory

Samples of  $\text{Ti}_3\text{SiC}_2$  and  $\text{Ti}_3\text{AlC}_2$  were prepared for irradiation experiments at INL ATR, using similar methods as for the MITR set. Samples of CVD cubic phase SiC for TEM and resistivity experiments were purchased from Dow Chemical as a reference for comparison.

**$\text{Ti}_3\text{AlC}_2$ :** The  $\text{Ti}_3\text{AlC}_2$  samples were fabricated by ball milling stoichiometric mixtures of pre-reacted  $\text{Ti}_2\text{AlC}$  (Kanthal, Hallstahammar, Sweden) and TiC powders (Alfa Aesar, Ward Hill, MA, USA) for 24 h. The mixture was HPed at 1400 °C for 4 h under a load corresponding to a stress of  $\sim 40$  MPa and a vacuum of  $10^{-1}$  Pa.

**$\text{Ti}_3\text{SiC}_2$ :** Samples of  $\text{Ti}_3\text{SiC}_2$  were prepared by ball milling stoichiometric mixtures of Ti (99.9%, -325 mesh, Alfa Aesar, Ward Hill, MA, USA), Si (99.5%, -325 mesh, Alfa Aesar, Ward Hill, MA, USA), and C powders (99.9%, Alfa Aesar, Ward Hill, MA, USA) for 24 h, which were then HPed at 1450 °C for 6 h under a load corresponding to a stress of  $\sim 40$  MPa and a vacuum of  $10^{-1}$  Pa.

### 3.1.3. Irradiation Specimens: Machining

For both irradiation experiments, small test parts were machined from hot pressed blanks in order to fit into restrictive capsule designs (Figure 3.2). Test specimens were electro-discharged machined, EDM, into  $1.5 \times 1.5 \times 25.4$  mm<sup>3</sup> resistivity bars,  $16 \times 6 \times 0.7$  mm<sup>3</sup> tensile dogbones, and 3 mm dia.  $\times$  0.3 mm thick discs for TEM observation (Figure 3.3). Details of the arrangement of these samples into the irradiation capsules are provided later.





Figure 3.2 Hot pressed blank of  $\text{Ti}_3\text{SiC}_2$ , with miniature tensile bars machined from a similar blank.

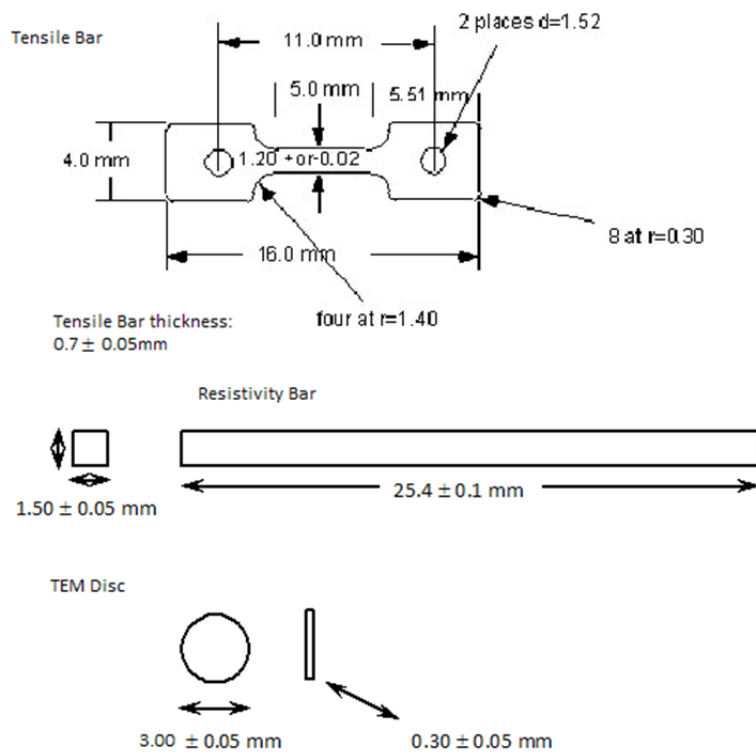


Figure 3.3 Sample geometries for MITR and ATR irradiation studies.

### 3.1.4. Diffusion Couple Specimens

In order to determine the interaction between Zircaloy-4, Zr-4, a common fuel cladding material, and  $\text{Ti}_3\text{SiC}_2$  or  $\text{Ti}_2\text{AlC}$ , diffusion couples were investigated. Samples of  $\text{Ti}_3\text{SiC}_2$  and  $\text{Ti}_2\text{AlC}$  were fabricated specifically for diffusion couple experiments.

**$\text{Ti}_3\text{SiC}_2$ :** Samples of  $\text{Ti}_3\text{SiC}_2$  were prepared by pouring pre-reacted  $\text{Ti}_3\text{SiC}_2$  powders (Kanthal, Hallstahammar, Sweden) into a graphite die that, in turn, was HPed at 1500 °C for 4 h under a uniaxial load corresponding to a stress of  $\sim 40$  MPa and a vacuum of  $10^{-1}$  Pa.

**$\text{Ti}_2\text{AlC}$ :** Samples of  $\text{Ti}_2\text{AlC}$  were prepared by pouring prereacted  $\text{Ti}_2\text{AlC}$  powders (Kanthal, Hallstahammar, Sweden) into a graphite die that was HPed at 1300 °C for 4 h under a uniaxial load corresponding to a stress of  $\sim 40$  MPa and a vacuum of  $10^{-1}$  Pa.

Samples were sectioned via high-speed diamond saw into nominally  $12 \times 12 \times 3$  mm<sup>3</sup> plates. Zr-4 samples (Westinghouse, Cranberry Township, PA, USA) were machined from a 10 mm diameter rod stock into 3 mm thick discs via EDM. The top and bottom faces of all samples were then ground parallel with 1200 grit silicon carbide grit paper and polished to a final surface finish with a 3  $\mu\text{m}$  diamond suspension to form parallel surfaces.

### 3.1.5. Thermal Diffusivity Specimens

Samples of  $\text{Ti}_3\text{SiC}_2$ -FG,  $\text{Ti}_3\text{SiC}_2$ -CG,  $\text{Ti}_3\text{AlC}_2$ ,  $\text{Ti}_2\text{AlC}$ , and  $\text{Ti}_2\text{AlN}$  were taken from leftover blanks from the MTR samples sets and machined into 12.5 mm dia.  $\times$  3mm thick discs for diffusivity measurements. In addition several solid solutions containing Nb, Zr, and Ti, as well as  $\text{Cr}_2\text{AlC}$ , were fabricated for thermal diffusivity, and machined to size.

**$(\text{Nb}_{0.5}\text{Zr}_{0.5})_2\text{AlC}$ :** Samples of  $(\text{Nb}_{0.5}\text{Zr}_{0.5})_2\text{AlC}$  were prepared by ball milling mixtures of Nb, Zr, Al (-325 mesh, 99.5%, Alfa Aesar, Ward Hill, MA), and graphite (-325 mesh, 99%, Alfa Aesar, Ward Hill, MA, USA) powders in a 1 Nb: 1 Zr : 1.1 Al: 1 C ratio for 24 h with zirconia milling media. The homogeneous mixture was then heated in an alumina crucible at

5 °C/min up to 1600 °C for a total of 4 h in a tube furnace under flowing argon, Ar, atmosphere to pre-react the powders. The resultant porous block was mechanically end-milled into powder, sieved through a -325 mesh, poured into a graphite die and HPed at 1400 °C for 4 h under a load corresponding to  $\sim 40$  MPa and a vacuum of  $10^{-1}$  Pa.

**(Nb<sub>0.75</sub>Zr<sub>0.25</sub>)<sub>2</sub>AlC:** Samples of (Nb<sub>0.75</sub>Zr<sub>0.25</sub>)<sub>2</sub>AlC were prepared by ball milling mixtures of Nb, Zr, Al (-325 mesh, 99.5%, Alfa Aesar, Ward Hill, MA), and graphite (-325 mesh, 99%, Alfa Aesar, Ward Hill, MA, USA) powders in a 1.5 Nb: 0.5 Zr : 1.1 Al: 1 C ratio for 24 h. The homogeneous mixture was then pre-reacted, milled and HPed as above at 1400 °C for 4 h.

**(Ti<sub>0.75</sub>Zr<sub>0.25</sub>)<sub>2</sub>AlC:** Samples of (Ti<sub>0.75</sub>Zr<sub>0.25</sub>)<sub>2</sub>AlC were prepared by ball milling mixtures of Ti, Zr, Al (-325 mesh, 99.5%, Alfa Aesar, Ward Hill, MA), and graphite (-325 mesh, 99%, Alfa Aesar, Ward Hill, MA, USA) powders in a 1.5 Ti: 0.5 Zr : 1.1 Al: 1 C ratio for 24 h. The homogeneous mixture was then pre-reacted, milled and HPed as above at 1400 °C for 4 h.

**Cr<sub>2</sub>AlC:** Samples of Cr<sub>2</sub>AlC were prepared by ball milling a 2:1:1 stoichiometric mixture of Cr (-325 mesh, 99%, Alfa Aesar, Ward Hill, MA), Al (-325 mesh, 99.5%, Alfa Aesar, Ward Hill, MA), and graphite (-325 mesh, 99%, Alfa Aesar, Ward Hill, MA) powders for 24 h. This mixture was then poured into a graphite mold and HPed at 1400 °C for 4 h.

Test specimens were machined via EDM into 12.5 mm dia.  $\times$  3 mm thick discs and polished down to a final surface preparation of 3 $\mu$ m diamond suspension on both sides to form parallel faces. Prior to testing with the laser flash analysis technique, the surfaces of each sample were plasma coated with graphite to ensure absorption of the laser pulses.

### 3.1.6. Helium Permeability Specimens

Samples of  $\text{Ti}_3\text{SiC}_2$ ,  $\text{Ti}_3\text{AlC}_2$ , and  $\text{Ti}_2\text{AlC}$  were prepared for helium, He, permeation experiments. Discs of 12 mm dia.  $\times$  3 mm thickness were machined via EDM, and both faces were polished parallel down to a final preparation of 3  $\mu\text{m}$  diamond suspension.

**Ti<sub>2</sub>AlC:** Samples of  $\text{Ti}_2\text{AlC}$  were prepared by pouring pre-reacted  $\text{Ti}_2\text{AlC}$  powders (Kanthal, Hallstahammar, Sweden) into a graphite die and HPed at 1300 °C for 4 h under a load corresponding to a stress of  $\sim$  40 MPa and a vacuum of  $10^{-1}$  Pa.

**Ti<sub>3</sub>AlC<sub>2</sub>:** The  $\text{Ti}_3\text{AlC}_2$  samples were fabricated by ball milling stoichiometric mixtures of pre-reacted  $\text{Ti}_2\text{AlC}$  and  $\text{TiC}$  powders (Alfa Aesar, Ward Hill, MA, USA) for 24 h. The mixture was, in turn, HPed as above at 1400 °C for 4 h.

**Ti<sub>3</sub>SiC<sub>2</sub>:** Samples of  $\text{Ti}_3\text{SiC}_2$  were prepared by pouring pre-reacted  $\text{Ti}_3\text{SiC}_2$  powders (Kanthal, Hallstahammar, Sweden) into a graphite die and HPed as above at 1500 °C for 4 h.

## 3.2. Metallography

---

The MAX phases polish remarkably well, due to the presence of metallic bonding. They are readily machined to a mirror finish. Metallography was performed to assess the grain size and microstructure of samples after fabrication. Samples were sectioned using a high speed diamond saw (Accutom-5, Struers Inc., Cleveland, Ohio, USA) and encapsulated in a metallographic mount of either a 2-part slow cure epoxy, or Bakelite mount via a hot mounting press (Labopress-3, Struers Inc., Cleveland, Ohio, USA). Samples were polished to a final surface preparation of 3  $\mu\text{m}$  diamond suspension for observation under an optical microscope, OM, using an automatic polisher (Rotopol-2 with Pedemat, Struers Inc.,

Cleveland, Ohio, USA). The grinding and polishing procedure using various SiC grinding paper and diamond suspension is detailed in Table 3.1.

**Table 3.1 Metallographic procedure used for polishing MAX phases within this thesis.**

Grit	Time (Min.)	Force (N)	Rotation**	Water
600	3	30	Counter CW	On
800	5	30	Counter CW	On
1200	8	25	CW	On
*3 $\mu$ m	10	25	CW	Off

\*DP-Suspension A, diamond suspension applied to MD-Plus lapping cloth, used with alcohol based DP-Lubricant Blue. (Struers Inc., Cleveland, Ohio, USA)

\*\*Direction of polishing head rotation with respect to the clock wise, CW, rotation of the polishing wheel.

The MAX phase microstructure was exposed with an etchant composed of a 1:1:1 parts-by-volume solution of hydrofluoric acid (50 vol.%, Thermo Fisher Scientific Inc., Waltham, MA, USA), nitric acid (70 vol.%, Thermo Fisher Scientific Inc., Waltham, MA, USA), and deionized water, which was applied with a cotton swab to the surface for < 30 s and rinsed. This etchant resulted in vibrantly colored MAX phase grains, notably in  $Ti_3AlC_2$  and  $Ti_3SiC_2$ , with well-exposed grain boundaries. After etching, impurity TiC grains appeared as bright white grains, and were easily distinguished from their surrounding MAX phase grains. The length,  $d_l$ , and thickness,  $d_t$ , of >100 grains per sample were measured from OM micrographs. The equivalent grain size was calculated as the geometric mean value of the grain dimensions, i.e.  $\sqrt[3]{d_l^2 \cdot d_t}$ .

Optical microscopy, OM, micrographs of the MITR irradiation samples were fully dense, with some evidence of pull out, and predominately single phase, with randomly aligned plate like grains (Figure 3.4). The average grain sizes of the FG- $Ti_3SiC_2$  and CG- $Ti_3SiC_2$ , were  $8 \pm 3$

and  $50 \pm 20 \mu\text{m}$ , respectively. The average grain sizes of  $\text{Ti}_2\text{AlC}$ ,  $\text{Ti}_2\text{AlN}$  and  $\text{Ti}_3\text{AlC}_2$  were  $10 \pm 4$ ,  $15 \pm 2$  and  $16 \pm 6 \mu\text{m}$ , respectively.

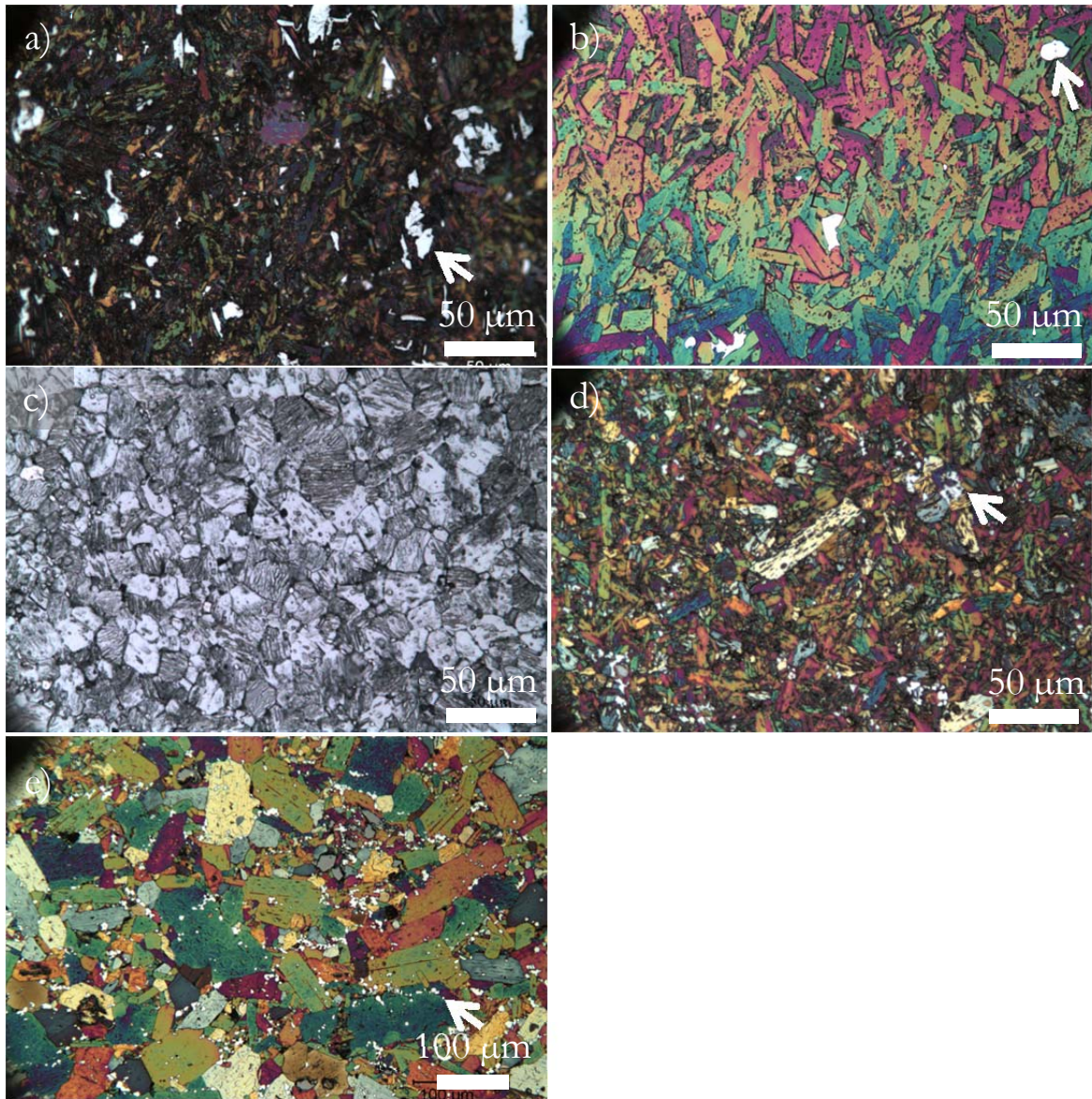


Figure 3.4 Representative optical micrographs of a)  $\text{Ti}_2\text{AlC}$ , b)  $\text{Ti}_3\text{AlC}_2$ , c)  $\text{Ti}_2\text{AlN}$ , d) FG- $\text{Ti}_3\text{SiC}_2$ , and e) CG- $\text{Ti}_3\text{SiC}_2$  microstructures after etching with a solution of hydrofluoric acid, nitric acid, and water. The MAX phase samples were fully dense and predominately single phase, with randomly aligned plate like grains, which are vibrantly colored after etching. TiC appears as bright white grains, denoted by white arrows.

### 3.3. X-ray Diffraction

---

X-ray diffraction, XRD, is a powerful nondestructive technique that provides a wealth of knowledge about material composition and structure. As a bulk method, XRD can probe a large volume of the material and provides statistically relevant results of phase composition, lattice distortion, and microstrains.

#### 3.3.1. X-ray Diffraction Experiments

XRD patterns from the surfaces of samples of  $\text{Ti}_2\text{AlC}$ ,  $\text{Ti}_3\text{AlC}_2$ ,  $\text{Ti}_2\text{AlN}$ ,  $\text{Ti}_3\text{SiC}_2$ -FG and  $\text{Ti}_3\text{SiC}_2$ -CG were obtained using two identical, but separate diffractometers (Bruker D8, Madison, WI, USA) in the Bragg–Brentano configuration, for pristine and irradiated conditions. The diffractograms were collected using step scans of  $0.02^\circ$  in the  $5^\circ$ – $120^\circ$   $2\theta$  range, with a step time of 2 s. Scans were made with Cu  $K\alpha$  radiation ( $\lambda = 1.54$  nm, 45 kV and 40 mA).

#### 3.3.2. Profile Refinement

Standards, such as single crystal  $\text{LaB}_6$ , can be used to evaluate systemic errors present in the XRD data. Rietveld refinement is used to evaluate the peak locations, full width half maximums (FWHM), peak shape, and intensity ratios of the peaks in collected XRD patterns. A theoretical pattern, produced by the combination of structure factors of phases predicted to be present in the sample, is fitted to the experimental data. Through iterative calculations, the structures and phases are incrementally refined until a goodness of fit is reached. The resultant theoretical pattern is used to determine accurate phase composition, lattice parameters, atomic positions, atomic displacement parameters, occupancies, microstrain, and nanocrystallite size. Results of refinement of the XRD patterns collected from the irradiated samples are presented in Chapter 4.

The accuracy of each diffractometer in determining lattice parameters, and their instrumental peak-shape function parameters were calibrated using a LaB<sub>6</sub> standard (NIST 660A). All diffractograms were analyzed by the Rietveld refinement method, using the FULLPROF code [72, 73]. A systematic shift of 0.02% was found, and corrected for, in the evaluation of lattice parameters, LP, as compared to the reported values of the LaB<sub>6</sub> standard. For each data set, a model containing TiC and each specific MAX phase, *e.g.*, Ti<sub>3</sub>SiC<sub>2</sub>, Ti<sub>3</sub>AlC<sub>2</sub>, or Ti<sub>2</sub>AlC was refined. For Ti<sub>2</sub>AlN, the model was refined with TiN and Ti<sub>4</sub>AlN<sub>3</sub> phases.

The Thompson-Cox-Hastings pseudo-Voigt model was used to refine the peak-shape of each phase's reflections. Lattice strains and particle sizes were also estimated assuming isotropic Lorentzian and Gaussian contributions to the peak shape function [74]. The micro strain was calculated from the full width half max, FWHM, parameter U from each sample, according to the following equation:

$$\% \mu \epsilon = \frac{\pi}{1.8} \left( \sqrt{U_{sample} - U_{std}} \right) \quad (3.1)$$

where  $U_{std}$  was refined from the LaB<sub>6</sub> standard. If  $U_{sample}$  refined lower than  $U_{std}$ , the microstrain was unresolvable for that specimen. The  $U_{std}$  values were 0.006(2) and 0.014(2) for the standards scanned on the diffractometers for pristine and irradiated samples, respectively.

### 3.4. Neutron Irradiation Experiments

---

In this work, two concomitant neutron irradiation experiments were carried out. By coordinating two reactor studies, a wider range of doses and temperatures were explored within a limited timeframe. Designators for irradiation conditions studied within this thesis



are summarized in Table 3.2. The response of  $\text{Ti}_3\text{SiC}_2$  and  $\text{Ti}_3\text{AlC}_2$  to neutron irradiation was explored in the Advanced Test Reactor (ATR) at Idaho National Laboratory (INL) at temperatures up to 1000 °C as a function of neutron fluence up to 9 dpa Table 3.3. The response of a wider array of MAX phase compositions to neutron irradiation was investigated in the research reactor, MITR, at Massachusetts Institute of Technology Nuclear Reactor Laboratory at temperatures up to 710 °C as a function of dose up to 0.7 dpa Table 3.3. The irradiation conditions for each sample set are summarized below.

#### 3.4.1. MITR Irradiation Experiments


The irradiation occurred in three phases at the 6 MW MITR Research Reactor. The neutron spectrum similar to that of a light water power reactor (Figure 3.5). Phase I was from 10/13-12/4 2010, Phase II from 12/4/2010-3/8/2011, and Phase III from 3/8-12/22 2011. Details of the irradiation phases are provided in Table 3.4. The low dose, M-D1, sample sets were exposed only in Phase I; the medium dose, M-D2, sample sets were exposed in Phase III; and the high dose, M-D3, samples were exposed in all three phases.

The samples were irradiated in an inert gas atmosphere consisting of a mixture of high purity (>99.99%) helium, He, and neon, Ne, and were in contact only with clean titanium, Ti, (CP Grade 2). The effluent gas was periodically monitored for impurities using a residual gas analyzer, capable of analyzing oxygen and water of a few ppm. The irradiation temperature was monitored using a thermocouple in each capsule. Calculations using Fluent <sup>TM</sup> show that the temperature variation across each sample capsule was less than about +/-10 K. While 60 and 650 °C were the initial temperature targets for this experiment, the capsule designs and their positions within the reactor resulted in higher temperatures being reached, as given in Table 3.4. The average capsule temperatures for T2 and T4, the two temperature regimes targeted at MITR, were 350(40) and 710(50) °C, respectively.

Table 3.2 Irradiation temperature and dose designators.

Dose Designator	Nominal Dose (dpa)	MITR	ATR	Temp. Designator	Nominal Temp. (°C)	MITR	ATR
D1	0.1	✓	✓	T1	100	-	✓
D2	0.4	✓	-	T2	350	✓	-
D3	0.7	✓	-	T3	500	-	✓
D4	1.0	-	✓	T4	710	✓	-
D5	9.0	-	✓	T5	1000	-	✓

Table 3.3 Irradiation condition labels for each reactor experiment.

Irradiation Condition*	Samples Irradiated
M-D1-T2	 $Ti_3SiC_2$ -FG $Ti_3SiC_2$ -CG $Ti_3AlC_2$ $Ti_2AlC$ $Ti_2AlN$ $Ti_2SC$ SiC
M-D1-T4	
M-D2-T2	
M-D2-T4	
M-D3-T2	
M-D3-T4	
A-D1-T1	
A-D1-T3	
A-D1-T5	
A-D4-T1	
A-D4-T3	
A-D4-T5	
A-D5-T1	
A-D5-T3	
A-D5-T5	

\*M – MITR, A – ATR denoting location of irradiation experiments.

Table 3.4 Irradiation exposure parameters for the MITR experiments.

Condition	Temperature (°C)	Irradiation Dates	Exposure (MWh)	Fluence (>0.1 MeV) (n/cm <sup>2</sup> )	Total Fluence (n/cm <sup>2</sup> )	dpa (4×10 <sup>21</sup> n/cm <sup>2</sup> = 1 dpa)
M-D1-T2	360(20)	10/13-12/4 2010	5,000	2.40×10 <sup>20</sup>	3.40×10 <sup>20</sup>	0.1
M-D1-T4	695(25)	10/13-12/4 2010	5,000	3.50×10 <sup>20</sup>	4.80×10 <sup>20</sup>	0.1
M-D2-T2	340(20)	3/8-12/22-2011	20,200	9.80×10 <sup>20</sup>	1.40×10 <sup>21</sup>	0.4
M-D2-T4	740(20)	3/8-12/22-2011	20,200	1.40×10 <sup>21</sup>	1.90×10 <sup>21</sup>	0.5
M-D3-T2	380(10) *300(10)	10/13/2010-12/22/2011	29,300	1.40×10 <sup>21</sup>	2.00×10 <sup>21</sup>	0.5
M-D3-T2	750(30) *650(15)	10/13/2010-12/22/2011	29,300	2.00×10 <sup>21</sup>	2.80×10 <sup>21</sup>	0.7

\*-The reactor was operated at a lower temperature for a several weeks awaiting permission to increase reactor temperature after phase 2 shut down. Average values for T2 and T4 were 350(40) and 710(50) °C.

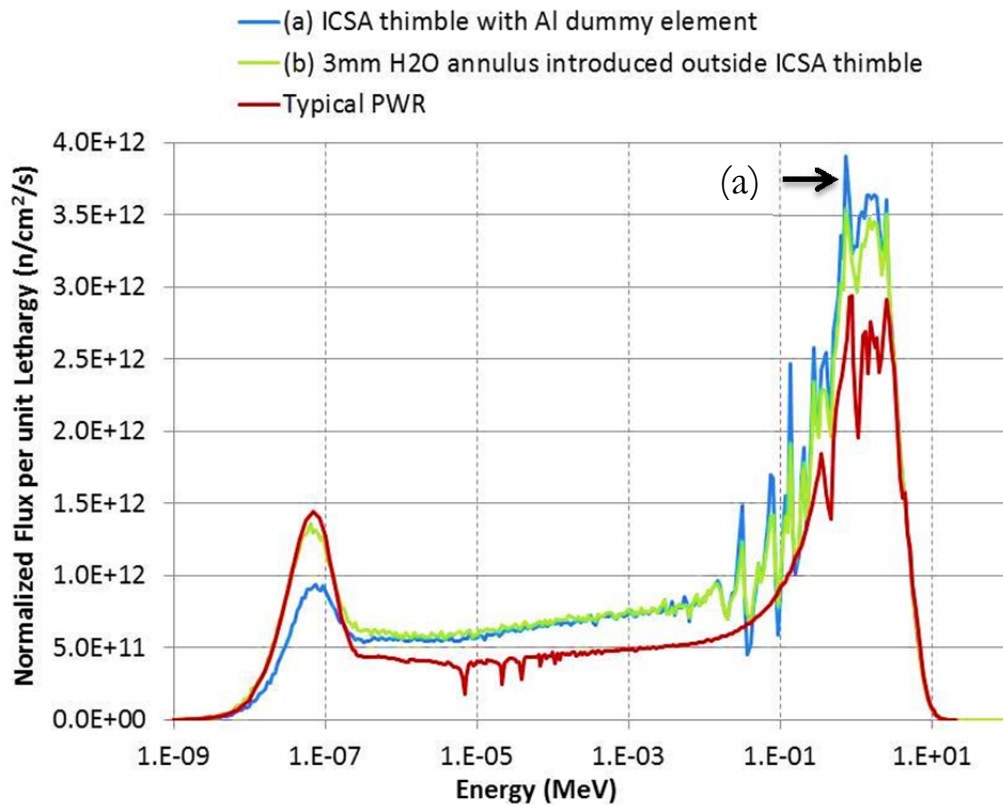


Figure 3.5 Normalized flux per unit lethargy of typical PWR and of in-core sample assembly, ICSA, configurations of a) ICSA thimble with aluminum dummy element (standard), b) 3mm H<sub>2</sub>O annulus introduced outside ICSA thimble. Note that the MAX phase irradiation took place with an approximately 1-mm water gap with the spectrum corresponding to curve (a). Flux per unit lethargy is equal to the flux divided by the natural log of the total energy range of the neutrons.

The total irradiation exposures expressed in MWh (reactor power multiplied by time at power) were: Phase I, 5,000; Phase II, 4,100; and Phase III, 20,200. Specimens were irradiated to a maximum fluence ranging from  $2.0 \times 10^{20}$  n/cm<sup>2</sup> to  $2.8 \times 10^{21}$  n/cm<sup>2</sup> (E>1 MeV) at T2 and T4, respectively. Note that the fluences are based on the actual integrated MWh for each set of specimens and Monte Carlo N-Particle Transport Code, MCNP, calculated flux levels at the irradiation positions. Based on the SiC damage cross-sections reported in [75] and the neutron spectrum in another in-core experimental facility, the damage rate for SiC has been previously calculated to be  $4 \times 10^{21}$  n/cm<sup>2</sup> = 1 dpa. In the absence of other damage cross-sectional information, we used this damage rate for the MAX phases herein. It follows that in this work we explored the irradiation response in the 0.1, 0.5, and 0.7 dpa regimes, henceforth denoted as D1, D2 and D3, respectively (Table 3.2). After irradiation, samples were stored in cooling pools while they awaited post-irradiation examination, PIE.

Delays in irradiation, and increased cooling periods led to a ripple effect in the majority of the characterization experiments. Reviewed later in this thesis, resistivity testing and XRD refinement have been completed for all low dose MAX phase samples. TEM characterization of irradiation defects has been performed on as-received samples of FG-Ti<sub>3</sub>SiC<sub>2</sub> and Ti<sub>2</sub>AlC, as well as samples M-D1-T2, M-D1-T4, and M-D2-T2, listed in Table 3.4.

Ti<sub>2</sub>SC was found to be unexpectedly problematic during this project due to a significantly higher neutron activation compared to all other samples. Ta and Hf impurities in the Ti<sub>2</sub>SC pre-reacted powders resulted in the formation of long lived isotopes, which led to unsafe dose counts for the radiological workers. In concurrence with the technical point of contact, Douglas Marshall, Ti<sub>2</sub>SC was abandoned early on.

### 3.4.2. INL ATR Irradiation Experiments

Details of the irradiation experiments conducted at INL ATR are provided. The irradiation was carried out at the 106 MW INL ATR facility in multiple phases depending on the target dose of the sample sets. A wide range of doses ( $0.7 - 70 \times 10^{20}$  n/cm<sup>2</sup>,  $E > 1$  MeV) and temperatures (100, 500 and 1000 °C) were reached, and the details of the irradiation conditions are shown in Table 3.5. The high dose irradiations, A-D4 and A-D5, were carried out in the inboard location A-3 of ATR (Figure 3.6) with a high fast neutron flux (average peak fast flux  $\sim 1.9 \times 10^{14}$  n/cm<sup>2</sup>-sec,  $E > 1.0$  MeV). The low dose irradiation, A-D1, utilized the ATR Hydraulic Shutter Irradiation System (HSIS), also referred to as the Rabbit system, at the B-7 position (Figure 3.6) (average peak fast flux  $\sim 8.1 \times 10^{13}$  n/cm<sup>2</sup>-sec,  $E > 1$  MeV). The capsules at the A-3 and B-7 positions were in direct contact with coolant water, and were filled with a mixture of He and Ar to provide necessary thermal conductivity to achieve desired irradiation temperatures.

**Table 3.5 Nominal irradiation exposure parameters for the ATR experiments**

Condition	Temperature (°C)	Irradiation Dates	Exposure (MWh)	Fluence (>1 MeV) (n/cm <sup>2</sup> )	dpa ( $7 \times 10^{20}$ n/cm <sup>2</sup> = 1 dpa)
A-D1-T1	100	-	25000	$7.0 \times 10^{19}$	0.1
A-D1-T3	500	-	25000	$7.0 \times 10^{19}$	0.1
A-D1-T5	1000	-	25000	$7.0 \times 10^{19}$	0.1
A-D4-T1	100	2/19-4/8/2011	125000	$7.0 \times 10^{20}$	1.0
A-D4-T3	500	2/19-4/8/2011	125000	$7.0 \times 10^{20}$	1.0
A-D4-T5	1000	4/23-6/10/2011	125000	$7.0 \times 10^{20}$	1.0
A-D5-T1	100	12/11/2010-8/4/2012	1086000	$7.0 \times 10^{21}$	9
A-D5-T3	500	12/11/2010-8/4/2012	1086000	$7.0 \times 10^{21}$	9
A-D5-T5	1000	12/11/2010-8/4/2012	1086000	$7.0 \times 10^{21}$	9

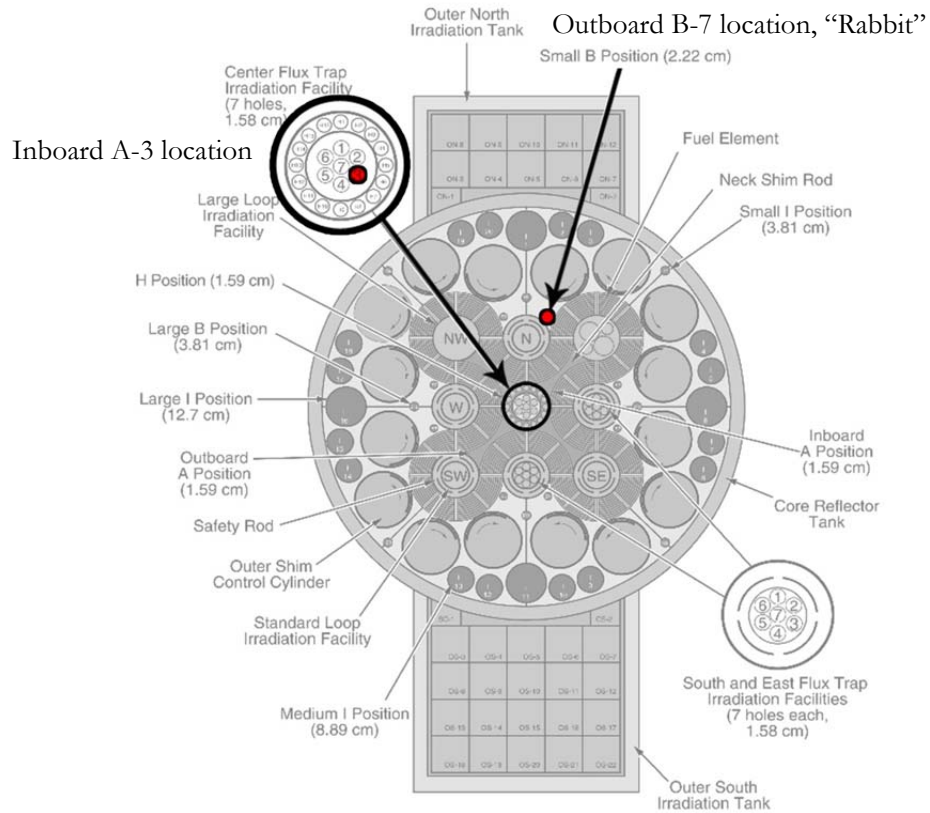
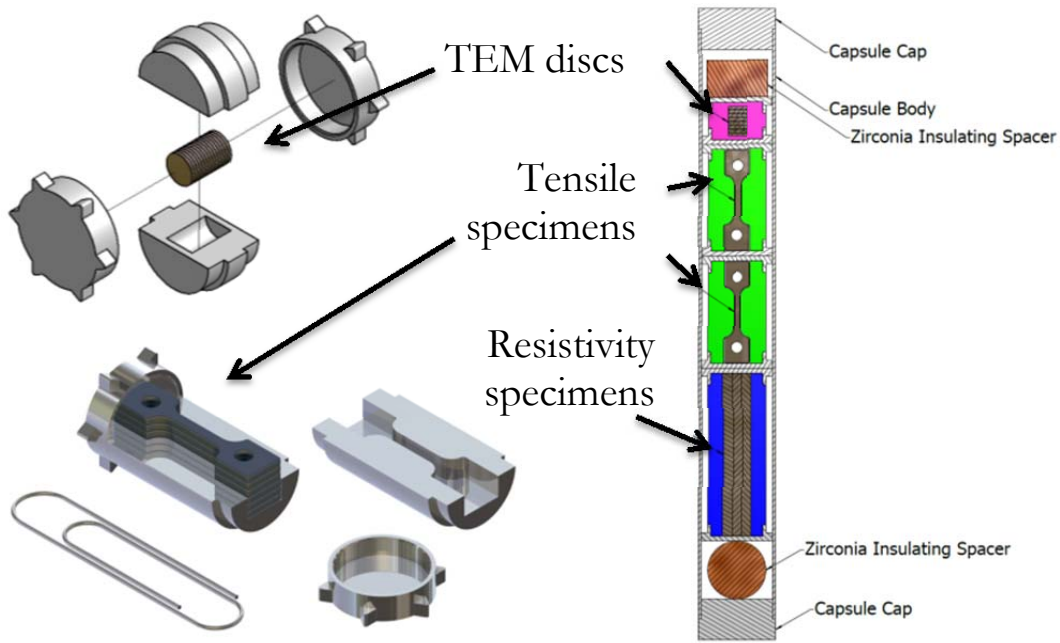


Figure 3.6 Representative capsule locations in the ATR loading positions.

For irradiation at the inboard A-3 position (A-D2, A-D5) in ATR, samples were loaded into 3.75 inch long capsules containing identical material content and sample loading configuration (Figure 3.7) composed of:

- One TEM fixture loaded with (15) TEM discs (1 × 5 pieces × 3 materials)
- Two tensile fixtures each loaded with (6) tensile specimens (2 × 2 pieces × 3 materials)
- One resistivity fixture loaded with (9) resistivity specimens (1 × 3 pieces × 3 materials)

- One zirconia ceramic spacer for thermal insulation (8.0 mm diameter, 6.35 or 12.7 mm thick)



**Figure 3.7 Specimen loading configuration for the ATR irradiation capsules. Samples of each type were arranged in stainless steel holders and loaded vertically into the capsule tube.**

The overall stack height of these fixtures, with fins welded on each end of the fixture (for holding and centering), and the thermal insulator discs at the bottom of the capsules were approximately 76.2 mm (~ 3.0"). The internal heating for each capsule was calculated using the MCNP Coupled with ORIGEN2 (MCWO) analysis methodology, and the necessary insulation gap sizes were determined. Schematics of gap size and specimen fixture for tensile, TEM and resistivity samples for three different irradiation temperatures are shown in Figure 3.8.

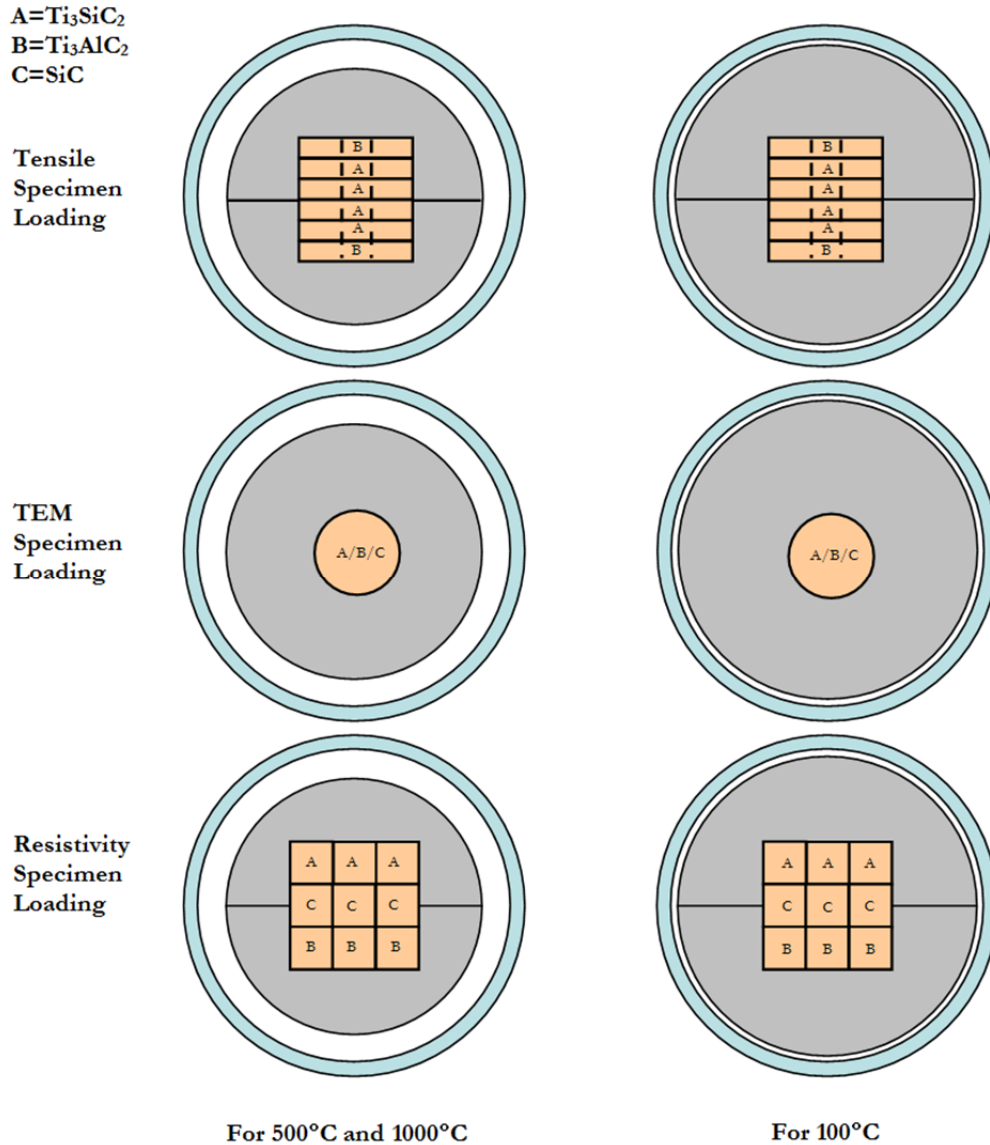


Figure 3.8 Fixture configurations for tensile (top), TEM (middle) and resistivity (bottom) samples for irradiation temperatures of 500 °C and 1000 °C (left: gap 0.97 mm) and 100 °C (right: gap 0.05 mm). Capsule inner dia. is 11.0 mm.

The low dose irradiation, A-D1, using the HSIS (Rabbit) system, was not constrained by the ATR irradiation cycle with the exception of outage periods. Sample sets were loaded into six 2.0 inch long titanium capsules. The 0.1 dpa irradiation for all 6 capsules was completed in one Rabbit run. All 6 short capsules, with a stack length of 12 inches, were loaded to the



core midplane position B-7 and irradiated at the peak fast flux to maintain a heat generation rate adequate for the, relatively, high irradiation temperatures of 500 to 1000°C. The corresponding irradiation time for 0.1 dpa at B-7 core midplane was approximately 240 h.

After irradiations were completed, all sample capsules were removed and stored in the cooling canal until PIE work was coordinated.

### **3.5. Transmission Electron Microscopy**

---

Transmission electron microscopy, TEM, is widely used to visualize and quantify irradiation defects. Irradiation induced defects range from point defects to dislocation loops and dislocation networks. In image mode, the electron beam can be used to excite defects and features, using brightfield and darkfield imaging. Selected area electron diffraction patterns can be used to identify crystal orientation, dislocation Burgers vectors, and lattice distortions. Samples for TEM must be thin enough, then, to be electron transparent. Too thick, however, and the defects will not be resolvable in the resultant TEM images, or appear in too high of a density to quantify.

#### **3.5.1. Sample Preparation**

TEM foils were prepared using a focused ion beam, FIB, microscope (Quanta 3D FEG, FEI Company, USA) (Figure 3.9a), by milling out  $20 \times 2 \times 15 \mu\text{m}^3$  sections from the pristine and irradiated samples, which were then lifted out onto copper TEM grids. Following the thinning procedure detailed in Table 3.6, foils were thinned from the liftouts by milling away from alternating sides at the described angles. Progressively gentler beams were used to

finely polish the foils. Samples were thinned in the FIB through stage 5 (Table 3.6) until small perforations were observed. FIB damage was then cleaned with a final polish using 2 kV at 27 pA ion emission current. TEM foils were thinned to thicknesses of 100-200 nm.

Secondary electron, SE, micrographs showing the surface microstructure of samples prior to FIB milling were taken using the scanning electron microscope, SEM, which was a part of the FIB microscope (Quanta 3D FEG, FEI Company, USA).

**Table 3.6 Focus ion beam milling procedure for MAX phase thin foils for TEM observation.**

Step	Voltage (kV)	Emission Current	Thin until thickness (nm)	Z depth ( $\mu\text{m}$ )	Tilt angles ( $\theta^\circ$ )	Mill Type	Time (Min.)
1	30	3 nA	1000	3	50.5-53.5	*CCS	3-5
2	30	1 nA	500	1	50.5-53.5	*CCS	3-5
3	30	0.3 nA	250	0.5	50.5-53.5	*CCS	3
4	30	0.1 nA	~150	0.2	50.5-53.5	*CCS	3
5	5	77 pA	-	0.1	45-49	Regular	5
6	2	27 pA	-	0.1	45-49	Regular	1

\*CCS- Cleaning cross section mode.



Figure 3.9 a) Quanta 3D FEG focused ion beam used to prepare TEM foils and b) FEI TF30-FEG STwin STEM used to characterize the pristine and irradiated samples.

### 3.5.2. TEM Observation and Characterization

Microstructural analysis of irradiation defects was carried out on the FG-Ti<sub>3</sub>SiC<sub>2</sub> and Ti<sub>2</sub>AlC samples using a TEM (TEM, TF30-FEG STwin STEM, FEI Company, USA) equipped with an electron energy loss spectroscope (EELS) and an energy dispersive X-ray spectroscope, EDX, (EDAX Inc., Mahwah, NJ, USA) (Figure 3.9b). Brightfield, BF, and darkfield, DF, micrographs were collected in order to characterize irradiation induced defects, as well as selected area electron diffraction patterns. In order to determine the Burgers vector,  $\mathbf{b}$ , of dislocations, the  $\mathbf{b} \cdot \mathbf{g} = 0$  criteria was used, and various tilt experiments were conducted to excite specific  $g$  planes in kinematic 2-beam conditions (Figure 3.10)[76]. By tilting to at least two  $g$ 's that resulted in minimum contrast for the dislocation loops,  $\mathbf{b}$  was determined as the cross product of those two  $g$ 's.

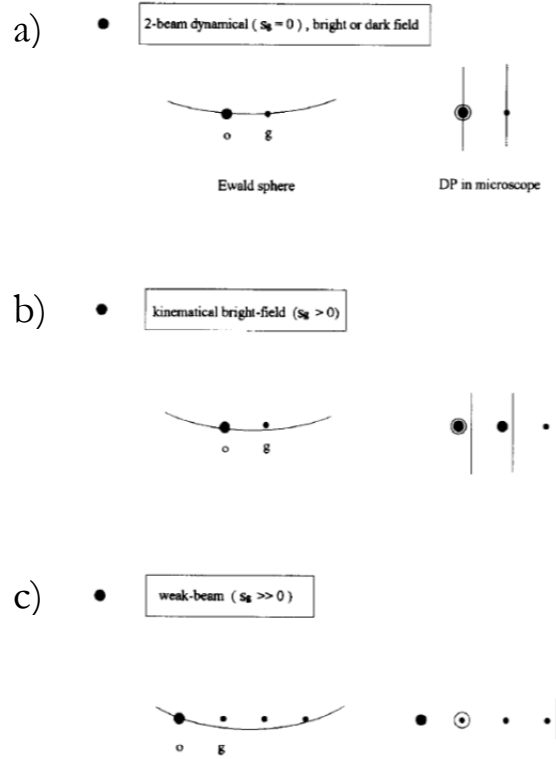


Figure 3.10 Schematic representation of the different diffraction conditions used in diffraction-contrast imaging: a) 2-beam dynamical, b) 2-beam kinematical, and c) weak-beam. In each case the Ewald sphere is sketched on the left-hand side, and a schematic diffraction pattern (DP) showing the position of the relevant Kikuchi lines on the right-hand side. The curvature of the Ewald sphere is exaggerated for clarity. The open circle represents the objective aperture [76].

### 3.5.3. TEM Foil Thickness Calculation

The TEM foil thickness was calculated using the inelastic mean free path, IMFP,  $\lambda$ , for transmission of electrons through a solid, following the equation developed by Iakoubovskii et al. [77],

$$\lambda = \frac{200FE_0}{11\rho^{0.3} \ln\left[\frac{\alpha^2 + \beta^2 + 2\theta_E^2 + |\alpha^2 - \beta^2|}{\alpha^2 + \beta^2 + 2\theta_C^2 + |\alpha^2 - \beta^2|} \times \left(\frac{\theta_C^2}{\theta_E^2}\right)\right]} \quad (3.2)$$

where  $\rho$  is the sample density,  $F = (1+E_0/1022)/(1+E_0/511)^2$  is a relativistic factor,  $E_0$  is the electron energy,  $\alpha$  is the convergence angle,  $\beta$  is the collection semiangle,  $\theta_E = 5.5 \times \rho^{0.3}/(FE_0)$  and  $\theta_C = 20$  mrad.

Log-ratio thickness measurements of EELS spectra were collected for various regions with defects to generate a relative mean free path, RMFP, used to calculate the foil thicknesses,  $t$ , for defect density calculations, as  $\lambda \times \text{log-ratio} = t$ . The diameter and lengths of more than 200 loops at each condition were measured and averaged using image analysis software (ImageJ, NIH, Bethesda, MD, USA).

### 3.6. Room Temperature Resistivity of Irradiated MAX phases

---

Pre- and post-irradiation room temperature, RT, resistivity,  $\rho$ , measurements were obtained for all samples using a 4-point probe technique and a constant current of 100 mA. Three resistivity bars of each material were irradiated at each condition, and the recorded values were averaged from the multiple bars tested. Some resistivity bars were broken upon retrieval, and in those cases the average of only 2 resistivity bars was reported.

Voltages were recorded once per second for 3 minutes to allow the scans to reach steady state, and averaged over time. Resistivity was calculated using the following formula:

$$\rho = \frac{VA}{IL} \quad (3.3)$$

where  $A$  is the cross sectional area,  $L$  is the lead separation,  $I$  is the applied current, and  $V$  is the measured voltage. For most samples, a time-independent voltage signal was recorded. Occasionally, a  $\text{Ti}_3\text{AlC}_2$  or a  $\text{Ti}_2\text{AlC}$  sample would exhibit a noisy signal due to surface roughness impeding contact with the test leads. Lightly polishing the surfaces with 600 grit grinding paper solved the problem and resulted in steady voltage measurements.

### 3.7. Thermal Diffusivity, Non-irradiated

---

The thermal diffusivity of pristine samples of  $\text{Ti}_3\text{SiC}_2$ ,  $\text{Ti}_3\text{AlC}_2$ ,  $\text{Ti}_2\text{AlC}$ ,  $\text{Cr}_2\text{AlC}$ , and solid solutions of  $(\text{Nb}_{0.5}\text{Zr}_{0.5})_2\text{AlC}$ ,  $(\text{Nb}_{0.75}\text{Zr}_{0.25})_2\text{AlC}$ , and  $(\text{Ti}_{0.75}\text{Zr}_{0.25})_2\text{AlC}$  were measured as a function of temperature. The samples were loaded into a laser flash analysis device (LFA 427, Netzsch, Burlington, MA, USA), which measures the time-dependent temperature increase of the sample due to energy pulses applied to one side, i.e. thermal diffusivity,  $\alpha$ . Thermal conductivity,  $\kappa_{th}$ , is related to thermal diffusivity by the following equation:

$$\alpha = \frac{\kappa_{th}}{d c_p} \quad (3.4)$$

where,  $d$  and  $c_p$  are density and specific heat, respectively. When available in the literature, for the above MAX phases, the  $c_p$  as a function of temperature was used in the calculations. It has also been shown that  $c_p$  of a given MAX phase is closely correlated to that of its binary MX counterpart, by a factor of  $n+1$  [25]. Using this relationship, the  $c_p$  for the  $(\text{Nb}_x\text{Zr}_{1-x})_2\text{AlC}$  and  $(\text{Ti}_x\text{Zr}_{1-x})_2\text{AlC}$  compounds was estimated using  $2 \times c_p$  values for NbC and TiC, respectively. Thermal diffusivity was measured in 25 K increments over the range of 298 – 1223 K. Using available  $c_p$  data for the MAX phases, density, and the diffusivity results, thermal conductivity was calculated as a function of temperature.

### 3.8. Diffusion Bonding, Non-irradiated

---

Diffusion couples were formed with Zircaloy-4, Zr-4, foil typically sandwiched between two different non-irradiated MAX phases. Alumina plates were placed in between the MAX

phases and the graphite punch that was used to transfer an applied load corresponding to a stress of  $\sim 5$  MPa (Figure 3.11). The entire assembly was then placed into a 36 mm diameter graphite die. The diffusion tests were performed in a vacuum hot press at temperatures of 1100, 1200, and 1300 °C for 1, 2, 10 and 30 h, under a vacuum of  $10^{-1}$  Pa, before furnace cooling.

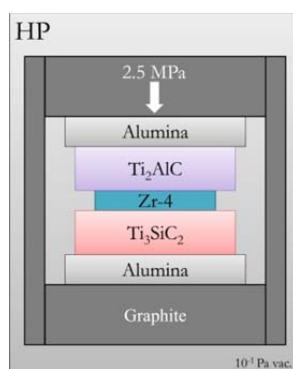


**Figure 3.11 Schematic of the diffusion couple loading assembly that was in turn placed in the hot press.**

The resulting diffusion couples were cross-sectioned with a high speed diamond saw (Accutom-5, Struers Inc., Cleveland, Ohio, USA), mounted for metallographic inspection, and polished with a final surface preparation of 3  $\mu\text{m}$  diamond suspension polish.

Diffusion profiles were obtained using a SEM, (Carl Zeiss Supra 50VP, Germany) equipped with an energy-dispersive X-ray spectroscope, EDX, (Oxford Inca X-Sight, Oxfordshire, UK). EDX line scans were used to generate elemental concentration profiles across the various interfaces. Point scans were also used to identify the chemical composition of the various intermetallic diffusion layers.

Calculation of diffusion coefficients from the diffusion profiles was problematic since in most cases more than one distinct intermetallic layers had formed, each presumably with its

own diffusion coefficient. To partially solve this problem and partially quantify the kinetics, the total diffusion distance,  $x$ , in m, defined here as the total thickness of all intermetallic phases was measured as a function of time,  $t$ , in s. If the overall process is diffusion controlled and:

$$x = \sqrt{2D_A t} \quad (3.5)$$

then plots of  $x$  vs.  $t^{1/2}$  should yield straight lines with slopes that are proportional to the effective chemical diffusion coefficient,  $D_A$ , of the solute species into Zr-4. The temperature dependence of  $D_A$  then follows the Arrhenius equation:

$$D_A = D_o e^{\left(\frac{-Q_A}{RT}\right)} \quad (3.6)$$

where  $D_o$  is the pre-exponential term,  $Q_A$  is activation energy for diffusion,  $R$  is the universal gas constant, and  $T$  is temperature, in Kelvin.

### 3.9. Helium Permeability

---

He permeability tests were performed at 850 °C and 950 °C for three MAX phase samples:  $Ti_2AlC$ ,  $Ti_3AlC_2$  and  $Ti_3SiC_2$  following a similar procedure described in the ASTM D1434 [78].

A customized differential pressure (DP) rig, as shown in Figure 3.12, was designed by SRNL personnel to mount the samples for the high temperature tests. The samples were supported by a sintered disc in order to prevent mechanical failure. The DP rig had two parts that clamped into the sample, each with a stainless steel Swagelok fitting to which gas lines to the external system were connected. After clamping the edges of the samples, the



area exposed was 10 mm diameter. The sample chamber was housed in a furnace that was capable of reaching up to 1000 °C. Just outside of the furnace, pressure gauges were fitted; an analogue high pressure gauge on the high pressure line, and a digital vacuum gauge on the low pressure line. The lines were controlled with valves to allow either gas in (on the high pressure test gas side) or vacuum (on both sides). The pressure was regulated from a nearby cylinder with a reservoir attached to prevent the regulator from controlling the rate. The readings from the digital vacuum gauge were logged.

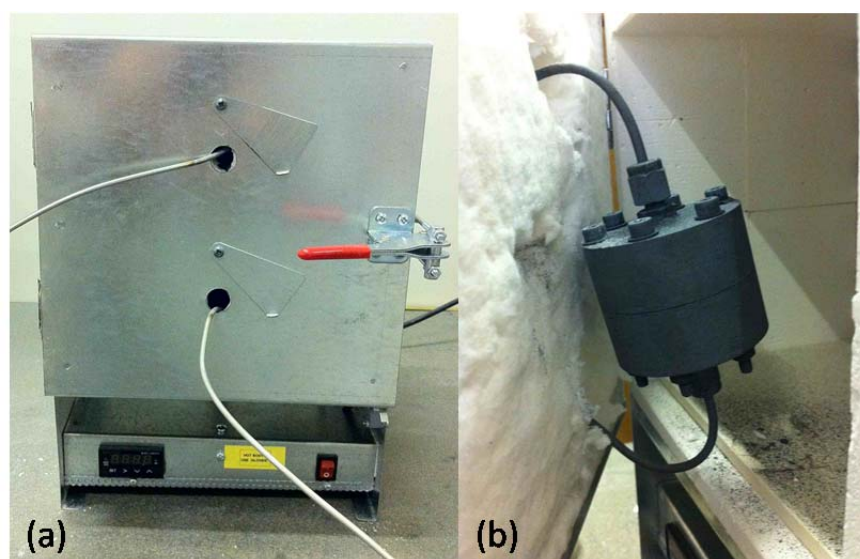


**Figure 3.12** a) Small furnace and b) sample chamber used for permeability testing.

In the DP tests, both sides of the sample chamber were evacuated and then the system was isolated. The sample chamber was then allowed to stand for the test period of 2 h and the increase in pressure in the low pressure side was regarded as the baseline. Subsequently, another evacuation was performed and He gas was supplied at 0.5 bar to the high pressure side. The pressure on the high-pressure side was maintained throughout the test run at 0.5 bar, whereas the pressure on the low pressure side was allowed to rise and the rate at which

this occurred was measured. A LabVIEW program was used to calculate and record the permeation rate dynamically

## 4. IRRADIATED STRUCTURES AND PHASE STABILITY

---

As described in previous chapters, irradiation with neutrons can cause significant changes to the crystal structure and composition of materials. This chapter is focused on detailing the theory of, and experimental results obtained from, x-ray diffraction, XRD. This wave-scattering technique produces an intensity spectrum of diffracted x-rays, generated by the beam's interaction with the atomic ordering of crystalline solids. In this thesis, XRD is used to investigate the changes in microstructure and composition of the MAX phases as a function of irradiation dose. Rietveld refinement of the resultant XRD patterns is provided to assess distortions in the unit cell, as well as increases in microstrain in samples after irradiation. Results are compared with previous heavy ion studies, and assessment of structural stability under irradiation is summarized.

XRD is one of several diffraction techniques available for crystal structure investigation. Selected area electron diffraction, SAED, is utilized in Chapter 5 to assist in analysis of irradiation defects. XRD patterns in this chapter were obtained utilizing x-ray diffractometers at the collaborating radiological laboratories; Savannah River National Lab, for the MITR samples, and Idaho National Lab, for the ATR samples. A discussion of diffraction theory is provided, as well as details of the refinement methods used to interpret the XRD spectra presented here. Following the theory, experimental results are presented and discussed, with an emphasis on phase stability and microstructural changes. Lastly, a possible explanation of the resultant defective microstructure is hypothesized, with incorporation of previous DFT modelling results and the structural changes experienced herein.

## 4.1. Diffraction Origins and Theory

---

In 1912, Max von Laue and his colleagues discovered that x-ray radiation was able to diffract from the periodicity in crystalline materials. Later, in 1913, Sir W. H. Bragg and his son Sir W. L. Bragg developed a relationship between the wavelength,  $\lambda$ , of diffracted light and atomic layer spacing, known as Bragg's Law (see Section 4.1.1). This observation of reflected x-ray beams at distinctive angles of incidence became known as x-ray diffraction, XRD, and provided direct evidence for the previously postulated theory of periodic atomic structure of crystals. XRD has since become an invaluable tool for exploring the atomic structure of materials, used in various fields, including, but not limited to, materials science, geology, biology, and physics.

Crystalline materials are depicted by the long range, orderly arrangement of atoms. The unit cell of a crystalline material is the basic repeating unit of atoms in a particular arrangement. Parallel planes of atoms within that unit cell have defined planar spacings,  $d_{hkl}$ , using Miller indices notation, which are unique for specific materials and crystal structures. X-rays are photons with a typical energy range of 100eV-100 keV. For diffraction studies, hard x-rays, with shorter wavelengths on the order of 1 angstrom,  $\text{\AA}$ , intentionally on the same order as the d-spacings, are used to probe atomic structures. X-rays are produced by x-ray tubes where they are filtered to generate monochromatic wavelengths, e.g. Cu x-rays with  $\lambda = 1.54 \text{\AA}$ , or by synchrotron radiation which can provide a range of wavelengths.

X-ray waves predominantly interact with the electron cloud of an atom, and do so in various ways. Elastically, the atoms of a crystal can coherently scatter x-rays. As the electron cloud interacts with the oscillating electric fields of the x-rays, this can result in a reflected x-ray with the same wavelength as the original. This is known as Thompson scattering, where

only momentum is transferred, and the wavelength is constant. X-rays can also be transmitted, absorbed, refracted, or scattered incoherently, though XRD does not take into account these other interactions.

Diffracted x-ray waves from different atoms tend to interfere, resulting in a distribution of reflected beams into various diffraction peaks, the intensity of which are dependent on the periodicity in a crystal. Measurements of the diffraction pattern can be used to understand the distribution of atoms in a material, and relevant d-spacings for specific crystals. The distribution of peak intensities and positions can be calculated for a given material by using Bragg's Law.

#### 4.1.1. Bragg's Law

When x-rays scatter from atoms in the crystal lattice, most combinations of wavelengths and incidence angles result in destructive interference, canceling out the waves of transmitted light. However, when the reflecting plane is aligned in a particular way, the reflected beams interfere constructively, and remain in phase, resulting in a diffraction peak. The relationship that relates this is known as Bragg's Law:

$$n\lambda = 2d_{hkl} \sin \theta \quad (4.1)$$

where  $n$  is an integer,  $\lambda$  is the wavelength of the x-ray,  $d_{hkl}$  is the spacing between parallel planes, or Bragg reflections,  $(hkl)$ , and  $\theta$  is the angle of incidence. This relationship is shown in Figure 4.1, where the incident wave is shown reflecting from a given plane must travel an extra distance equal to  $2d \sin \theta$ . Constructive interference occurs when this extra distance is equal to integer,  $n$ , multiples of  $\lambda$ , corresponding to a phase shift of  $360^\circ$ . Examination of d-spacings of crystalline materials is possible since only certain wavelengths and angles lead to constructive interference when using a fixed  $\lambda$  x-ray diffractometer. It then follows that, by scanning across a range of incident angles,  $\theta$ , grains oriented to the

proper directions will provide the necessary constructive interference, resulting in an intensity distribution spectrum profile. The location of specific peaks can then be converted to related d-spacings using Bragg's law.

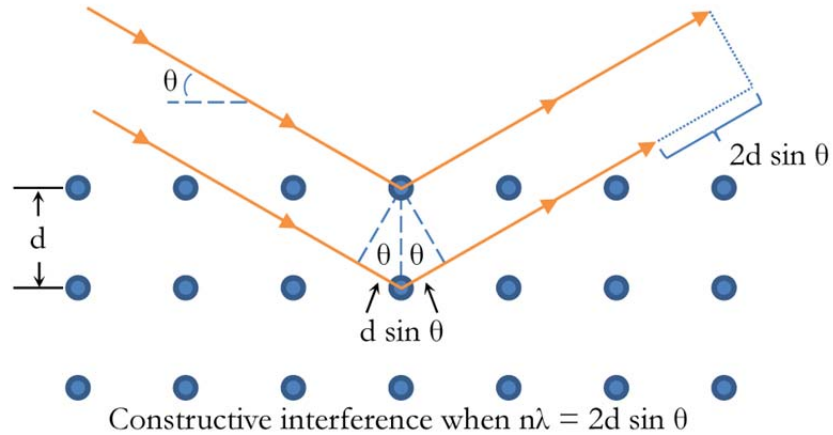


Figure 4.1 Schematic of Bragg's law.

#### 4.1.2. Elastic Scattering of X-rays

The amplitude of elastically scattered x-rays from a crystal structure is determined by the atomic arrangement in the diffracting  $(hkl)$  planes. The intensity of expected peaks can be described by:

$$I_{hkl} = |F_{hkl}|^2 \cdot LP \quad (4.2)$$

where  $F_{hkl}$  is the structure factor, and LP is a combined geometry and polarization factor dependent on experimental setup. The structure factor sums the result of scattering from all atoms in a unit cell forming a diffraction peak from the  $(hkl)$  plane, given by:

$$F_{hkl} = \sum_{j=1}^m N_j f_j e^{2\pi i(hx_j + ky_j + lz_j)} \quad (4.3)$$

where  $N_j$  is the occupied fraction of equivalent positions of atom  $j$  in coordinates  $(x_j, y_j, z_j)$ , and the scattering factor,  $f$ , described by:

$$|f|^2 = \left( f_0 e^{\frac{-B \sin^2 \theta}{\lambda^2}} + \Delta f' \right)^2 + (\Delta f'')^2 \quad (4.4)$$

which quantifies the relative efficiency of electron scattering of each atom. The pre-exponential  $f_0$  at  $0^\circ$   $\theta$  is equal to the number of electrons in the atom, and can be found using tables or equations derived experimentally as a function of  $(\sin\theta)/\lambda$ . The thermal motion correction, to account for atomic vibration, incorporates the Debye-Waller factor,  $B$ , where  $B = 8\pi^2 U^2$ , with  $U^2$  as the mean-square amplitude of atomic vibration.

#### 4.1.3. Profile Refinement

The previous sections describe the relationship between the crystalline arrangement of atoms in a material and the resultant scattering of x-rays. The diffraction patterns directly correlate to the crystal structure. In practice, it is desirable to fit, or refine, a structural model to compare with experimental data. Initially an approximation, or prediction, of relevant phase(s) is (are) needed to hypothesize an initial structure based on structural and instrumental parameters. The “goodness” of the fit between the measured and calculated profile is then assessed through a least squares analysis using both the instrumental and structural parameters. This is known as Rietveld refinement [72, 73].

Rietveld refinement, a method devised by Hugo Rietveld, takes advantage of the fact that the diffraction peaks from monochromatic sources are quite Gaussian in shape [73]. The calculated profile function includes structural parameter variables that can be refined to fit

peak positions and shapes, as well as instrument variables to account for systemic alignment. Details of the refinement parameter functions can be found in Ref. [73]

The Rietveld method involves minimizing the variance,  $\Delta$ , given by:

$$\Delta = \sum_i w_i (y_{obs,i} - y_{calc,i})^2 \quad (4.5)$$

where  $i$  refers to each data point at wavelength  $\lambda_i$ ,  $w_i$  is the weight, and  $y_{obs,i}$  and  $y_{calc,i}$  are the observed and calculated intensities, respectively. It is important to include various agreement indices, to measure the process of convergence, known as R-factors. The first to consider is the weighted profile R-factor,  $R_{wp}$ , which is related to the minimized quantity scaled by the weighted intensities as follows:

$$R_{wp}^2 = \frac{\sum_i w_i (y_{obs,i} - y_{calc,i})^2}{\sum_i w_i (y_{obs,i})^2} \quad (4.6)$$

The expected R-factor,  $R_{exp}$ , as a measure of quality of the data, represents the ideal model of the best possible fit, and is given by:

$$R_{exp}^2 = \frac{(N - P + C)}{\sum_i w_i (y_{obs,i})^2} \quad (4.7)$$

where  $N$  is the total number of observations,  $P$  is the number of parameters refined, and  $C$  is the number of constraints used in the refinement. It is common in typical powder XRD refinement for  $N$  to dominate over  $P+C$ , and thus the latter can be safely ignored. The ratio of these two R-factors, known as the chi-squared factor,  $\chi^2$ , represents the statistical average ratio, and for an ideal fit would approach unity, according to:

$$\chi^2 = \left( \frac{R_{wp}}{R_{exp}} \right)^2 \quad (4.8)$$



Initially,  $\chi^2$  is large when the calculated model is a poor fit to the observed data. Upon subsequent refinement steps, which improve the model,  $\chi^2$  decreases and approaches 1 indicating a better fit. While minimizing the differences between observed and calculated intensities can lead to a more accurate fit, it is important to understand that there is uncertainty in the refined parameters and fitted data. Error bars on plots, and standard deviations, shown in parentheses as the standard error of the last digit, are used throughout this thesis to display statistical error.

## 4.2. X-ray Diffraction Results: MITR Samples

---

The XRD patterns collected from the FG-Ti<sub>3</sub>SiC<sub>2</sub>, CG-Ti<sub>3</sub>SiC<sub>2</sub>, Ti<sub>3</sub>AlC<sub>2</sub>, Ti<sub>2</sub>AlC and Ti<sub>2</sub>AlN samples before and after the M-D1-T2 and M-D1-T4 irradiations are shown in Figures. 4.2-4.6. XRD patterns collected from the FG-Ti<sub>3</sub>SiC<sub>2</sub> and Ti<sub>2</sub>AlC samples after M-D2-T2 are shown in Figure 4.7. Each figure displays the observed data as open black circles, along with the calculated model in solid red. Beneath each plot, the variance between observed and modeled spectra is plotted, the flatness of which indicates the goodness of the fit. The results of the Rietveld analyses of these patterns are summarized in Table 4.1. Several structural parameters were refined for each sample; a- and c-lattice parameters, LP, atomic positions of Ti and C, overall B factor, and relative peak intensities to determine phase compositions. In addition, the full width half max (FWHM) parameter, U, was refined in order to calculate microstrain, as well as the Lorentzian peak shape parameter, Y, for determining nanocrystallite size.

#### 4.2.1. X-Ray Diffraction Refinement Results

In all cases, the neutron irradiations resulted in structural (Figure 4.8) as well as compositional changes compared to the materials' pristine state (Table 4.1). Changes in microstrain were also observed as a result of neutron irradiation. The best fit of the XRD patterns was achieved by including TiC during refinement of the carbide phases, and TiN for the Ti<sub>2</sub>AlN phase. Additionally, Ti<sub>4</sub>AlC<sub>3</sub> was included in the refinement of Ti<sub>2</sub>AlN:M-D1-T4, which showed an increased level of dissociation after irradiation. It is also important to note that the relative atomic positions of each MAX phase tested herein did not change significantly under the studied irradiation conditions (Table 4.1). Assessment of the Y parameter revealed no signs of peak distortion due to nanocrystallite grain sizes in any of the samples.

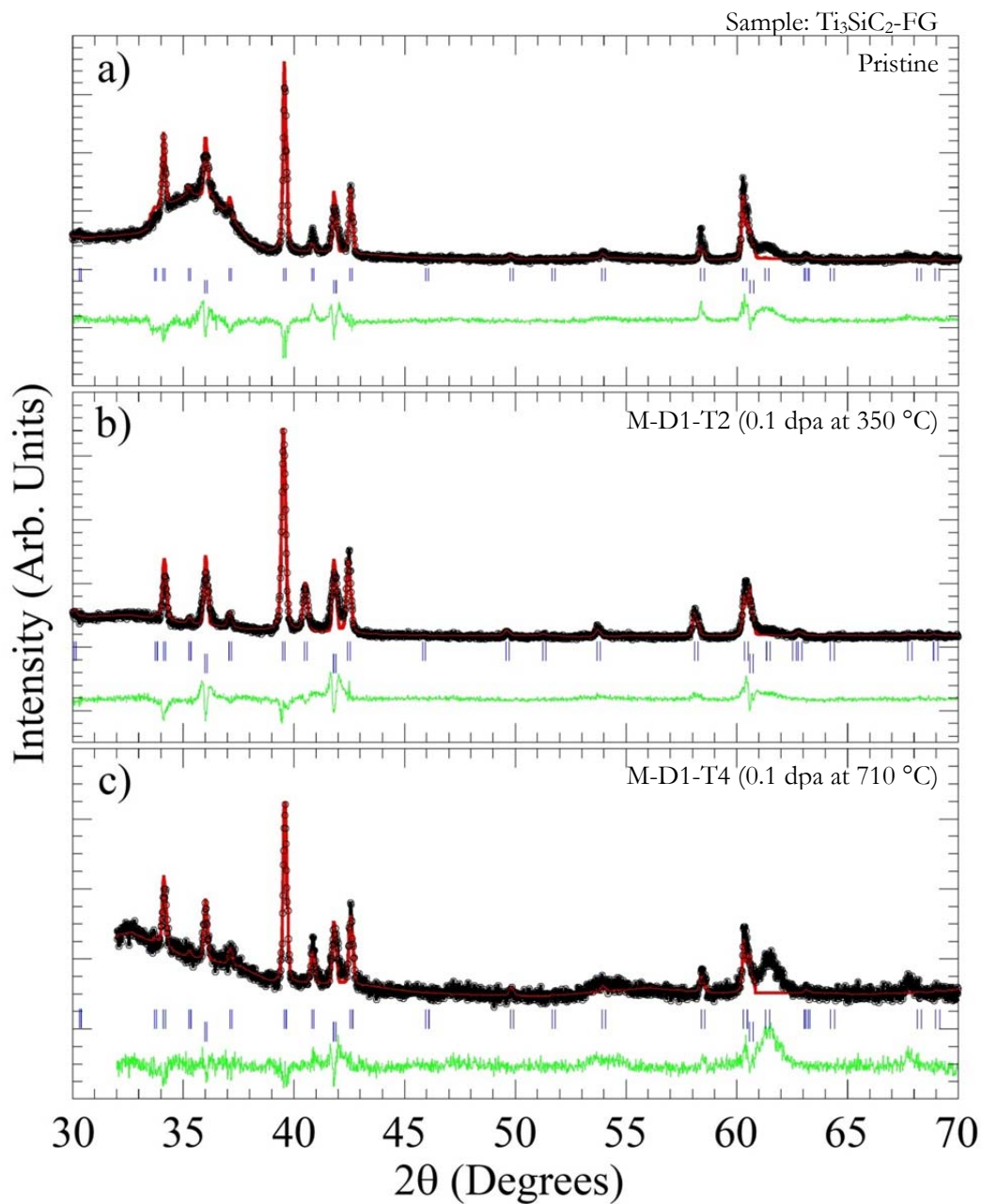


Figure 4.2 Rietveld analysis of XRD pattern of FG- $\text{Ti}_3\text{SiC}_2$ .

a) Pristine, and, b) FG- $\text{Ti}_3\text{SiC}_2$ :M-D1-T2 and, c) FG- $\text{Ti}_3\text{SiC}_2$ :M-D1-T4. Open circles, solid line, and solid line at the bottom, represent the observed data, calculated model, and the difference between the two, respectively. The two rows of vertical tags represent the calculated Bragg reflections' positions of  $\text{Ti}_3\text{SiC}_2$  (1st row) and TiC (2nd).

**FG-Ti<sub>3</sub>SiC<sub>2</sub>:**

The Rietveld refinement of the XRD pattern of the FG-Ti<sub>3</sub>SiC<sub>2</sub>:M-D1-T2 sample showed an increase in the c-LP from 17.680(5) to 17.812(9) Å and a decrease in the a-LP from 3.0685(6) to 3.0648(1) Å (Figure 4.2).

A microstrain of 0.27% was calculated for the distorted lattice; an increase from the pristine sample, at 0.19% (Table 4.1). The lattice of the FG-Ti<sub>3</sub>SiC<sub>2</sub>:M-D1-T4 was only slightly perturbed, with a c-LP of 17.668(1) and a-LP of 3.0674(1) (Figure 4.2, Table 4.1). The microstrain level was below that of the standard used to calibrate the diffractometer.

Refinement of FG-Ti<sub>3</sub>SiC<sub>2</sub>:M-D2-T2 patterns revealed an increasingly distorted lattice in comparison to the lower dose, D1, irradiation. The c-LP increased to 17.887(1) Å and the a-LP decreased to 3.0637(1) Å (Figure 4.7, Table 4.1). At 0.36%, the lattice microstrain was seen to increase from pristine condition, and was also larger than the M-D1-T2 sample.

**CG-Ti<sub>3</sub>SiC<sub>2</sub>:**

The CG-Ti<sub>3</sub>SiC<sub>2</sub> samples behaved similarly to their fine-grained counterparts (Figure 4.3). Refinement of the XRD patterns of the CG-Ti<sub>3</sub>SiC<sub>2</sub>:M-D1-T2 sample revealed an increase in the c-LP from 17.680(8) to 17.840(8) Å and a decrease in the a-LP from 3.0688(7) to 3.0647(8) Å. There was a simultaneous increase in microstrain to 0.33% (Table 4.1). The CG-Ti<sub>3</sub>SiC<sub>2</sub>:M-D1-T4 lattice was slightly distorted, with a c-LP of 17.669(6) Å, and an a-LP of 3.0674(8) Å (Fig. 7); the microstrain was only 0.06%.

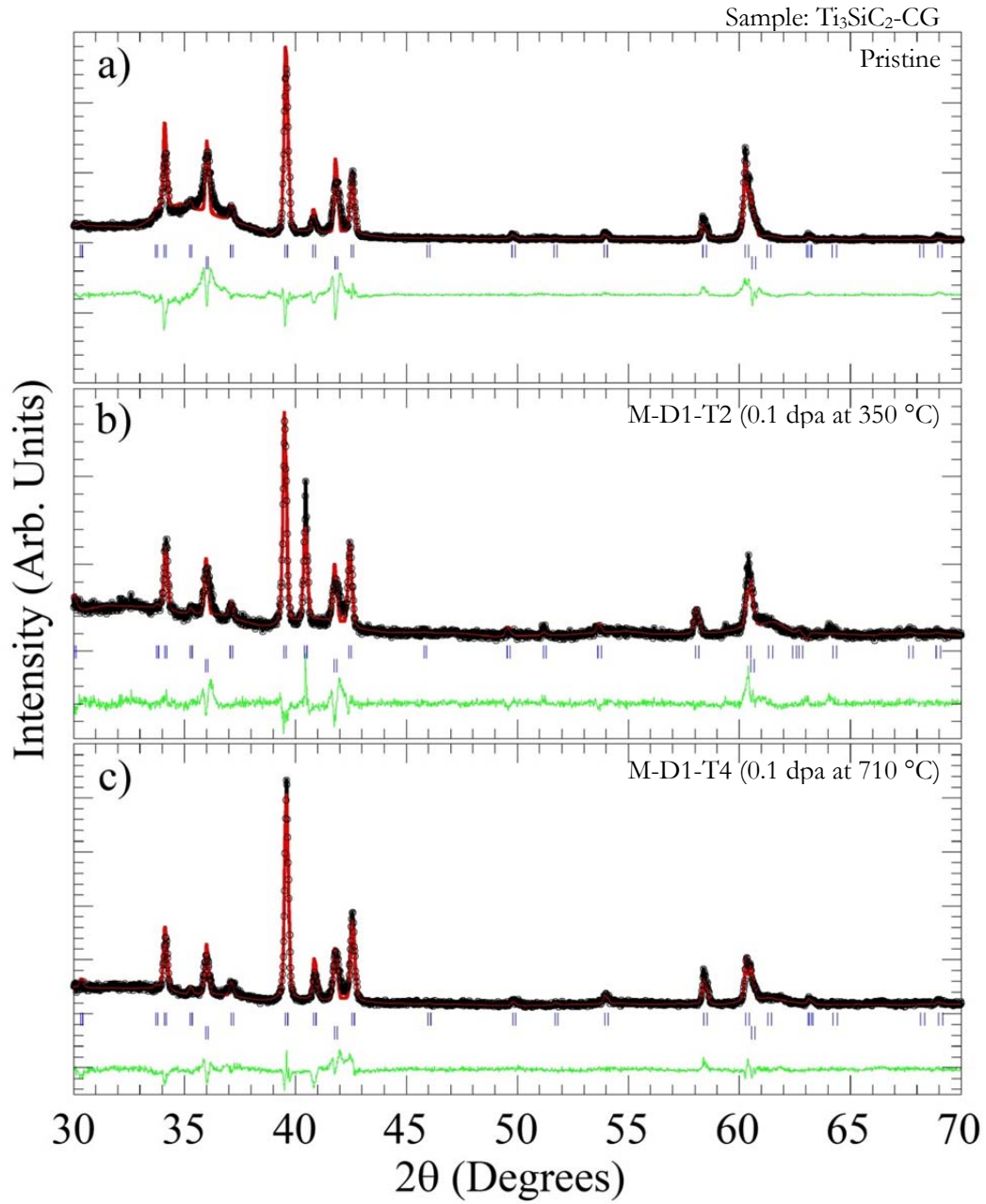


Figure 4.3 Rietveld analysis of XRD data of CG- $\text{Ti}_3\text{SiC}_2$ .

a) Pristine, and b) CG- $\text{Ti}_3\text{SiC}_2$ :M-D1-T2 and, c) CG- $\text{Ti}_3\text{SiC}_2$ :M-D1-T4. Open circles, solid line, and solid line at the bottom, represent the observed data, calculated model, and the difference between the two, respectively. The two rows of vertical tags represent the calculated Bragg reflections' positions of the  $\text{Ti}_3\text{SiC}_2$  (1st row), and TiC (2nd).

**Ti<sub>3</sub>AlC<sub>2</sub>:**

The Rietveld refinement of Ti<sub>3</sub>AlC<sub>2</sub>:M-D1-T2 XRD patterns (Figure 4.4) also showed an increase in the c-LP from 18.562(2) to 18.896(1) Å and a decrease in a-LP from 3.0736(2) to 3.0542(2) Å (Table 4.1). Concomitantly, there was an increase in microstrain from 0.1% to 0.39%. At 18.543(2) Å and 3.0699(2) Å, the c- and a-LPs, respectively, of the Ti<sub>3</sub>AlC<sub>2</sub>:M-D1-T4 samples were less distorted than those at T2. After irradiation at M-D1-T4, the microstrain was 0.34 %.

**Ti<sub>2</sub>AlC:**

The Rietveld refinement of the Ti<sub>2</sub>AlC XRD patterns revealed similar lattice distortion after irradiation (Figure 4.5). Refinement of the Ti<sub>2</sub>AlC:M-D1-T2 sample revealed an increase in the c-LP from 13.650(2) to 13.882(1) Å and a decrease in the a-LP from 3.0614(2) to 3.0367(2) Å. There was a simultaneous increase in microstrain to 0.66%, from below that of the standard used to calibrate the diffractometer at pristine. (Table 4.1). The Ti<sub>2</sub>AlC-M-D1-T4 lattice returned to near pristine dimensions, with a c-LP of 13.659(3) Å, and an a-LP of 3.0585(3) Å (Figure 4.8); and the microstrain was only 0.11%.

Refinement of Ti<sub>2</sub>AlC:M-D2-T2 patterns similarly revealed distorted lattice in comparison to the lower dose, D1, irradiation. The c-LP increased to 14.056(3) Å and the a-LP decreased to 3.0206(3) Å (Table 4.1). At 1.14%, the lattice microstrain was drastically increased from pristine condition.

**Ti<sub>2</sub>AlN:**

Rietveld refinement of the Ti<sub>2</sub>AlN samples revealed a similar trend in distorted LPs (Table 4.1). Ti<sub>2</sub>AlN:M-D1-T2 showed an increase in the c-LP from 13.640(2) to 13.714(4) Å and a decrease in a-LP from 2.9886(3) to 2.9808(6) Å (Figure 4.6).

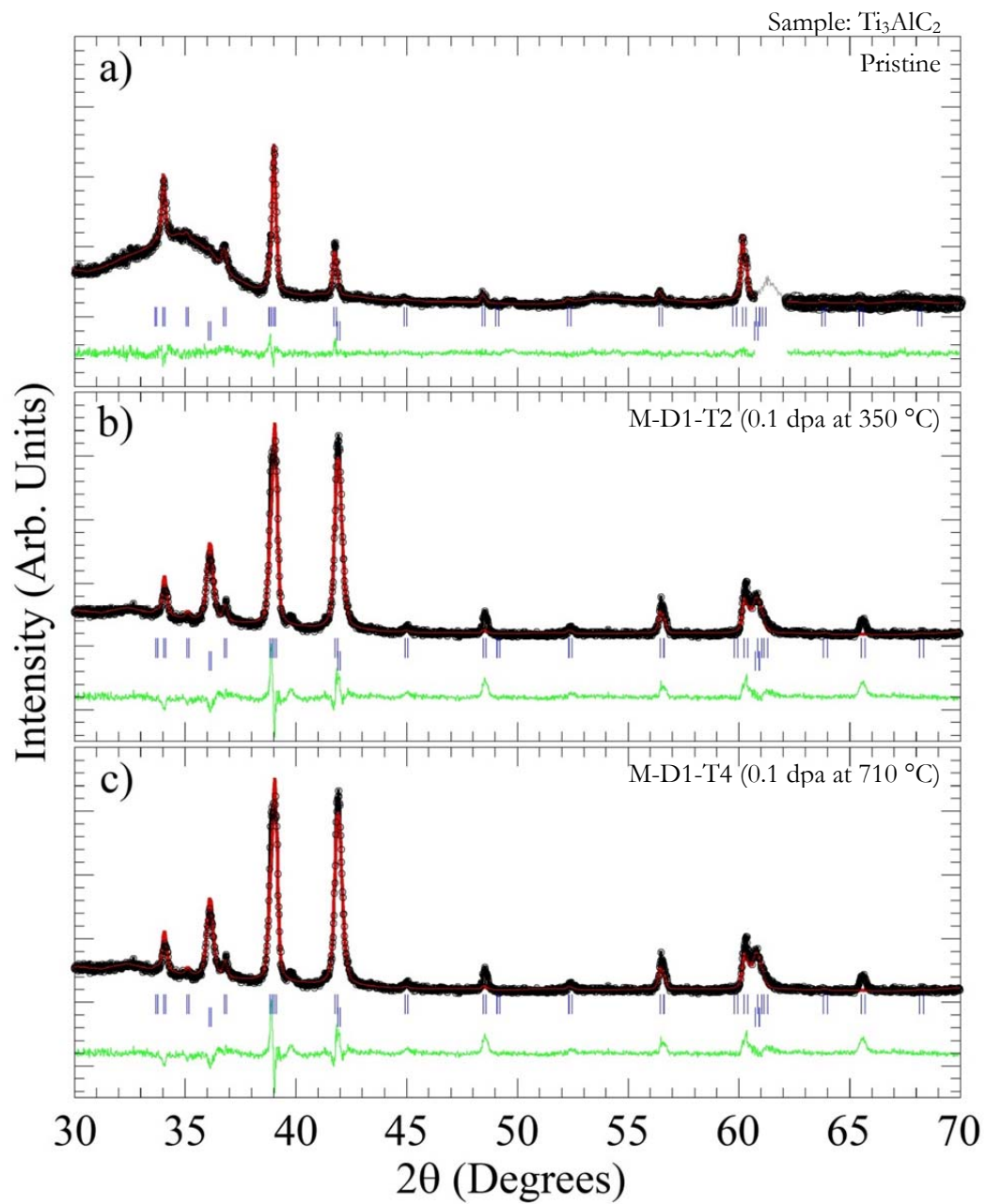


Figure 4.4 Rietveld analysis of XRD patterns of  $\text{Ti}_3\text{AlC}_2$ .  
 a) Pristine, and b)  $\text{Ti}_3\text{AlC}_2$ :M-D1-T2 and, c)  $\text{Ti}_3\text{AlC}_2$ :M-D1-T4. Open circles, solid line, and solid line at the bottom, represent the observed data, calculated model, and variance between the two, respectively. The two rows of vertical tags represent the calculated Bragg reflections' positions of the  $\text{Ti}_3\text{AlC}_2$  (1st row), and TiC (2nd).

At 0.2%, the microstrain after M-D1-T2 was increased from pristine, at 0.16%. At 13.664(4) Å and 3.0086(3) Å, the c- and a-LPs, respectively, of the Ti<sub>2</sub>AlN:M-D1-T4 samples were closer to pristine values (Figure 4.8). However, at 0.58 %, the micro-strain found in Ti<sub>2</sub>AlN-HT sample was significantly higher than all other samples irradiated at this condition.

### **TiC and TiN Formation:**

The formation of binary MX compounds is common during the fabrication of MAX phases via HP. Additionally, as the furnace operates under vacuum, an outer layer of TiC or TiN forms due to the preferential dissociation of Al or Si metal from the outside of the sample blanks. This was observed for all samples fabricated for this thesis, which is why the outer surfaces of each blank were purposefully machined off to remove this contamination layer. According to the XRD refinement of pristine samples, the TiC contents of the pristine Ti<sub>2</sub>AlC, Ti<sub>3</sub>AlC<sub>2</sub>, Ti<sub>3</sub>SiC<sub>2</sub>-FG and Ti<sub>3</sub>SiC<sub>2</sub>-CG samples, were found to be 8(1) wt.%, 1.9(6) wt.%, 23(1) wt.% and 18.2(5) wt.%, respectively. In pristine Ti<sub>2</sub>AlN, the TiN content was found to be 3.2(2) wt. %.

Irradiation of the Ti<sub>3</sub>AlC<sub>2</sub> samples resulted in the significant increase in the TiC content from 1.9(6) wt.% before irradiation, to 52.6(9) and 44.4(8) wt.%, after the M-D1-T2 and M-D1-T4 irradiations, respectively. Cross sections of these samples were also scanned by XRD confirming that the dissociation into TiC was not a surface phenomenon Figure 4.4.

The TiC content in the CG-Ti<sub>3</sub>SiC<sub>2</sub> samples changed from 18.2(5) wt.% as received to 23.3(6) and 17.0(4) wt.% after M-D1-T2 and M-D1-T4 irradiations, respectively (Table 4.1). Irradiation of FG-Ti<sub>3</sub>SiC<sub>2</sub> also yielded a change in TiC content, going from 23(1) wt.% initially to 22.7(5) and 25(1) wt.% after the M-D1-T2 and M-D1-T4 irradiations, respectively. The FG-Ti<sub>3</sub>SiC<sub>2</sub>:M-D2-T2 samples only showed a slight decrease in TiC, to 21.8(6) wt.%.



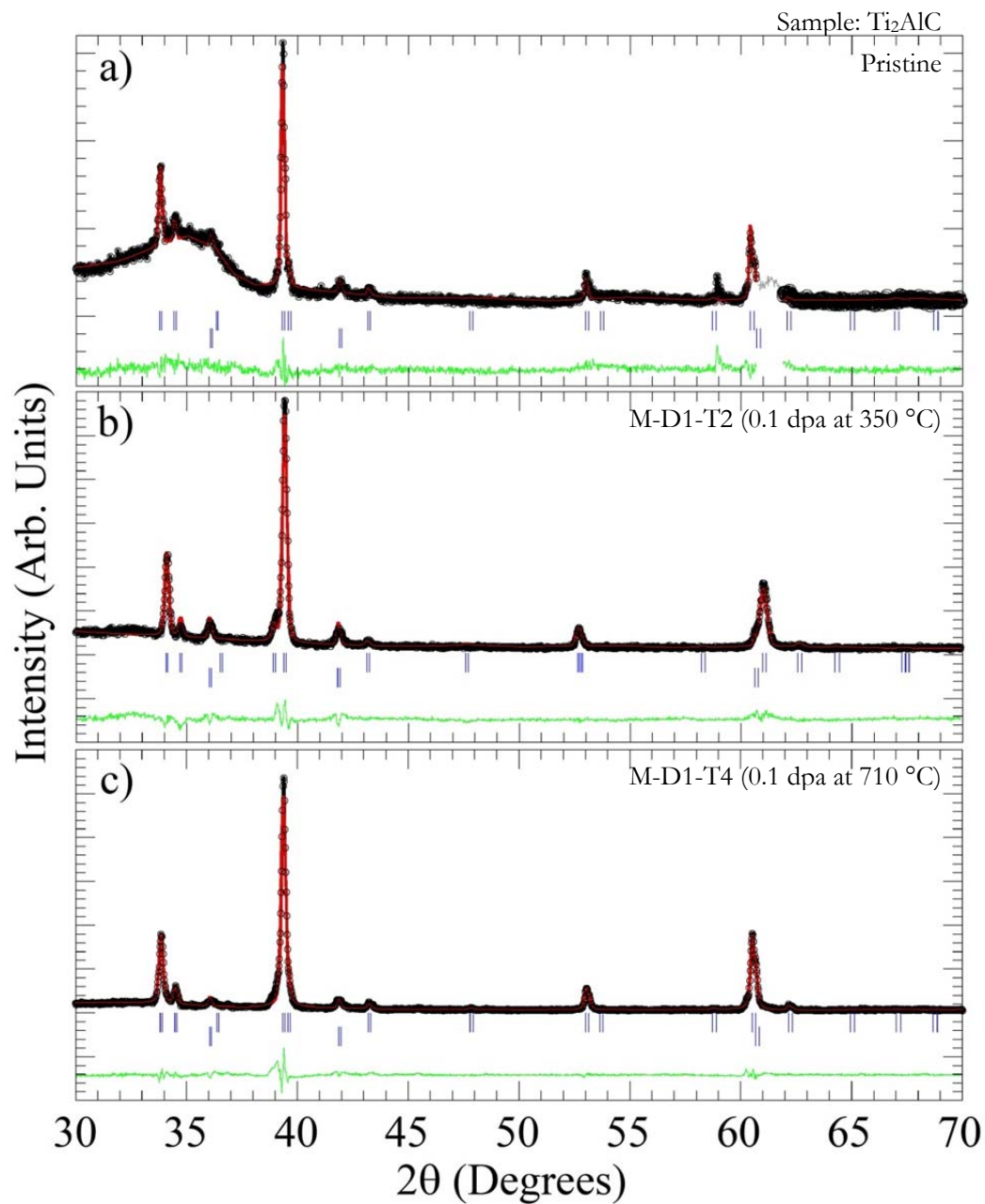


Figure 4.5 Rietveld analysis of XRD patterns of  $\text{Ti}_2\text{AlC}$ .

a) Pristine and, b)  $\text{Ti}_2\text{AlC}$ :M-D1-T2 and c)  $\text{Ti}_2\text{AlC}$ :M-D1-T4. Open circles, solid line, and solid line at the bottom, represent the observed data, calculated model, and the difference between the two, respectively. The two rows of vertical tags represent the calculated Bragg reflections' positions of the  $\text{Ti}_2\text{AlC}$  (1st row), and  $\text{TiC}$  (2nd).

At 8.3(3) wt.%, the TiC composition did not vary significantly for  $\text{Ti}_2\text{AlC}$  after the M-D1-T2 irradiation and was within the variability in TiC content obtained for these samples. Refinement also revealed that the  $\text{Ti}_2\text{AlC}$ :M-D1-T4 samples contained 4.3(1) wt.% TiC, a value lower than in the pristine samples. Furthermore, after M-D2-T2 irradiation, the  $\text{Ti}_2\text{AlC}$  samples showed 1.9(5) wt.% TiC, even lower than pristine. Since it is impossible to transform TiC to  $\text{Ti}_2\text{AlC}$  by neutron irradiation, this result simply shows that the initial TiC impurity phase distribution in these samples was inhomogeneous. This point is discussed in more detail below.

At 11.6(1) wt.%, the TiN content in  $\text{Ti}_2\text{AlN}$ :M-D1-T2 increased from pristine, at 3.23(2).  $\text{Ti}_2\text{AlN}$ -M-D1-T4 contained 13(1) wt.% TiN as well as 36(3) wt.%  $\text{Ti}_4\text{AlN}_3$ . An additional phase with peaks around 36, 41, and  $58.6^\circ$   $2\theta$  was unidentified, due to these peaks' low intensity and the high background noise.

While the a- and c-LPs for each MAX phase discussed above were distorted at T2 conditions (Figure 4.8), the a-LP for the TiC phase remained relatively constant under most conditions, showing at most an increase of  $\sim 0.2\%$  in the  $\text{Ti}_3\text{AlC}_2$ :M-D1-T2 samples (Table 4.1). While the TiC content increased in some cases, its LPs remained quite close to their values in the pristine samples. The only sample to show deviation was  $\text{Ti}_2\text{AlC}$ :M-D2-T2, where the a-LP for TiC decreased by  $\sim 1\%$ .

Table 4.1 Irradiation-induced structural and compositional changes in MITR irradiated MAX phases.

Condition	$\chi^2$	a-LP (Å)	c-LP (Å)	Ti <sub>ll_z</sub> position	C_z position	TiC content wt.%	TiC a-LP (Å)	FWHM Parameter, U	$\mu\epsilon\%$
Ti <sub>3</sub> SiC <sub>2</sub> FG-Pristine	2.10	3.0685(6)	17.680(5)	0.3658(3)	0.573(1)	23(1)	4.3200(2)	0.0174(2)	0.19
Ti <sub>3</sub> SiC <sub>2</sub> FG:M-D1-T2	3.08	3.0648(1)	17.812(9)	0.3661(3)	0.571(1)	22.7(5)	4.3192(1)	0.0385(7)	0.27
Ti <sub>3</sub> SiC <sub>2</sub> FG:M-D1-T4	1.83	3.0667(2)	17.675(1)	0.3675(7)	0.556(3)	25(1)	4.3195(2)	0.0133(5)	-
Ti <sub>3</sub> SiC <sub>2</sub> FG:M-D2-T2	2.43	3.0634(2)	17.887(1)	0.3657(3)	0.558(2)	22(1)	4.3217(1)	0.057(1)	0.36
Ti <sub>3</sub> SiC <sub>2</sub> CG-Pristine	16.7	3.0688(7)	17.680(1)	0.3662(4)	0.572(2)	18.2(5)	4.3185(1)	0.0042(1)	-
Ti <sub>3</sub> SiC <sub>2</sub> CG:M-D1-T2	1.84	3.0647(1)	17.840(1)	0.3664(3)	0.565(1)	23.3(5)	4.3238(2)	0.0488(1)	0.33
Ti <sub>3</sub> SiC <sub>2</sub> CG:M-D1-T4	2.79	3.0674(8)	17.669(1)	0.3660(4)	0.556(2)	17.0(4)	4.3215(1)	0.0150(2)	0.06
Ti <sub>3</sub> SiC <sub>2</sub> CG:M-D2-T2	2.36	3.0626(2)	17.900(1)	0.3656(4)	0.559(2)	21.3(7)	4.3235(2)	0.03768(8)	0.27
Ti <sub>3</sub> AlC <sub>2</sub> -Pristine	1.88	3.0736(2)	18.562(2)	0.1291(5)	0.564(2)	1.9(6)	4.3114(2)	0.0094(7)	0.10
Ti <sub>3</sub> AlC <sub>2</sub> :M-D1-T2	2.63	3.0542(2)	18.896(1)	0.1251(3)	0.600(1)	52.6(9)	4.3197(3)	0.064(1)	0.39
Ti <sub>3</sub> AlC <sub>2</sub> :M-D1-T4	3.73	3.0699(2)	18.543(2)	0.1313(4)	0.599(1)	44.4(8)	4.3082(3)	0.05(1)	0.34
Ti <sub>3</sub> AlC <sub>2</sub> :M-D2-T2									
Condition	$\chi^2$	a-LP (Å)	c-LP (Å)	Ti <sub>ll_z</sub> position	C_z position	TiC content wt.%	TiC a-LP (Å)	FWHM Parameter, U	$\mu\epsilon\%$
Ti <sub>2</sub> AlC-Pristine	1.95	3.0614(2)	13.650(2)	0.589(1)	<sup>a</sup> n/a	8(1)	4.3068(9)	0.0060(1)	-
Ti <sub>2</sub> AlC:M-D1-T2	3.17	3.0367(2)	13.882(1)	0.5843(5)	<sup>a</sup> n/a	8.3(3)	4.3168(3)	0.157(1)	0.66
Ti <sub>2</sub> AlC:M-D1-T4	2.44	3.0585(3)	13.659(3)	0.585(3)	<sup>a</sup> n/a	4.3(1)	4.3128(1)	0.0176(2)	0.11
Ti <sub>2</sub> AlC:M-D2-T2	1.9	3.0206(3)	14.056(3)	0.586(2)	<sup>a</sup> n/a	1.9(5)	4.264(1)	0.4378(4)	1.14
Condition	$\chi^2$	a-LP (Å)	c-LP (Å)	Ti <sub>ll_z</sub> position	C_z position	TiN content wt.%	TiN a-LP (Å)	FWHM Parameter, U	$\mu\epsilon\%$
Ti <sub>2</sub> AlN-Pristine	1.6	2.9886(3)	13.640(2)	0.587(2)	<sup>a</sup> n/a	3.23(2)	4.2329(2)	0.015(1)	0.16
Ti <sub>2</sub> AlN:M-D1-T2	2.2	2.9808(6)	13.714(4)	0.590(1)	<sup>a</sup> n/a	11.6(1)	4.2336(1)	0.0262(2)	0.20
<sup>b</sup> Ti <sub>2</sub> AlN:M-D1-T4	2.6	3.0086(3)	13.664(4)	0.570(2)	<sup>a</sup> n/a	13(1)	4.2223(3)	0.125(2)	0.58
Ti <sub>2</sub> AlN:M-D2-T2									

Numbers in parenthesis represent one standard deviation of the last significant digit.

a- In M<sub>2</sub>AX compounds, the C-atom z position is fixed at the origin.

b- In the case of Ti<sub>2</sub>AlN:M-D1-T4, 36(3) wt.% Ti<sub>4</sub>AlN<sub>3</sub> content was detected. With a-LP of 2.9931 and c-LP of 22.986, the lattice was distorted from pristine, at 2.988 and 23.372, for a-LP and c-LP, respectively.

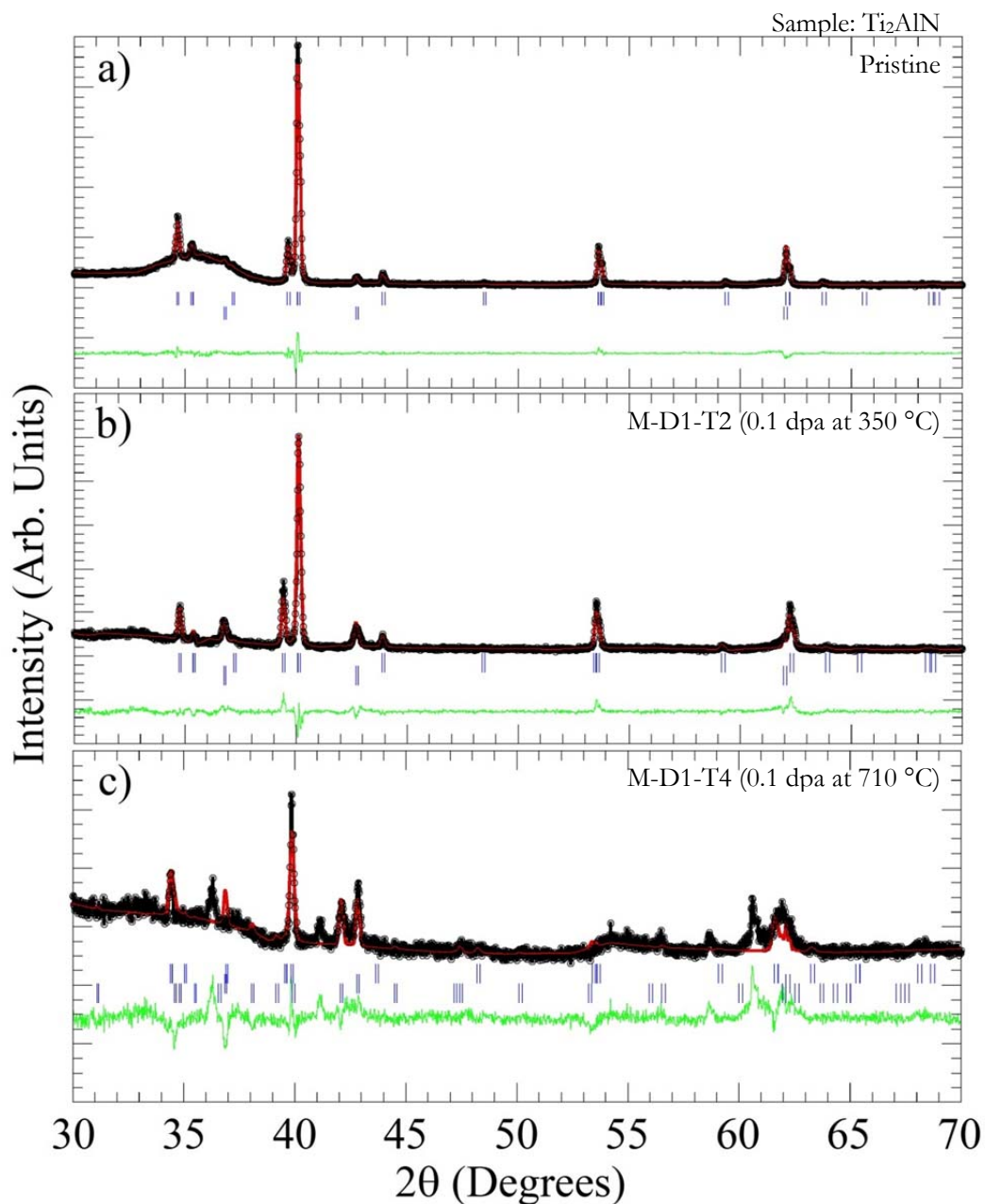


Figure 4.6 Rietveld analysis of XRD pattern of  $\text{Ti}_2\text{AlN}$ .

a) Pristine and, b)  $\text{Ti}_2\text{AlN}$ :M-D1-T2 and c)  $\text{Ti}_2\text{AlN}$ :M-D1-T4. Open circles, solid line, and solid line at the bottom, represent the observed data, calculated model, and the difference between the two, respectively. The two rows of vertical tags represent the calculated Bragg reflections' positions of the  $\text{Ti}_2\text{AlN}$  (1st row) and  $\text{TiN}$  (2nd). In c), the best fit for  $\text{Ti}_2\text{AlN}$ :M-D1-T4 pattern was achieved by including  $\text{Ti}_4\text{AlN}_3$  in the refinement (3rd row). Peaks around 36, 41, and  $58.6^\circ$   $2\theta$  were unidentified due to their low intensity and the high background noise.

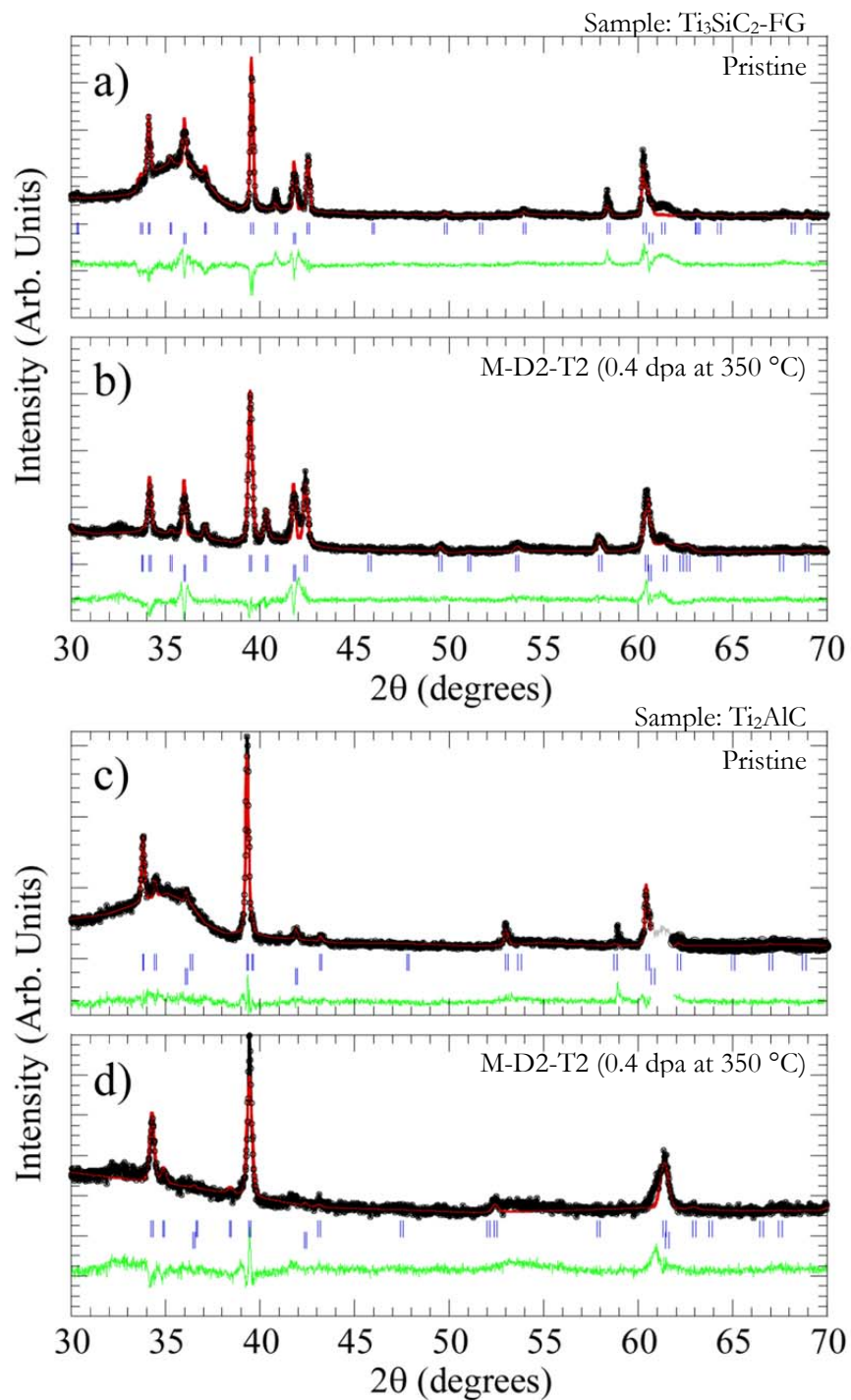


Figure 4.7 Rietveld analysis of XRD patterns of M-D2-T2 samples of FG-Ti<sub>3</sub>SiC<sub>2</sub> and Ti<sub>2</sub>AlC a) pristine Ti<sub>3</sub>SiC<sub>2</sub>-FG and, b) FG-Ti<sub>3</sub>SiC<sub>2</sub>:M-D2-T2. The two rows of vertical tags represent the calculated Bragg reflections' positions of the Ti<sub>3</sub>SiC<sub>2</sub> (1st row) and TiC (2nd). c) Pristine Ti<sub>2</sub>AlC and, d) Ti<sub>2</sub>AlC:M-D2-T2. The two rows of vertical tags represent the calculated Bragg reflections' positions of the Ti<sub>2</sub>AlC (1st row), and TiC (2nd). Circles, solid line, and solid line at the bottom, represent the observed data, calculated model, and the difference between the two, respectively.

#### 4.2.2. Stable Compositions

As materials are exposed to neutron irradiation, the formation of new phases would demonstrate an inability to cope with irradiation damage. Based on the XRD results,  $\text{Ti}_3\text{SiC}_2$  and  $\text{Ti}_2\text{AlC}$  showed the highest phase stability after neutron irradiation.

$\text{Ti}_3\text{SiC}_2$ , both fine and coarse grained, showed a slight variation in TiC content when irradiated at M-D1-T2 and M-D1-T4 conditions. Given the fluctuations in the TiC contents of the pristine and irradiated samples, it is difficult to conclude if any dissociation occurred at all. Results of  $\text{Ti}_3\text{SiC}_2$ -FG:M-D2-T2 (Table 4.1) also show minimal decrease in TiC content confirming that  $\text{Ti}_3\text{SiC}_2$ -FG remains stable, even with increasing dose.

As noted in Chapter 3, pristine  $\text{Ti}_2\text{AlC}$  samples were fabricated starting with commercially available MAX powders (Kanthal, Sweden), resulting in an initial TiC volume fraction of 8(1) wt. %. At 8.3(3) wt.%, the TiC composition was slightly higher in the  $\text{Ti}_2\text{AlC}$ :M-D1-T2 samples and was likely within the error of the TiC content measured. Refinement of the  $\text{Ti}_2\text{AlC}$ :M-D1-T4 samples revealed 4.3(1) wt.% TiC, a value lower than in the pristine samples. At 1.9(5) wt.%, the TiC content in  $\text{Ti}_2\text{AlC}$ :M-D2-T2 was even further below that of the pristine sample, which suggests a somewhat inhomogeneous distribution of the TiC impurity phase in these samples. It is possible that the specimens scanned for the pristine condition were machined from the outer regions of the blank, thus possessing a higher TiC content. These comments notwithstanding, the fact that the TiC content does not increase shows that the  $\text{Ti}_2\text{AlC}$  phase remained stable after irradiation.

#### 4.2.3. Unstable Compositions

What is noteworthy and completely unexpected however, was the dissociation of roughly 50 wt.% of the  $\text{Ti}_3\text{AlC}_2$  into TiC Table 4.1. One of the reasons this was unexpected is that it was never observed or reported on in any of the heavy ion irradiation work [3, 22, 60-64, 66,

67, 69, 71]. This is an important result since it is clear that  $\text{Ti}_3\text{AlC}_2$  may not be as resistant to neutrons as previously assumed. Clearly, the dissociation of  $\text{Ti}_3\text{AlC}_2$  into TiC appears to be enhanced by the neutron irradiation, the extent of which increased at the lower irradiation temperature.

$\text{Ti}_2\text{AlN}$  also was seen to dissociate, increasing TiN content from 3.23(2) wt.% to 11.6(1) and 13(1) wt.% after M-D1-T2 and M-D1-T4, respectively. Unique among all MAX phases tested herein,  $\text{Ti}_2\text{AlN}$ :M-D1-T4 resulted in the formation of 36(3) wt.%  $\text{Ti}_4\text{AlN}_3$ , a MAX phase morphology with more TiN layers between Al-layers. An additional phase with peaks around 36, 41, and  $58.6^\circ 2\theta$  was unidentified, due to these peaks' low intensity and the high background noise.

Also of note is the resiliency of TiC after irradiation at these conditions. While the  $\text{Ti}_3\text{AlC}_2$  and  $\text{Ti}_2\text{AlC}$  samples showed significant lattice distortion after T2 irradiation, the a-LP of the TiC phase remained largely unperturbed, at most increasing by 0.19 % in the  $\text{Ti}_3\text{AlC}_2$  samples. It is plausible then that the TiC which forms via dissociation of  $\text{Ti}_3\text{AlC}_2$  relieves the lattice strains. While the large scale dissociation of  $\text{Ti}_3\text{AlC}_2$  into TiC may be detrimental to its future in nuclear applications, it is unclear if the presence of small volume fractions will be problematic for other MAX phases, since commercially available  $\text{Ti}_2\text{AlC}$  and  $\text{Ti}_3\text{SiC}_2$  often contain  $\sim 10$  wt.% TiC.

#### 4.2.4. Lattice Parameter Distortions

Rietveld refinement revealed a distortion of LPs under neutron irradiation of the FG- $\text{Ti}_3\text{SiC}_2$ , CG- $\text{Ti}_3\text{SiC}_2$ ,  $\text{Ti}_3\text{AlC}_2$ ,  $\text{Ti}_2\text{AlC}$  and  $\text{Ti}_2\text{AlN}$  samples (Figure 4.8). This result concurs with previous work where heavy ions and He irradiations were shown to result in lattice distortions [3, 22, 60-64, 66, 67, 69, 71]. After M-D1-T2 irradiation,  $\text{Ti}_3\text{AlC}_2$  and  $\text{Ti}_2\text{AlC}$  showed the largest increase in c-LPs, while  $\text{Ti}_2\text{AlN}$  showed the least (Figure 4.8a). The a-

LPs decreased after M-D1-T2 irradiation, with  $\text{Ti}_2\text{AlC}$  showing the largest deviation from pristine (Figure 4.8b). In contradistinction, after M-D1-T2 irradiation, the LPs for most materials tested were distorted by  $\leq 0.1\%$ , confirming the dynamic recovery capabilities of the MAX phases. There were little observable differences between the fine and coarse grained  $\text{Ti}_3\text{SiC}_2$  samples, both of which showed less extensive distortion than  $\text{Ti}_3\text{AlC}_2$ .

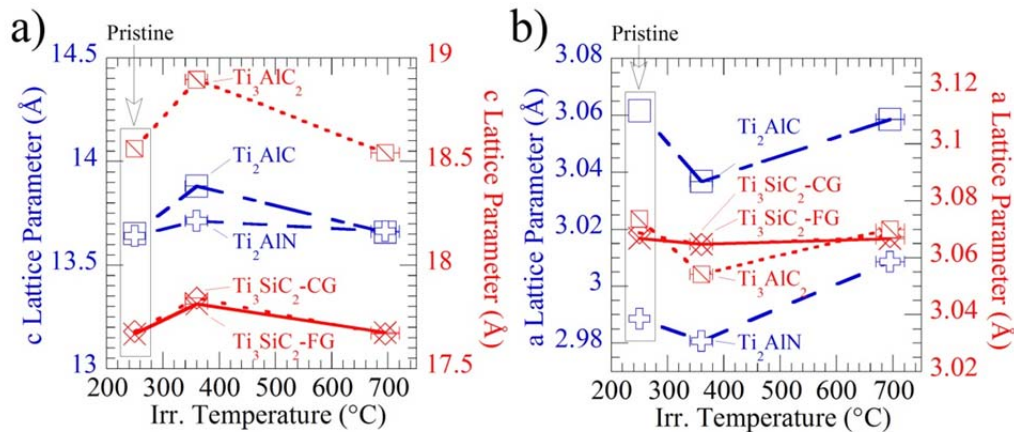


**Figure 4.8** Lattice parameters of MAX phases as a function of irradiation temperature. Plots comparing a) c-LPs and b) a-LPs as a function of irradiation temperature for the MAX phases FG- $\text{Ti}_3\text{SiC}_2$ , CG- $\text{Ti}_3\text{SiC}_2$ ,  $\text{Ti}_3\text{AlC}_2$ ,  $\text{Ti}_2\text{AlC}$ , and  $\text{Ti}_2\text{AlN}$  show an increase in c-LP and a decrease in a-LP after irradiation at M-D1-T2. After irradiation at M-D1-T4, however, the LPs are seen to return closer to pristine values, which have been plotted for reference.

Figure 4.8 summarizes the effect of irradiation temperature on the LPs of each MAX phase tested herein. In all cases, irradiation at condition M-D1-T2 resulted in an expansion in the c-LP and a reduction in the a-LP. The  $\text{Ti}_3\text{AlC}_2$  showed the largest increase in c-LP, with  $\text{Ti}_2\text{AlN}$  showing the least.  $\text{Ti}_2\text{AlC}$  had the largest reduction in a-LP, while the  $\text{Ti}_3\text{SiC}_2$  samples had the least. Unsurprisingly, the FG and CG  $\text{Ti}_3\text{SiC}_2$  samples responded similarly. For most samples, irradiation at T4 resulted in LPs that were only slightly distorted from pristine dimensions.  $\text{Ti}_2\text{AlN}$  revealed an increase in a-LP at T4, in contrast to all other samples tested. This is attributed to the extensive distortion observed in the XRD spectrum



(Figure 4.6c) seen by the increased background intensity, and the formation of several impurity phases after irradiation.

In summary, at temperatures as low as 710(50) °C, the MAX phases show remarkable recovery of lattice parameters after irradiation to 0.1dpa. Lattice distortion is nearly completely reverted back to pristine values in all samples, save for  $\text{Ti}_2\text{AlN}$  which resulted in the formation of multiple new phases at 710(50) °C, leading to increased microstrains.  $\text{Ti}_3\text{AlC}_2$  also showed extensive dissociation, having ~50 wt.% TiC content after irradiation. These results indicate that the  $\text{Ti}_3\text{AlC}_2$  and  $\text{Ti}_2\text{AlN}$  compositions used herein were unable to withstand irradiation induced segregation and solute migration which resulted in the drastic removal of Al from the MAX phase unit cells.

Potential reactor applications require radiation tolerant materials, able to withstand the effects of irradiation induced defects.  $\text{Ti}_3\text{SiC}_2$  and  $\text{Ti}_2\text{AlC}$  showed remarkable phase stability and lattice recovery at all conditions. Therefore, focus was given specifically to these two compositions as having the most potential for use in reactors. TEM investigation of the irradiation defects is presented in Chapter 5.

### 4.3. Theoretical Defective Structures

---

The previous sections describe in detail the results of Rietveld refinement of XRD patterns collected from pristine and irradiated MAX phases. The following section attempts to explain the changes in lattice dimensions and microstrains in relation to the material structure evolutions induced by irradiation.

Attempts have been made to understand the irradiation response of MAX phases by using density functional theory, DFT, calculations of point defect formation and migration. Several recent first principles studies [79-82] have concluded that the presence of the A-layer could provide significant irradiation tolerance for the MAX phases. The general trends showed that Frenkel pairs, FPs, of Ti, A (either Si or Al), and C elements readily form as interstitials within the A-layer and/or in the space between the A and Ti layers (Figure 4.9).

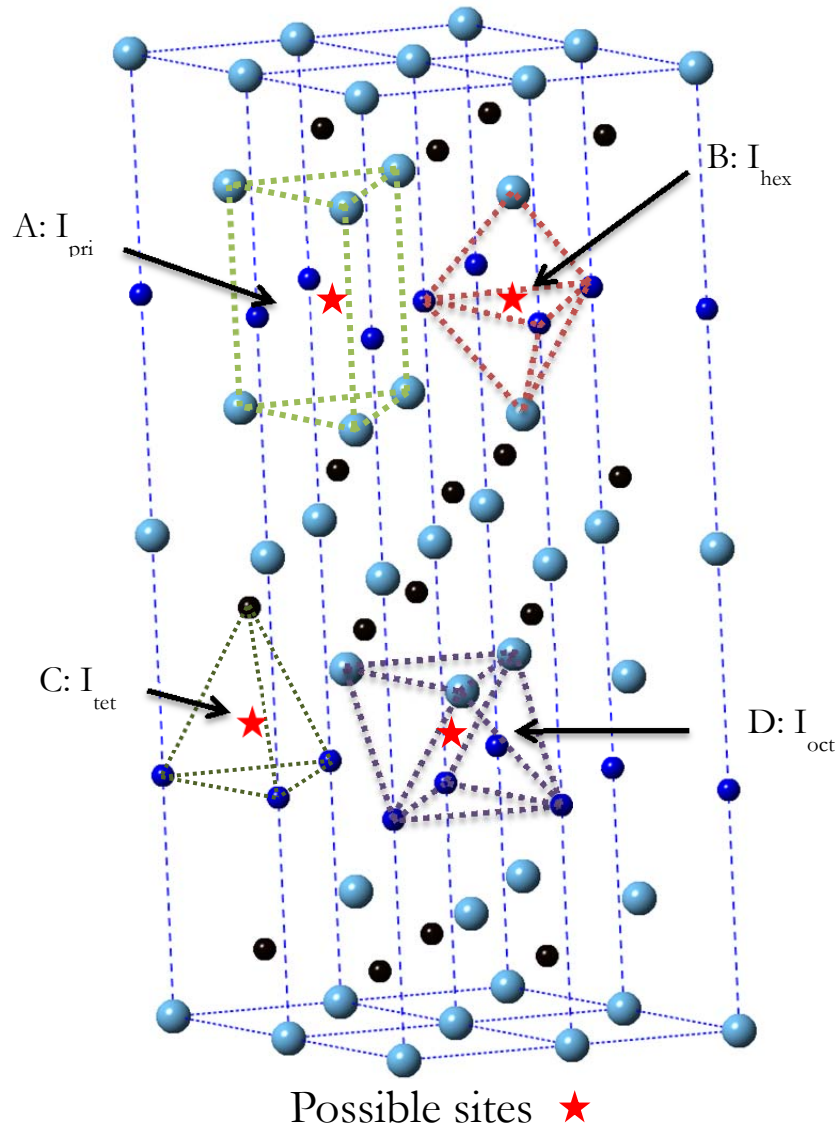


Figure 4.9 Possible interstitial sites in the  $M_3AX_2$  structure include A:  $I_{pri}$ , B:  $I_{hex}$ , C:  $I_{tet}$ , and D:  $I_{oct}$  [79].

While varying in values due to differences in calculation methods, the energy of formations,  $E_f$ 's, for point defects, eg.  $C_i$  or  $V_A$ , in the A-layers were consistently much lower, by  $\sim 1-3$  eV, compared to defects within the TiC blocks,  $> 9$  eV [79-82]. Antisite defects, e.g.  $Ti_{Al}$ , were also shown to have quite low  $E_f$ ,  $\sim 2$  eV, comparable to A-layer Frenkel pairs. Middleburg *et al.* showed that the lowest energy  $C_i$  in hexagonal coordination with 3 basal Si and 2 Ti forms bond lengths similar to those found in TiC and SiC (Site B in Figure 4.10) [82]. The low energy requirements for the formation of antisite and point defects within the A-layer indicate that the A-layer can act as potent defect sinks within each nanolaminate layer.

In comparing various A-elements, Wang *et al.* showed that  $C_{FP}$  and  $Si_{FP}$  with  $E_f = 1.5$  and  $2.1$  eV, respectively, were the lowest energy defects in  $Ti_3SiC_2$  [80]. In contrast, the  $Ti_{Al}Al_{Ti}$  antisite defects, requiring  $1.6$  eV to form, were the lowest energy defects in  $Ti_3AlC_2$  [80]. At  $2.96$  eV, the same antisite defect was also the lowest energy defect in  $Ti_2AlC$  [79]. Xiao *et al.* further described the effect of bond character between various MAX compositions, stating that the more ionic character of the Ti-Al bonds found in  $Ti_3AlC_2$  and  $Ti_2AlC$  would lead to enhanced irradiation tolerance compared to  $Ti_3SiC_2$  by allowing for easier recovery of the lattice damage [79].

With a higher Al:TiC block ratio, and thus a larger volume of point defect sinks,  $Ti_2AlC$  was predicted to have higher irradiation tolerance than its 312 counterpart [79]. It was then theorized that the Al-containing phases would have better irradiation tolerance, due to the ease of forming stable antisite defects over Frenkel pairs, which would allow them to recover irradiation damage more easily.

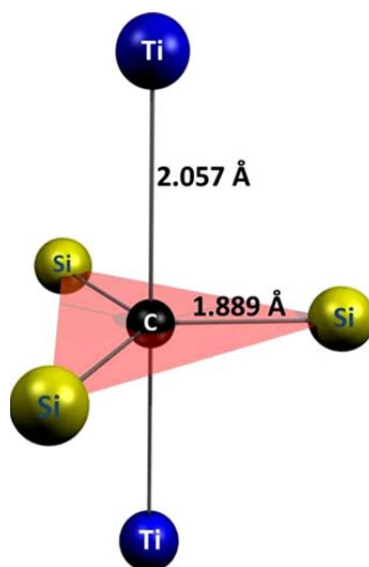


Figure 4.10 Schematic of the lowest energy C interstitial arrangement showing the nearest neighbor bonds to the Si atoms within the basal layer and to the Ti atoms in the z-direction [82].

However, XRD analysis of neutron irradiated MAX phase samples discussed herein showed a decrease in a-LP and an increase in c-LP after irradiation at lower temperatures, e.g. T2 (350 °C). In order to describe what structural change results in this shift, it is instructive to look back at several theoretical studies of the MAX phases and MX binaries. In the case of  $\text{Ti}_2\text{AlC}$ , deficiency in Al resulted in a decrease in c-LP, while the a-LP remains constant [83]. This was explained by loss of Ti-Al bonding between layers, resulting in shrinkage of the c-LP. The a-LP was determined to be highly dependent on the  $\text{Ti}_{n+1}\text{C}_n$  block structure, and remained constant [83]. Furthermore, exploration of structural relaxation in  $\text{TiC}_{1-x}$  showed that vacancies in the TiC rock salt structure resulted in a decrease in a-LP [84]. Therefore, in order for the MAX phase structure to contract in the a-direction, carbon vacancies,  $\text{C}_v$ , must be introduced during neutron irradiation. This is not unexpected, as  $\text{V}_\text{C}$  is well understood to have low  $E_f$ , ~2-3 eV, in both  $\text{Ti}_3\text{SiC}_2$  and  $\text{Ti}_3\text{AlC}_2$  [79-82]. Additionally, at ~4 eV, the migration energy,  $E_m$ , of  $\text{V}_\text{C}$  is relatively high for diffusion along the  $\text{M}_3\text{C}_2$  blocks [82]. This higher barrier for migration, in conjunction with the lower formation energy, would result in

$V_c$  that are less likely to migrate within the  $M_3C_2$  block. In contrast, the lower  $E_m$  of  $C_i$  within the A-layer,  $\sim 0.5$ -1 eV, indicates the ease in which C defects migrate within the layer [79-82].

Middleburgh *et al.*, through DFT calculations, proposed that C and Ti interstitials would dominate in  $Ti_3SiC_2$ , while  $M_A-A_M$  antisites would dominate in  $Ti_3AlC_2$  and  $Ti_2AlC$  [82]. Interestingly, most DFT calculations reported that the most likely point defects would be located within the A-layers, residing in a hexagonal bi-pyramidal configuration in-plane between 3 A atoms, and between 2 M atoms (Site B in Figure 4.9). This, however, would lead to an increase in the bond lengths between neighboring A atoms, resulting in, if any distortion, an *increase* in the a-LP. As the XRD results presented reveal a decrease in a-LP with an increase in c-LP, it is clear that some other defect configuration was stabilized after neutron irradiation in these materials.

I propose that a more complex defect structure, which transforms the unirradiated lattice (Figure 4.11a), is needed to explain the results deduced from XRD refinements.

#### 4.3.1. Low Temperature Irradiation ( $\leq 350$ °C)

First, consider C Frenkel pairs, where C vacancies formed in the TiC block would lead to a decreased a-LP for the overall structure. As the C interstitials preferentially fill the in-plane hexagonal interstitial sites (Site B in Figure 4.9), subsequent A or M interstitials might then be more favorably located in the octahedral site between 3 A atoms and 3 Ti atoms, above or below the plane of A atoms (Site D in Figure 4.9). This would result in a bilayer positioning of the A or M atom within the M-A layer, resulting in a distortion of the M-A bonding along the c-axis. The combination of  $V_c$  in the  $Ti_3C_2$  block with increased atomic spacing in the c-direction could produce the LP distortions observed in the XRD results (Figure 4.8).

The separation of interstitials and vacancies must also be considered. As discussed above the  $E_m$  of A and X interstitials, have been shown to be very low when migrating along the A-layers, on the order of 0.5-1 eV [82]. The M interstitials, on the other hand, have a higher  $E_f$  and  $E_m$  [79, 81]. Additionally, diffusion across the  $M_{n+1}X$  block has been shown to be very difficult, with very large energy barriers and can be ruled out. It would then follow that A or X Frenkel pairs that form, and are separated by the  $M_{n+1}X$  blocks, are much less likely to recombine. It is not unexpected that such interstitials can form after neutron irradiation, thus the proposed defect structure becomes plausible. At low irradiation temperatures, where defect mobility is limited, interstitials that become separated from their respective vacancies by the impenetrable  $M_{n+1}X_n$  blocks could likely form a complex structure, resulting in c-LP expansion (Figure 4.11b).

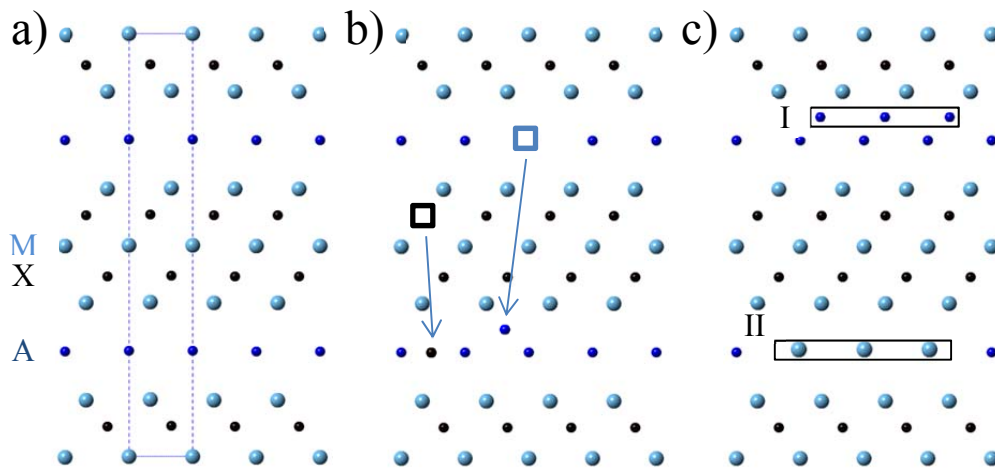


Figure 4.11  $(10\bar{1}0)$  view of  $M_3AX_2$  structure a) pristine, b) after irradiation at low temperatures (350 °C), and c) after irradiation at higher (700 °C) temperatures. Region I shows coherent interstitial loops; region II shows M atom antisite layers. Combinations of the two types of defects in a single layer are also possible. The unit cell is shown by the dotted line in a.

#### 4.3.2. High Temperature Irradiation ( $\geq 500$ °C)

At higher irradiation temperatures, defect mobility is increased, leading to increased agglomeration and/or annihilation of point defects. As point defects cluster together, the defect platelets could eventually collapse into dislocation loops. Larger defect structures, which become coherent with the lattice, would lead to less distortion of the unit cell overall. As seen herein, the XRD refinement results show that the lattice parameters of the MAX phases tend to return to their pristine values after high temperature irradiations. A possible structure that could accommodate for the observed lattice parameters is proposed in Figure 4.11c.

As the point defects discussed above being to interact and cluster together, being restricted to the basal plane, specifically within the free volume in and around the A-layer, could result in limited possibilities for defect arrangements. Interstitial atoms, likely A or M in nature, might agglomerate into a platelet between the A and M layers, with the atoms sitting more favorably in the  $I_{\text{oct}}$  positions (Region I in Figure 4.11c). Alternatively, substitutional antisite defects, likely M atoms on the A-sublattice positions, could also form into a platelet in the A-layer (Region II in Figure 4.11c). At higher irradiation temperatures, where the defect mobility is increased, if localized regions of defect clusters coherently form dislocation loops of this nature, the result would be an overall relaxation of the crystal lattices, with dislocation or antisite loops throughout. The XRD results suggest that this configuration is plausible, based on the relaxation of unit cell parameters at higher temperatures Figure 4.8. Furthermore, evidence of dislocation loops that fit these descriptions is provided and discussed further in Chapter 5.

#### 4.4. Conclusions

---

The first ever reported neutron irradiation of bulk MAX phases shows that  $\text{Ti}_3\text{SiC}_2$ ,  $\text{Ti}_3\text{AlC}_2$ ,  $\text{Ti}_2\text{AlC}$  and  $\text{Ti}_2\text{AlN}$  remain crystalline after neutron irradiation up to 0.1 dpa at 350 °C and 710 °C and also at 0.4 dpa at 350 °C. Rietveld analysis of post-irradiation XRD patterns of  $\text{Ti}_2\text{AlC}$  and  $\text{Ti}_3\text{AlC}_2$  reveal a drastic difference in irradiation tolerance between the two compounds. Roughly 50 wt.% of the  $\text{Ti}_3\text{AlC}_2$  sample was converted to  $\text{TiC}$  with a 1.7% increase in c-LP and a 0.6% decrease in a-LP after irradiation to 0.1 dpa at 350 °C (Table 4.1). This dissociation was not mitigated by irradiation at 0.1 dpa at 710 °C, though the lattice parameters showed less distortion, being close to pristine. This same trend in lattice parameters is seen in  $\text{Ti}_2\text{AlC}$ , however, no dissociation into  $\text{TiC}$  was observed in this case.  $\text{Ti}_2\text{AlN}$  was seen to dissociate into 13(1) wt.%  $\text{TiN}$  and 36(3) wt.%  $\text{Ti}_4\text{AlN}_3$ , resulting in significant lattice strains after irradiation at T4.

$\text{Ti}_3\text{SiC}_2$  also showed lattice distortion, but to a lesser extent than  $\text{Ti}_3\text{AlC}_2$  or  $\text{Ti}_2\text{AlC}$ , with only ~1% increase in c-LP and 0.6% decrease in a-LP after 0.1 dpa at 350 °C. The Ti-Si bonding has been shown to be stronger than Ti-Al bonding in the MAX phases, which could explain the lesser distortion of the lattice [85]. There also appears to be no differences in the lattice response as a function of grain size. Irradiation at higher doses, up to 0.4 dpa at 350 °C, revealed even greater distortions of  $\text{Ti}_3\text{SiC}_2$ -FG and  $\text{Ti}_2\text{AlC}$  LPs, and significantly higher microstrains were measured in the latter, at 1.14%.

In an effort to explain the distorted lattice structures at low irradiation temperatures, i.e. 350 °C, recent DFT calculations were incorporated into a model structure (Figure 4.11). Carbon interstitials, preferentially forming in the A-sublattice could force subsequent point defects into a position between the A and  $\text{Ti}_{II}$  layers (Site B in Figure 4.9), resulting in an expansion



along the *c*-direction. The resultant C vacancies in each  $Ti_{n+1}C_n$  block would then result in a decrease in *a*-LP, as predicted by theoretical studies. This defect-defect interaction, previously unaccounted for in DFT modelling of the MAX phases, would be plausible during neutron irradiation.

As XRD has shown a global effect on crystal structure and phase composition induced by irradiation, it is necessary to understand how the irradiation defects interact on the nanoscale. The following chapter discusses the formation and nature of the irradiation induced defects utilizing transmission electron microscopy. As  $Ti_3SiC_2$  and  $Ti_2AlC$  showed a greater resistance to decomposition, these phases remain potential candidates for nuclear applications. TEM investigations are focused on these two compositions.

## 5. IRRADIATION INDUCED DEFECTS

---

The interaction of irradiation induced defects leads to many structural and behavioral changes in materials. XRD analysis provided a bulk statistical analysis of structural parameters in the MAX phases. Irradiation with neutrons resulted in lattice distortions and phase instability in some phases. These structural changes were thus presumed to have been caused by irradiation induced defects. TEM, which is able to resolve nanoscale defects, was used to investigate the irradiation induced defects in these materials. With increasing dose and temperature, point defects are seen to agglomerate into larger defect structures. The majority of this chapter explores the effect of irradiation on defect formation in  $\text{Ti}_3\text{SiC}_2$  and  $\text{Ti}_2\text{AlC}$ , as investigated by transmission electron microscopy. Results are then compared with previous heavy ion studies.

### 5.1. Transmission Electron Microscopy, TEM

---

Based on results from XRD discussed in Chapter 4, it was found that  $\text{Ti}_3\text{SiC}_2$  and  $\text{Ti}_2\text{AlC}$  samples remained phase pure after irradiation at MITR, while  $\text{Ti}_3\text{AlC}_2$  and  $\text{Ti}_2\text{AlN}$  showed signs of dissociation. Therefore, the remaining efforts to characterize the irradiation defects were focused on  $\text{Ti}_3\text{SiC}_2$  and  $\text{Ti}_2\text{AlC}$ . Samples of FG- $\text{Ti}_3\text{SiC}_2$  and  $\text{Ti}_2\text{AlC}$  were made using FIB techniques to mill electron transparent lamella for TEM analysis. From analysis of the XRD results, there was found to be little difference in irradiation response on lattice distortions between FG- $\text{Ti}_3\text{SiC}_2$  and CG- $\text{Ti}_3\text{SiC}_2$ . Thus, investigations were concentrated on FG- $\text{Ti}_3\text{SiC}_2$ , simply to allow for observation of more grains per sample in the TEM.

## 5.2. TEM Results: MITR Samples

---

TEM micrographs of unirradiated FG-Ti<sub>3</sub>SiC<sub>2</sub> (Figure 5.1a and b) and Ti<sub>2</sub>AlC (Figure 5.1c and d) lamella reveal the types of defects present before irradiation. The majority of grains appear clear of damage, lacking significant dislocation density. Occasionally, as seen in Figure 5.1, some grains contain perfect basal dislocations throughout, as well as growth dislocation arrays and stacking faults, SFs. SFs in the MAX phases occur only as growth defects, when missing A-layers leave close-packed MX stacking [86]. In Ti<sub>2</sub>AlC, dislocations can be seen emanating from a grain boundary (Figure 5.1c and d). The samples are fully crystalline and contain some impurity phases, such as TiC or Al<sub>2</sub>O<sub>3</sub> particles.

This section is divided further detailing the type of defect structures observed in the post-irradiated samples.

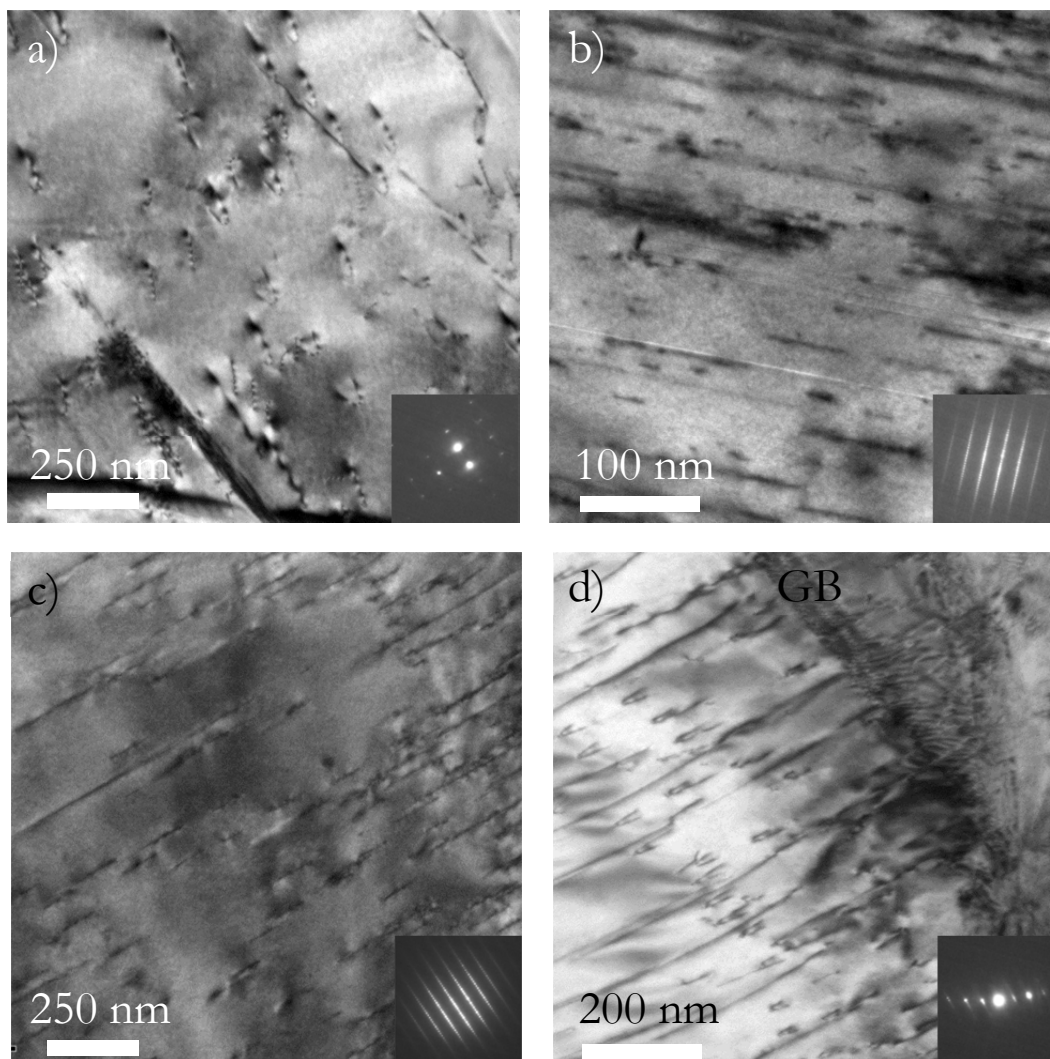


**Figure 5.1** Representative TEM micrographs of unirradiated FG-Ti<sub>3</sub>SiC<sub>2</sub> and Ti<sub>2</sub>AlC.

a) FG-Ti<sub>3</sub>SiC<sub>2</sub>, brightfield, using a 2-beam condition near the  $[11\bar{2}0]$  zone; b) FG-Ti<sub>3</sub>SiC<sub>2</sub> from another region on zone showing dislocation arrays commonly observed in pristine samples; c) Ti<sub>2</sub>AlC taken on zone down the  $[11\bar{2}0]$  axis, and, d) Ti<sub>2</sub>AlC tilted off zone to a 2 beam condition revealing dislocation arrays and SFs. Dislocations appear to be straight lines when viewed on zone in (c), but in fact are curved within the basal planes, and some appear to emanate from a grain boundary, as seen when tilted in (d).

### 5.2.1. Black Spots and/or Defect Clusters

Samples of FG-Ti<sub>3</sub>SiC<sub>2</sub> irradiated to 0.1 dpa, M-D1, at 350(40) °C, T2, revealed limited signs of irradiation induced defects, and remained fully crystalline with no amorphization as observed in the SAEDs (shown as insets in Figure 5.2a and b). If any defect clusters formed

within the  $\text{Ti}_3\text{SiC}_2$  areas, they were beyond the resolution of the TEM. Stacking faults and basal dislocations (Figure 5.2a), closely resembling preexisting defects observed in the unirradiated samples (Figure 5.1a), were observed in a grain tilted near the  $[11\bar{2}0]$  zone axis.

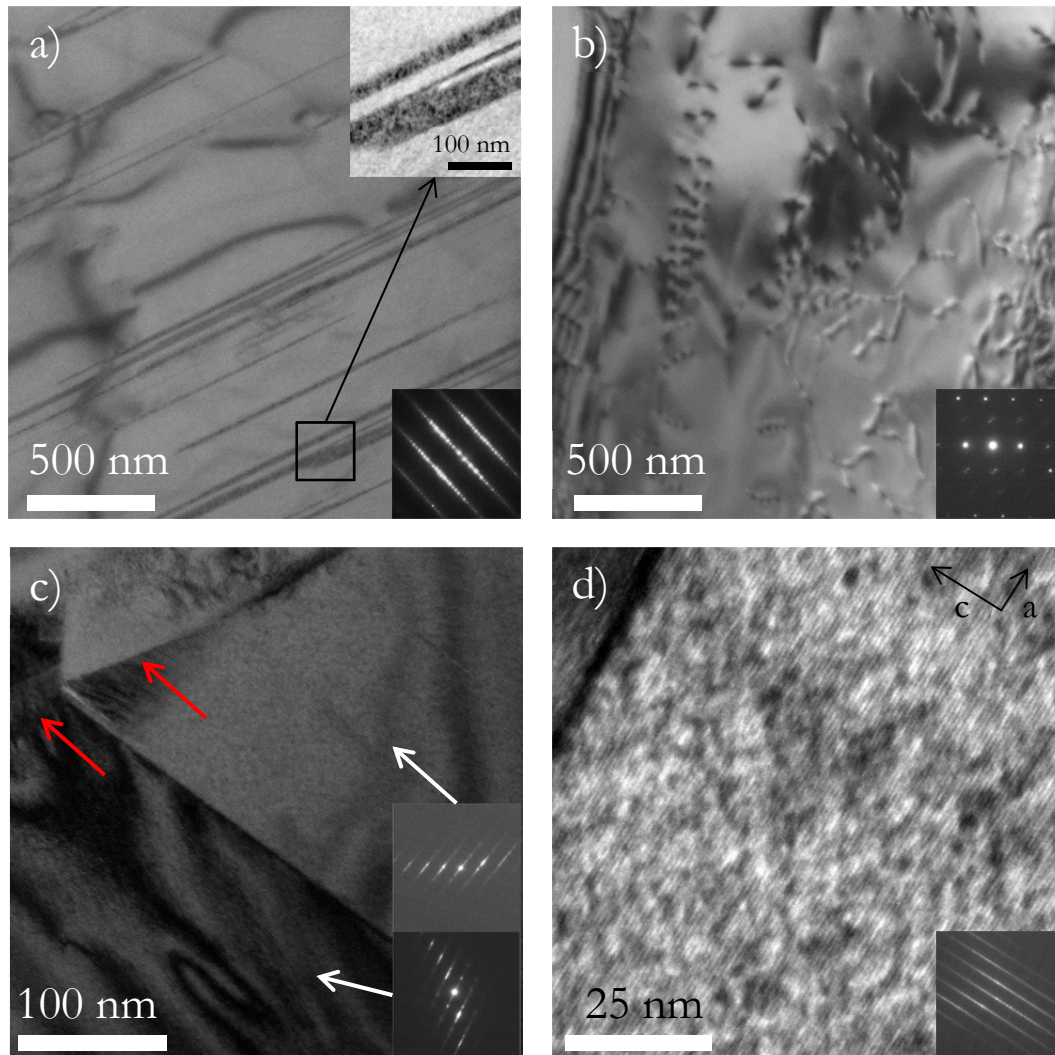


**Figure 5.2** Representative brightfield TEM micrographs of FG- $\text{Ti}_3\text{SiC}_2$  after T2 irradiations. a) FG- $\text{Ti}_3\text{SiC}_2$  irradiated to M-D1-T2 reveals no signs of irradiation induced defects the MAX phase matrix. Defect clusters are observed within the stacking faults throughout the grain (top inset); b) in another region at the same irradiation condition as (a) shows dislocation arrays commonly observed in pristine samples; c) irradiated to M-D2-T2 reveals kink boundaries (red arrows) in grains near the  $[11\bar{2}0]$  orientation, with inset SAEDs of each grain indicated by white arrows; d) at high resolution of a region near (c) showing disorder in the layered structure and defect clusters and/or black spots.

Within the stacking faults, small defect clusters can be observed (Figure 5.2a, top inset). Arrays of basal dislocations are observed, which are most likely preexisting as well (Figure 5.2b).

Samples of FG-Ti<sub>3</sub>SiC<sub>2</sub> remain crystalline after irradiation to 0.4 dpa, M-D2, at T2 as seen by the SAED patterns (insets in Figure 5.2c and d). HRTEM of the sample near a kink boundary reveals the presence of black spots and defect clusters (Figure 5.2d). The defect clusters are observed throughout the grains. With the sample viewed edge-on, i.e. down the [11 $\bar{2}$ 0] zone axis, no missing spots are observed in the SAED pattern (inset in Figure 5.2d) indicating no loss of long range ordering of the structure.

Examples of larger dislocations, similar to those seen in the unirradiated samples (Figure 5.1c and d) are also observed in the Ti<sub>2</sub>AlC samples irradiated at M-D1-T2 (Figure 5.3a) and M-D2-T2 (Figure 5.3c). HRTEM micrographs of Ti<sub>2</sub>AlC irradiated to M-D1-T2 reveal distorted basal planes and irradiation induced black spots (Figure 5.3b). The size and apparent density of these black spots increase in the M-D2-T2 samples (Figure 5.3d).

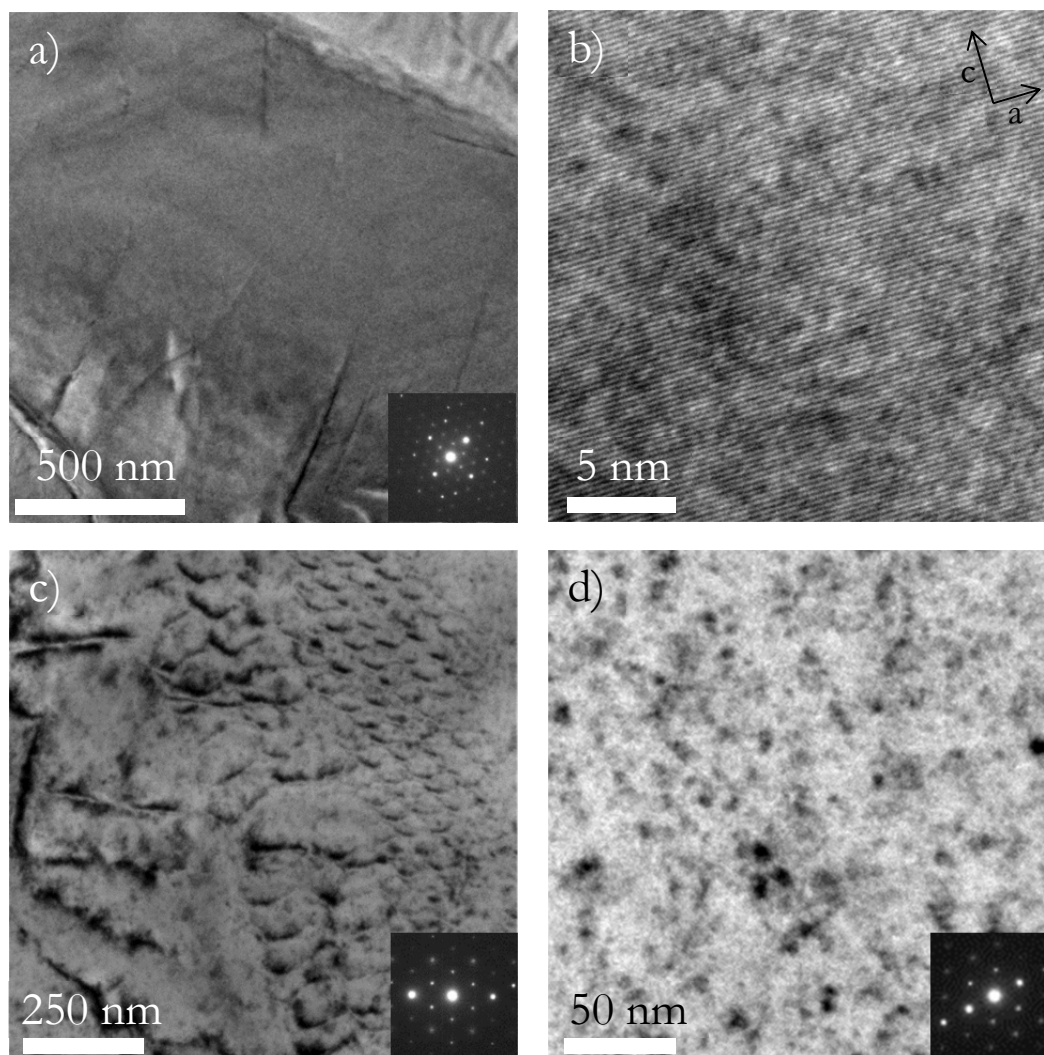
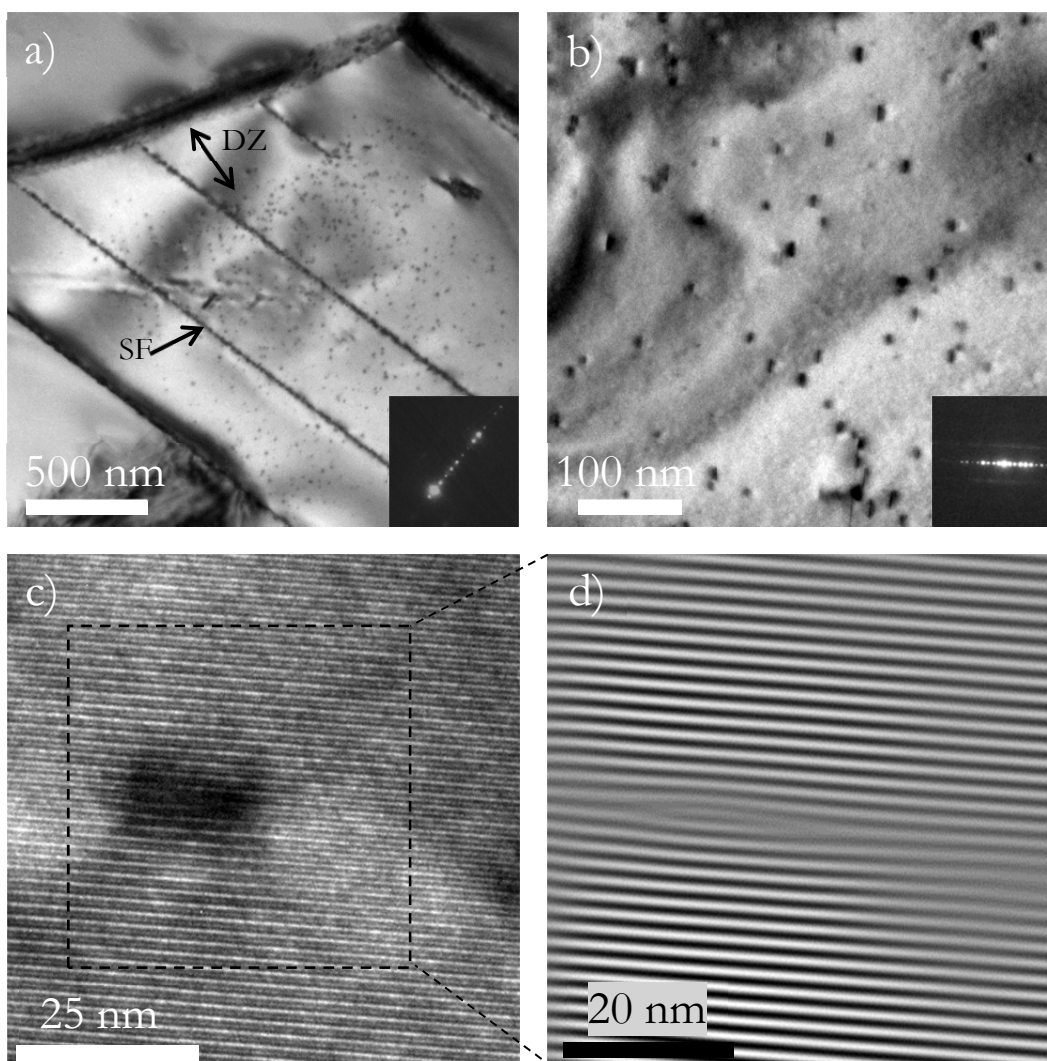


Figure 5.3 Representative brightfield TEM micrographs of  $\text{Ti}_2\text{AlC}$  after T2 irradiations. a)  $\text{Ti}_2\text{AlC}$  irradiated to M-D1-T2 reveals dislocations threading through the grain as seen in pristine MAX phases; b) high resolution micrograph of another grain seen edge on reveals disorder of the basal planes and the presence of defect clusters and/or black spots, c) M-D2-T2 sample taken in 2 beam condition near the  $[0001]$  zone axis showing overlapping basal plane dislocation networks; d) Higher magnification of same region as (c) tilted further removing contrast from dislocation arrays, and revealing only black spots and defect clusters.

### 5.2.2. Dislocation Loops

TEM micrographs of FG- $\text{Ti}_3\text{SiC}_2$  samples irradiated to M-D1 at T4, 710(50) °C, reveal the presence of dislocation loops (Figure 5.4). Extensive tilting experiments revealed that their Burgers vector is  $\mathbf{b} = 1/2 [0001]$ , i.e. perpendicular to the observed (0001) basal habit planes. In some cases, the loops can be seen to accumulate along stacking faults (Figure

5.4a). The dislocation loops observed in FG-Ti<sub>3</sub>SiC<sub>2</sub> were found to be 9(3) nm long with a defect density of  $3 \times 10^{21}$  loops/m<sup>3</sup>. The loops appear in the bulk of the grains with black and white lobe contrast (Figure 5.4b).



**Figure 5.4** Representative brightfield TEM micrographs of FG-Ti<sub>3</sub>SiC<sub>2</sub> irradiated to M-D1-T4  
 a) showing dislocation loops imaged near the [1120] zone axis, i.e. parallel to the basal plane. A denuded zone, DZ, of ~200 nm width is observed at the grain boundaries. b) a region nearby (a) showing an even distribution of loops with black/white lobe contrast due to strain induced in the surrounding lattice with an average loop diameter of 9(3) nm and a loop density of  $3.4 \times 10^{21}$  loops/m<sup>3</sup>. c) at high resolution of a single loop in (a), with d) a Fourier filtered image (dotted square) showing the interstitial character of the loop.



HRTEM of an individual loop shows significant strain contrast all around the affected region (Figure 5.4c), and a Fourier filtered image of the region shows the addition of atomic layers (Figure 5.4d). A  $\sim 300$  nm loop-denuded zone in grains where defects are imaged was also observed (Figure 5.4a).

Brightfield and darkfield TEM micrographs of a region in the  $\text{Ti}_2\text{AlC}$  sample irradiated to M-D1-T4 also showed evidence of dislocation loops (Figure 5.5a and b). Taken near the  $[11\bar{2}0]$  zone, the loops appear with bright white contrast in the darkfield, DF, image (Figure 5.5b). Imaged near the  $[\bar{3}301]$  zone axis, the loops appear as open ellipses (Figure 5.5c). Viewed edge on, near the  $[11\bar{2}0]$  zone axis, the basal plane loops appear as parallel lines lying in the basal planes, with a high density throughout the grain (Figure 5.5d). The average length of these loops was 10(5) nm. In this case there does not seem to be any preferred accumulation near stacking faults. At  $1 \times 10^{23}$  loops/ $\text{m}^3$ , the loop density is 1.5 orders of magnitude *greater* than that observed in FG- $\text{Ti}_3\text{SiC}_2$  exposed to the same conditions.

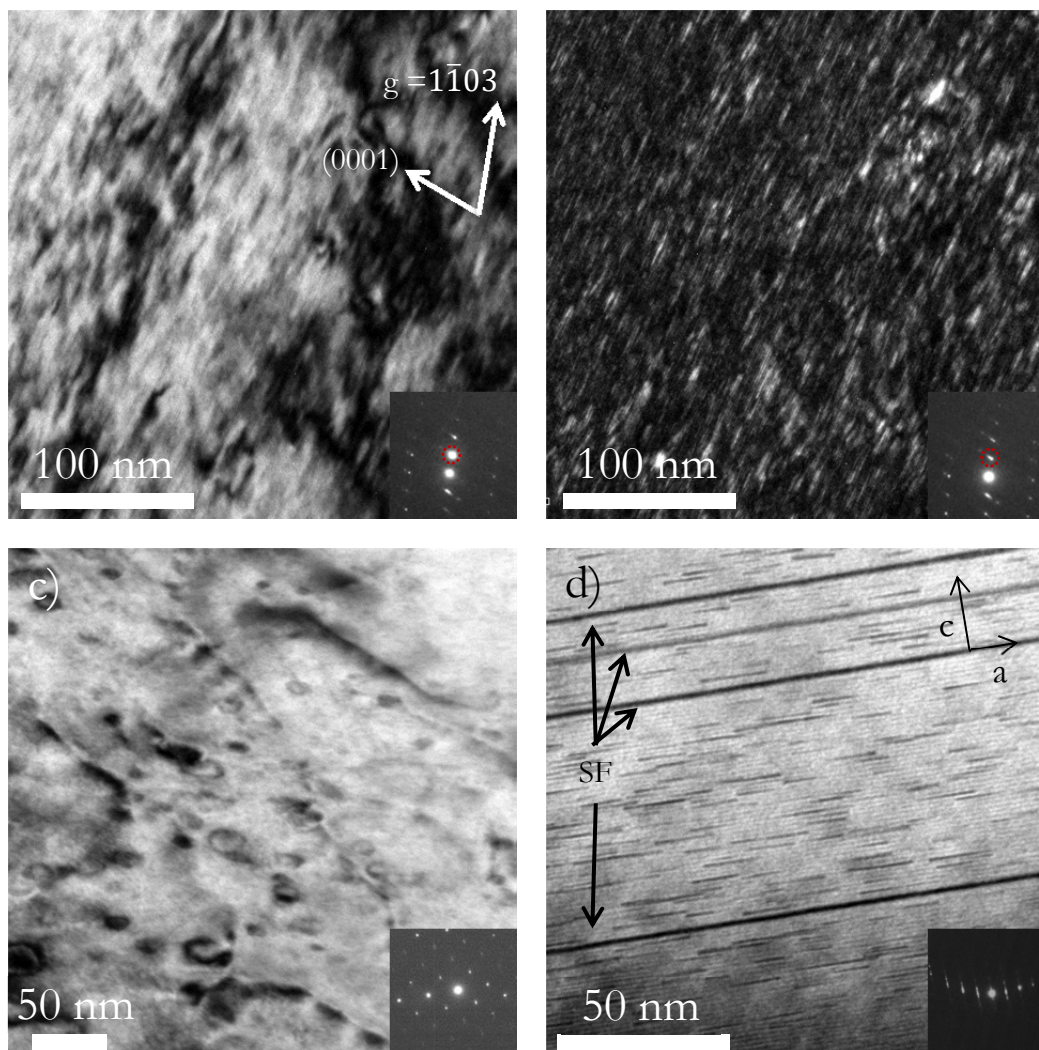


Figure 5.5 Representative TEM micrographs of  $\text{Ti}_2\text{AlC}$  irradiated to M-D1-T4.

a) brightfield and, b) darkfield condition using  $g = 1\bar{1}03$  near the  $[11\bar{2}0]$  zone showing dislocation loops within the basal planes. The red circles in the inset SAED patterns denote location of objective aperture used for darkfield imaging. The dislocation loops appear as strong white contrast in (b). c) near the  $[\bar{3}301]$  zone axis, showing the dislocation loops as open ellipses. d) near the  $[11\bar{2}0]$  zone axis showing edge on loops with an average diameter of 10(5) nm and a defect density of  $1.1 \times 10^{23}$  loops/ $\text{m}^3$ . The lines of bold dark contrast in (d) are SFs (black arrows).

### 5.2.3. Stacking Faults, SF

When imaged down the  $[11\bar{2}0]$  zone axis, one area of the FG-  $\text{Ti}_3\text{SiC}_2$ :M-D1-T4 sample showed significantly damaged regions near stacking faults (Figure 5.6a). Loops were found to cluster in, and around, these SFs as opposed to the relatively clear areas in the

surrounding MAX phase matrix (Figure 5.6a). This same region, tilted to excite  $g = 11\bar{2}0$  which rendered the basal plane defects in FG-Ti<sub>3</sub>SiC<sub>2</sub> invisible, is seen to have a high density of loops and spots within the wider stacking faults, (see regions A, B and C in Figure 5.6b). Stacking faults in Ti<sub>2</sub>AlC irradiated to the same condition are more numerous and appear to span the entire grains (Figure 5.6c). HRTEM within the stacking faults reveals cubic TiC layers within the band (Figure 5.6d). EDS line scans across the stacking fault A in Fig. 8a confirm the absence of Si within the fault (Figure 5.6e). Analysis of the stacking faults imaged edge on, in both FG-Ti<sub>3</sub>SiC<sub>2</sub> and Ti<sub>2</sub>AlC samples reveals a broader distribution of widths in the former, with most SF in Ti<sub>2</sub>AlC being < 7 nm wide (Figure 5.6f). Several SF in FG-Ti<sub>3</sub>SiC<sub>2</sub> were > 15 nm wide, all of which show a high concentration of defects within them (Figure 5.6a).

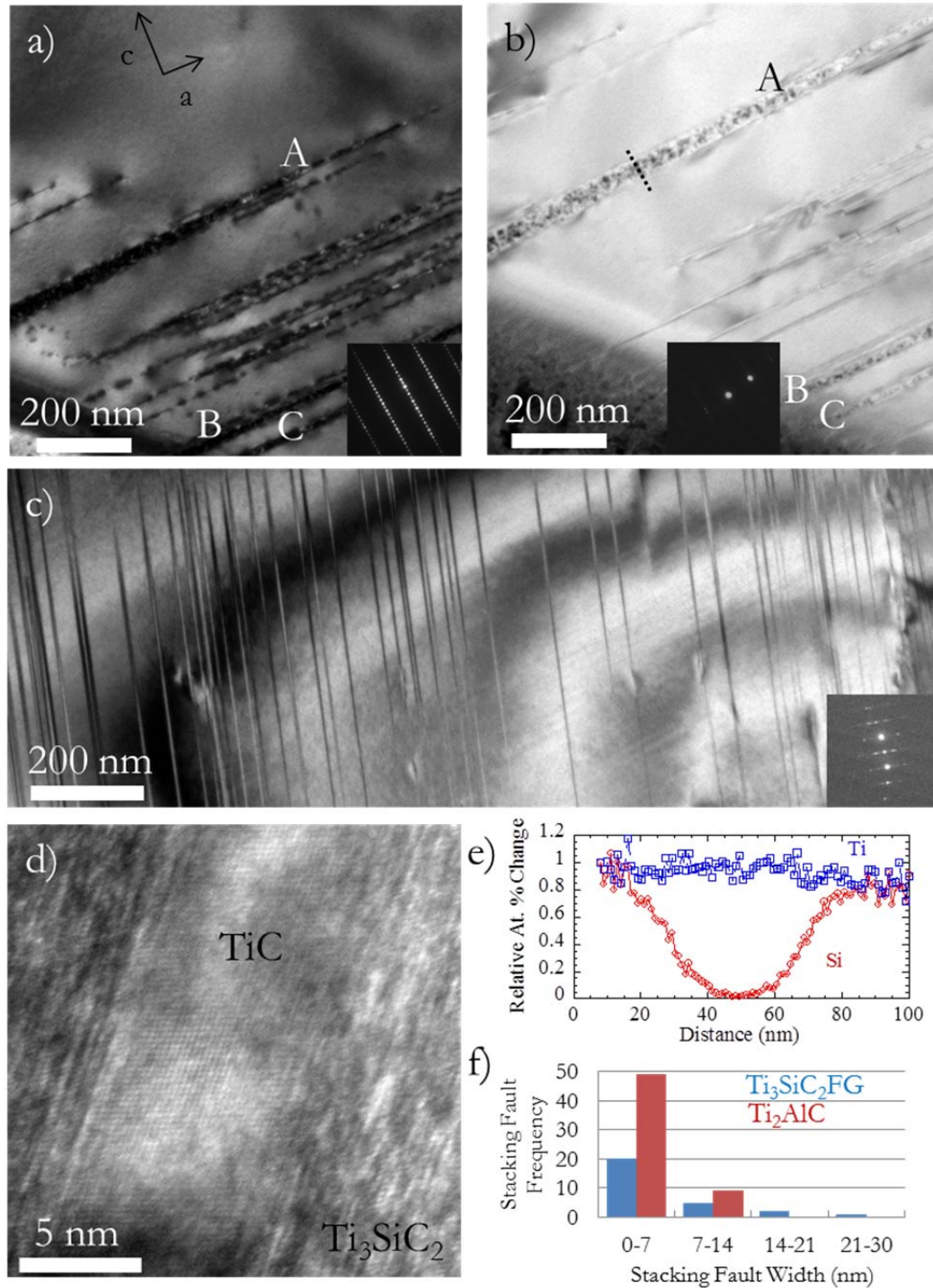


Figure 5.6 TEM micrographs detailing stacking faults in FG-Ti<sub>3</sub>SiC<sub>2</sub> and Ti<sub>2</sub>AlC

a) Brightfield TEM micrograph taken on the  $[11\bar{2}0]$  zone shows extensive damage around and within stacking faults in FG-Ti<sub>3</sub>SiC<sub>2</sub>:M-D1-T4. b) In a 2 beam condition with  $g = 1\bar{1}00$ , the basal loops in FG-Ti<sub>3</sub>SiC<sub>2</sub> reach the  $b \cdot g = 0$  criterion for weak diffraction contrast, and are thus invisible. c) Ti<sub>2</sub>AlC:M-D1-T4 imaged in a similar 2 beam condition showing extensive stacking fault number. d) HRTEM micrograph of a wider SF in (b) reveals de-twinned TiC layers within the band. e) A composition profile across the SFs (dotted line in (b)) confirms the absence of Si. f) Distribution of SF widths in FG-Ti<sub>3</sub>SiC<sub>2</sub> and Ti<sub>2</sub>AlC after M-D1-T4 irradiation. The wider, de-twinned stacking faults are seen to have black spots and defect clusters within the TiC phase platelet.

#### 5.2.4. Grain Boundaries and Impurity Phases

A grain boundary in the FG-Ti<sub>3</sub>SiC<sub>2</sub>:M-D1-T4 sample appears to have grown along the *a*-direction – into a neighboring grain (Figure 5.7a). Such stepped and jagged grain boundaries were not observed in the as-received samples.

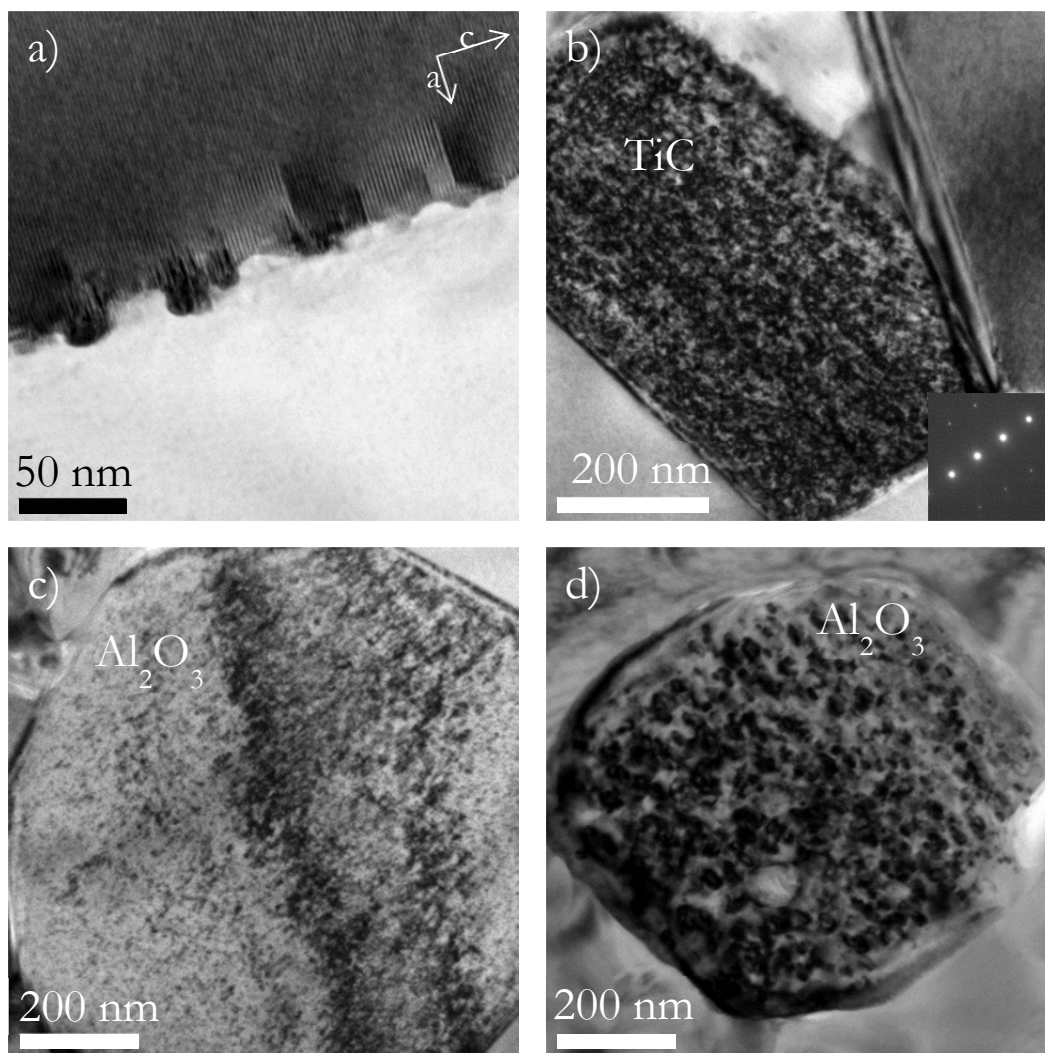


Figure 5.7 a) Brightfield TEM micrograph of a grain boundary found in FG-Ti<sub>3</sub>SiC<sub>2</sub>:M-D1-T4. The jagged features imply irradiation induced growth has occurred along the *a*-direction. b) Representative TEM micrograph of preexisting TiC particle found in the FG-Ti<sub>3</sub>SiC<sub>2</sub>:M-D1-T2 sample showing extensive microstructural damage compared to the relatively clean surrounding Ti<sub>3</sub>SiC<sub>2</sub> matrix. Representative TEM micrograph of Al<sub>2</sub>O<sub>3</sub> impurity particles observed in Ti<sub>2</sub>AlC samples irradiated to, c) M-D1-T2 and, d) M-D2-T2. Density of irradiation induced defects is larger in (d) than in (c) and in both cases, significantly higher than the defects in the surrounding Ti<sub>2</sub>AlC.

TEM micrographs of the TiC impurity particles in FG-Ti<sub>3</sub>SiC<sub>2</sub> samples exposed to M-D1-T2 show a high density of defect clusters (Figure 5.7b). The surrounding FG-Ti<sub>3</sub>SiC<sub>2</sub> grains, on the other hand, are relatively clear of defects. Impurity Al<sub>2</sub>O<sub>3</sub> particles in the Ti<sub>2</sub>AlC sample were also highly damaged after irradiation at M-D1-T2 (Figure 5.7c) and M-D2-T2 (Figure 5.7d), with larger defect clusters in the latter condition.

### 5.3. TEM Results: ATR Samples

---

In order to explore higher dose conditions, samples of Ti<sub>3</sub>SiC<sub>2</sub> and Ti<sub>3</sub>AlC<sub>2</sub> were irradiated at the Idaho National Laboratory's Advanced Test Reactor. Due to delays in sample access and radiological assistance beyond our control, the majority of ATR samples remain uncharacterized. Preliminary access to the high dose samples is presented below. Samples of Ti<sub>3</sub>SiC<sub>2</sub> irradiated at the INL ATR reactor reached doses of 1 dpa, A-D4, and 9 dpa, A-D5, at 500 °C, T3.

#### 5.3.1. Dislocation loops and Denuded Zones

TEM micrographs of Ti<sub>3</sub>SiC<sub>2</sub> irradiated at A-D4-T3 reveal dislocation loops, within the 0001 habit plane (Figure 5.8a and b). The loops had an average length of 21(6) nm and a density of  $5 \times 10^{20}$  loops/m<sup>3</sup>. The loops were larger than those observed after M-D1-T4, but were of the same type, confirmed to have a Burgers vector  $\mathbf{b} = 1/2 [0001]$ .

Irradiation to the highest dose, 9dpa, resulted in the largest observed loops, with an average length of 30(8) nm and a lower density of  $2 \times 10^{20}$  loops/m<sup>3</sup> (Figure 5.8c and d). Again, the loops were confirmed to have the same Burgers vector as the loops observed in all of the

lower dose samples. This further illustrates that all defects induced by irradiation are strictly limited to the free volumes within the basal planes.

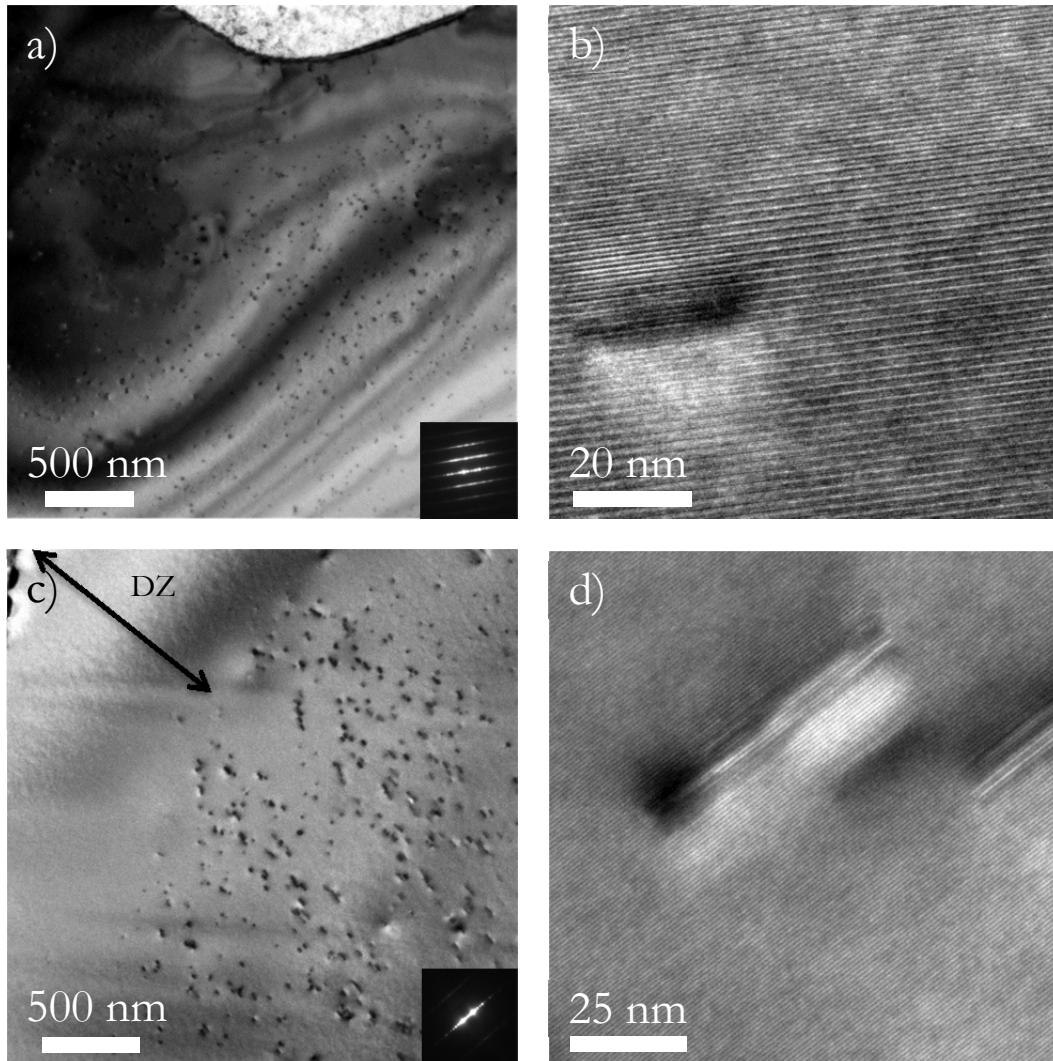


**Figure 5.8** Brightfield TEM micrographs of  $\text{Ti}_3\text{SiC}_2$  irradiated at ATR at T3

a)  $\text{Ti}_3\text{SiC}_2$ :A-D4-T3 showing dislocation loops imaged on the  $[11\bar{2}0]$  zone axis, i.e. parallel to the basal plane, with an average loop diameter of 21(6) nm and a loop density of  $5 \times 10^{20}$  loops/ $\text{m}^3$ . b) High resolution image of a single loop in (a), showing strain contrast due to interstitial character of the loop. c)  $\text{Ti}_3\text{SiC}_2$ :A-D5-T3 showing dislocation loops imaged near the  $[11\bar{2}0]$  zone axis, with an average loop diameter of 30(8) nm and a loop density of  $2 \times 10^{20}$  loops/ $\text{m}^3$ . A large denuded zone of  $\sim 0.9 \mu\text{m}$  is observed near the grain boundary off to the upper left. d) High resolution image of several loops in (c).

What is more remarkable is the presence of a defect denuded zone almost 1  $\mu\text{m}$  wide (Figure 5.8c and Figure 5.9a). Such a wide denuded region is quite rare, especially such a moderate

irradiation temperature of 500 °C. In comparison, SiC irradiated to ~2dpa at 1380 °C resulted in at most a DZ of 57 nm, drastically smaller than observed herein for  $\text{Ti}_3\text{SiC}_2$  [87]. Even irradiation at very high temperatures in SiC is not inductive to forming large DZs. This result further proves the ease of which defects can diffuse along the basal planes. Grain boundaries in the MAX phases are apparently strong defect sinks. This bodes well for MAX phases in general, as increased grain boundary defect sink strength will lead to improved irradiation tolerance at higher irradiation temperatures. To this effect, nanocrystalline materials are investigated for nuclear applications. The results herein indicate that ultra-fine grained samples of  $\text{Ti}_3\text{SiC}_2$ , with grain sizes on the order of 1  $\mu\text{m}$  might prove to have superior radiation tolerance at temperatures as low as 500 °C.

### 5.3.2. Grain Boundary Voids

Unique to the highest dose irradiations, at 9 dpa, voids were observed at the grain boundaries of  $\text{Ti}_3\text{SiC}_2$ :A-D5-T3 (Figure 5.9b). In light of observing large denuded zones, it is apparent that point defects are easily absorbed to the GBs from a far distance away. Agglomeration of vacancies would result in the formation of voids. From this evidence, it is clear that vacancies have diffused towards the GB and resulted in forming small spherical voids, on average 7(2) nm in diameter.



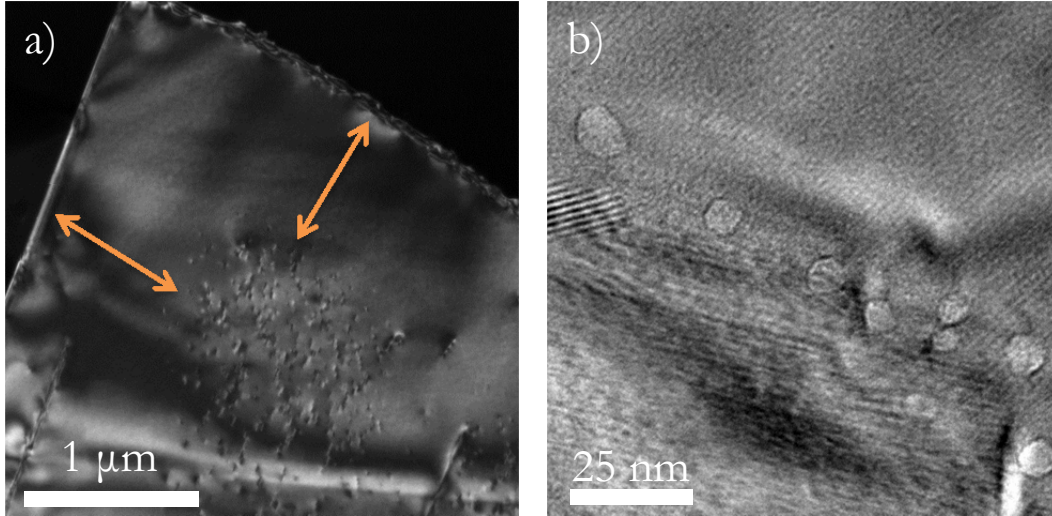


Figure 5.9 TEM micrographs of  $\text{Ti}_3\text{SiC}_2\text{:A-D5-T3}$

a) Darkfield micrograph showing wide denuded zones, DZ (orange arrows), of 860(90) nm in width. b) Brightfield micrograph showing spherical voids which formed at the grain boundaries after irradiation, with an average diameter of 7(2) nm.

#### 5.4. Comparison with Ion Irradiation Studies

The differences between charged particles and neutrons for irradiation are well known, each varying in energy range, penetration depth, volume of interaction, and length of irradiation exposure [17]. The correlation between irradiation temperature and damage rate is also well known, allowing for comparison of various particles used for irradiation at a fixed dose, assuming a recombination dominant regime [88]. In this case, the solution for the correlation which assumes that the ratio of defects lost to sinks,  $R_s = N_{sv}/N_{si}$ , is invariant is more accepted for comparing defect structures, given by:

$$T_2 - T_1 = \frac{\left(\frac{kT_1^2}{E_m^v + 2E_f^v}\right)\ln\left(\frac{\phi_2}{\phi_1}\right)}{1 - \left(\frac{kT_1}{E_m^v + 2E_f^v}\right)\ln\left(\frac{\phi_2}{\phi_1}\right)} \quad (5.1)$$

where  $E_f^v$ ,  $E_m^v$ ,  $\phi$ ,  $T$ , and  $k$  are the energy of formation of a vacancy, energy of migration of a vacancy, damage rate in dpa/s, irradiation temperature in K, and Boltzmann's constant, respectively. Based on the irradiation dose rate herein, the damage rate for irradiation at MITR is assumed to be  $4.7 \times 10^{-9}$  dpa/s. As  $\text{Ti}_3\text{AlC}_2$  dissociated into TiC by way of Al migration out of the layered structure, the correlation was calculated based on Al vacancies with  $E_f = 4$  eV and  $E_m = 0.61$  eV, based on density functional theory calculations[82]. According to the dose rates reported in [22], the damage rate for 1 MeV Xe irradiation of  $\text{Ti}_3\text{AlC}_2$  was roughly  $2.5 \times 10^{-3}$  dpa/s, in good agreement with typical heavy ion irradiation studies [17]. The irradiation temperatures of the study herein were 350 °C and 710 °C. Based on this alone, to expect similar defect structures at 0.1 dpa, heavy ion irradiation studies would need to be conducted at  $\sim 420$  °C and  $\sim 840$  °C, respectively. This required increase in irradiation temperature could explain the lack of irradiation defects and phase decomposition shown in ref [22], which was conducted at room temperature. Such high temperature ion irradiation studies were lacking in the literature. High temperature ion irradiation should more thoroughly be explored to better correlate defect results with neutron irradiation.

## 5.5. Benefits of the A-layer in MAX Phase Structure

---

As discussed in Chapter 4, DFT calculations have shown that the A-layer in MAX phases offers the most preferential sites for point defects with low formation energies, allowing for accommodation of point defects and dislocation loops. In concurrence with theoretical studies [79-81], the irradiation tolerance of FG- $\text{Ti}_3\text{SiC}_2$  appears to be unequivocally greater than that of its binary counterpart TiC. TiC impurity particles (Figure 5.7b) and de-twinned

TiC platelets within SFs (Figure 5.6a) are seen to form dislocation loops and defect clusters, a response similar to a recent proton irradiation study [89]. The same is true of  $\text{Ti}_2\text{AlC}$  in comparison with impurity  $\text{Al}_2\text{O}_3$  particles (Figure 5.7c and d). The presence of the A-layer, and the low energy of formation of defects within the layer, clearly provides a defect sink at the nanoscale level. SFs in FG- $\text{Ti}_3\text{SiC}_2$  appear to promote dislocation loop formation, as loops are seen to accumulate nearby (Figure 5.4a and Figure 5.6a). At this point, it is fairly well established that when the A-group element from the MAX phases diffuses out of the basal planes, the resulting highly twinned TiC blocks can de-twin, aligning the (111) TiC planes with the (0001) basal planes of the MAX structure [90, 91]. The loss of the A-element also results in a  $\sim 15\%$  volume shrinkage [90, 91]. Irradiation of presumably preexisting SFs resulted in varied defect microstructures (Figure 5.6). Above a certain width, the SFs are comprised of de-twinned TiC, which accumulates a high density of black spots and small loops after irradiation (Figure 5.6b). Not surprisingly, the morphology of these spots are similar to the ones seen in the TiC impurity particles (Figure 5.7b). While it is unclear at this time whether the increase in stacking fault widths was induced by irradiation, the density of stacking faults observed appear to be quite high, notably in  $\text{Ti}_2\text{AlC:M-D1-T4}$  (Figure 5.6). Future studies at higher irradiation doses would reveal if these SF are indeed irradiation induced, as one would expect to see an even further increase in stacking fault density.

## 5.6. Conclusions

---

Analysis of defects formed after neutron irradiation of bulk MAX phases show that FG- $\text{Ti}_3\text{SiC}_2$  and  $\text{Ti}_2\text{AlC}$  remain crystalline under neutron irradiations up to 0.4 dpa at 350(40) °C.

Neutron irradiation resulted in the formation of black spots and defect clusters in  $\text{Ti}_2\text{AlC}$  after irradiation at 0.1 dpa at 350(40) °C and in both  $\text{Ti}_2\text{AlC}$  and FG- $\text{Ti}_3\text{SiC}_2$  after 0.4 dpa at 350(40) °C. The size and density of spots increased with irradiation dose. Dislocation loops were observed in FG- $\text{Ti}_3\text{SiC}_2$  and  $\text{Ti}_2\text{AlC}$  after irradiation at 0.1 dpa at 710(50) °C. At  $1 \times 10^{23}$  loops/ $\text{m}^3$ , the loop density in  $\text{Ti}_2\text{AlC}$  is 1.5 orders of magnitude greater than that observed in FG- $\text{Ti}_3\text{SiC}_2$ , at  $3 \times 10^{21}$  loops/ $\text{m}^3$ . Through extensive tilting experiments, the dislocation loops were found to have a Burgers vector  $\mathbf{b} = 1/2 [0001]$ , and lie in basal planes, with diameters of 9(3) nm and 10(5) nm, for FG- $\text{Ti}_3\text{SiC}_2$  and  $\text{Ti}_2\text{AlC}$ , respectively. As predicted by first principles, all dislocation loops observed have been restricted to within the basal planes. These results also concur with the proposed high temperature defect structure shown in Chapter 4.

Impurity particles, such as TiC and  $\text{Al}_2\text{O}_3$ , were found to be significantly more damaged than the surrounding MAX phase matrices, indirectly confirming an important conclusion of this work, which is the presence of the A-layers act as potent sinks to neutron radiation damage. In FG- $\text{Ti}_3\text{SiC}_2$ , wide stacking faults, composed of de-twinned TiC layers, showed extensive defect and dislocation loop formation. It is unclear at this time if the increased stacking fault width and density are induced by neutron irradiation. As the MAX phase lattice is anisotropic, evidence of irradiation grain growth is unsurprising. A few grains were seen to have grown along the a-direction, with the boundaries impinging into neighboring grains.

Based on the results presented throughout, the microstrain increases described in Chapter 4 could be caused by several reasons. They include irradiation induced defects, increased lattice disorder, highly damaged impurity grains and possibly anisotropic grain growth. At higher irradiation temperatures, some of the point defects presumably anneal out or agglomerate into larger coherent structures, reducing lattice strain and distortion, and relieving microstrain within the material.

These results suggest that  $\text{Ti}_3\text{SiC}_2$  remains a potential candidate for future nuclear applications, though more work is needed in fully understand the role of the A-layer in providing irradiation resistance. Commercially available  $\text{Ti}_2\text{AlC}$  has shown significant damage after irradiation to relatively low dose, both in defect morphology and microstructure. More work is required to explore the role that antisite defects play in the irradiation tolerance for this material, and if it should be considered for nuclear applications. While the presence of the A-layer in the MAX phases clearly improves damage tolerance over binary MX compounds, the antisite criterion proposed by Wang *et al.* [80] alone does not sufficiently predict irradiation tolerance between members of the MAX phase family.

The TEM results have provided insight on the types of irradiation induced defects that form within  $\text{Ti}_3\text{SiC}_2$  and  $\text{Ti}_2\text{AlC}$  and, by association, all MAX phases. Next, in Chapter 6, the effect of these defects on bulk material properties is investigated.

## 6. EFFECT OF IRRADIATION ON PROPERTIES

---

As previously described, neutron irradiation leads to the formation of point defects and larger defect structures throughout the bulk of a material. As material properties are closely linked with the microstructure of materials, it follows that irradiation would lead to a change in material behavior. This chapter explores the effect of neutron irradiation on the physical and mechanical properties of  $\text{Ti}_3\text{SiC}_2$ ,  $\text{Ti}_3\text{AlC}_2$ ,  $\text{Ti}_2\text{AlC}$  and  $\text{Ti}_2\text{AlN}$ . Properties reviewed here include microcracking, electrical resistivity, thermal conductivity, hardness, and Young's modulus. Neutron activation of samples is also discussed.

### 6.1. Macroscopic Structure Post-irradiation

---

In preparation of samples for FIB liftouts, SEM micrographs were taken showing the surface microstructures of samples irradiated at MITR. The resultant microstructure revealed an increase in porosity and/or microcracking and pullouts, which could affect material properties. The surface morphology is investigated below.

#### 6.1.1. Microcracking

Unirradiated, pristine samples of FG- $\text{Ti}_3\text{SiC}_2$  and  $\text{Ti}_2\text{AlC}$  shown in Figure 6.1a and e, respectively, were essentially fully dense. The dark spots seen in the micrographs are either pullouts and/or small pores. Post-irradiation SEM micrographs of roughly polished FG- $\text{Ti}_3\text{SiC}_2$  and  $\text{Ti}_2\text{AlC}$  revealed an increase of what appears to be porosity, but is more likely a combination of pullouts and microcracking in both samples, but more pervasively in the

Ti<sub>2</sub>AlC sample Figure 6.1. In both materials, after irradiation to 0.1 dpa, M-D1, more pores are observed after irradiation at 350(40) °C, T2, (Figure 6.1b and f) compared to those irradiated at 710(50) °C, T4, (Figure 6.1c and g). The higher temperature T4 irradiation appears to somewhat mitigate the effects. In the FG-Ti<sub>3</sub>SiC<sub>2</sub> samples irradiated to 0.4 dpa, M-D2, at T2 (Figure 6.1d), the extent of microcracking is similar to that of M-D1-T2 (Figure 6.1b). In contradistinction, the Ti<sub>2</sub>AlC:M-D2-T2 sample exhibited extensive pullout between grains, with cracks surrounding most grains, highlighted by arrows in Figure 6.1h. Also of note, the friability of these samples was increased after irradiation, indicating that surface layer cracking was leading to sloughing off of material.

TEM micrographs taken near the (0001) zone axis of Ti<sub>2</sub>AlC:M-D1-T2 samples reveal microcracks that extend across the entire lamella (Figure 6.2a). Intragranular cracking was often seen to extend beyond grain boundaries (e.g. region B in Figure 6.2b). Based on the zone axis of the micrograph taken of the lamella, for the most part, these cracks were parallel to the basal planes, and propagate throughout (Figure 6.2a). The cracks are seen to interact and overlap at the lamella edges (Figure 6.2 6a, region A). Occasional microcracking was observed in the FG-Ti<sub>3</sub>SiC<sub>2</sub> samples, though not to the extent seen in Ti<sub>2</sub>AlC.

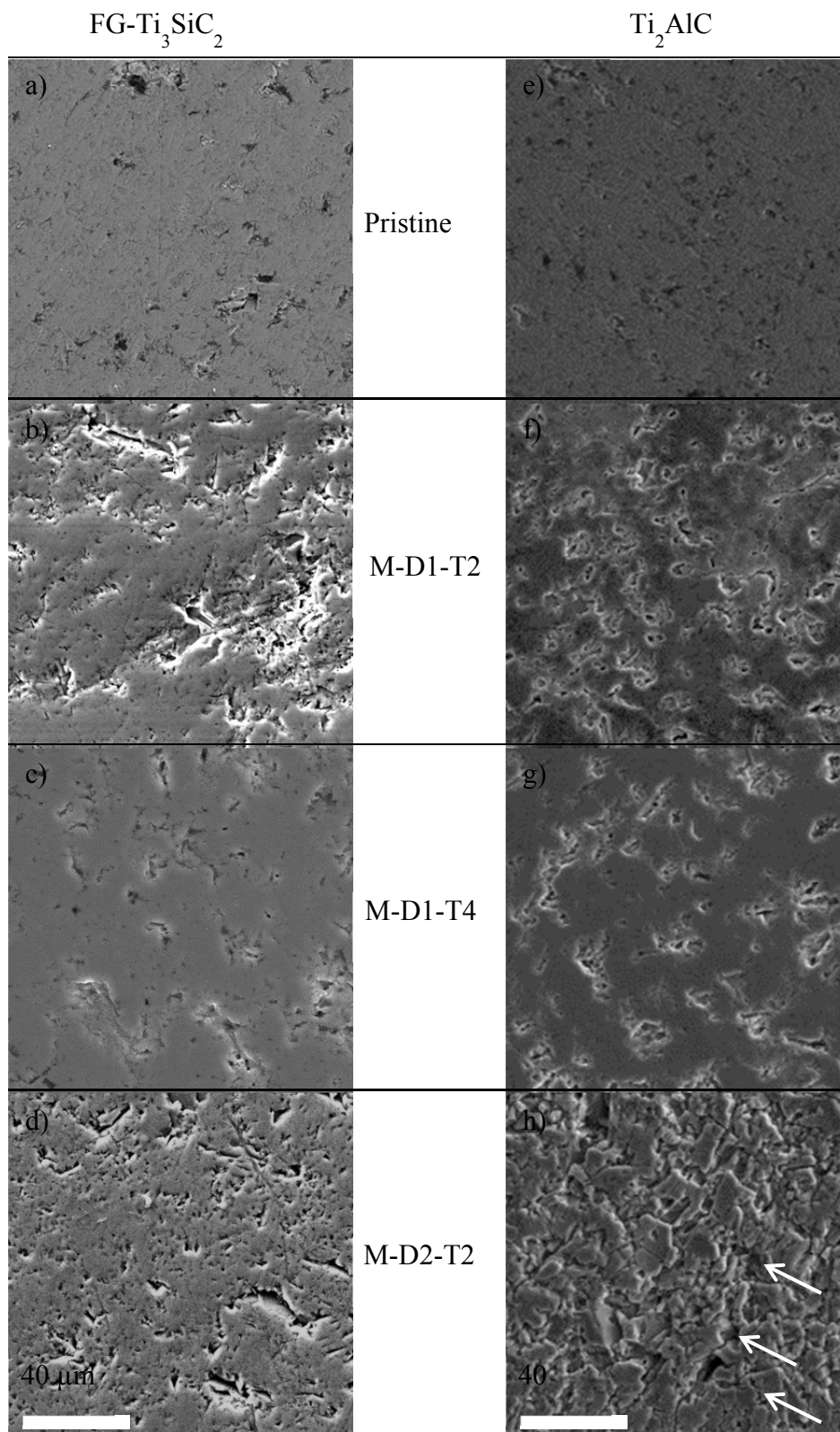


Figure 6.1 SEM micrographs of FG-Ti<sub>3</sub>SiC<sub>2</sub> a) pristine, and irradiated to, b) M-D1-T2, c) M-D1-T4, and d) M-D2-T2, and Ti<sub>2</sub>AlC e) pristine, and irradiated to f) M-D1-T2, g) M-D1-T4, and h) M-D2-T2.



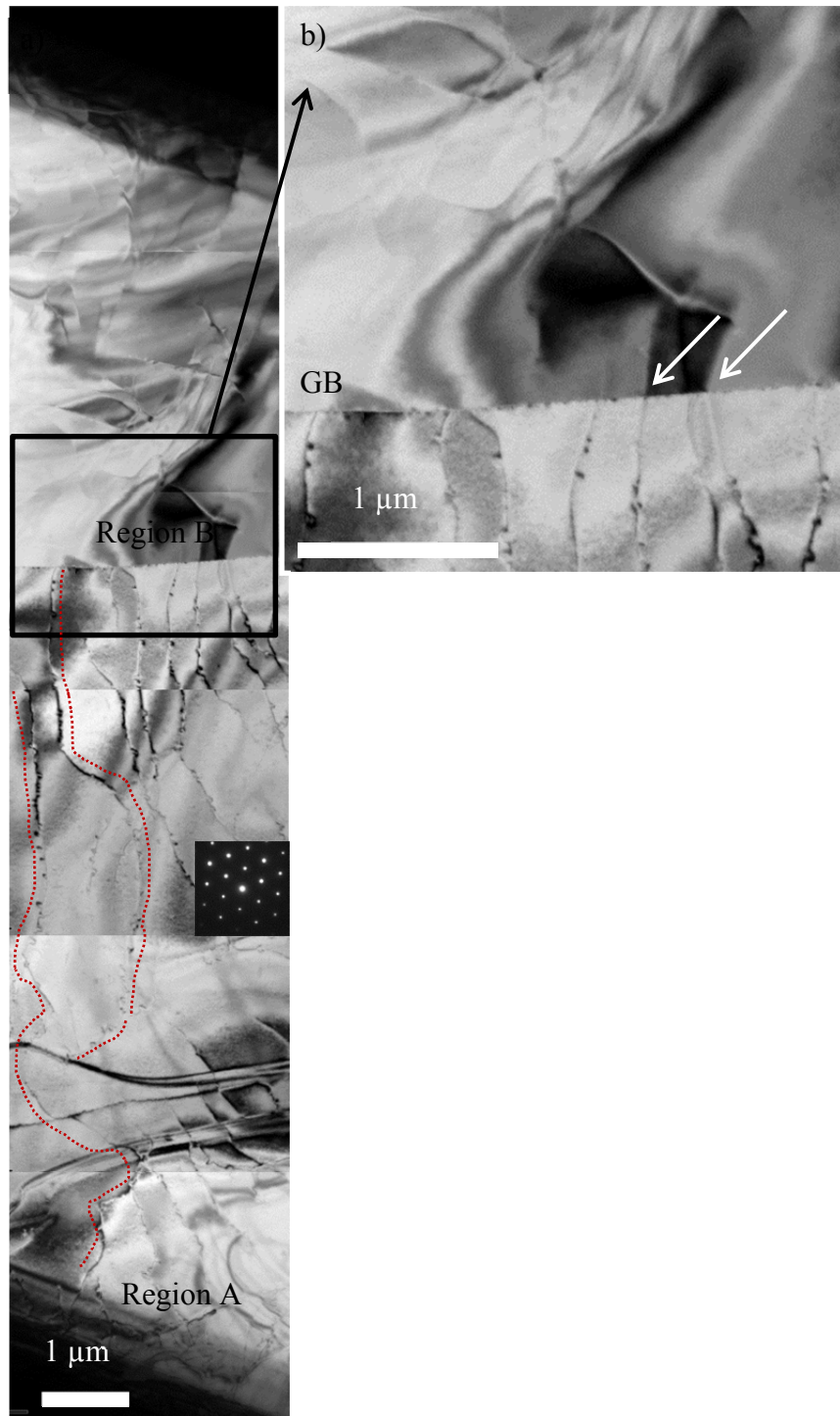


Figure 6.2 a) Composite TEM micrographs of the  $\text{Ti}_2\text{AlC}$  lift-out irradiated to M-D1-T2. Networks of long microcracks (red trace) are seen to traverse the entire liftout. Cracks are seen to overlap and interact near the edge of the lamella (region A). b) Enlarged region of a) where several cracks (white arrows) are seen to extend beyond a grain boundary (region B).

## 6.2. Room Temperature Electrical Resistivity of Irradiated MAX Phases

---

The electrical resistivity,  $\rho$ , is a measure of the ease of electron conduction through a material, also described as the inverse of conductivity,  $\sigma$ . Introduction of point defects and substitutional atoms lead to an increase in resistivity by increasingly scattering electrons as they conduct through the material. Total  $\sigma$ , and inversely  $\rho$ , is described by :

$$\frac{1}{\rho} = \sigma = ne\mu_e + pe\mu_h \quad (6.1)$$

where  $e$  is charge of an electron,  $n$  and  $p$  are the number density of electrons and holes, respectively, and  $\mu_e$  and  $\mu_h$  are the mobility of electrons and holes, respectively.

The electron mobility, related to an applied electric field,  $E$ , is described by:

$$\mu_e = \frac{v_d}{E} \quad (6.2)$$

where  $v_d$  is the electron drift velocity. Mobility is strongly dependent on temperatures and impurities. As temperature increases, increasing atomic vibrations increase and impede electron transport, diminishing the drift velocity. This leads to an increase in resistivity for conductors. Similarly, defects in the crystal lattice, such as interstitial atoms and vacancies, can also impede electron conduction. Therefore, the resistivity of a defective material can be explored as a function of defect density.

As described in previous sections, irradiation of the MAX phases results in the generation of point defects and larger defect structures. Resistivity is a material property that is directly impacted by the irradiation defects. Results are presented in following sections as a function of irradiation temperature and dose.

### 6.2.1. Effect of Irradiation Temperature

Room temperature, RT,  $\rho$  of pristine and irradiated samples was measured to assess the effect of residual defects that formed after irradiation. The RT  $\rho$  of the pristine MAX phases in this work compares well with those previously reported (Table 6.1) [92-96]. After M-D1-T2 irradiation, the RT  $\rho$  values were 4-10 times greater than before irradiation (Table 6.1). The largest increase in RT  $\rho$  was seen in the  $\text{Ti}_3\text{AlC}_2$  samples, with 2.84(2)  $\mu\Omega\text{-m}$  after irradiated as compared to 0.262(8)  $\mu\Omega\text{-m}$  before (Figure 6.3). At 2.2(1)  $\mu\Omega\text{-m}$ , the CG- $\text{Ti}_3\text{SiC}_2$  samples had a higher RT  $\rho$  compared to FG- $\text{Ti}_3\text{SiC}_2$ , at 1.1(1)  $\mu\Omega\text{-m}$ , both of which increased from the pristine values of 0.21(1) and 0.21(1), respectively. The RT  $\rho$  of the  $\text{Ti}_2\text{AlN}$ :M-D1-T2 samples increased from 0.37(1)  $\mu\Omega\text{-m}$  as pristine to 1.46(1)  $\mu\Omega\text{-m}$  irradiated. At 0.75(1)  $\mu\Omega\text{-m}$ ,  $\text{Ti}_2\text{AlC}$  yielded the lowest increase in RT  $\rho$  compared to 0.31(4)  $\mu\Omega\text{-m}$  as pristine. In contradistinction to the low temperature irradiations, samples irradiated to M-D1-T4 experienced only a slight increase in  $\rho$ , ranging from 0.23(1) for FG- $\text{Ti}_3\text{SiC}_2$  to 0.44(1) for  $\text{Ti}_2\text{AlC}$  (Table 6.1).

**Table 6.1 Room temperature resistivity of MAX Phases before and after MITR irradiations.**

Composition	$\rho$ ( $\mu\Omega\text{-m}$ )				
	Pristine	Reference	M-D1-T2	M-D1-T4	M-D2-T2
$\text{Ti}_2\text{AlC}$	0.31(4)	0.32 [93] 0.23 [95] 0.39 [96]	0.75(1)	0.44(1)	8.3(1)
$\text{Ti}_3\text{AlC}_2$	0.262(8)	0.353 [93] 0.287 [95]	2.84(2)	0.39(1)	8(2)
$\text{Ti}_2\text{AlN}$	0.37(1)	0.25 [93] 0.343 [93]	1.46(1)	0.25(1)	3.34(1)
FG- $\text{Ti}_3\text{SiC}_2$	0.21(1)	0.23 [92] 0.23 [94]	1.1(1)	0.23(1)	1.43(1)
CG- $\text{Ti}_3\text{SiC}_2$	0.21(1)	0.23 [92] 0.23 [94]	2.2(1)	0.24(1)	2.82(1)

The collision of high energy neutrons with lattice atoms is known to create point defects, increase the dangling bond density, and result in an increase in resistivity [97]. Post-irradiation RT  $\rho$  values of samples irradiated at M-D1-T2 conditions were found to be almost an order of magnitude higher than seen for pristine samples, notably visualized in Figure 6.3, confirming that T2 neutron irradiation generated a significant amount of point defects. After irradiation,  $\text{Ti}_3\text{AlC}_2$  possessed the highest RT  $\rho$ , presumably due to formation of a large density of point defects. The RT  $\rho$  of CG- $\text{Ti}_3\text{SiC}_2$  was twice that of FG- $\text{Ti}_3\text{SiC}_2$ , which is attributed to the increase in grain boundary fraction present in the fine grained samples, likely resulting in fewer residual defects after irradiation, due to the increase in available defect sinks.

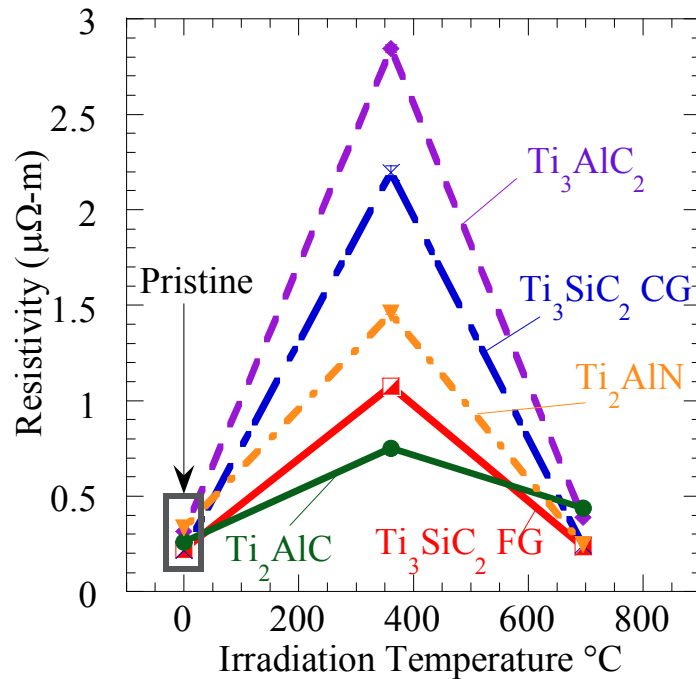


Figure 6.3 RT resistivity as a function of irradiation temperature for M-D1 samples.

With increasing temperatures, if the defect mobility is high enough, they can start to agglomerate and/or annihilate. As observed in Chapter 5, defect clusters are also seen to interact and coalesce into fewer but larger defect structures, notably dislocation loops, with increasing temperatures [17]. Annihilation of the point defects reduces the dangling bond density, resulting in a decrease in resistivity. This was confirmed herein for all M-D1-T4 samples; all showed only a slight increase in RT  $\rho$  (Table 6.1) compared to their RT  $\rho$  values prior to irradiation. M-D1-T4 irradiation resulted in the agglomeration of the small defect clusters into larger dislocation loop structures (See Chapter 5). The low resistivity values of samples irradiated M-D1-T4 is strong evidence for the MAX phases' dynamic recovery at temperatures as low as T4 (e.g. 710 °C).

### 6.2.2. Effect of Irradiation Dose

As shown above, RT  $\rho$  increased with neutron irradiation. This trend continued after irradiation at the higher dose of 0.4 dpa, M-D2, at T2 Table 6.1. At 8.3(1) and 8(2)  $\mu\Omega\cdot\text{m}$ , the  $\text{Ti}_2\text{AlC}$  and  $\text{Ti}_3\text{AlC}_2$  samples, respectively, showed the highest increases in RT  $\rho$  after M-D2-T2 irradiation. The  $\text{Ti}_2\text{AlN}$  sample did not increase as much as its  $\text{Ti}_2\text{AlC}$  counterpart, with a value of 3.34(1)  $\mu\Omega\cdot\text{m}$ . Interestingly, RT  $\rho$  of both FG- $\text{Ti}_3\text{SiC}_2$  and CG- $\text{Ti}_3\text{SiC}_2$  appear to approach a saturation point after the M-D2-T2 irradiation Figure 6.4. At 1.43(1)  $\mu\Omega\cdot\text{m}$ , the RT  $\rho$  for the FG- $\text{Ti}_3\text{SiC}_2$  was half that of its coarse-grained counterpart, at 2.82(1)  $\mu\Omega\cdot\text{m}$  after M-D2-T2 irradiation. This is an important result because it further suggests that the increased grain boundary area in the FG- $\text{Ti}_3\text{SiC}_2$  sample yields more available defect sinks compared to its CG- $\text{Ti}_3\text{SiC}_2$  counterpart, effectively removing more irradiation defects from the grains.

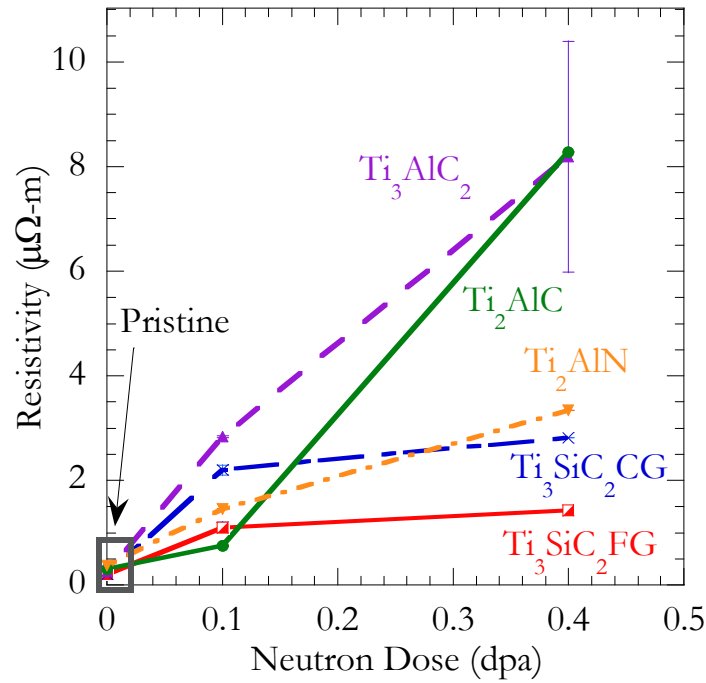


Figure 6.4 RT resistivity as a function of irradiation dose of M-T2 samples.

As the defect density, particularly point defects, increases the resistivity increases because these defects are effective scatterers of conduction electrons [97]. This is particularly true of the binary early transition carbides [98, 99] and the MAX phases [25]. Point defect formation also increases as a function of irradiation dose. Post-irradiation  $\rho$  values of samples irradiated M-D2-T2 increased by several orders of magnitude compared to unirradiated samples, and were greater than those reported for the M-D1-T2 samples Figure 6.4. At  $\sim 8 \mu\Omega\text{m}$ , RT  $\rho$  for both  $\text{Ti}_2\text{AlC}$  and  $\text{Ti}_3\text{AlC}_2$  increased to comparable values. The latter values are 2 to 3 times those of  $\text{Ti}_3\text{SiC}_2$ . This large increase in RT  $\rho$  can also be partially ascribed to the extensive microcracking observed (Section 6.1).

### 6.3. Thermal Conductivity of the MAX Phases

---

Thermal conductivity is one of the more important properties required for fuel cladding materials in nuclear reactors. In order to remove generated heat from the fuel pellets, fuel cladding must show high thermal conductivity, and maintain it at elevated temperatures and irradiation doses. SiC has shown a significant decrease in thermal conductivity with irradiation[97]. In this section, the thermal diffusivity of several non-irradiated MAX phases and solid solution MAX phases is presented. Additionally, a relationship between electrical resistivity and thermal conductivity is applied for the irradiated MITR samples, as most of the MAX phases show a major contribution to thermal conductivity, by way of high electron conduction.

#### 6.3.1. Thermal Diffusivity Results

The thermal diffusivity,  $\alpha$ , of pristine samples of FG-Ti<sub>3</sub>SiC<sub>2</sub>, CG-Ti<sub>3</sub>SiC<sub>2</sub>, Ti<sub>3</sub>AlC<sub>2</sub>, Ti<sub>2</sub>AlC, Cr<sub>2</sub>AlC, and solid solutions of (Nb<sub>0.5</sub>Zr<sub>0.5</sub>)<sub>2</sub>AlC, (Nb<sub>0.75</sub>Zr<sub>0.25</sub>)<sub>2</sub>AlC, and (Ti<sub>0.75</sub>Zr<sub>0.25</sub>)<sub>2</sub>AlC were measured by laser flash analysis. The solid solutions were explored in order to begin analysis of Zr containing MAX phases for use in thermal reactor applications where low neutron cross section is desirable. Pure Zr<sub>2</sub>AlC is not thermodynamically stable, thus solid solutions with Nb and Ti were prepared to explore the addition of Zr. As presented earlier, thermal conductivity,  $\kappa_{th}$ , is described by:

$$\kappa_{th} = \alpha * c_p * d \quad (6.3)$$

where,  $d$  and  $c_p$  are density and specific heat, respectively. Specific heat,  $c_p$ , of each MAX phase was gathered from literature [100, 101]. It has also been shown that  $c_p$  of a given MAX phase is comparable to the associated MX binary, by a factor of n+1 [25]. Using this

relationship, the  $c_p$  for the  $(\text{Nb}_x\text{Zr}_{1-x})_2\text{AlC}$  and  $(\text{Ti}_x\text{Zr}_{1-x})_2\text{AlC}$  compounds was estimated using  $2 \times c_p$  values for NbC and TiC, respectively [102]. The effect of thermal expansion on density was assumed negligible, in comparison with the other parameters. By combining the results for  $\alpha$  with literature values of  $c_p$  and density,  $\kappa_{th}$  was calculated, and is shown as a function of temperature in Figure 6.5.

The results compare well with previously reported thermal conductivity data (Table 6.3) [93, 100, 101, 103]. While the  $\kappa_{th}$  values for  $\text{Ti}_2\text{AlC}$  and the solid solutions are lower than expected, it is known that the quality of the samples can negatively affect thermal conductivity. The presence of impurity phases and vacancies impede phonon and electron conduction. The Nb containing samples have a positive correlation with temperature, similar to previously reported Nb-containing MAX phases [25]. The remaining samples showed a decrease in  $\kappa_{th}$  with increasing temperature.  $\text{Ti}_3\text{AlC}_2$  and  $\text{Cr}_2\text{AlC}$  showed an increase in thermal conductivity at higher temperatures.

Table 6.2 Thermal conductivity  $\kappa_{th}$  of various MAX phases as measured by laser flash analysis.

$\kappa_{th}$ (W/m-K)	Experimental		Literature		
	300 K	1200 K	300K	1300K	[Ref]
<b>Sample</b>					
<b>FG-<math>\text{Ti}_3\text{SiC}_2</math></b>	38.2	35.9	37	33	[100]
<b>CG-<math>\text{Ti}_3\text{SiC}_2</math></b>	39.4	34.1	37	33	[100]
<b><math>\text{Ti}_3\text{AlC}_2</math></b>	39.9	33.8	40	-	[93]
<b><math>\text{Ti}_2\text{AlC}</math></b>	31.6	27.8	46	36	[103]
<b><math>(\text{Nb}_{0.5}\text{Zr}_{0.5})_2\text{AlC}</math></b>	7.3	17.3	17a	24a	[103]
<b><math>(\text{Nb}_{0.75}\text{Zr}_{0.25})_2\text{AlC}</math></b>	10.3	17.0	17a	24a	[103]
<b><math>(\text{Ti}_{0.75}\text{Zr}_{0.25})_2\text{AlC}</math></b>	9.3	21.6	17a	24a	[103]
<b><math>\text{Cr}_2\text{AlC}</math></b>	20.4	20.0	19	16b-	[101]

a- Comparison is made with  $\text{TiNbAlC}$ , a similar solid solution, as values for these solid solutions are previously unreported.

b- Extrapolated



Notably,  $\kappa_{th}$  does not decrease significantly for  $\text{Ti}_3\text{SiC}_2$ ,  $\text{Ti}_3\text{AlC}_2$ ,  $\text{Ti}_2\text{AlC}$  or  $\text{Cr}_2\text{AlC}$  over the wide range of temperatures studied. These results bode well for MAX phases to be used as fuel cladding material, as  $\kappa_{th}$  was maintained at high temperatures. Irradiation defects will only decrease  $\kappa_{th}$ , thus possessing a high baseline at elevated temperatures is a promising result.

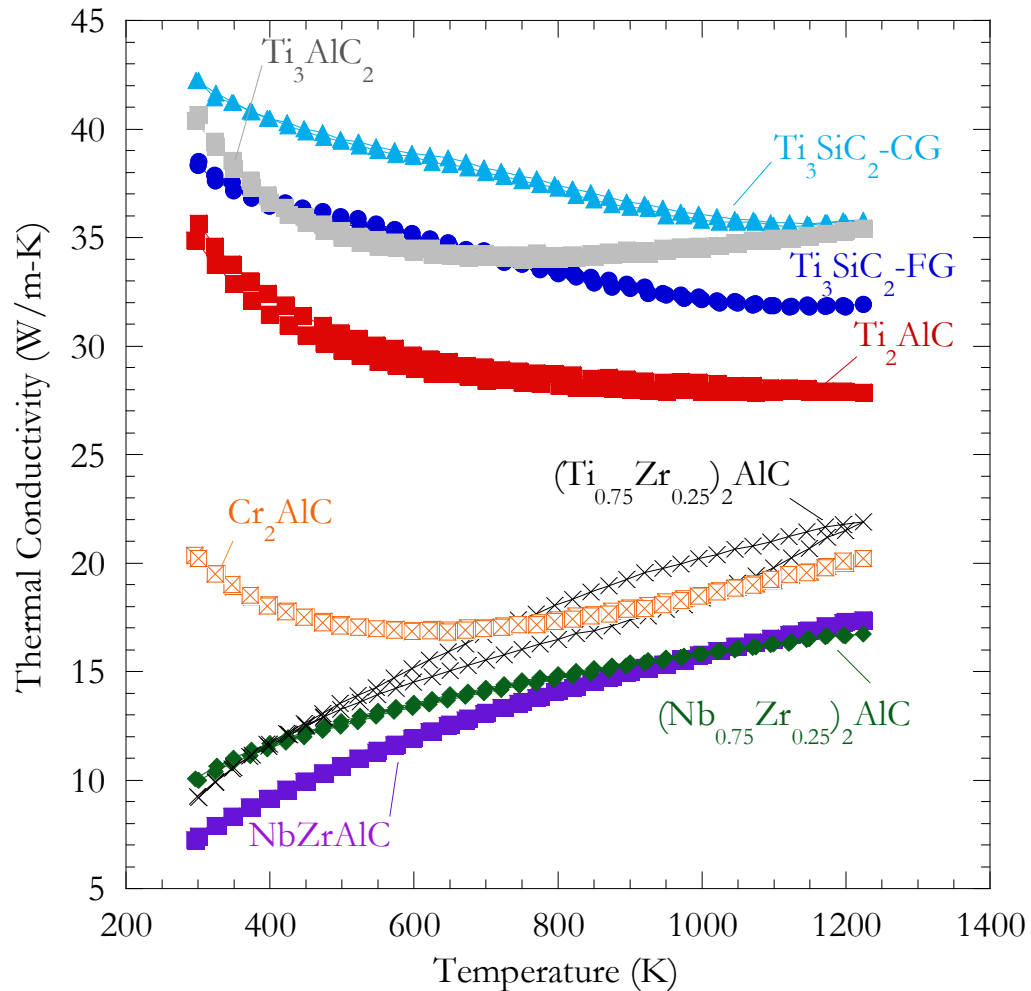


Figure 6.5 Thermal conductivities of various MAX phases as a function of temperature.

### 6.3.2. Electrical Contributions to Thermal Conductivity

The total thermal conductivity  $\kappa_{th}$  is a combination of both electronic  $\kappa_e$  and phononic  $\kappa_p$  thermal conductivities, given by:

$$\kappa_{th} = \kappa_e + \kappa_p \quad (6.4)$$

For a metallic conductor, as heat and electrical transport both involve the free electrons in the metal, the Wiedmann-Franz law can be used to approximate  $\kappa_e$  as a function of electrical resistivity,  $\rho$ , given by:

$$\kappa_e = \frac{L_0 T}{\rho} \quad (6.5)$$

where  $L_0$  is the Lorenz number, having a value of  $2.45 \times 10^{-8} \text{ W } \Omega \text{ K}^{-2}$ . For some MAX phases, notably  $\text{Ti}_3\text{SiC}_2$ , the overwhelming majority of  $\kappa_{th}$  is due to  $\kappa_e$  contributions [25]. This relationship was used to estimate RT  $\kappa_e$  of the irradiated materials using the measured electrical resistivity values from the 4-pt probe experiments.

### 6.3.3. Thermal Conductivity Estimation of Irradiated Samples

Using the above formulas,  $\kappa_e$  was estimated for  $\text{Ti}_3\text{SiC}_2$ ,  $\text{Ti}_3\text{AlC}_2$ ,  $\text{Ti}_2\text{AlC}$ , and  $\text{Ti}_2\text{AlN}$  after irradiation at MITR, and the results are compiled in Table 6.3. The % contributions [25] of  $\kappa_e$  for  $\text{Ti}_3\text{SiC}_2$ ,  $\text{Ti}_3\text{AlC}_2$ ,  $\text{Ti}_2\text{AlC}$ , and  $\text{Ti}_2\text{AlN}$ , at 97%, 52%, 43%, and 67%, respectively, were used to extrapolate the total  $\kappa_{th}$  at 298K.

Table 6.3 Calculated thermal  $\kappa_e$  from RT  $\rho$  using the Wiedmann-Franz law.

Sample	M-D1-T2			M-D1-T4			M-D2-T2		
	$\rho$ ( $\mu\Omega\text{-m}$ )	$\kappa_e$ (W/m-K)	$\kappa_{th}$ (W/m-K)	$\rho$ ( $\mu\Omega\text{-m}$ )	$\kappa_e$ (W/m-K)	$\kappa_{th}$ (W/m-K)	$\rho$ ( $\mu\Omega\text{-m}$ )	$\kappa_e$ (W/m-K)	$\kappa_{th}$ (W/m-K)
FG-Ti <sub>3</sub> SiC <sub>2</sub>	1.1(1)	6.8	7.0	0.23(1)	31.3	32.2	1.43(1)	5.1	5.3
CG-Ti <sub>3</sub> SiC <sub>2</sub>	2.2(1)	3.3	3.4	0.24(1)	30.1	31.1	2.82(1)	2.6	2.7
Ti <sub>3</sub> AlC <sub>2</sub>	2.84(2)	2.6	4.9	0.39(1)	18.7	36.0	8(2)	0.9	1.8
Ti <sub>2</sub> AlC	0.75(1)	9.7	22.7	0.44(1)	16.7	38.6	8.3(1)	0.9	2.0
Ti <sub>2</sub> AlN	1.46(1)	5.0	7.5	0.25(1)	29.7	44.3	3.34(1)	2.2	3.3

From these results, it is clear that irradiation at temperatures as low as 710 °C (T4) results in good recovery of thermal conductivity for these MAX phases. These results compare well with  $\kappa_{th}$  values of the MAX phases measured at 300K by laser flash analysis earlier in this section. It follows that the possible saturation in electrical resistivity for the Ti<sub>3</sub>SiC<sub>2</sub> with dose (Figure 6.4) bodes well for its use in any nuclear application where thermal transport is important. This is in sharp contrast to SiC, for e.g. wherein the thermal conductivity is sharply reduced with small irradiation doses [97].

#### 6.4. Nanoindentation: Mechanical Properties of Ti<sub>3</sub>SiC<sub>2</sub> and Ti<sub>2</sub>AlC

---

The mechanical properties of materials can be widely affected by irradiation with energetic particles. The formation of point defects and larger dislocation structures often leads to embrittlement and hardness increases. Metals tend to lose ductility, and fail more unpredictably due to the increased dislocation density, and pinning effects from point defects. While the bulk of the planned mechanical testing of the irradiated samples was not completed for this thesis, nanoindentation was performed to determine the effect of

irradiation on hardness and moduli of the FG-Ti<sub>3</sub>SiC<sub>2</sub> and Ti<sub>2</sub>AlC samples irradiated at MITR.

#### 6.4.1. Berkovich Tip Nanoindentation

Nanoindentation is a valuable tool used to explore the mechanical properties of a material by deforming small volumes of the material. Indentations for this work were made using a Berkovich nanoindenter, which is a 3-sided pyramidal shape. A schematic representation of a typical data set from Berkovich indentation is presented in Figure 6.6, where P designates the load, and h is the displacement relative to the initial surface [104, 105].

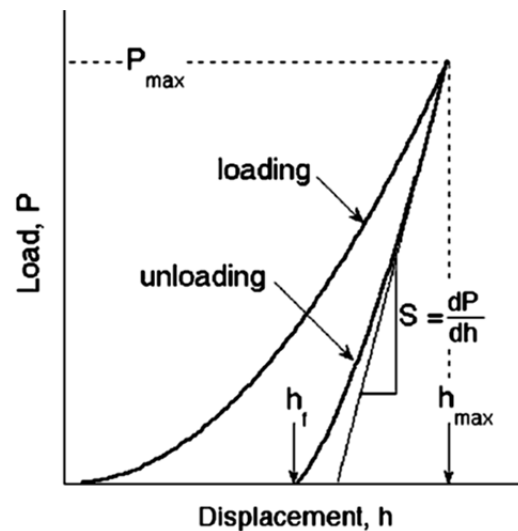


Figure 6.6 Schematic illustration of indentation load-displacement data [104, 105].

Quantities necessary for calculating hardness and modulus data can be obtained from the P-h curve, including: the maximum load,  $P_{max}$ , the maximum displacement,  $h_{max}$ , the final depth,  $h_f$ , and the elastic unloading stiffness, S, defined as the slope of the unloading curve

during initial stages of unloading [104, 105]. This type of indenter can be modeled by a conical indenter with a half-included angle,  $\varphi = 70.3^\circ$ , that gives the same depth-to-area relationship. As the indenter sinks in to the surface, assuming negligible pile-up of the material, elastic models show that the amount of sink-in,  $h_s$ , is given by [104]:

$$h_s = \epsilon \frac{P_{max}}{S} \quad (6.6)$$

where  $\epsilon$  is a constant equal to 0.75 for Berkovich tips. It follows then, that the depth of contact between the indenter and specimen,  $h_c = h_{max} - h_s$ , is:

$$h_c = h_{max} - \epsilon \frac{P_{max}}{S} \quad . \quad (6.6)$$

The contact area,  $A$ , can then be described using an area function,  $F(d)$ , that describes the projected area of the indenter at a distance  $d$  from its tip, given by:

$$A = F(h_c) \quad (6.7)$$

This shape function was calibrated for the specific indenter used for experiments by indenting a quartz standard material.

Having an understanding of the contact area for the indenter, the hardness can then be estimated by [104]:

$$H = \frac{P_{max}}{A} \quad (6.8)$$

Measurement of the elastic modulus extends from the relationship with contact area and the unload stiffness,  $S$ , by:

$$S = \beta \frac{2}{\sqrt{\pi}} E_{eff} \sqrt{A} \quad (6.9)$$

where  $\beta$  is a dimensionless parameter taken as unity, and  $E_{eff}$  is the effective elastic modulus defined by:

$$\frac{1}{E_{eff}} = \frac{1 - \nu^2}{E} + \frac{1 - \nu_i^2}{E_i} \quad (6.10)$$

which takes into account the Young's modulus,  $E$ , and Poisson's ratio,  $\nu$ , of the sample, and those of the indenter,  $E_i$  and  $\nu_i$  [104].

#### 6.4.2. Nanoindentation Results: MITR

Samples of FG-Ti<sub>3</sub>SiC<sub>2</sub> and Ti<sub>2</sub>AlC from the MITR experiments were investigated using nanoindentation at room temperature. Samples were indented following a strain controlled method to specific depths of 500, 1000, 1500, and 2000 nm (Figure 6.7). The results for hardness and modulus values are compiled in Table 6.2.

Care must be taken with these results, as the surfaces of each sample were not ideally polished for proper nanoindentation experiments. As a result, the standard error of the results is rather large in all cases. The indenter often encountered porosity or cracks in the surface, which introduce unavoidable complications with the data. These results are presented to form general trends.

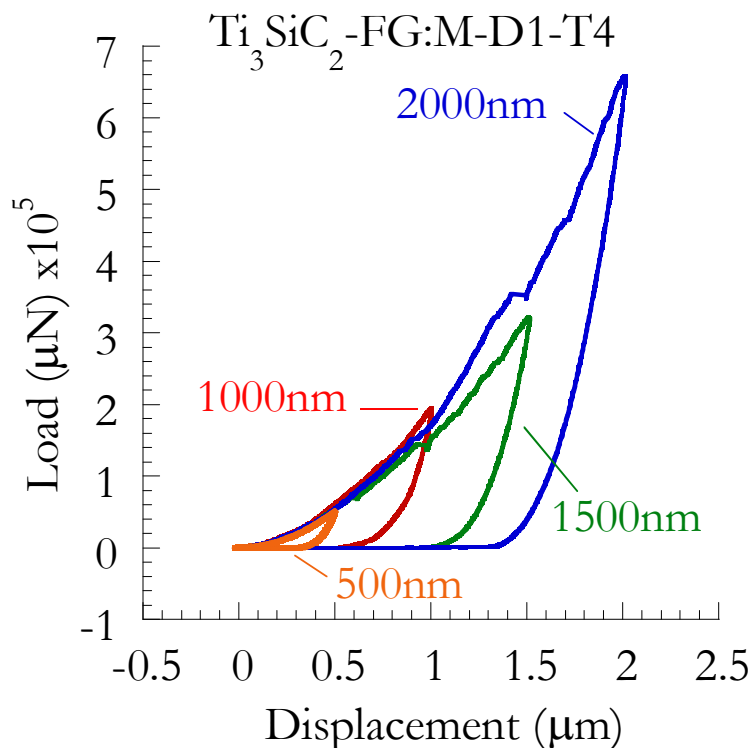


Figure 6.7 Typical load-displacement curves of indentations in FG- $\text{Ti}_3\text{SiC}_2$ :M-D1-T4 to various depths.

Table 6.4 Young's modulus and hardness as determined from Berkovich nanoindentation\*.

Condition	E (GPa)	H (GPa)
$\text{Ti}_3\text{SiC}_2$ FG-Pristine	320 [25]	5 [25]
$\text{Ti}_3\text{SiC}_2$ FG:M-D1-T2	316(62)	11(4)
$\text{Ti}_3\text{SiC}_2$ FG:M-D1-T4	230(84)	7(4)
$\text{Ti}_3\text{SiC}_2$ FG:M-D2-T2	248(60)	13(6)
$\text{Ti}_2\text{AlC}$ -Pristine	240 [25]	4 [25]
$\text{Ti}_2\text{AlC}$ :M-D1-T2	149(80)	7(5)
$\text{Ti}_2\text{AlC}$ :M-D1-T4	170(100)	5(4)
$\text{Ti}_2\text{AlC}$ :M-D2-T2	115(76)	5(4)

\*Results are to be taken qualitatively, as sample surfaces were not well prepared for nanoindentation.

After all irradiation conditions, hardness values were seen to increase for both FG- $\text{Ti}_3\text{SiC}_2$  and  $\text{Ti}_2\text{AlC}$ . Irradiation at T2 (350 °C) resulted in a drastic increase in hardness in FG-

$\text{Ti}_3\text{SiC}_2$ , with values of 11(4) and 13(6) GPa after D1 and D2, respectively (Figure 6.8). At 7(4) GPa, the hardness of FG- $\text{Ti}_3\text{SiC}_2$ :M-D1-T4 was closer to that of pristine samples, at 5 GPa, showing a recovery at higher temperature irradiations. The same trend was observed in  $\text{Ti}_2\text{AlC}$ :M-D1-T4, with values closer to pristine after T4 irradiation (Table 6.4). This hardness increase was expected after neutron irradiation, and is attributed to the increase in defect densities, which would lead to embrittlement and hardening of the materials. The decrease in hardness at M-D1-T4 demonstrates that FG- $\text{Ti}_3\text{SiC}_2$  and  $\text{Ti}_2\text{AlC}$  undergo defect recovery, alleviating some of the effects of point defects on the mechanical properties. Evidence for this was observed in Chapter 5, where TEM results confirmed that coherent dislocation loops formed from the agglomeration of point defects.

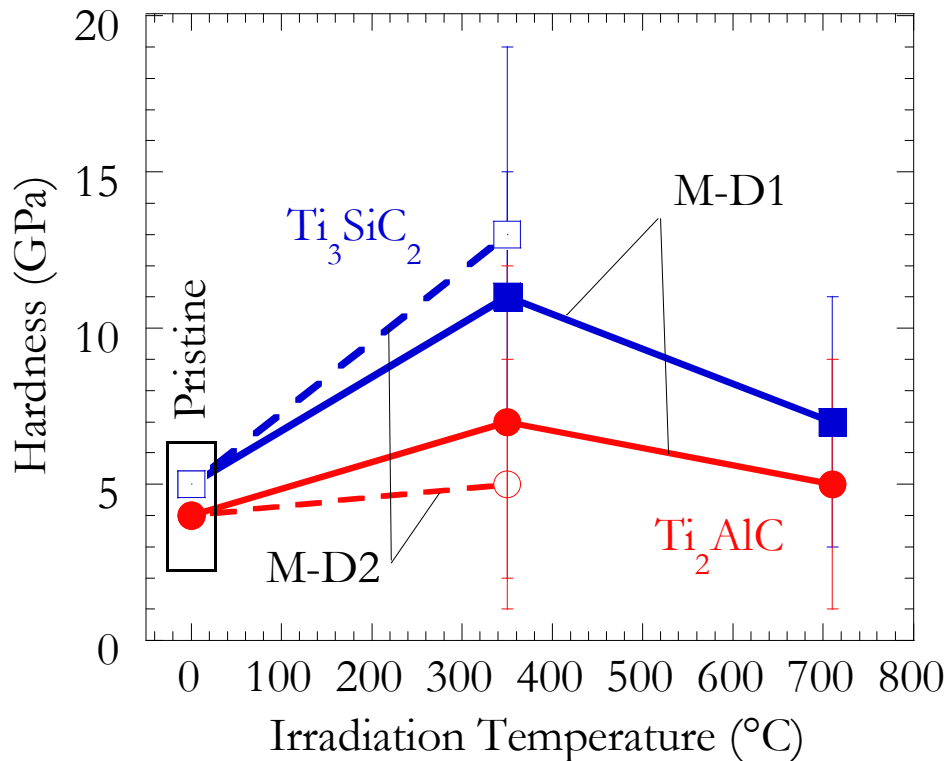


Figure 6.8 Effect of irradiation temperature on nanoindentation hardness of FG- $\text{Ti}_3\text{SiC}_2$  and  $\text{Ti}_2\text{AlC}$ .



With the exception of FG-Ti<sub>3</sub>SiC<sub>2</sub>:M-D1-T<sub>2</sub>, the Young's modulus was seen to decrease after irradiation. At 316(62) GPa, the Ti<sub>3</sub>SiC<sub>2</sub>:M-D1-T<sub>2</sub> modulus was close to pristine, ~320 GPa. The moduli of the remaining samples decreased without any apparent trends with respect to dose or temperature. The modulus of a material is determined by the bond strengths. It is assumed that the neutron irradiation defects do not alter significantly the bonding of the elements within the MAX phases, especially since the lattice parameters at higher temperature irradiation were seen to be near pristine.

Another possible cause could be porosity. The presence of porosity would lead to the decrease in modulus observed due to a reduction in the effective contact area for modulus calculations. This effect has been previously reported for other ceramics [106, 107], and well modelled for various porous systems [108]. Microcracking can also reduce modulus. It is therefore most plausible that neutron irradiation of Ti<sub>3</sub>SiC<sub>2</sub> and Ti<sub>2</sub>AlC resulted in the formation of microcracks and internal porosity, with a greater impact on the latter. This can clearly be seen in the SEM microstructures of the sample surfaces, where increased microcracking and grain pullout is observed (Figure 6.1). These pullouts are an indirect manifestation of the extent of neutron-induced microcracking. Note that as the irradiation temperature is increased, the extent of microcracking, and concomitant grain pullouts, decreases suggesting that microcracks may either not form at all, or heal at higher temperatures.

## 6.5. Neutron Activation

---

In preparing samples of Ti<sub>3</sub>SiC<sub>2</sub> and Ti<sub>3</sub>AlC<sub>2</sub>, irradiated at ATR, for PIE, an intriguing discovery was made regarding the activation of the samples. Before samples could be

transferred between facilities, contact radioactivity counts were surveyed for each sample. For the most part, especially for samples irradiated up to M-D2 from MITR, the activation counts, measured in Roentgen, R, per hour, were low; they measured <30 mR/h on contact, which was an acceptable safe dose for radiological workers to conduct extended length tasks, such as resistivity measurements. An exception was noticed for  $Ti_3AlC_2$ . At 160 and 190 mR/h on contact, samples of  $Ti_3AlC_2$ :A-D1-T1 and  $Ti_3AlC_2$ :A-D1-T2, respectively, showed a 10 fold increase in activity compared to  $Ti_3SiC_2$  irradiated at the same conditions. Further, the  $Ti_3AlC_2$  sample irradiated to 9 dpa, A-D5, at 500 °C, T3, resulted in a measured contact activity of 1860 mR/h on contact, which was 3 orders of magnitude higher than  $Ti_3SiC_2$ , even after more than 2 years had passed after irradiation. Such high levels of activity indicate the presence of long lived isotopes giving off hard gamma radiation. This result was very concerning at the time of discovery, as the activation of these samples approached the limit that was allowable for me, as a non-employee public citizen, to work with the sample. The cause of the activation has been attributed to the presence of impurities in the materials prior to irradiation, which subsequently became highly activated after irradiation. Upon survey of the measurable isotopes in the sample, Cobalt-60 was identified, which is radioactive isotope of Co with a half-life of 5.27 years. This result explains the significantly higher activation in the Al- containing samples, which showed a noticeable increase in activation after higher doses. At this time, the source of the Co remains unknown. However, it has been shown that elemental Al can contain parts per million traces of Co from natural occurring sources [109]. It is plausible then that trace amounts of Co were present in the starting powders used for fabrication of the  $Ti_3AlC_2$  samples, sourced from Kanthal, which after sufficient irradiation dose reach a detectable level of activation. It goes without saying then that future irradiation studies would need to incorporate stricter control of material purity for eventual utilization in nuclear applications.

## 6.6. Conclusions

---

Neutron irradiation of  $\text{Ti}_3\text{SiC}_2$ ,  $\text{Ti}_3\text{AlC}_2$ ,  $\text{Ti}_2\text{AlC}$ , and  $\text{Ti}_2\text{AlN}$  has shown a significant impact on several material properties. Microcracking was observed in  $\text{Ti}_2\text{AlC}$ , which in combination with point defects produced by irradiation lead to drastic increases in electrical resistivity after irradiation to 0.1 and 0.4 dpa at 710(50) °C.  $\text{Ti}_3\text{AlC}_2$  showed similar resistivity trends, and is assumed to have also experienced microcracking, especially as 50% of the material dissociated into TiC (Chapter 4). As shown in Chapter 5, irradiation induced point defects were annihilated at defect sinks and agglomerated into dislocation loops at high temperature irradiation, 0.1 dpa at 710(50) °C. This was directly evident by the almost full recovery of the electrical resistivity measured in samples from that condition. The dislocation loops that formed within the basal planes are more likely than not coherent with the lattice, and thus do not contribute significantly to electron scattering.

SiC is known to drastically lose thermal conductivity with irradiation dose [14]. The results in this thesis show that MAX phases recover their electrical conductivities should be maintained after higher irradiation temperatures. It follows that their good thermal conductivities significantly when irradiated at elevated temperatures. This result is promising for Gen IV reactors, which are designed to operate at temperatures ranging from 550-1000 °C. As defects are annihilated and agglomerated at higher temperatures, the negative effect on the thermal and electrical resistivity should be mitigated. Further work is needed to fully understand the effect of grain size on these results.

Typically, finer grained samples show a decrease in thermal conductivity, mainly due to the increase in grain boundary area which leads to scattering of phonons and electrons. This was observed in the non-irradiated thermal flash analysis experiments between FG- $\text{Ti}_3\text{SiC}_2$

and CG-Ti<sub>3</sub>SiC<sub>2</sub>. However, post-irradiated resistivity of FG-Ti<sub>3</sub>SiC<sub>2</sub> was consistently half that of its coarse-grained counterpart (Section 6.2), which should, in principle, translate into higher thermal conductivities. This result signifies the improved ability for fine grained materials to resist irradiation damage, as the increased grain boundary area improves defect annihilation to grain boundary defect sinks. From these results, the fine grain contribution to defect recombination is greater than the effect that the GBs have on decreasing thermal conductivity. Ultra-fine-grained and/or grain boundary engineered samples of MAX phases, notably Ti<sub>3</sub>SiC<sub>2</sub>, should become the focus of future irradiation studies to fully explore the effect of grain boundaries on the irradiation response in these materials.

Results from this chapter illustrate the recovery of material properties in these MAX phases at elevated temperatures. This reveals a promising trend for these materials for use in high temperature irradiation applications. The next and final chapter explores the compatibility of several MAX phases with possible reactor components such as Zircaloy-4 cladding and high temperature helium gas.

## 7. Interaction with Reactor Components

---

The majority of this thesis details the effect of neutron irradiation on a range of MAX phases. It is also important to consider how these materials interact with other components and materials present in the reactor environment. For current reactors, a commonly used cladding material is Zircaloy-4, Zr-4, an alloy of zirconium with small additions of tin, iron, chromium, and nickel. In an effort to explore MAX phases as a potential cladding coating to improve oxidation resistance of Zr-4 in high temperature accident conditions, the reactivity of  $\text{Ti}_3\text{SiC}_2$  and  $\text{Ti}_2\text{AlC}$  with Zr-4 was investigated.

Additionally, while helium, He, is commonly generated during reactor operation due to beta decay of fuel components, some Gen IV reactors are designed to use high temperature He as a coolant medium. A major application of fuel cladding is to contain the generated gasses during fission. An assessment of helium permeation in  $\text{Ti}_3\text{SiC}_2$ ,  $\text{Ti}_3\text{AlC}_2$ , and  $\text{Ti}_2\text{AlC}$  is given. In the following chapter, the materials studied were not irradiated.

### 7.1. Reactivity with Zircaloy-4 Fuel Cladding

---

Zr-4 is widely used as fuel cladding in light water reactors, LWR, mainly due to its high strength, corrosion resistance and low neutron cross section. However, its poor oxidation resistance can lead to its failure under loss of coolant conditions [36, 49, 110]. Up to 850 °C,  $\alpha$ -zirconium ( $\alpha$ -Zr) maintains an HCP structure. Above 950 °C, a phase change occurs resulting in FCC  $\beta$ -zirconium ( $\beta$ -Zr) [34]. LWRs nominally operate up to 400 °C, well within the  $\alpha$ -Zr range for Zr-4 [15]. Loss-of-coolant accidents (LOCA), however, can lead

to fuel rods experiencing temperatures in excess of 1200 °C, their rupture due to increased pressure, and exposure to the atmosphere with catastrophic consequences [34].

Another issue with Zr-4 cladding is its susceptibility to water corrosion, specifically hydrogen pickup and embrittlement [35]. Dissolved oxygen in the coolant water reacts with the metal surface, leading to the formation of a protective layer of  $ZrO_2$ . Simultaneously, the hydrogen produced from the oxidation diffuses into the cladding, resulting in the generation of zirconium hydride,  $ZrH_2$ , precipitates, which leads to hydrogen embrittlement, decreases in fracture toughness and the acceleration of corrosion and irradiation swelling [35]. Mitigation of hydrogen pickup and cladding oxidation is thus vital for the longevity and accident tolerance of fuel rod assemblies used in LWRs. Isolating the Zr-cladding during normal operating conditions could allow for higher burn-up and possibly higher operating temperatures. One solution to the corrosion problem, and a means to increase the safety margins of a LWR in LOCA, is to hermetically seal them from their surroundings. Recently, several studies have explored the thermal and cold spraying of MAX phases in general, and  $Ti_2AlC$  in particular, as a means to apply a thin coating of MAX onto substrates, such as mild steel or Zr-4 [111-115].

#### 7.1.1. Diffusivities of A-layers

More germane to this work are the several studies that have investigated the interdiffusion of silicon, Si or Al into Zr. Kidson *et al.* showed that bonding Al to Zr for hydrogen mitigation led to the formation of a singular  $ZrAl_3$  bonding layer, even though 10 intermetallics are known to form between the two elements [116]. Yue *et al.* explored the diffusion profile of Al that was laser clad onto a Zr substrate. The resulting diffusion layer was composed of a series of phases:  $(Zr) \rightarrow Zr + AlZr_2 + AlZr_3 \rightarrow Al_4Zr_5 + Al_3Zr_2 \rightarrow Al_3Zr_2 + AlZr_2 \rightarrow Al_2Zr \rightarrow Al_2Zr + Al_3Zr$  [117]. Laik *et al.* reported the activation energy of diffusion,  $Q_d$ , of  $-220 \pm$

3.33 kJ/mol and  $D_0$  of  $5.57_{-1.8}^{+2.6} \times 10^{-6}$  m<sup>2</sup>/s for the temperature dependence of Al impurity diffusion into  $\beta$ -Zr, in the 1203 - 1323 K temperature range [118].

The Si-Zr system is known to have seven intermetallics: ZrSi<sub>2</sub>, ZrSi, Zr<sub>5</sub>Si<sub>4</sub>, Zr<sub>3</sub>Si<sub>2</sub>, Zr<sub>5</sub>Si<sub>3</sub>, Zr<sub>2</sub>Si, and Zr<sub>3</sub>Si [119]. Bertolino *et al.* reported the formation of a double layered diffusion layer between Zr and Si in the 1173–1623 K temperature range [120]. After long enough annealing times, ZrSi<sub>2</sub> became the major phase on the Si-rich side. The thickness of that layer increased parabolically with time and its thickness was temperature dependent. On the Zr side, a thin ZrSi layer, whose thickness only depended on temperature, formed.

Diffusion bonding of the MAX phases has also been the subject of several papers. Gao and Miyamoto investigated joining Ti<sub>3</sub>SiC<sub>2</sub> with a Ti-6Al-4V alloy, resulting in of the formation of Ti<sub>5</sub>Si<sub>3</sub>C<sub>x</sub> and TiC interfacial phases. Above 1350 °C, a liquid-state was presumed to have formed [53]. Yin *et al.* successfully joined Ti<sub>3</sub>SiC<sub>2</sub> to itself by using an Al-interlayer [54]. Ganguly *et al.* reported the interdiffusion coefficients for the A-group element (Si, Ge) to be more than 300 times greater than the M-elements (Ti and Nb) [50]. Dong *et al.* successfully bonded SiC parts to themselves, in the 1200 to 1600 °C temperature range, using an intermediate Ti<sub>3</sub>SiC<sub>2</sub> layer. The strength of the bond was good because of the chemical bonds formed and the plasticity and thermal stress relaxation of the Ti<sub>3</sub>SiC<sub>2</sub> layer [52]. Above 1000 °C, Gu *et al.* bonded Ti<sub>3</sub>SiC<sub>2</sub> to itself using Ti-metal layer that resulted in the formation of TiC<sub>x</sub>, Ti<sub>5</sub>Si<sub>3</sub> and TiSi<sub>2</sub> within the diffusion zone [121].

### 7.1.2. Diffusion Bonding with Zircaloy-4: Results

Like most MAX phases' interactions with other solids, herein the A-group element – Al or Si – diffused out of the MAX phases' basal planes and formed intermetallics with the surrounding Zr-4 matrices. In the Al case, was also found deeper in the Zr matrices. SEM micrographs of the diffusion zones between Zr-4, on the one hand, and Ti<sub>3</sub>SiC<sub>2</sub> and Ti<sub>2</sub>AlC,

on the other, reveal the formation of multiple intermetallic layers (Figure 7.1, Figure 7.2). Diffusion profiles across the interfaces reveal that the diffusion of Ti and Zr was quite limited. In the following sections, first the interactions of Zr-4 with  $\text{Ti}_3\text{SiC}_2$  and  $\text{Ti}_2\text{AlC}$  are discussed separately. In the final section, the diffusivities in, and behavior of, the two systems are compared and contrasted.

### 7.1.3. $\text{Ti}_3\text{SiC}_2$ with Zircaloy-4

Typical SEM micrographs of  $\text{Ti}_3\text{SiC}_2/\text{Zr}$  diffusion couples are shown in Figure 7.1. Table 7.1 summarizes the phases formed as a function of time and temperature. Based on the totality of our results the following conclusions can be reached:

- The main intermetallic phase that forms is ZrSi (Figure 7.1). At 1100 °C after less than 10 h, the ZrSi does not contain Ti (Table 7.1). At higher temperatures, in areas adjacent to the  $\text{Ti}_3\text{SiC}_2$  phase, some Ti dissolves in the ZrSi phase (Table 7.1).
- $\text{ZrSi}_3$  forms under all conditions save for 30h at 1300 °C. For the most part, its thickness is less than that of ZrSi.
- After annealing for 30 h at 1100 °C (Fig. 1a),  $t > 1$  h at 1200 °C (Figure 7.1 and Figure 7.5) and at all times at 1300 °C (Table 7.1), the  $\text{Zr}_2\text{Si}$  phase is present.
- Not surprisingly, at the highest temperatures, the number of phases and their intermixing increase substantially (Figure 7.1 and Table 7.1).

As noted above, Bertolino *et al.* reported that two phases –  $\text{ZrSi}_2$  and ZrSi – formed when Si and Zr diffusion couples were annealed [120]. The thickness of the  $\text{ZrSi}_2$  layer increased parabolically with time and its thickness was temperature dependent. On the Zr side, a thinner ZrSi layer, whose thickness only depended on temperature, formed.



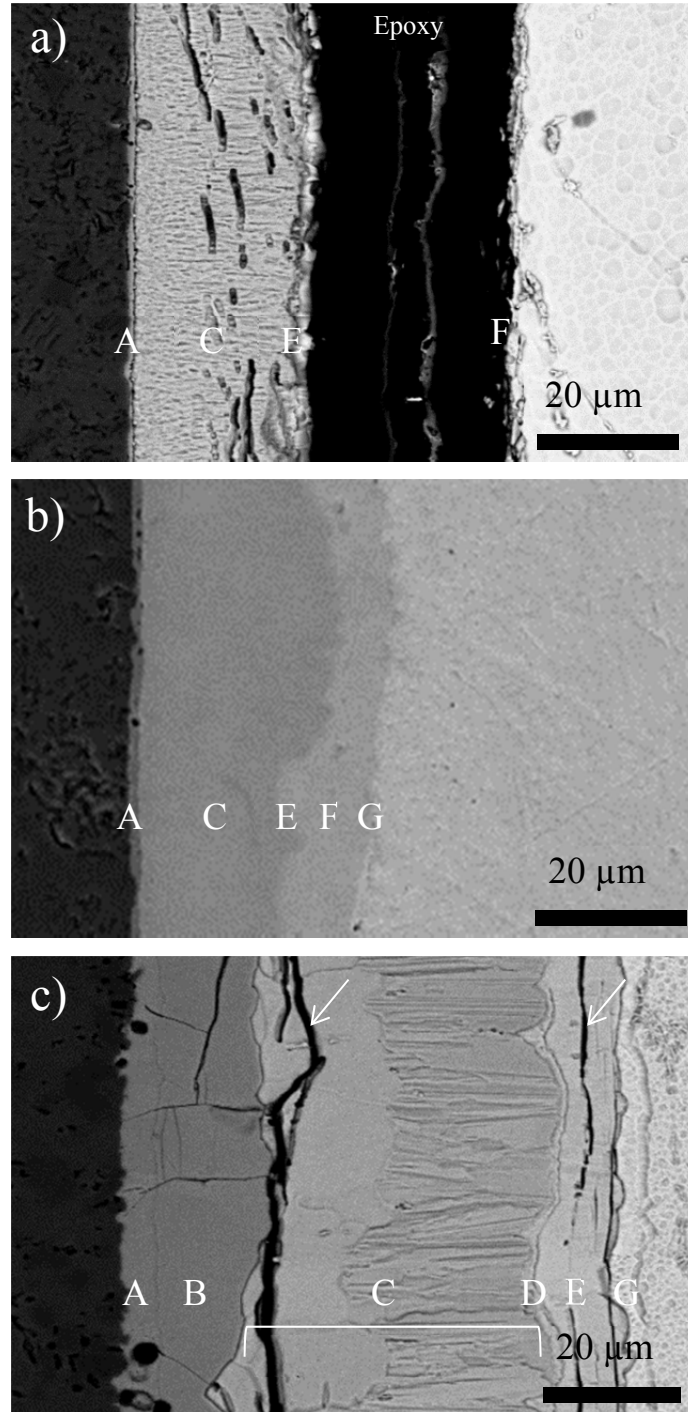


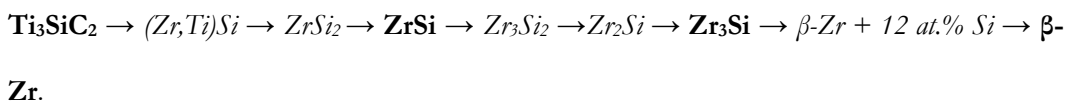
Figure 7.1 Typical backscattered electron SEM micrographs of  $\text{Ti}_3\text{SiC}_2/\text{Zr-4}$  diffusion couples annealed at a) 1100 °C (etched), b) 1200 °C, and c) 1300 °C (etched) for 30 h. The layers A, B, C, D, E, F, and G correspond to the phases  $(\text{Zr,Ti})\text{Si}$ ,  $\text{ZrSi}_2$ ,  $\text{ZrSi}$ ,  $\text{Zr}_3\text{Si}_2$ ,  $\text{Zr}_2\text{Si}$ ,  $\text{Zr}_3\text{Si}$ , and  $\beta\text{-Zr+Si}$ , respectively. In each case, a thin layer of porosity is observed at the interface. The predominant layer is composed of  $\text{ZrSi}$ . Occasional cracks, denoted by white arrows, are observed parallel to the interface. A layer of epoxy is seen in a) where the diffusion couple fractured during sample mounting.

Table 7.1 Summary of phase compositions and their thicknesses, in  $\mu\text{m}$ , across the  $\text{Ti}_3\text{SiC}_2/\text{Zr-4}$  diffusion couples - starting with  $\text{Ti}_3\text{SiC}_2$  - as a function of time and temperature. The last column lists the total thickness of the reaction layer and is the one plotted in Fig. 7.6.

Time (h)	(ZrTi)Si	ZrSi <sub>2</sub>	ZrSi	Zr <sub>3</sub> Si <sub>2</sub>	Zr <sub>2</sub> Si	Zr <sub>3</sub> Si	$\beta$ -Zr + Si	Total Diffusion Thickness
<b>1100 °C</b>								
1	-	-	6.2(1)		-	1.4(1)	-	7.6(2)
2	-	-	6.4(1)		-	1.4(1)	-	7.8(1)
10	0.4(1)	-	15.4(1)	1.2(1)	-	1.8(1)	-	18.7(2)
30	0.9(1)	-	22.7(1)	-	2.2(1)	2.2(1)	-	27.9(3)
<b>1200 °C</b>								
1	0.5(1)	-	6.4(1)	-	-	1.3(1)	-	8.2(1)
2	0.8(1)	-	7.2(1)	1.3(1)	0.7(1)	5.4(1) 8%Ti	2.13(7)	17.5(2)
10	-	-	15.7(3) 3%Ti		4.0(1) 1%Ti	3.1(1)	-	23.0(4)
30	1.3(1)	-	24.7(5) 5%Ti		1.6(1)	7.4(2)	1.9(3)	36.9(7)
<b>1300 °C</b>								
2	0.84(4)	-	20.7(2)	-	2.9(1)	1.0(1)	-	25.5(2)
10	3.1(2)	8.1(3) 5%Ti	5.0(4) 5%Ti	-	10.4(3)	7.6(2)	2.0(1)	36.2(8)
30	4.7(1)	15.4(3) 5%Ti	40.3(6)	2.0(2)	10.0(2)	-	2.6(1)	75.2(8)

‡ Standard deviation of last digit = (1)

Based on these results it is reasonable to conclude that the overall reaction or diffusion path between  $\text{Ti}_3\text{SiC}_2$  and Zr-4 is:



Phases shown in bold formed under most conditions. A layer close to the  $\text{Ti}_3\text{SiC}_2$  side with a phase corresponding to a solid solution (Zr, Ti)Si was observed after 10 h at 1100 °C and at both 1200 and 1300 °C. Only at 1300 °C after 10 h and 30 h was a ZrSi<sub>2</sub> phase observed. A thin layer of a composition corresponding to Zr<sub>3</sub>Si<sub>2</sub> was sporadically observed after annealing for 10 h at 1100 °C, 2 h at 1200 °C, and 30 h at 1300 °C. The Zr<sub>2</sub>Si phase was more common after longer times and higher temperatures, appearing after 30 h at 1100 °C and at times longer than 1 h at both 1200 and 1300 °C.

No precipitates were seen to form beyond the intermetallic layers. Slight porosity at the interface was observed at 1100 °C after annealing for 30 h and at 1200 °C and above (Figure 7.1a-c). Occasional cracks were observed parallel to the interface (Figure 7.1 and Figure 7.5). In general, the  $\text{Ti}_3\text{SiC}_2$  diffusion couples resulted in firmly bonded interfaces that were able to withstand the clamping forces applied during sectioning, polishing, etc.

#### 7.1.4. $\text{Ti}_2\text{AlC}$ with Zircaloy-4

At all temperatures studied,  $\text{Ti}_2\text{AlC}$  formed numerous distinct layers, the thicknesses of which increased with annealing temperatures and times (Figure 7.2). Table 7.2 summarizes the phases formed between Zr-4 and  $\text{Ti}_2\text{AlC}$  as a function of time and temperature. From the totality of these results it is reasonable to conclude that:

- The main intermetallic phases that form at all temperatures are  $\text{Zr}_2\text{Al}_3$  and  $\text{Zr}_3\text{Al}_2$ .
- A layer with a consistent composition of 45% Al / 55% Zr, corresponding to  $\text{Zr}_3\text{Al}_4$ , is also seen at all conditions, though nominally thinner than the layers described above. The layer appears homogeneous; no precipitates can be seen (Figure 7.2).
- A thin  $\text{Zr}_3\text{Al}$  layer is observed closest to the Zr-4 side at all times at 1100 °C and after 1h at 1200 °C (Table 7.2). At higher temperatures,  $\text{Zr}_2\text{Al}$  is seen to form in addition, eventually replacing  $\text{Zr}_3\text{Al}$  all together at 1300 °C.

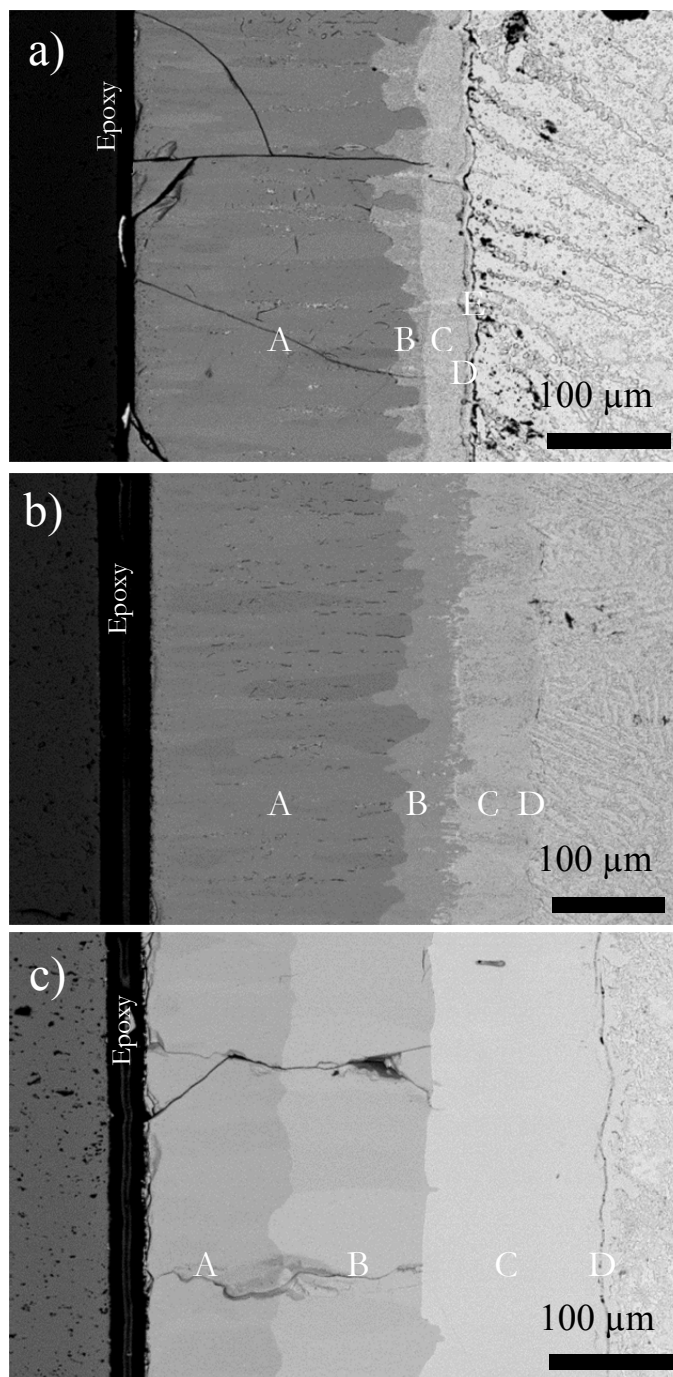
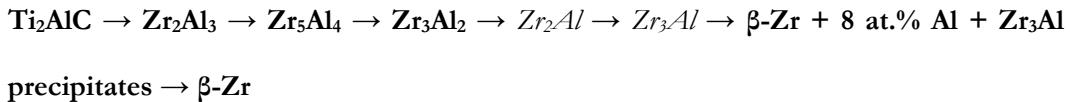


Figure 7.2 Typical backscattered electron SEM micrographs of  $\text{Ti}_2\text{AlC}$  /Zr-4 diffusion couples annealed at a) 1100 °C (etched), b) 1200 °C (etched), and c) 1300 °C for 30 h. The layers A, B, C, D, and E correspond to the phases  $\text{Zr}_2\text{Al}_3$ ,  $\text{Zr}_5\text{Al}_4$ ,  $\text{Zr}_3\text{Al}_2$ ,  $\text{Zr}_2\text{Al}$ , and  $\text{Zr}_3\text{Al}$ , respectively. In all cases, a layer of epoxy is seen where the diffusion couple fractured during sample mounting.  $\text{Zr}_3\text{Al}$  precipitates are observed along the  $\beta$ -Zr grain boundaries beyond the intermetallic layers. At 1300 °C, no single layer dominates. Significant cracking of the intermetallic layers is observed parallel and perpendicular to the original interface.

- Deep into the Zr-4 and beyond the intermetallic layers,  $Zr_3Al$  precipitates decorate the grain boundaries of the  $\beta$ -Zr phase (Figure 7.2). Additionally, the latter contains  $\approx 8$  at.% Al in solid solution. The solubility of 8 at.% corresponds to a temperature of about 900 °C, which suggests that is the temperature below which the diffusivities of Al in the  $\beta$ -Zr phase are too low. Interestingly and consistent with this interpretation is that the 8 at.% does not appear to be a function of annealing time or temperature. In other words, it is most probably determined upon cooling from the annealing temperature.
- In contrast to  $Ti_3SiC_2/Zr-4$ , Ti from  $Ti_2AlC$  was not seen to diffuse into the Zr-4. There was slight counter diffusion of Zr towards  $Ti_2AlC$ .

Based on the aforementioned results it is reasonable to conclude that the overall reaction or diffusion path between  $Ti_2AlC$  and Zr-4 is:



Phases shown in bold were present after all anneals. The  $Zr_2Al_3$  layer was the thickest layer at all conditions (Figure 7.2, Table 7.2). In contradistinction to the  $Ti_3SiC_2/Zr-4$  interfaces, the ones between Zr-4 and  $Ti_2AlC$ , more often than not, fractured simply in handling the samples or after clamping them for sectioning. Transverse cracks were also more frequently observed in the intermetallic layers (Figure 7.2). Both observations can be attributed to thermal stresses induced on cooling together with, presumably, the presence of a weak interface.

**Table 7.2 Summary of phase compositions and their thicknesses, in  $\mu\text{m}$ , across the  $\text{Ti}_2\text{AlC}/\text{Zr-4}$  diffusion couples – starting with  $\text{Ti}_2\text{AlC}$  – as a function of time and temperature. The last column lists the total thickness of the reaction layer and is the one plotted in Fig. 7.6.**

Time (h)	$\text{Zr}_2\text{Al}_3$	$\text{Zr}_5\text{Al}_4$	$\text{Zr}_3\text{Al}_2$	$\text{Zr}_2\text{Al}$	$\text{Zr}_3\text{Al}$	Total Diffusion Thickness‡
<b>1100 °C</b>						
1	39.3(4)	2.9(2)	5.5(2)	-	2.6(1)	50.3(7)
10	158(1)	10(1)	13.6(5)	-	4.5(2)	186(2)
30	212(2)	17(1)	30.7(7)	3.9(2)	4.5(1)	268(2)
<b>1200 °C</b>						
1	76.4(5)	4.6(3)	11.9(3)	2.4(1)	3.5(1)	99.3(8)
2	82.8(5)	7.1(3)	12.5(3)	-	6.9(3)	109.2(8)
10	142(1)	26(1)	23(1)	11(1)	-	201(2)
30	230(2)	48(2)	58(1)	9.7(8)	-	346(3)
<b>1300 °C</b>						
1	90.2(6)	9.7(3)	14.0(4)	10.4(5)	-	124(1)
10	147.7(6)	44.7(8)	58(1)	16(1)	-	267(2)
30	130(1)	114(1)	126(1)	19.7(9)	-	390(2)

‡ Does not include the region with  $\text{Zr}_3\text{Al}$  precipitates.

In some cases, the  $\text{Ti}_2\text{AlC}$  grains deep in the MAX phase were surrounded by a thin white/grey layer, identified in SEM/EDX as  $\text{TiC}$  (Figure 7.5d). Based on the extensive diffusion of Al seen in Figure 7.6b, the  $\text{TiC}$  layers did not appear to act as a diffusion barrier. Interestingly, no  $\text{TiC}$  boundary layers were observed in the  $\text{Ti}_3\text{SiC}_2$  samples, likely due to the significantly less Si diffusion from within the sample.

As shown in other studies of MAX diffusion bonding, it is apparent that the Al from the  $\text{Ti}_2\text{AlC}$  acts as a transient liquid phase, diffusing out of the basal planes in the grain boundaries (Figure 7.5d) and readily diffusing throughout the Zr-4, that resulted in the growth of  $\text{Zr}_3\text{Al}$  precipitates along the Zr-4 grain far away from the interface (Figure 7.2).

#### 7.1.5. Comparison of the Diffusion Couples

There are a number of important similarities and differences between the results obtained from the various diffusion couples. In terms of similarities, in all cases, the main diffusing species is the A-group element. Given what is known about the reactivity of the A-group

elements in the MAX phases this is far from surprising [25]. As early as 1999, it was shown that when  $\text{Ti}_3\text{SiC}_2$  was immersed in cryolite, the Si was selectively etched by diffusing along the  $\text{Ti}_3\text{SiC}_2$  grain boundaries [90]. Over the years the same was shown for other MAX phases in many environments. More recently it was shown that the Al can be etched out of the basal planes of Al-containing MAX phase by immersing their powders, at room temperature, in hydrofluoric acid, HF, solutions [122]. At all temperatures there was some intermixing of the Ti and Zr atoms, suggesting at least some solubility of Zr in all these MAX phases. Under the conditions explored herein and within the resolution of our EDX measurements, no C appears to have diffused into the Zr-4 or the intermetallics formed.

Since the solubility of Si in Zr is negligible, even at  $T > 1600$  °C, only a thin layer of Si in solution is detected beyond the intermetallic layers at 1200 °C, 2 and 10 h, and  $> 10$  h at 1300 °C. In sharp contradistinction, the solubility of Al in Zr at 1200 °C is of the order of 20 at.% [123]. It is presumably this significant solubility that accounts for the presence of Al deep beyond the intermetallic layers that form. Furthermore, at  $T < 1019$  °C, for Al concentrations  $> 8$  at.% and  $< 25$  at.%, the equilibrium phase is  $\text{Zr}_3\text{Al}$  as observed in all cases. It is worth noting that while the initial Zr-phase was the  $\alpha$ -Zr polymorph, after the high temperature anneals, it was transformed to  $\beta$ -Zr, as is evidenced by the shape of the Zr grains after annealing which are clearly decorated by the  $\text{Zr}_3\text{Al}$  particles that precipitate along their grain boundaries (e.g. see Figure 7.2a, b, and c). The initial Zr-4 microstructure (not shown) was comprised of small equiaxed grains.

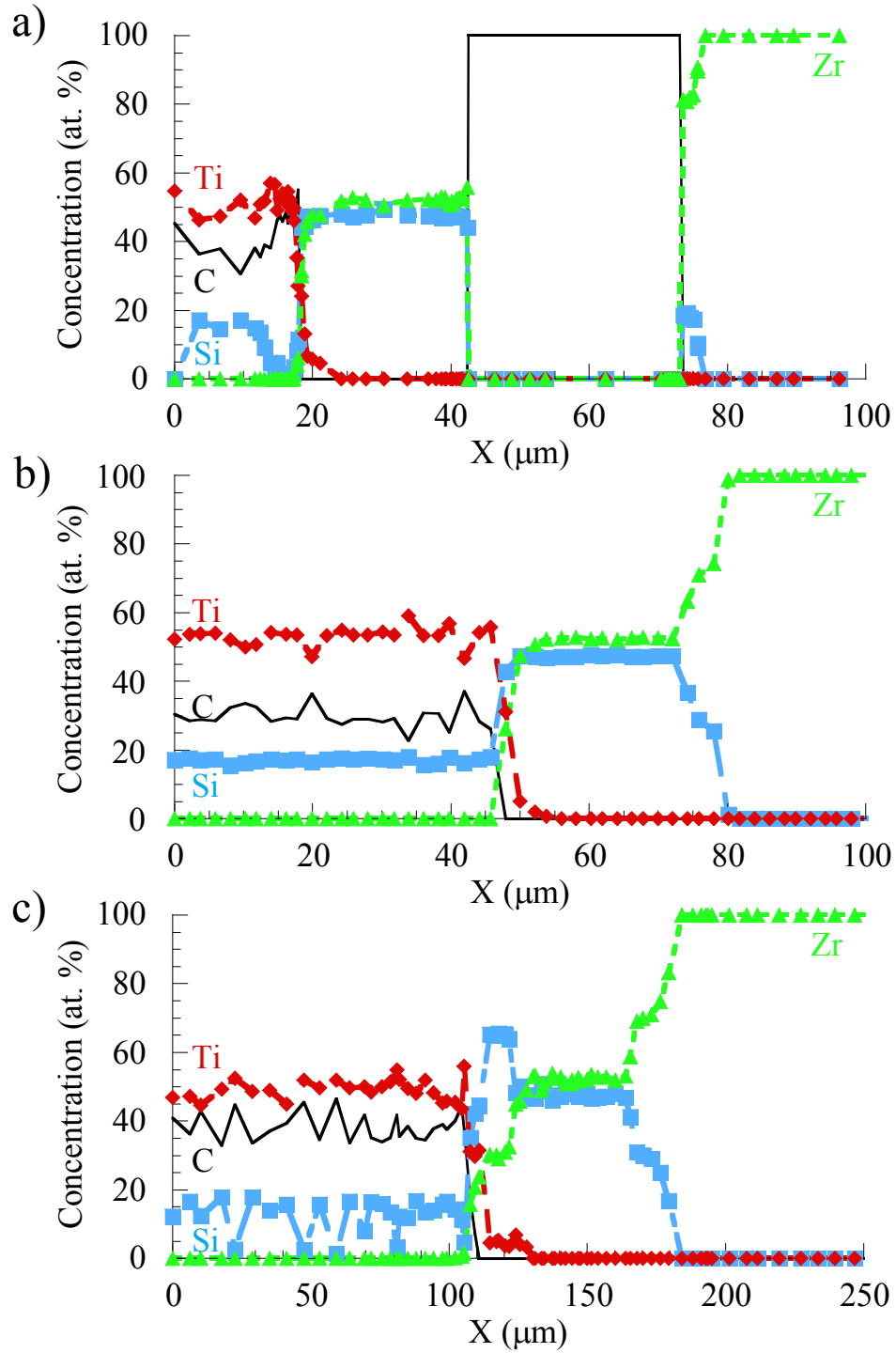


Figure 7.3 Typical composition profiles determined by EDX line scans of the  $\text{Ti}_3\text{SiC}_2/\text{Zr-4}$  interfaces obtained after annealing at, a) 1100 °C, b) 1200 °C, and c) 1300 °C for 30 h reveal the formation of several intermetallic layers with distinct compositions. A depletion of Si is seen on the  $\text{Ti}_3\text{SiC}_2$  side at 1100 °C (a), though not at higher temperatures. There is a slight counter diffusion of Ti and Zr, though Si is the dominant diffusing species. At 1300 °C, a layer of  $\text{ZrSi}_2$  is observed.



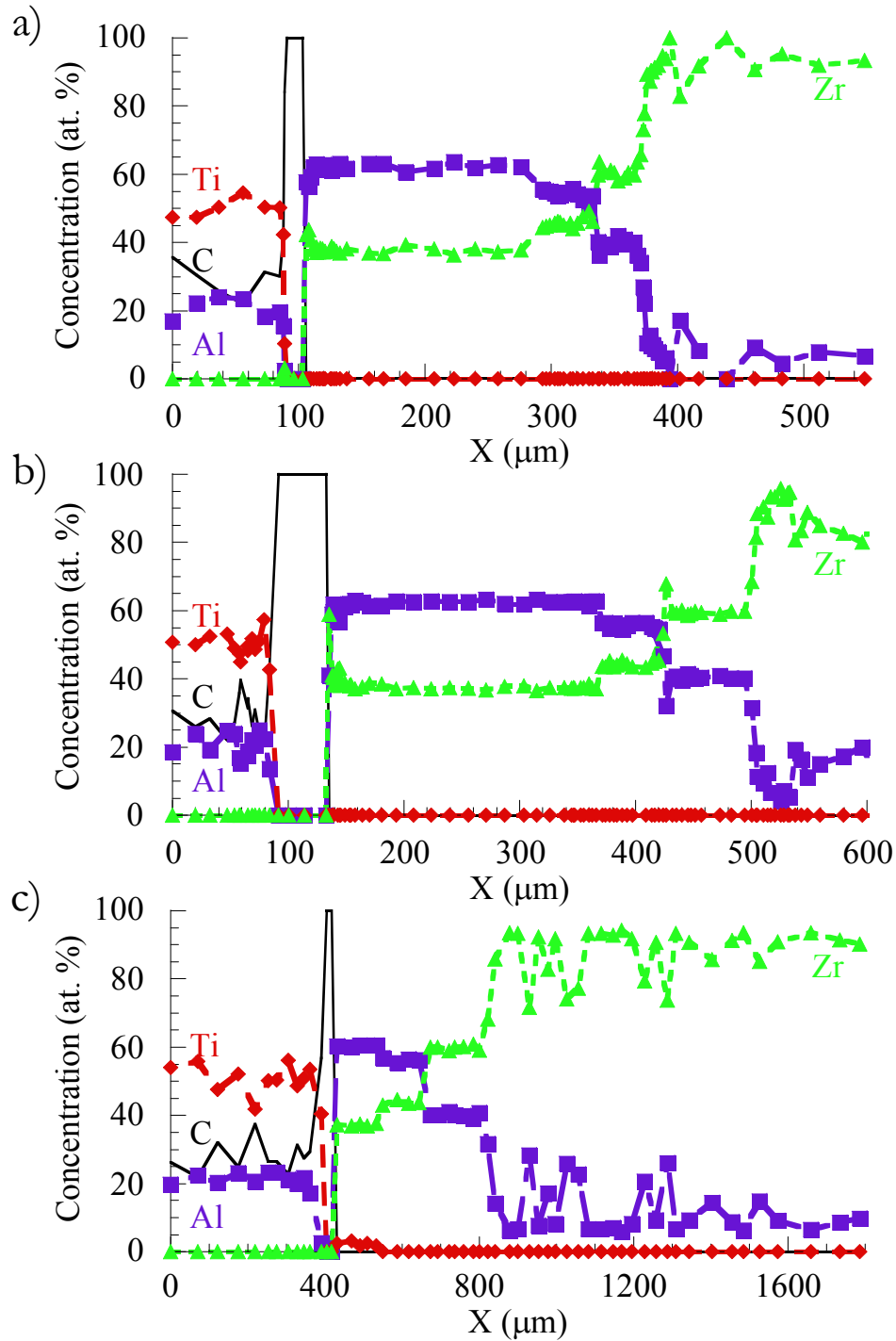
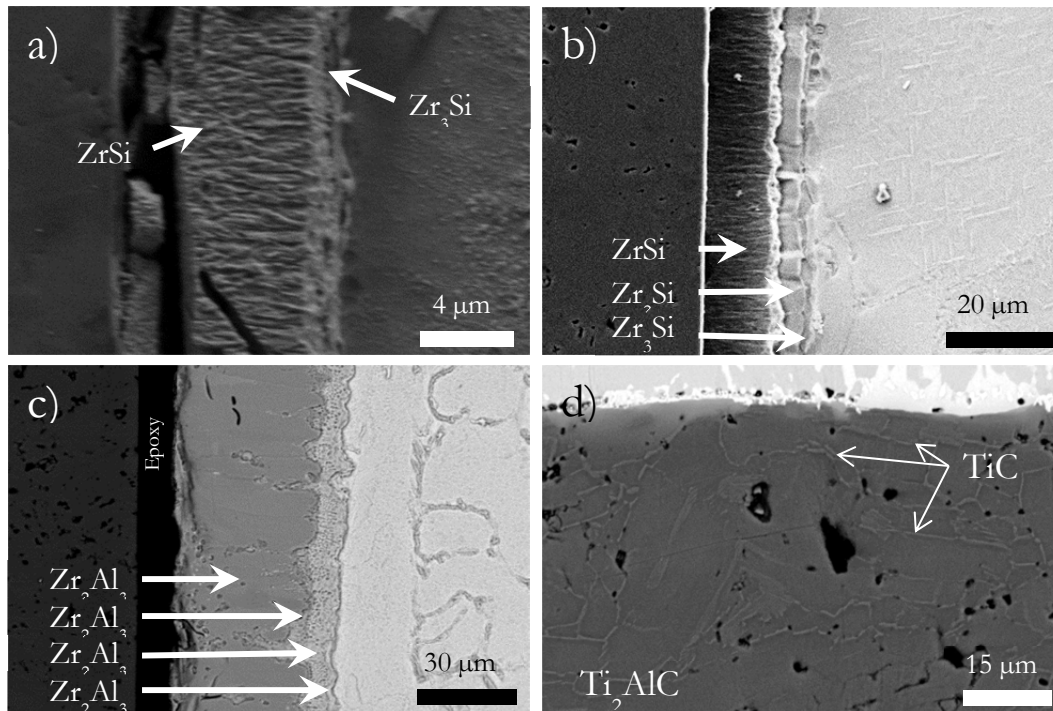


Figure 7.4 Typical composition profiles determined by EDX line scans of the  $\text{Ti}_2\text{AlC}$  / Zr-4 interfaces obtained after annealing at, a) 1100 °C, b) 1200 °C, and c) 1300 °C for 30 h reveal the formation of several intermetallic layers with distinct compositions. Each condition tested resulted in similar phase compositions, with layer thickness increasing with temperature. During annealing at the temperatures tested, the Al dissolves into solution with  $\beta$ -Zr beyond the intermetallic layers on the Zr-4 side. Upon cooling, Al segregation at the grain boundaries likely resulted in the precipitation of  $\text{Zr}_3\text{Al}$  structures, seen in Figure 7.2.



**Figure 7.5** Typical backscattered electron SEM micrographs of etched diffusion couples of  $\text{Ti}_3\text{SiC}_2/\text{Zr-4}$  annealed at, a)  $1100\text{ }^\circ\text{C}$  for 1 h, b)  $1200\text{ }^\circ\text{C}$  for 10 h, and, c)  $\text{Ti}_2\text{AlC}/\text{Zr-4}$  annealed at  $1100\text{ }^\circ\text{C}$  for 1 h. At the same conditions, the diffusion layer thicknesses observed for the  $\text{Ti}_2\text{AlC}/\text{Zr-4}$  couples are almost an order of magnitude larger. Tunnel like pores are seen in the  $\text{ZrSi}$  layer in a). d) SEM micrograph of the etched  $\text{Ti}_2\text{AlC}/\text{Zr-4}$  diffusion couple annealed at  $1300\text{ }^\circ\text{C}$  for 1 h shows  $\text{TiC}$  layers that formed surrounding the  $\text{Ti}_2\text{AlC}$  grains near the interface.

In all diffusion profiles, the Si and Al concentrations in the MAX phases are lower than their concentrations in the adjacent intermetallics (Figure 7.3, Figure 7.4). This uphill diffusion implies that the activities of the A-group elements in the MAX phases are considerably higher than their concentration would suggest. It is this enhanced activity that is responsible for crack healing in  $\text{Ti}_2\text{AlC}$  and  $\text{Ti}_3\text{AlC}_2$  [45, 124, 125].

All else being equal, the diffusion layer thicknesses observed when Zr-4 was in contact with  $\text{Ti}_2\text{AlC}$  were up to an order of magnitude larger than when it was in contact with  $\text{Ti}_3\text{SiC}_2$  (Figure 7.5a, c). This is especially noted in the  $1200\text{ }^\circ\text{C}$ , 30 h condition (Figure 7.2b) where, at  $346(3)\text{ }\mu\text{m}$ , the intermetallic layer depth in TAC is an order of magnitude greater than  $\text{Ti}_3\text{SiC}_2$ , at  $36.9(7)\text{ }\mu\text{m}$  (Figure 7.1b).

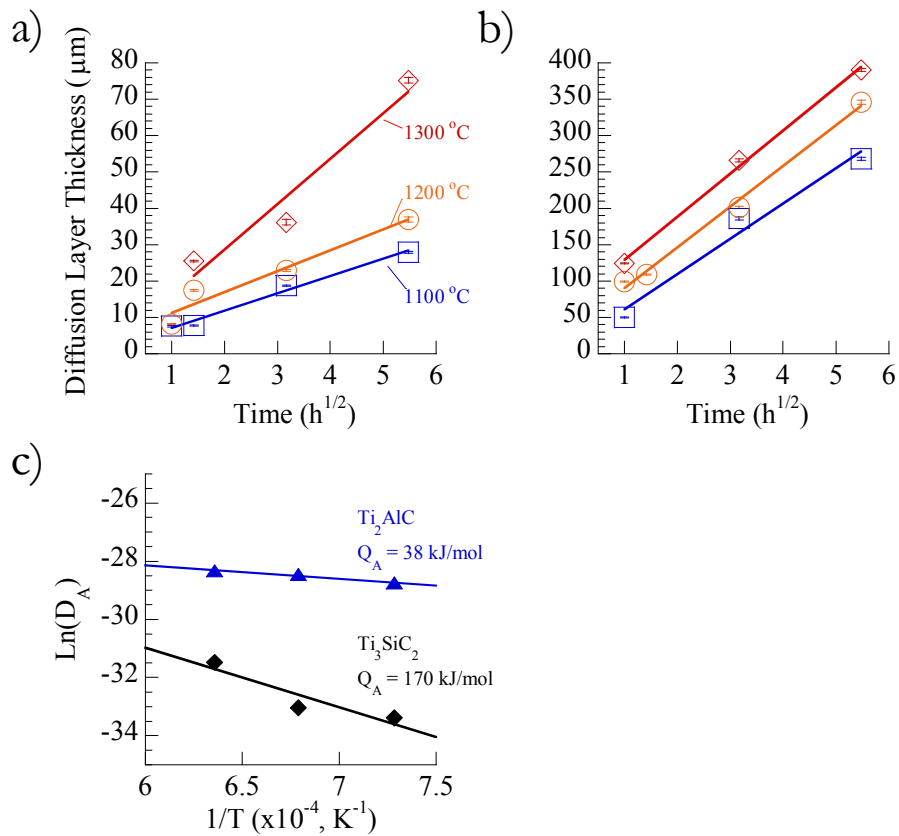


**Figure 7.6** Total diffusion distance ( $x$ ) vs.  $t^{1/2}$  for diffusion couples of: a) Ti<sub>3</sub>SiC<sub>2</sub> and, b) Ti<sub>2</sub>AlC with Zr-4 in the temperature range of 1100-1300 °C. In all cases, Ti<sub>3</sub>SiC<sub>2</sub> results in a shallower diffusion length. These trends show a parabolic diffusion behavior as  $x \approx (2Dt)^{1/2}$ . c) Arrhenius plot of the effective diffusion coefficients,  $D_A$ .

Total diffusion distances,  $x$ , vs.  $t^{1/2}$  for diffusion couples of Zr-4 with Ti<sub>3</sub>SiC<sub>2</sub> (Figure 7.6a) and Ti<sub>2</sub>AlC (Figure 7.6b) in the temperature range of 1100-1300 °C reveal that, for both materials, a linear fit with  $t^{1/2}$  was observed, indicating that the diffusion obeyed a parabolic law in each case. The temperature dependence of the effective diffusion coefficients,  $D_A$ , of the A-group elements through the reaction layers was fit to a linear regression of an Arrhenius plot (Figure 7.6c). For Ti<sub>3</sub>SiC<sub>2</sub>/Zr-4, the temperature dependence is described by:

$$D_{Si}\left(\frac{m^2}{s}\right) = 7.4 \times 10^{-9} \exp\left(\frac{-170 \text{ kJ/mol}}{RT}\right) \quad (7.1)$$

and for  $Ti_2AlC / Zr-4$ , the temperature dependence is described by:

$$D_{Al}\left(\frac{m^2}{s}\right) = 9.2 \times 10^{-12} \exp\left(\frac{-38 \text{ kJ/mol}}{RT}\right) \quad (7.2)$$

At 38 kJ/mol, the activation energy for  $D_{Al}$  is significantly lower than the 170 kJ/mol of  $D_{Si}$ . These results for  $Ti_3SiC_2/Zr-4$  compare well with previous diffusion studies, where activation energies of various diffusion couples were reported as 118, 132, and 156 kJ/mol for  $Ti_3SiC_2/Ni$  [51],  $Ti_3SiC_2/Si$  [126], and  $Ti_3SiC_2/Ti-6Al-4V$  [53], respectively.

In general, and under all conditions tested, the diffusion layer thicknesses observed were larger when Al was present in the system than when Si was. Figure 7.5 compares SEM micrographs of diffusion couple interfaces between Zr-4 bonded with  $Ti_3SiC_2$  in (a), and with  $Ti_2AlC$  in (c). Despite the relatively short diffusion time of 1 h and the relatively low diffusion temperature, 1100 °C, it is obvious that the Si penetration depth in the Zr-4 is significantly less than Al. This difference is more dramatically realized when Zr-4 and  $Ti_2AlC$  were diffusion bonded at 1300 °C for 30 h are compared (Figure 7.1c and Figure 7.2c). The reaction layer thickness in the  $Ti_2AlC$  case was of the order of 390  $\mu m$ . The reaction layer thickness that formed under identical conditions when  $Ti_3SiC_2$  was in contact with Zr-4 was  $\approx 75 \mu m$  (Figure 7.1c).

#### 7.1.6. Successful Bonding in LOCA Conditions

The reactivity between Zr-4 with  $Ti_3SiC_2$  and  $Ti_2AlC$ , over the 1100-1300 °C temperature range, was studied by setting up  $Ti_3SiC_2/Zr-4$  and  $Ti_2AlC /Zr-4$  diffusion couples. Based on the results shown, and similar to previous work in the Zr/Al system, it is clear that Al-diffusion into Zr was extensive, and resulted in a large affected diffusion zone with several

$Zr_xAl_y$  intermetallic layers [116-118].  $Zr_3Al$  precipitates were observed up to 200  $\mu m$  into the Zr-4 bulk after annealing at all conditions. The Al diffused out of the  $Ti_2AlC$  basal planes and through the grain boundaries, resulting in the formation of TiC rings around  $Ti_2AlC$  grains near the bonding interface.

Diffusion of Si from  $Ti_3SiC_2$  generally formed two intermetallic layers:  $ZrSi$  and  $Zr_3Si$ . At higher temperatures, layers of  $ZrSi_2$ ,  $Zr_3Si_2$ , and  $Zr_2Si$  also formed. In this case, TiC layers were not seen to form around any of the  $Ti_3SiC_2$  grains.

Overall, diffusion depths from  $Ti_3SiC_2$  were an order of magnitude shallower than the Al-containing MAX phases at 1100 and 1200  $^{\circ}C$ , and 5-7 times shallower at 1300  $^{\circ}C$ . The diffusion of both Si and Al is seen to follow the parabolic law, and the microstructure of the diffusion bonded regions is indicative of the diffusion controlled reaction.

## 7.2. Helium Permeability

---

During reactor operation, many gases, such as krypton, are generated as by-products from the fission process. Additionally, alpha particles are released from the decay processes of radioactive isotopes that form during the reaction cycle. Alpha radiation is essentially the nucleus of a helium, He, atom without electrons, which can lead to ionization of atoms in surround materials. He accumulation at high temperatures can also lead to the formation of voids and bubbles within reactor component microstructures, inducing embrittlement and swelling, along with unpredictable failure modes. Fuel cladding materials must be able to contain fission gases and prevent the transport of He through their structure. He permeability, which is a measure of diffusion of He atoms through a material, can be investigated to understand a materials' ability to limit He transport.

### 7.2.1. Permeation

In the literature, permeation is commonly reported in terms of a permeability coefficient, which is also called the permeation or permeability constant, or just permeability. In some cases, the models used to calculate the permeability are different or a variety of units are used making the comparison of the results not a straight forward task. Often, the terms permeability and permeance are confused as well. Permeability is not dependent on the thickness of the material while permeance does depend on the on the thickness of the material. In this section, the following definitions and units are used to report permeation.

Permeation is the transmission of a fluid through a solid. For a gas, the permeation involves the gas dissolving into the surface of the solid, diffusing through the solid; and desorbing from it. However, the diffusion is the slowest step and, hence, the permeation rate is determined by the diffusion process. The permeation of gases through solids is directly related to the concentration gradient of the gas across the material and the properties of such material. For steady state, the permeation can be formulated based on the diffusion process given by Fick's law:

$$J = -D\nabla c \quad (7.3)$$

where  $J$  is the flux of the diffusing gas,  $c$  is the concentration of gas within the solid, and  $D$  is the diffusion coefficient. The concentration of the diffusing gas in the solid's surface is given by Henry's law:

$$c = Sp \quad (7.4)$$

where  $S$  is the solubility coefficient and  $p$  is the gas pressure. For a one-dimensional flux across the material, and substituting Eq. (7.4) into Eq. (7.3) gives:

$$J = -K \frac{dp}{dx} \quad (7.5)$$

where  $K$ , the permeation constant, which has units of  $(\text{mol m})/(\text{m}^2 \text{ s Pa})$  and is equal to the product of the solubility coefficient,  $S$ , and diffusion coefficient,  $D$ . The permeation constant is multiplied by the differential pressure across the material thickness,  $(dp/dx)$  to give the flux of gas.

The flux of gas is the amount of gas in moles,  $n$ , passing through the material per unit time,  $t$ , and per unit area,  $A$ .

$$J = \frac{n}{tA} \quad (7.6)$$

For a gas, the amount of gas can be expressed in terms of volume,  $V$ , using the ideal gas law as:

$$V = \frac{nRT}{P} \quad (7.7)$$

where  $R$ , is the gas constant and  $T$  is the absolute temperature. Combining Eq. (7.5) to (7.7) gives the average flow velocity,  $v$ , as:

$$v = \frac{V}{tA} = \left(\frac{nRT}{P}\right) \left(\frac{1}{tA}\right) = -\left(\frac{RT}{P}\right) K \frac{dp}{dx} \quad (7.8)$$

or

$$v = -K' \frac{dp}{dx} \quad (7.9)$$

where  $K'$  is the permeation constant in  $(\text{m}^3 \text{ m})/(\text{m}^2 \text{ s Pa})$ . The units of volume in this constant are sometimes expressed at standard temperature and pressure (STP,  $0^\circ\text{C}$  and 1 atm).

Another common unit for expressing the permeation constant can be obtained by the product of the average flow velocity and the dynamic viscosity,  $\mu$ , of the gas as:

$$v\mu = -k' \frac{dp}{dx} \quad (7.10)$$

where  $k'$  is the apparent permeation constant in  $\text{m}^2$ . Eq. (7.10) is known as the Darcy's equation where  $k'$  takes into account the gas as the permeation fluid instead of a compressible fluid [127, 128].

In summary, the three major forms of the permeability constant found in the literature are expressed in terms of Eq. (7.5), (7.9) and (7.10). By comparing these equations, the following relationship is obtained:

$$K' = \left(\frac{RT}{P}\right) K = \frac{k'}{\mu} \quad (7.11)$$

### 7.2.2. High Temperature Helium Permeation in $\text{Ti}_3\text{SiC}_2$ , $\text{Ti}_3\text{AlC}_2$ , and $\text{Ti}_2\text{AlC}$

Results for the He permeability performed at 850°C and 950°C for the three MAX phases,  $\text{Ti}_2\text{AlC}$ ,  $\text{Ti}_3\text{AlC}_2$  and  $\text{Ti}_3\text{SiC}_2$ , are shown in Table 7.3, showing the permeability values based on Eq. (7.5) and Eq. (7.9). The results in terms of Darcy's permeability coefficient, Eq. (7.10), are presented in Table 7.4. The dynamic viscosity for He used with Eq. (7.11) were  $5.16 \times 10^{-5}$  and  $5.56 \times 10^{-5}$  kg/(m s) at 850°C and 950°C, respectively [129].

In general, the results from the three materials show that the permeability at a constant temperature of 850°C or 950°C decreases for the material type as follows:  $\text{Ti}_2\text{AlC} > \text{Ti}_3\text{SiC}_2 > \text{Ti}_3\text{AlC}_2$  by about 1 order of magnitude difference. Also, the He permeability increased from 850°C to 950°C by 15.5%, 30.2%, and 35.3% for  $\text{Ti}_2\text{AlC}$ ,  $\text{Ti}_3\text{SiC}_2$ , and  $\text{Ti}_3\text{AlC}_2$ , respectively.



Table 7.3 Permeability of  $Ti_2AlC$ ,  $Ti_3AlC_2$  and  $Ti_3SiC_2$  at 850°C and 950°C.

Sample	Permeability (K)			
	(mol m)/(m <sup>2</sup> s Pa)		(m <sup>3</sup> (STP)m/(m <sup>2</sup> s Pa)	
	850 °C	950 °C	850 °C	950 °C
$Ti_2AlC$	$1.72 \times 10^{-7}$	$1.99 \times 10^{-7}$	$3.87 \times 10^{-9}$	$4.46 \times 10^{-9}$
$Ti_3SiC_2$	$4.48 \times 10^{-8}$	$5.83 \times 10^{-8}$	$1.00 \times 10^{-9}$	$1.31 \times 10^{-9}$
$Ti_3AlC_2$	$6.05 \times 10^{-9}$	$8.18 \times 10^{-9}$	$1.36 \times 10^{-10}$	$1.83 \times 10^{-10}$

Table 7.4 Equivalent Darcy's permeability coefficient of  $Ti_2AlC$ ,  $Ti_3AlC_2$  and  $Ti_3SiC_2$  at 850°C and 950°C.

Sample	Equivalent Darcy's Permeability Coefficient(k')	
	(m <sup>2</sup> )	
	850 °C	950 °C
$Ti_2AlC$	$8.20 \times 10^{-13}$	$1.00 \times 10^{-12}$
$Ti_3SiC_2$	$2.13 \times 10^{-13}$	$2.93 \times 10^{-13}$
$Ti_3AlC_2$	$2.88 \times 10^{-14}$	$4.11 \times 10^{-14}$

### 7.2.3. Comparison with Other Ceramics

The permeability results for the MAX phase materials tested show values of what would be expected for sintered samples. For example, Pulkrabek *et al.* [127, 128] measured the apparent permeability,  $k'$ , of He through alumina over an extended temperature range (Figure 7.7). The results from this figure for He permeation at 850°C and 950°C were compared with values for the MAX phases (Figure 7.8). This comparison shows that the He

permeability of the MAX phases tested is about the same order of magnitude as the He permeability of alumina at the same temperatures.

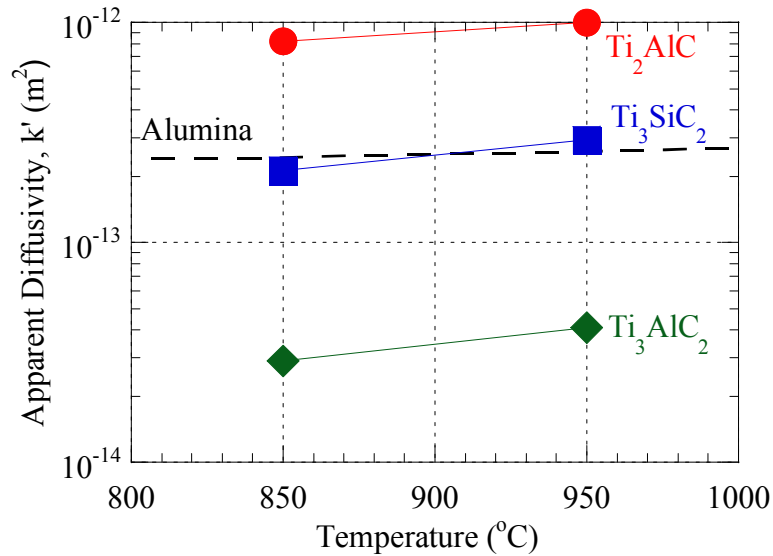


Figure 7.7 Apparent diffusivity,  $k'$ , of He in  $\text{Ti}_3\text{SiC}_2$ ,  $\text{Ti}_3\text{AlC}_2$ , and  $\text{Ti}_2\text{AlC}$  compared to Alumina [128].

The results for permeability,  $K$ , also compare well with various SiC/SiC fiber composites investigated for fusion reactor applications [130]. At  $1.83 \times 10^{-10} \text{ m}^2/\text{s}$  for  $\text{Ti}_3\text{AlC}_2$  and  $4.46 \times 10^{-9} \text{ m}^2/\text{s}$  for  $\text{Ti}_2\text{AlC}$ , the permeability constants for the MAX phases at 950 °C were similar to the room temperature permeability of fully dense SiC/SiC woven fiber plates, fabricated via liquid phase sintering and HPing, ranging from  $4.0 \times 10^{-11}$  to  $1.0 \times 10^{-9} \text{ m}^2/\text{s}$  [130]. This result indicates a considerable advantage of reduced permeability compared to SiC parts designed for fusion reactors, as permeability of those parts would increase with increasing temperatures

### 7.3. Conclusions

---

Based on these results, it is clear that at temperatures in excess of 1000 °C a diffusion bond can be formed between  $\text{Ti}_3\text{SiC}_2$  or  $\text{Ti}_2\text{AlC}$  and Zr-4. Below that temperature, bonding was unsuccessful. For fuel cladding applications, this bodes well for the MAX phases to be used as a coating to improve safety performance of fuel rods. While not explored in this thesis, methods of applying a coating of  $\text{Ti}_3\text{SiC}_2$  or  $\text{Ti}_2\text{AlC}$  have been investigated, including thermal spray and cold spray techniques. These methods make use of mechanical bonding of MAX particles to a rough Zr-4 surface. During normal operation, at temperatures ranging from 300-500 °C, the MAX coating would provide mechanical impact protection, while allowing for thermal conduction of heat generated in the fuel pellets. During an accident condition, where coolant may be lost, the fuel rods can heat up to temperatures in excess of 1200 C, and be exposed to steam. The rapid oxidation of the Zr-4 rods leads to hydrogen production, which can diffuse into the cladding and form brittle zirconium hydrides, weakening the Zr-4, not to mention also collecting in the reactor vessels and become an explosion hazard. By forming a hermetically sealed coating of  $\text{Ti}_3\text{SiC}_2$  or  $\text{Ti}_2\text{AlC}$ , which would provide advanced oxidation resistance, there is potential for improving the safety tolerances of fuel cladding, increasing the length of time before cladding failure. The difference between minutes and hours for emergency response before fuel cladding failure during LOCA events could prove incredibly beneficial.

He permeability tests were performed at 850°C and 950°C for three MAX phase material samples:  $\text{Ti}_2\text{AlC}$ ,  $\text{Ti}_3\text{AlC}_2$  and  $\text{Ti}_3\text{SiC}_2$ . At constant temperature, the He permeability decreases for the material type as follows:  $\text{Ti}_2\text{AlC} > \text{Ti}_3\text{SiC}_2 > \text{Ti}_3\text{AlC}_2$  about 1 order of magnitude difference between each value. These materials showed between 15.5% and 35.3% increase in the He permeability at 950°C as compared to their respective

permeabilities at 850°C. These He permeability results are comparable to those in literature for alumina at similar temperatures, and show the same order of magnitude of permeability at high temperatures as room temperature measurements in SiC/SiC composites. These results indicate a significant ability for these MAX phases to contain and limit the transport of He through bulk.

## 8. GENERAL CONCLUSIONS AND PERSPECTIVES

---

### 8.1. Principle Discoveries

---

The main objective of this thesis was to study the behavior of select MAX phases in response to neutron irradiation. To this end, we chose to irradiate several MAX phase chemistries, and characterize them as a function of irradiation dose and temperature using X-ray diffraction, XRD, and transmission electron microscopy, TEM. Rietveld refinement analysis of the post-irradiation XRD patterns was conducted to document the structural and compositional changes due to irradiation. TEM was utilized to explore the nanoscale morphology and nature of defects induced by irradiation. Further, electrical resistivity and nanoindentation experiments were explored to understand the effect of irradiation on properties.

Neutron irradiation of hot pressed polycrystalline samples of  $\text{Ti}_3\text{SiC}_2$ ,  $\text{Ti}_3\text{AlC}_2$ ,  $\text{Ti}_2\text{AlC}$ , and  $\text{Ti}_2\text{AlN}$  was successfully completed at MITR and INL ATR, with exposures ranging from 0.1-9 dpa and irradiation temperatures of 100 to 1000 °C. This thesis marks the first ever neutron irradiation of bulk MAX phases.

Rietveld refinement of XRD patterns revealed that all phases studied remained crystalline - and were thus resistant to amorphization- after irradiation to doses of 0.1 to 0.4 dpa at 350 and 710 °C. Additionally,  $\text{Ti}_3\text{SiC}_2$  retained its crystallinity after neutron irradiation to a dose of 9 dpa at a temperature of 500 °C.

After irradiation to 0.1 and 0.4 dpa at 350 °C, the c-LPs increased, while the a-LPs decreased.  $\text{Ti}_3\text{SiC}_2$ , with near identical LP values for both fine-grained (FG) and coarse-

grained (CG), showed the least distortion in LPs. Refinement of the XRD patterns also revealed an increase in microstrains in the samples irradiated to 0.1 dpa at 350 °C. The microstrains were seen to further increase when the dpa was increased to 0.4 at the same temperature. These results indicate that defects induced upon exposure to low temperature irradiation resulted in a global distortion of the crystal lattice of each phase. Furthermore, the  $\text{Ti}_3\text{AlC}_2$  and  $\text{Ti}_2\text{AlN}$  phases exhibited an unacceptable level of phase decomposition, forming significant fractions of  $\text{TiC}$  or  $\text{TiN} + \text{Ti}_4\text{AlC}_3$ , respectively, after irradiations as low as 0.1 dpa at 350 °C. As a result, it was concluded that their future as possible fuel cladding materials is dim. The focus then shifted to  $\text{Ti}_3\text{SiC}_2$  and  $\text{Ti}_2\text{AlC}$ , both of which showed compositional stability up to 0.4 dpa at 350 °C, meriting further study.

After irradiation at 710 °C, the LPs were close to the unirradiated values for all irradiated samples, one exception being  $\text{Ti}_2\text{AlN}$  due its decomposition. Microstrains also diminished at this temperature. These results indicate that after irradiation at higher temperatures, some of the point defects presumably anneal out or agglomerate into larger coherent structures, reducing overall lattice strains and distortions.

Based on the TEM micrographs, it was concluded that neutron irradiation resulted in the formation of defect clusters and dislocation loops. Defect clusters were observed in  $\text{Ti}_2\text{AlC}$  after irradiation to 0.1 dpa at 350 °C and in both  $\text{Ti}_2\text{AlC}$  and FG- $\text{Ti}_3\text{SiC}_2$  after 0.4 dpa at 350 °C. Dislocation loops were observed in both materials after irradiation to 0.1 dpa at 710 °C. At  $1 \times 10^{23}$  loops/ $\text{m}^3$ , the loop density in  $\text{Ti}_2\text{AlC}$  was 1.5 orders of magnitude greater than that observed in FG- $\text{Ti}_3\text{SiC}_2$ , at  $3 \times 10^{21}$  loops/ $\text{m}^3$ . Based on these results, it is reasonable to conclude that  $\text{Ti}_3\text{SiC}_2$  is more resistant to neutron irradiation damage, at least in terms of loop density. Through extensive TEM tilting experiments, the dislocation loops were found to have a Burgers vector  $\mathbf{b} = \frac{1}{2} [0001]$ , and thus lie in the basal planes. The average loop diameters were 9(3) nm and 10(5) nm, for FG- $\text{Ti}_3\text{SiC}_2$  and  $\text{Ti}_2\text{AlC}$ , respectively. Irradiation

of  $\text{Ti}_3\text{SiC}_2$  at 500 °C, up to 1 and 9 dpa, resulted in larger dislocation loops, with average diameters of 21(6) and 30(8) nm, respectively. The dislocation loops densities decreased from  $5 \times 10^{20}$  loops/ $\text{m}^3$  at 1 dpa to  $2 \times 10^{20}$  loops/ $\text{m}^3$  at 9 dpa, indicating that loop coarsening occurred with increased dose. Also of note, after irradiation to 9 dpa at 500 °C, denuded zones approaching 1  $\mu\text{m}$  in width were observed next to most grain boundaries in  $\text{Ti}_3\text{SiC}_2$ . This suggests that the combination of A-layers and grain boundaries in  $\text{Ti}_3\text{SiC}_2$  serve as potent defect sinks. This result is quite remarkable, and is in need of further study to understand.

In light of the XRD and TEM results, and by incorporating recent DFT calculations of point defects in the MAX phases, we propose a model that can explain the evolution of the distorted lattice structures after irradiation. From DFT studies, the presence of the A-layers in the MAX phases was predicted to provide a significant radiation tolerance, due to the low formation energy and stability of point defects residing in, and near, the A-layers. In order to account for the observed distortion of lattice parameters, the low temperature structure model assumes the formation of excess X vacancies in the  $\text{M}_{n+1}\text{X}_n$  blocks accompanied by A or M interstitials in the free volume sites between the A and M layers. As neutron irradiation is known to produce drastic localized disorder of atoms during cascade events, it is not implausible that these defects could form.

The high temperature irradiation resulted in larger defect structures, coherent with the lattice. TEM micrographs confirmed that the interstitial atoms precipitated as interstitial dislocation loops between the A and M layers, or potentially as platelets of  $\text{M}_A$  antisite defects within the A-layer. Defects of this nature, i.e. within the basal planes, were observed in samples irradiated to all doses at 500 and 710 °C. Additional studies are needed to fully characterize the composition of the loops that form, however. What is surprising, however, is that the loops were predominately interstitial in nature. As the concentration of vacancies

and interstitials are presumably equal, more work is required to understand the propensity of interstitial loops to form over vacancy type loops.

Furthermore, these results confirmed the ability of the A-layers to accommodate defects while maintaining crystallinity. This was indisputably evidenced by the fact that TiC and alumina impurity particles showed extensive irradiation damage, directly adjacent to relatively undamaged grains of  $\text{Ti}_3\text{SiC}_2$ .

To assess the effect of the irradiation defects described above on material properties, measurements of electrical resistivity, hardness and modulus were conducted. The results further illustrate the high temperature recoverability of MAX phases. Resistivity values were seen to increase with irradiation at 350 °C, for the most part linearly with dose, with  $\text{Ti}_3\text{SiC}_2$  showing saturation at 0.4 dpa. Point defects are potent scatterers of electrons, and the TEM results confirm that low temperature irradiation resulted in the formation of point defect clusters. After irradiation at 710 °C, however, the resistivity values recovered almost fully, presumably due to the fact that the dislocation loops were coherent and thus having less of an impact on electron transport. Additionally, black spots and/or defect clusters were not observed in the presence of the dislocation loops, therefore it is reasonable to conclude that the former are transformed into the latter. It is known that in most MAX phases, a majority (>90% in  $\text{Ti}_3\text{SiC}_2$ ) of the thermal conductivity is due to electron transport. Said otherwise, electrical resistivity is a good measure of the magnitude of the thermal conductivity. It follows that the possible saturation and recovery in electrical resistivity for  $\text{Ti}_3\text{SiC}_2$  bodes well for its use in any nuclear application where thermal transport is important. This is in sharp contrast to SiC, wherein the thermal conductivity is sharply reduced with small irradiation doses.

Nanoindentation results for FG- $\text{Ti}_3\text{SiC}_2$  and  $\text{Ti}_2\text{AlC}$  provided evidence for irradiation induced hardening, which was expected for the irradiated materials. The Young's moduli



were quite low, however, and most probably due to the formation of microcracks. The latter were quite profuse throughout the  $\text{Ti}_2\text{AlC}$  samples irradiated to 0.1 and 0.4 dpa at 350 °C.

Lastly, the interactions of select MAX phases with Zircaloy-4, Zr-4, and helium, He, gas were investigated to assess their compatibility with reactor components. Zr-4 is a common fuel cladding material used in current reactors, and He is a proposed Gen IV coolant, as well as a fission reaction product. With the possibility of using MAX phases as a protective coating for existing cladding, the diffusion bonding of Zr-4 to  $\text{Ti}_3\text{SiC}_2$  and  $\text{Ti}_2\text{AlC}$  was studied to understand what would happen under LOCA conditions. Results over a temperature range from 1100 to 1300 °C showed extensive diffusion of the A-layer elements into Zr-4 which led to the formation of several intermetallic layers. Overall, diffusion depths from  $\text{Ti}_3\text{SiC}_2$  were an order of magnitude shallower than  $\text{Ti}_2\text{AlC}$  at 1100 and 1200 °C, and 5-7 times shallower at 1300 °C. The bonds were strong between Zr-4 and  $\text{Ti}_3\text{SiC}_2$ , but quite weak for the  $\text{Ti}_2\text{AlC}$  couples. As these temperatures are well above the normal operating temperature for conventional reactors, as well as the typical Zr-4 heat treatment temperatures, bonding of the MAX phases to the Zr-4 substrate would need to rely on other means for adhesion. One possible solution would be to cold spray a MAX coating, which adheres by mechanical deformation of the sprayed powder. During accident conditions, however, temperatures can easily exceed those studied here. Thus, it is likely that this enhanced diffusion at high temperatures will improve the bonding of the MAX layer to the Zr-4 substrate, and help provide extended oxidation and impact resistance. Ideally, this would increase the available response time for emergency action before fuel containment failure would occur.

He permeability in  $\text{Ti}_3\text{SiC}_2$ ,  $\text{Ti}_2\text{AlC}$  and  $\text{Ti}_3\text{AlC}_2$ , at temperatures of 850 and 950 °C, was found to be comparable to other sintered ceramics, and was similar to room temperature permeability of SiC/SiC fiber composites. This indicates that He transport is quite limited

through the MAX phases at high temperatures, showing promise for these ceramics to contain gaseous fission products.

The work presented in this thesis, all of which being the first of its kind, is only a preliminary study of select MAX phase behavior under neutron irradiation. These results represent the start of the foundation for the knowledge base of neutron irradiation response in the MAX phases, and provide the necessary groundwork for future studies. These results highlight the need for characterization of the systematic effect of the irradiation over larger temperature and dose ranges. Notably, what critical irradiation temperature is required to form dislocation loops, and what dependence chemistry or grain size may have on this transition point, remains unknown. The samples studied here are part of a larger family of similarly structured phases. As such, the damage tolerance might be optimized through compositional and structural tuning. The results of this work also hint to the effects of grain size on damage tolerance, seeing a lesser increase in resistivity for the fine-grained samples as compared to their coarse-grained counterparts, and thus demonstrate the need to characterize future samples with systematic grain size variations. With denuded zones approaching 1  $\mu\text{m}$  in width, which appear to be isotropic regardless of grain boundary orientation, it would not be unexpected to see quite limited irradiation damage in very fine grained samples. Of all phases studied herein,  $\text{Ti}_3\text{SiC}_2$  has shown the greatest potential for use in reactor applications, and warrants further study.

## 8.2. Future Work

---

Following this work, it is pragmatic to mention some potential paths forward. The following areas deserve particular attention.

With regret, analysis of mechanical properties was unobtainable for this work. Before MAX phases can be considered for incorporation into irradiation applications, the effect of irradiation on mechanical properties such as modulus, strength, fracture toughness, hardness, and creep should be investigated thoroughly. Additionally, the statistical variation in these properties, using Weibull statistics, is commonly expected for ceramic materials in the nuclear field, and should thus be incorporated. It is imperative that correlations be made between the defects observed herein with mechanical properties, which can be explored in future research projects.

As described in Chapter 5, this work shows evidence for irradiation defects, i.e. dislocation loops, which have not been previously observed in the MAX phases. Those previous irradiation studies used a wide variety of irradiation particles, and the majority of these studies were conducted at room temperature. Calculations using the theories developed for equivalent dose comparison suggest that to obtain microstructures similar to the ones obtained here would require higher temperature ion irradiation studies than reported to date. Understanding of the neutron irradiation response is necessary before these materials can be incorporated into reactor components. However, access to neutron irradiation is limited, time consuming, and costly, not to mention that the resultant test samples become radioactive, requiring extensive protective measures during characterization. Ion irradiation studies, as surrogate radiation particles, are vastly easier to conduct and characterize. Therefore, it is imperative that future studies attempt to adjust and refine their conditions to more closely match those induced by neutrons in these materials.

Lastly, it should be stated that further theoretical simulations can always be beneficial. DFT models are quite capable of predicting point defect structures. Neutron irradiation, however, results in significant interactions between defects, on a much larger scale. Molecular dynamics, MD, is capable of modeling and predicting defect structures on the scale of

irradiation defects, and should thusly be explored. It is understood, however, that the MAX phase structure is quite complex, in terms of MD. Future work will have to begin by generating the necessary potentials used for MD, as they currently, as far as I know, do not exist for the MAX phases. The results in this thesis could then be used as possible computational starting points in an effort to model the formation of dislocation loops in these remarkable ceramics.

## REFERENCES

- [1] D.J. Tallman, E.N. Hoffman, E.a.N. Caspi, B.L. Garcia-Diaz, G. Kohse, R.L. Sindelar, M.W. Barsoum. Effect of neutron irradiation on select MAX phases, *Acta Mater.* 85 (2015) 132-143.
- [2] E.N. Hoffman, D.W. Vinson, R.L. Sindelar, D.J. Tallman, G. Kohse, M.W. Barsoum. MAX phase carbides and nitrides: Properties for future nuclear power plant in-core applications and neutron transmutation analysis, *Nucl. Eng. Des.* 244 (2012) 17-24.
- [3] M.K. Patel, D.J. Tallman, J.A. Valdez, J. Aguiar, O. Anderoglu, M. Tang, J. Griggs, E. Fu, Y. Wang, M.W. Barsoum. Effect of helium irradiation on  $Ti_3AlC_2$  at 500 °C, *Scripta Mater.* 77 (2014) 1-4.
- [4] D.J. Tallman, B. Anasori, M.W. Barsoum. A Critical Review of the Oxidation of  $Ti_2AlC$ ,  $Ti_3AlC_2$  and  $Cr_2AlC$  in Air, *Mater. Res. Let.* 1 (2013) 115-125.
- [5] D.J. Tallman, M. Naguib, B. Anasori, M.W. Barsoum. Tensile creep of  $Ti_2AlC$  in air in the temperature range 1000–1150 °C, *Scripta Mater.* 66 (2012) 805-808.
- [6] D.J. Tallman, J. Yang, L. Pan, B. Anasori, M.W. Barsoum. Reactivity of Zircaloy-4 with  $Ti_3SiC_2$  and  $Ti_2AlC$  in the 1100–1300 °C temperature range, *J. Nucl. Mater.* 460 (2015) 122-129.
- [7] D.J. Tallman, L. He, B.L. Garcia-Diaz, E.N. Hoffman, R.L. Sindelar, M.W. Barsoum. Effect of Neutron Irradiation on Defect Evolution in  $Ti_3SiC_2$  and  $Ti_2AlC$ , *J. Nucl. Mater.* (Accepted) (2015).
- [8] T. Abram, S. Ion. Generation-IV nuclear power: A review of the state of the science, *Energy Policy* 36 (2008) 4323-4330.
- [9] L.K. Mansur, A.F. Rowcliffe, R.K. Nanstad, S.J. Zinkle, W.R. Corwin, R.E. Stoller. Materials needs for fusion, Generation IV fission reactors and spallation neutron sources – similarities and differences, *J. Nucl. Mater.* 329-333, Part A (2004) 166-172.
- [10] U.S. DOE. A Technology Roadmap for Generation IV Nuclear Energy Systems. In: Forum USDNERACatGII, (Ed.), 2002.
- [11] S.J. Zinkle, J.T. Busby. Structural materials for fission & fusion energy, *Materials Today* 12 (2009) 12-19.
- [12] K. Minato, T. Ogawa, K. Fukuda, M. Shimizu, Y. Tayama, I. Takahashi. Fission product behavior in Triso-coated  $UO_2$  fuel particles, *J. Nucl. Mater.* 208 (1994) 266-281.
- [13] W. Schenk, G. Pott, H. Nabielek. Fuel accident performance testing for small HTRs, *J. Nucl. Mater.* 171 (1990) 19-30.
- [14] L.L. Snead, T. Nozawa, Y. Katoh, T.-S. Byun, S. Kondo, D.A. Petti. Handbook of SiC properties for fuel performance modeling, *J. Nucl. Mater.* 371 (2007) 329-377.
- [15] C.R.F. Azevedo. Selection of fuel cladding material for nuclear fission reactors, *Engineering Failure Analysis* 18 (2011) 1943-1962.

- [16] G.S. Was, T. Allen. Radiation-induced segregation in multicomponent alloys: Effect of particle type, *Materials Characterization* 32 (1994) 239-255.
- [17] G.S. Was. *Fundamentals of radiation materials science: metals and alloys*, Springer, 2007.
- [18] D. Hull, D.J. Bacon. Chapter 6 - Dislocations in Other Crystal Structures. in: Hull D, Bacon DJ, (Eds.). *Introduction to Dislocations (Fifth Edition)*. Butterworth-Heinemann, Oxford, 2011. pp. 109-136.
- [19] B.F. Gromov, Y.S. Belomitcev, E.I. Yefimov, M.P. Leonchuk, P.N. Martinov, Y.I. Orlov, D.V. Pankratov, Y.G. Pashkin, G.I. Toshinsky, V.V. Chekunov, B.A. Shmatko, V.S. Stepanov. Use of lead-bismuth coolant in nuclear reactors and accelerator-driven systems, *Nucl. Eng. Des.* 173 (1997) 207-217.
- [20] J.H. Kim, H.J. Ryu, J.H. Baek, S.J. Oh, B.O. Lee, C.B. Lee, Y.S. Yoon. Performance of a diffusion barrier under a fuel-clad chemical interaction (FCCI), *J. Nucl. Mater.* 394 (2009) 144-150.
- [21] H.J. Ryu, B.O. Lee, S.J. Oh, J.H. Kim, C.B. Lee. Performance of FCCI barrier foils for U-Zr-X metallic fuel, *J. Nucl. Mater.* 392 (2009) 206-212.
- [22] K.R. Whittle, M.G. Blackford, R.D. Aughterson, S. Moricca, G.R. Lumpkin, D.P. Riley, N.J. Zaluzec. Radiation tolerance of  $M_{n+1}AX_n$  phases,  $Ti_3AlC_2$  and  $Ti_3SiC_2$ , *Acta Mater.* 58 (2010) 4362-4368.
- [23] G. Roma. Palladium in cubic silicon carbide: Stability and kinetics, *J. Appl. Phys.* 106 (2009) 123504.
- [24] P. Demkowicz, K. Wright, J. Gan, D. Petti. High temperature interface reactions of TiC, TiN, and SiC with palladium and rhodium, *Solid State Ionics* 179 (2008) 2313-2321.
- [25] M.W. Barsoum. *MAX Phases: Properties of Machinable Carbides and Nitrides*, Wiley VCH GmbH & Co. , 2013.
- [26] H. Nowotny. Strukturchemie Einiger Verbindungen der Übergangsmetalle mit den elementen C, Si, Ge, Sn, *Prog. Solid State Chem.* 2 (1970) 27-70.
- [27] M.W. Barsoum, B. Houg. Transient Plastic Phase Processing of Titanium-Boron-Carbon Composites, *JOM* 76 (1993) 1445-1451.
- [28] M.W. Barsoum. The  $M_{n+1}AX_n$  Phases and their Properties. in: Riedel R, I.-W. Chen, (Ed.). *Ceramics Science and Technology*. Wiley-VCH Verlag GmbH & Co. KGaA, Weinheim, German, 2010. pp. 299-347.
- [29] M.W. Barsoum, T. El-Raghy. Room-temperature ductile carbides, *Metall. Mater. Trans. A* 30 (1999) 363-369.
- [30] M. Radovic, M.W. Barsoum, T. El-Raghy, J. Seidensticker, S. Wiederhorn. Tensile properties of  $Ti_3SiC_2$  in the 25-1300 °C temperature range, *Acta Mater.* 48 (2000) 453-459.
- [31] M. Radovic, M.W. Barsoum, T. El-Raghy, S.M. Wiederhorn, W.E. Luecke. Effect of temperature, strain rate and grain size on the mechanical response of  $Ti_3SiC_2$  in tension, *Acta Mater.* 50 (2002) 1297-1306.

- [32] M.W. Barsoum, M. Radovic, P. Finkel, T. El-Raghy.  $\text{Ti}_3\text{SiC}_2$  and ice, *Appl. Phys. Lett.* 79 (2001) 479-481.
- [33] M.W. Barsoum, M. Radovic. Mechanical Properties of the MAX Phases. in: Buschow KHJ, Robert WC, Merton CF, Bernard I, Edward JK, Subhash M, Patrick V, (Eds.). *Encyclopedia of Materials: Science and Technology*. Elsevier, Oxford, 2004. pp. 1-16.
- [34] T. Alam, M.K. Khan, M. Pathak, K. Ravi, R. Singh, S.K. Gupta. A review on the clad failure studies, *Nucl. Eng. Des.* 241 (2011) 3658-3677.
- [35] T.R. Allen, R.J.M. Konings, A.T. Motta. 5.03 - Corrosion of Zirconium Alloys. in: Konings RJM, (Ed.). *Comprehensive Nuclear Materials*. Elsevier, Oxford, 2012. pp. 49-68.
- [36] P. Berger, R. El Tahhann, G. Moulin, M. Viennot. High temperature oxidation of zirconium and zircaloy-4 under applied load: Nuclear microprobe study of the growth of the oxide, *Nuclear Instruments and Methods in Physics Research Section B: Beam Interactions with Materials and Atoms* 210 (2003) 519-525.
- [37] M.W. Barsoum, T. El-Raghy, L.U.J.T. Ogbuji. Oxidation Of  $\text{Ti}_3\text{SiC}_2$  in Air, *J. Electrochem. Soc.* 144 (1997) 2508-2516.
- [38] M.W. Barsoum. Oxidation of  $\text{Ti}_{n+1}\text{AlX}_n$  ( $n=1-3$  and  $X= C, N$ ): I. Model, *J. Electrochem. Soc.* 148 (2001) C544-C550.
- [39] M.W. Barsoum, N. Tzenov, A. Procopio, T. El-Raghy, M. Ali. Oxidation of  $\text{Ti}_{n+1}\text{AlX}_n$  ( $n= 1-3$  and  $X= C, N$ ): II. Experimental Results, *J. Electrochem. Soc.* 148 (2001) C551-C562.
- [40] M.W. Barsoum. Long Time Oxidation Study of  $\text{Ti}_3\text{SiC}_2$ ,  $\text{Ti}_3\text{SiC}_2/\text{SiC}$ , and  $\text{Ti}_3\text{SiC}_2/\text{TiC}$  Composites in Air, *J. Electrochem. Soc.* 150 (2003) B166-B175.
- [41] X.H. Wang, Y.C. Zhou. Oxidation behavior of  $\text{Ti}_3\text{AlC}_2$  at 1000-1400 °C in air, *Corrosion Science* 45 (2003) 891-907.
- [42] X.H. Wang, Y.C. Zhou. High-Temperature Oxidation Behavior of  $\text{Ti}_2\text{AlC}$  in Air, *Oxidation of Metals* 59 (2003) 303-320.
- [43] D.B. Lee, T.D. Nguyen, J.H. Han, S.W. Park. Oxidation of  $\text{Cr}_2\text{AlC}$  at 1300 °C in air, *Corrosion Science* 49 (2007) 3926-3934.
- [44] D.B. Lee, T.D. Nguyen. Cyclic oxidation of  $\text{Cr}_2\text{AlC}$  between 1000 and 1300 °C in air, *Journal of Alloys and Compounds* 464 (2008) 434-439.
- [45] G.M. Song, Y.T. Pei, W.G. Sloof, S.B. Li, J.T.M. De Hosson, S. van der Zwaag. Oxidation-induced Crack Healing in  $\text{Ti}_3\text{AlC}_2$  Ceramics, *Scripta Mater.* 58 (2008) 13-16.
- [46] B. Cui, D.D. Jayaseelan, W.E. Lee. Microstructural evolution during high-temperature oxidation of  $\text{Ti}_2\text{AlC}$  ceramics, *Acta Mater.* 59 (2011) 4116-4125.
- [47] S. Basu, N. Obando, A. Gowdy, I. Karaman, M. Radovic. Long-Term Oxidation of  $\text{Ti}_2\text{AlC}$  in Air and Water Vapor at 1000-1300 °C Temperature Range, *J. Electrochem. Soc.* 159 (2012) C90-C96.
- [48] S. Li, L. Xiao, G. Song, X. Wu, W.G. Sloof, S. van der Zwaag. Oxidation and Crack Healing Behavior of a Fine-Grained  $\text{Cr}_2\text{AlC}$  Ceramic, *J. Am. Ceram. Soc.* (2013) 892-899.

- [49] M. Steinbrück, J. Birchley, A.V. Boldyrev, A.V. Goryachev, M. Grosse, T.J. Haste, Z. Hózer, A.E. Kisselev, V.I. Nalivaev, V.P. Semishkin, L. Sepold, J. Stuckert, N. Vér, M.S. Veshchunov. High-temperature oxidation and quench behaviour of Zircaloy-4 and E110 cladding alloys, *Progress in Nuclear Energy* 52 (2010) 19-36.
- [50] A. Ganguly, M.W. Barsoum, R.D. Doherty. Interdiffusion Between  $\text{Ti}_3\text{SiC}_2$ – $\text{Ti}_3\text{GeC}_2$  and  $\text{Ti}_2\text{AlC}$ – $\text{Nb}_2\text{AlC}$  Diffusion Couples, *J. Am. Ceram. Soc.* 90 (2007) 2200-2204.
- [51] X.H. Yin, M.S. Li, Y.C. Zhou. Microstructure and mechanical strength of diffusion-bonded  $\text{Ti}_3\text{SiC}_2/\text{Ni}$  joints, *J. Mater. Res.* 21 (2006) 2415-2421.
- [52] H. Dong, S. Li, Y. Teng, W. Ma. Joining of SiC ceramic-based materials with ternary carbide  $\text{Ti}_3\text{SiC}_2$ , *Materials Science and Engineering: B* 176 (2011) 60-64.
- [53] N.F. Gao, Y. Miyamoto. Joining of  $\text{Ti}_3\text{SiC}_2$  with Ti–6Al–4V Alloy, *J. Mater. Res.* 17 (2002) 52-59.
- [54] X.H. Yin, M.S. Li, Y.C. Zhou. Microstructure and mechanical strength of transient liquid phase bonded  $\text{Ti}_3\text{SiC}_2$  joints using Al interlayer, *J. Eur. Ceram. Soc.* 27 (2007) 3539-3544.
- [55] J.F. Li, W. Pan, F. Sato, R. Watanabe. Mechanical properties of polycrystalline  $\text{Ti}_3\text{SiC}_2$  at ambient and elevated temperatures, *Acta Mater.* 49 (2001) 937-945.
- [56] M. Radovic, M.W. Barsoum, T. El-Raghy, S. Wiederhorn. Tensile creep of fine grained (3-5  $\mu\text{m}$ )  $\text{Ti}_3\text{SiC}_2$  in the 1000-1200 °C temperature range, *Acta Mater.* 49 (2001) 4103-4112.
- [57] Y.W. Bao, Y.C. Zhou. Bending Creep and Stress Relaxation of  $\text{Ti}_3\text{AlC}_2$  at High Temperature, *Key Engineering Materials* 280-283 (2005) 1373-1378.
- [58] T. Zhen, M.W. Barsoum, S.R. Kalidindi. Effects of temperature, strain rate and grain size on the compressive properties of  $\text{Ti}_3\text{SiC}_2$ , *Acta Mater.* 53 (2005) 4163-4171.
- [59] T. Zhen, M.W. Barsoum, S.R. Kalidindi, M. Radovic, Z.M. Sun, T. El-Raghy. Compressive creep of fine and coarse-grained  $\text{Ti}_3\text{SiC}_2$  in air in the 1100–1300 °C temperature range, *Acta Mater.* 53 (2005) 4963-4973.
- [60] J.C. Nappé, P. Grosseau, F. Audubert, B. Guilhot, M. Beauvy, M. Benabdesselam, I. Monnet. Damages induced by heavy ions in titanium silicon carbide: Effects of nuclear and electronic interactions at room temperature, *J. Nucl. Mater.* 385 (2009) 304-307.
- [61] J.C. Nappé, C. Maurice, P. Grosseau, F. Audubert, L. Thomé, B. Guilhot, M. Beauvy, M. Benabdesselam. Microstructural changes induced by low energy heavy ion irradiation in titanium silicon carbide, *J. Eur. Ceram. Soc.* 31 (2011) 1503-1511.
- [62] J.C. Nappé, I. Monnet, F. Audubert, P. Grosseau, M. Beauvy, M. Benabdesselam. Formation of nanosized hills on  $\text{Ti}_3\text{SiC}_2$  oxide layer irradiated with swift heavy ions, *Nucl. Instrum. Meth. B* 270 (2012) 36-43.
- [63] J.C. Nappé, I. Monnet, P. Grosseau, F. Audubert, B. Guilhot, M. Beauvy, M. Benabdesselam, L. Thome. Structural changes induced by heavy ion irradiation in titanium silicon carbide, *J. Nucl. Mater.* 409 (2011) 53-61.



- [64] X.M. Liu, M. Le Flem, J.L. Béchade, I. Monnet. Nanoindentation investigation of heavy ion irradiated  $\text{Ti}_3(\text{Si,Al})\text{C}_2$ , *J. Nucl. Mater.* 401 (2010) 149-153.
- [65] X.M. Liu, M. Le Flem, J.L. Bechade, F. Onimus, T. Cozzika, I. Monnet. XRD investigation of ion irradiated  $\text{Ti}_3\text{Si}_{0.90}\text{Al}_{0.10}\text{C}_2$ , *Nucl. Instrum. Meth. B* 268 (2010) 506-512.
- [66] M. Le Flem, X. Liu, S. Doriot, T. Cozzika, I. Monnet. Irradiation Damage in  $\text{Ti}_3(\text{Si,Al})\text{C}_2$ : a TEM Investigation, *Int. J. Appl. Ceram. Tec.* 7 (2010) 766-775.
- [67] M. Le Flem, I. Monnet. Saturation of irradiation damage in  $(\text{Ti,Zr})_3(\text{Si,Al})\text{C}_2$  compounds, *J. Nucl. Mater.* 433 (2013) 534-537.
- [68] L. Zhang, Q. Qi, L.Q. Shi, D.J. O'Connor, B.V. King, E.H. Kisi, D.K. Venkatachalam. Damage tolerance of  $\text{Ti}_3\text{SiC}_2$  to high energy iodine irradiation, *Appl. Surf. Sci.* 258 (2012) 6281-6287.
- [69] M. Bugnet, T. Cabioch, V. Mauchamp, P. Guérin, M. Marteau, M. Jaouen. Stability of the nitrogen-deficient  $\text{Ti}_2\text{AlN}_x$  MAX phase in  $\text{Ar}^{2+}$ -irradiated  $(\text{Ti,Al})\text{N}/\text{Ti}_2\text{AlN}_x$  multilayers, *J. Mater. Sci.* 45 (2010) 5547-5552.
- [70] J. Xiao, C. Wang, T. Yang, S. Kong, J. Xue, Y. Wang. Theoretical investigation on helium incorporation in  $\text{Ti}_3\text{AlC}_2$ , *Nuclear Instruments and Methods in Physics Research Section B: Beam Interactions with Materials and Atoms* 304 (2013) 27-31.
- [71] C. Wang, T. Yang, S. Kong, J. Xiao, J. Xue, Q. Wang, C. Hu, Q. Huang, Y. Wang. Effects of He irradiation on  $\text{Ti}_3\text{AlC}_2$ : Damage evolution and behavior of He bubbles, *J. Nucl. Mater.* 440 (2013) 606-611.
- [72] J. Rodríguez-Carvajal. Recent advances in magnetic structure determination by neutron powder diffraction, *Physica B* 192 (1993) 55-69.
- [73] H. Rietveld. A profile refinement method for nuclear and magnetic structures, *J. Appl. Crystallogr.* 2 (1969) 65-71.
- [74] J. Rodriguez-Carvajal, M.T. Fernandez-Diaz, J.L. Martinez. Neutron diffraction study on structural and magnetic properties of  $\text{La}_2\text{NiO}_4$ , *J. Phys.-Condens. Mat.* 3 (1991) 3215-3234.
- [75] H.L. Heinisch, L.R. Greenwood, W.J. Weber, R.E. Williford. Displacement damage in silicon carbide irradiated in fission reactors, *J. Nucl. Mater.* 327 (2004) 175-181.
- [76] M.L. Jenkins. Characterisation of radiation-damage microstructures by TEM, *J. Nucl. Mater.* 216 (1994) 124-156.
- [77] K. Iakoubovskii, K. Mitsuishi, Y. Nakayama, K. Furuya. Thickness measurements with electron energy loss spectroscopy, *Microsc. Res. Techniq.* 71 (2008) 626-631.
- [78] ASTM. Standard Test Method for Determining Gas Permeability Characteristics of Plastic Film and Sheeting. ASTM D1434 – 82, 2009.
- [79] J. Xiao, T. Yang, C. Wang, J. Xue, Y. Wang. Investigations on Radiation Tolerance of  $\text{M}_{n+1}\text{AX}_n$  Phases: Study of  $\text{Ti}_3\text{SiC}_2$ ,  $\text{Ti}_3\text{AlC}_2$ ,  $\text{Cr}_2\text{AlC}$ ,  $\text{Cr}_2\text{GeC}$ ,  $\text{Ti}_2\text{AlC}$ , and  $\text{Ti}_2\text{AlN}$ , *J. Am. Ceram. Soc.* 98 (2015) 1323-1331.

- [80] J. Wang, B. Liu, J. Wang, Y. Zhou. Theoretical investigation of thermodynamic stability and mobility of the intrinsic point defects in  $Ti_3AC_2$  ( $A = Si, Al$ ), *Phys. Chem. Chem. Phys.* 17 (2015) 8927-8934.
- [81] S. Zhao, J. Xue, Y. Wang, Q. Huang. First-principles investigation of the intrinsic defects in  $Ti_3SiC_2$ , *J. Phys. Chem. Solids* 75 (2014) 384-390.
- [82] S.C. Middleburgh, G.R. Lumpkin, D. Riley. Accommodation, Accumulation, and Migration of Defects in  $Ti_3SiC_2$  and  $Ti_3AlC_2$  MAX Phases, *J. Am. Ceram. Soc.* 96 (2013) 3196-3201.
- [83] J. Wang, Y. Zhou, T. Liao, J. Zhang, Z. Lin. A first-principles investigation of the phase stability of  $Ti_2AlC$  with Al vacancies, *Scripta Mater.* 58 (2008) 227-230.
- [84] H.W. Hugosson, P. Korzhavyi, U. Jansson, B. Johansson, O. Eriksson. Phase stabilities and structural relaxations in substoichiometric  $TiC_{1-x}$ , *Phys. Rev. B* 63 (2001) 165116.
- [85] M. Magnuson, J.P. Palmquist, M. Mattesini, S. Li, R. Ahuja, O. Eriksson, J. Emmerlich, O. Wilhelmsson, P. Eklund, H. Högberg, L. Hultman, U. Jansson. Electronic structure investigation of  $Ti_3AlC_2$ ,  $Ti_3SiC_2$ , and  $Ti_3GeC_2$  by soft x-ray emission spectroscopy, *Phys. Rev. B* 72 (2005) 245101.
- [86] L. Farber, M.W. Barsoum, A. Zavaliangos, T. El-Raghy, I. Levin. Dislocations and Stacking Faults in  $Ti_3SiC_2$ , *J. Am. Ceram. Soc.* 81 (1998) 1677-1681.
- [87] S. Kondo, Y. Katoh, L.L. Snead. Analysis of grain boundary sinks and interstitial diffusion in neutron-irradiated SiC, *Phys. Rev. B* 83 (2011) 075202.
- [88] L.K. Mansur. Void swelling in metals and alloys under irradiation: an assessment of the theory, *Nuclear Technology* 40 (1978) 5-34.
- [89] C. Dickerson, Y. Yang, T.R. Allen. Defects and microstructural evolution of proton irradiated titanium carbide, *J. Nucl. Mater.* 424 (2012) 62-68.
- [90] M.W. Barsoum, T. El'Raghy, L. Farber, M. Amer, R. Christini, A. Adams. The Topotactic Transformation of  $Ti_3SiC_2$  into a Partially Ordered Cubic Ti ( $C_{0.67}, Si_{0.06}$ ) Phase by the Diffusion of Si into Molten Cryolite, *J. Electrochem. Soc.* 146 (1999) 3919-3923.
- [91] J. Emmerlich, D. Music, P. Eklund, O. Wilhelmsson, U. Jansson, J.M. Schneider, H. Högberg, L. Hultman. Thermal stability of  $Ti_3SiC_2$  thin films, *Acta Mater.* 55 (2007) 1479-1488.
- [92] M.W. Barsoum, H.I. Yoo, I.K. Polushina, V.Y. Rud', Y.V. Rud', T. El-Raghy. Electrical conductivity, thermopower, and Hall effect of  $Ti_3AlC_2$ ,  $Ti_4AlN_3$ , and  $Ti_3SiC_2$ , *Phys. Rev. B* 62 (2000) 10194-10198.
- [93] T. Scabarozzi, A. Ganguly, J.D. Hettinger, S.E. Lofland, S. Amini, P. Finkel, T. El-Raghy, M.W. Barsoum. Electronic and thermal properties of  $Ti_3Al(C_{0.5}N_{0.5})_2$ ,  $Ti_2Al(C_{0.5}N_{0.5})$ , and  $Ti_2AlN$ , *J. Appl. Phys.* 104 (2008) 73713-73716.
- [94] P. Finkel, J.D. Hettinger, S.E. Lofland, M.W. Barsoum, T. El-Raghy. Magnetotransport properties of the ternary carbide  $Ti_3SiC_2$ : Hall effect, magnetoresistance, and magnetic susceptibility, *Phys. Rev. B* 65 (2001) 035113.

- [95] X.H. Wang, Y.C. Zhou. Microstructure and properties of  $Ti_3AlC_2$  prepared by the solid-liquid reaction synthesis and simultaneous in-situ hot pressing process, *Acta Mater.* 50 (2002) 3143-3151.
- [96] P. Wang, B.-c. Mei, X.-l. Hong, W.-b. Zhou. Synthesis of  $Ti_2AlC$  by hot pressing and its mechanical and electrical properties, *Transactions of Nonferrous Metals Society of China* 17 (2007) 1001-1004.
- [97] L.L. Snead. Limits on irradiation-induced thermal conductivity and electrical resistivity in silicon carbide materials, *J. Nucl. Mater.* 329-333, Part A (2004) 524-529.
- [98] J. Morillo, C.H. de Novion, J. Dural. Neutron and electron radiation defects in titanium and tantalum monocarbides: An electrical resistivity study, *Radiat. Eff.* 55 (1981) 67-77.
- [99] V.N. Lipatnikov, L.V. Zueva, A.I. Gusev, A. Kottar. Disorder-order phase transformations and electrical resistivity of nonstoichiometric titanium carbide, *Phys. Solid State* 40 (1998) 1211-1218.
- [100] M.W. Barsoum, T. El-Raghy, C.J. Rawn, W.D. Porter, H. Wang, E.A. Payzant, C.R. Hubbard. Thermal properties of  $Ti_3SiC_2$ , *J. Phys. Chem. Solids* 60 (1999) 429-439.
- [101] W. Tian, P. Wang, G. Zhang, Y. Kan, Y. Li, D. Yan. Synthesis and thermal and electrical properties of bulk  $Cr_2AlC$ , *Scripta Mater.* 54 (2006) 841-846.
- [102] S. Iikubo, H. Ohtani, M. Hasebe. First-Principles Calculations of the Specific Heats of Cubic Carbides and Nitrides, *MATERIALS TRANSACTIONS* 51 (2010) 574-577.
- [103] M.W. Barsoum, I. Salama, T. El-Raghy, J. Golczewski, H.J. Seifert, F. Aldinger, W.D. Porter, H. Wang. Thermal and electrical properties of  $Nb_2AlC$ ,  $(Ti, Nb)_2AlC$  and  $Ti_2AlC$ , *Metall. Mater. Trans. A* 33 (2002) 2775-2779.
- [104] W.C. Oliver, G.M. Pharr. Measurement of hardness and elastic modulus by instrumented indentation: Advances in understanding and refinements to methodology, *J. Mater. Res.* 19 (2004) 3-20.
- [105] W.C. Oliver, G.M. Pharr. An improved technique for determining hardness and elastic modulus using load and displacement sensing indentation experiments, *J. Mater. Res.* 7 (1992) 1564-1583.
- [106] R.L. Coble, W.D. Kingery. Effect of Porosity on Physical Properties of Alumina, *J. Amer. Cer. Soc.* 39 (1956) 377-385.
- [107] E.A. Dean, J.A. Lopez. Empirical Dependence of Elastic Moduli on Porosity for Ceramic Materials, *J. Am. Ceram. Soc.* 66 (1983) 366-370.
- [108] A.P. Roberts, E.J. Garboczi. Elastic Properties of Model Porous Ceramics, *J. Am. Ceram. Soc.* 83 (2000) 3041-3048.
- [109] J. Zaidi, M. Arif, I. Fatima, S. Ahmed, I. Qureshi. Radiochemical neutron activation analysis of trace impurities in high purity aluminum, *Journal of radioanalytical and nuclear chemistry* 241 (1999) 123-127.

- [110] E.A. Garcia, G. Béranger. Diffusion model for the oxidation of Zircaloy-4 at 400 °C in steam: The influence of metallurgical structure (precipitates and grain size), *J. Nucl. Mater.* 273 (1999) 221-227.
- [111] R. Trache, R. Puschmann, C. Leyens, L.-M. Berger, B. Matthey, M. Herrmann. Thermally Sprayed  $Ti_3SiC_2$  and  $Ti_2AlC$  MAX-Phase Coatings. *Thermal Spray 2013: Proceedings of the International Thermal Spray Conference, 2013.* p.74-78.
- [112] S. Rech, A. Surpi, S. Vezzu, A. Patelli, A. Trentin, J. Glor, J. Frodelius, L. Hultman, P. Eklund. Cold-spray deposition of  $Ti_2AlC$  coatings, *Vacuum* 94 (2013) 69-73.
- [113] H. Gutzmann, F. Gärtner, D. Höche, C. Blawert, T. Klassen. Cold spraying of  $Ti_2AlC$  MAX-phase coatings, *Journal of thermal spray technology* 22 (2013) 406-412.
- [114] J. Frodelius. Thick and thin  $Ti_2AlC$  coatings, (2010).
- [115] K. Barrett, S. Bragg-Sitton, D. Galicki. Advanced LWR Nuclear Fuel Cladding System Development Trade-off Study. INL/EXT-12-27090, INL external report, 2012.
- [116] G.V. Kidson, G.D. Miller. A study of the interdiffusion of aluminum and zirconium, *J. Nucl. Mater.* 12 (1964) 61-69.
- [117] T.M. Yue, H. Xie, X. Lin, H.O. Yang. Phase evolution and dendrite growth in laser cladding of aluminium on zirconium, *Journal of Alloys and Compounds* 509 (2011) 3705-3710.
- [118] A. Laik, K. Bhanumurthy, G.B. Kale. Single-phase diffusion study in  $\beta$ -Zr(Al), *J. Nucl. Mater.* 305 (2002) 124-133.
- [119] H. Okamoto. The Si-Zr (Silicon-Zirconium) system, *Bulletin of Alloy Phase Diagrams* 11 (1990) 513-519.
- [120] N. Bertolino, U. Anselmi-Tamburini, F. Maglia, G. Spinolo, Z.A. Munir. Combustion synthesis of Zr-Si intermetallic compounds, *Journal of Alloys and Compounds* 288 (1999) 238-248.
- [121] W.-l. Gu, Y.-c. Zhou. Reactions between Ti and  $Ti_3SiC_2$  in temperature range of 1273-1573 K, *Transactions of Nonferrous Metals Society of China* 16 (2006) 1281-1288.
- [122] M. Naguib, M. Kurtoglu, V. Presser, J. Lu, J. Niu, M. Heon, L. Hultman, Y. Gogotsi, M.W. Barsoum. Two-Dimensional Nanocrystals Produced by Exfoliation of  $Ti_3AlC_2$ , *Advanced Materials* 23 (2011) 4248-4253.
- [123] T. Wang, Z. Jin, J.-C. Zhao. Thermodynamic assessment of the Al-Zr binary system, *Journal of Phase Equilibria* 22 (2001) 544-551.
- [124] H.J. Yang, Y.T. Pei, J.C. Rao, J.T.M. De Hosson. Self-healing performance of  $Ti_2AlC$  ceramic, *J. Mater. Chem.* 22 (2012) 8304-8313.
- [125] S. Li, G. Song, K. Kwakernaak, S. van der Zwaag, W.G. Sloof. Multiple crack healing of a  $Ti_2AlC$  ceramic, *J. Eur. Ceram. Soc.* 32 (2012) 1813-1820.
- [126] T. El'Raghy, M.W. Barsoum. Diffusion kinetics of the carburization and silicidation of  $Ti_3SiC_2$ , *J. Appl. Phys.* 83 (1998) 112-119.

- [127] W.W. Pulkrabek, W.E. Ibele. The effect of temperature on the permeability of a porous material, *International Journal of Heat and Mass Transfer* 30 (1987) 1103-1109.
- [128] W.W. Pulkrabek, R.M. Wabrek, W.E. Ibele. The Permeability of Alumina over an Extended Temperature Range, *International Journal of Thermophysics* 11 (1990) 251-258.
- [129] C.L. Yaws. *Yaws' Handbook of Properties of the Chemical Elements*, Knovel, 2011.
- [130] Y. Hirohata, T. Jinushi, Y. Yamauchi, M. Hashiba, T. Hino, Y. Katoh, A. Kohyama. Gas permeability of SiC/SiC composites as fusion reactor material, *Fusion Engineering and Design* 61–62 (2002) 699-704.
- [131] M. Sundberg, G. Malmqvist, A. Magnusson, T. El-Raghy. Alumina forming high temperature silicides and carbides, *Ceramics International* 30 (2004) 1899-1904.
- [132] J. Byeon, J. Liu, M. Hopkins, W. Fischer, N. Garimella, K. Park, M. Brady, M. Radovic, T. El-Raghy, Y. Sohn. Microstructure and Residual Stress of Alumina Scale Formed on Ti<sub>2</sub>AlC at High Temperature in Air, *Oxidation of Metals* 68 (2007) 97-111.
- [133] X.H. Wang, Y.C. Zhou. Layered Machinable and Electrically Conductive Ti<sub>2</sub>AlC and Ti<sub>3</sub>AlC<sub>2</sub> Ceramics: a Review, *J. Mater. Sci. Technol.* 26 (2010) 385-416.
- [134] X. Qian, X.D. He, Y.B. Li, Y. Sun, H. Li, D.L. Xu. Cyclic oxidation of Ti<sub>3</sub>AlC<sub>2</sub> at 1000–1300 °C in air, *Corr. Science* 53 (2011) 290-295.
- [135] D.B. Lee, S.W. Park. High-temperature oxidation of Ti<sub>3</sub>AlC<sub>2</sub> between 1173 and 1473 K in air, *Mater. Sci. Eng. A* 434 (2006) 147–154.
- [136] Z.J. Lin, M.S. Li, J.Y. Wang, Y.C. Zhou. High-temperature oxidation and hot corrosion of Cr<sub>2</sub>AlC, *Acta Mater.* 55 (2007) 6182-6191.
- [137] D.E. Hajas, M. to Baben, B. Hallstedt, R. Iskandar, J. Mayer, J.M. Schneider. Oxidation of Cr<sub>2</sub>AlC coatings in the temperature range of 1230 to 1410 °C, *Surface and Coatings Technology* 206 (2011) 591-598.
- [138] S. Li, X. Chen, Y. Zhou, G. Song. Influence of grain size on high temperature oxidation behaviour of Cr<sub>2</sub>AlC ceramics, *Ceramics International* (2012) 2715–2721.
- [139] D.B. Lee, T.D. Nguyen, S.W. Park. Long-Time Oxidation of Cr<sub>2</sub>AlC Between 700 and 1,000 °C in Air, *Oxid. Metals* 77 (2012) 275-287.
- [140] W. Tian, P. Wang, Y. Kan, G. Zhang. Oxidation behavior of Cr<sub>2</sub>AlC ceramics at 1,100 and 1,250 °C, *J. Mater. Sci.* 43 (2008) 2785-2791.
- [141] B.A. Pint. Experimental Observations in Support of the Dynamic-Segregation Theory to Explain the Reactive-Element Effect *Oxid. Metals* 45 (1996) 1.
- [142] Z. Lin, M. Zhuo, Y. Zhou, M. Li, J. Wang. Microstructures and Adhesion of the Oxide Scale Formed on Titanium Aluminum Carbide Substrates, *J. Amer. Cer. Soc.* 89 (2006) 2964-2966.
- [143] H.J. Yang, Y.T. Pei, J.C. Rao, J.T.M. De Hosson, S.B. Li, G.M. Song. High temperature healing of Ti<sub>2</sub>AlC: On the origin of inhomogeneous oxide scale, *Scripta Mater.* 65 (2011) 135-138.

- [144] S. Gupta, D. Filimonov, M.W. Barsoum. Isothermal Oxidation of  $Ta_2AlC$  in Air, *J. Am. Ceram. Soc.* 89 (2006) 2974-2976.
- [145] S. Gupta, G. A., F. D., B.M. W. High-temperature oxidation of  $Ti_3GeC_2$  and  $Ti_3(Ge_{0.5}, Si_{0.5})C_2$  in air, Electrochemical Society, Pennington, NJ, ETATS-UNIS, 2006.
- [146] S. Gupta, E.N. Hoffman, M.W. Barsoum. Synthesis and oxidation of  $Ti_2InC$ ,  $Zr_2InC$ ,  $(Ti_{0.5}, Zr_{0.5})_2InC$  and  $(Ti_{0.5}, Hf_{0.5})_2InC$  in air, *Journal of Alloys and Compounds* 426 (2006) 168-175.
- [147] I. Salama, T. El-Raghy, M.W. Barsoum. Oxidation of  $Nb_2AlC$  and  $(Ti, Nb)_2AlC$  in air, *J. Electrochem. Soc.* 150 (2003) C152-C158.
- [148] M.W. Barsoum, L.H. Ho-Duc, M. Radovic, T. El-Raghy Long Time Oxidation Study of  $Ti_3SiC_2$ ,  $Ti_3SiC_2 / SiC$ , and  $Ti_3SiC_2 / TiC$  Composites in Air, *J. Electrochem. Soc.* 150 (2003) B166-B175.
- [149] S. Chakraborty, T. El-Raghy, M.W. Barsoum. Oxidation of  $Hf_2SnC$  and  $Nb_2SnC$  in Air in the 400-600 °C Temperature Range, *Oxidation of Metals* 59 (2003) 83-96.
- [150] S. Gupta, M.W. Barsoum Synthesis and Oxidation of  $V_2AlC$  and  $(Ti_{0.5}, V_{0.5})_2AlC$  in Air, *J. Electrochem. Soc.* 151 (2004) D24-D29.
- [151] S. Amini, A.R. McGhie, M.W. Barsoum. Isothermal Oxidation of  $Ti_2SC$  in Air, *J. Electrochem. Soc.* 156 (2009) P101-P106.
- [152] T.H. Scabarozzi, S. Amini, O. Leaffer, A. Ganguly, S. Gupta, W. Tambussi, S. Clipper, J.E. Spanier, M.W. Barsoum, J.D. Hettinger, S.E. Lofland. Thermal expansion of select  $M_{(n+1)}AX_n$  ( $M$  = early transition metal,  $A$  = A group element,  $X$  = C or N) phases measured by high temperature x-ray diffraction and dilatometry, *J. Appl. Phys.* 105 (2009) 13543-13548.
- [153] W.J. Quadakkers, D. Naumenko, E. Wessel, V. Kochubey, L. Singheiser. Growth Rates of Alumina Scales on Fe–Cr–Al Alloys, *Oxidation of Metals* 61 (2004) 17-37.
- [154] D. Naumenko, B. Gleeson, E. Wessel, L. Singheiser, W.J. Quadakkers. Correlation between the Microstructure, Growth Mechanism, and Growth Kinetics of Alumina Scales on a FeCrAlY Alloy, *Metall. Mater. Trans. A* 38 (2007) 2974-2983.
- [155] Z. Liu, W. Gao, Y. He. Modeling of Oxidation Kinetics of Y-Doped Fe–Cr–Al Alloys, *Oxidation of Metals* 53 (2000) 341-350.
- [156] D.P. Whittle, J. Stringer. Improvements in High Temperature Oxidation Resistance by Additions of Reactive Elements or Oxide Dispersions, *Philosophical Transactions of the Royal Society of London. Series A, Mathematical and Physical Sciences* 295 (1980) 309-329.
- [157] W.J. Quadakkers. Growth mechanisms of oxide scales on ODS alloys in the temperature range 1000–1100°C, *Materials and Corrosion* 41 (1990) 659-668.
- [158] D.J. Young, D. Naumenko, L. Niewolak, E. Wessel, L. Singheiser, W.J. Quadakkers. Oxidation kinetics of Y-doped FeCrAl-alloys in low and high  $pO_2$  gases, *Materials and Corrosion* 61 (2010) 838-844.
- [159] W.W. Smeltzer, R.R. Haering, J.S. Kirkaldy. Oxidation of metals by short circuit and lattice diffusion of oxygen, *Acta Metall.* 9 (1961) 880-885.

- [160] G.H.M. Neil Birks, F.S. Pettit. Introduction to the High Temperature Oxidation of Metals, Cambridge University Press, 2006.
- [161] A. Atkinson. Transport processes during the growth of oxide films at elevated temperature, *Rev. Mod. Phys.* 57 (1985) 437-470.
- [162] W.D. Kingery. Introduction to Ceramics. 4th ed., Wiley, New York, 1960.
- [163] M.W. Barsoum, L. Farber, T. El-Raghy. Dislocations, kink bands, and room-temperature plasticity of  $\text{Ti}_3\text{SiC}_2$ , *Metall. Mater. Trans. A* 30 (1999) 1727-1738.
- [164] M. Radovic, M.W. Barsoum, T. El-Raghy, S.M. Wiederhorn. Tensile creep of coarse-grained  $\text{Ti}_3\text{SiC}_2$  in the 1000-1200 °C temperature range, *Journal of Alloys and Compounds* 361 (2003) 299-312.
- [165] B.W. J. D. Parker. Rate-controlling processes during creep of super purity aluminum, *Philosophical Magazine A* 41 (1980) 665-680.
- [166] J.P. Poirier. Microscopic creep models and the interpretation of stress-drop tests during creep, *Acta Metall.* 25 (1977) 913-917.
- [167] F. Barcelo, S. Doriot, T. Cozzika, M. Le Flem, J.L. Béchade, M. Radovic, M.W. Barsoum. Electron-backscattered diffraction and transmission electron microscopy study of post-creep  $\text{Ti}_3\text{SiC}_2$ , *Journal of Alloys and Compounds* 488 (2009) 181-189.
- [168] J.D. French, S.M. Wiederhorn. Tensile Specimens from Ceramic Components, *J. Am. Ceram. Soc.* 79 (1996) 550-552.
- [169] D.F. Carroll, S.M. Wiederhorn, D.E. Roberts. Technique for Tensile Creep Testing of Ceramics, *J. Am. Ceram. Soc.* 72 (1989) 1610-1614.
- [170] W.E. Luecke, J.D. French. Sources of Strain-Measurement Error in Flag-Based Extensometry, *J. Am. Ceram. Soc.* 79 (1996) 1617-1626.
- [171] T. El'Raghy, M.W. Barsoum. Processing and Mechanical Properties of  $\text{Ti}_3\text{SiC}_2$ : I, Reaction Path and Microstructure Evolution, *J. Am. Ceram. Soc.* 82 (1999) 2849-2854.

# A1 A CRITICAL REVIEW OF THE OXIDATION OF $Ti_2AlC$ , $Ti_3AlC_2$ AND $Cr_2AlC$ IN AIR

---

This work was published in Materials Research Letters on September 1, 2013.

Of all the MAX phases, the most resistant to oxidation in air in the 900-1400 °C temperature range are  $Ti_2AlC$ ,  $Ti_3AlC_2$  and  $Cr_2AlC$ . A literature review, however, shows that while many claim the oxidation kinetics to be parabolic, others claim them to be cubic. Whether the kinetics are parabolic or better is of vital practical importance. By carefully re-plotting the results of others and carrying out one oxidation run for  $\approx 3000$  h at 1200 °C on a  $Ti_2AlC$  sample, we conclude that the oxidation kinetics are better described by cubic kinetics and that even that conclusion is an approximation. Lastly we present compelling evidence that the rate-limiting step during the oxidation of  $Ti_2AlC$  is oxygen diffusion down the alumina scale grain boundaries.

Keywords:  $Ti_2AlC$ ,  $Cr_2AlC$ ,  $Ti_3AlC_2$ , oxidation, cubic oxidation rate.



## A1.1 Introduction

---

The  $M_{n+1}AX_n$  (MAX) phases are a class of layered, machinable, early transition ternary metal carbides and/or nitrides, where M is an early transition metal, A is a group 13 to 16 elements, and X is C and/or N. These compounds are classified as thermodynamically stable nanolaminates having relatively high fracture toughness values (8-12 MPa $\sqrt{m}$ ), and yet are machinable, lightweight, and relatively soft [28-32]. Some also undergo a brittle-to-plastic transition at temperatures above 1000 °C. Some aluminum, Al, containing MAX phases, notably  $Ti_3AlC_2$ ,  $Ti_2AlC$  and  $Cr_2AlC$  show excellent oxidation resistance due to the formation of a dense and adherent alumina layer. These ternary carbides may prove useful in practical applications where high temperature oxidation resistance in air is required. However, before they can be used it is imperative to be able to predict the oxide thicknesses that would form after long times at elevated temperatures. This in turn implies that the oxidation kinetics be well understood and documented.

## A1.2 Literature Survey

---

The first papers to report on the oxidation of the  $Ti_{n+1}AlX_n$  phases were published in 2001 [38, 39]. In these papers, it was shown that the oxidation resulted in the formation of a rutile based solid solution with approximate chemistry of  $(Ti_{1-y}Al_y)O_{2-y/2}$ , where  $y \approx 0.05$  and alumina,  $Al_2O_3$  (Figure A1.1a). At longer times, kinetic demixing resulted in the formation of layers of rutile henceforth referred to as  $TiO_2$ ,  $Al_2O_3$  and porous layers (Figure A1.1b).

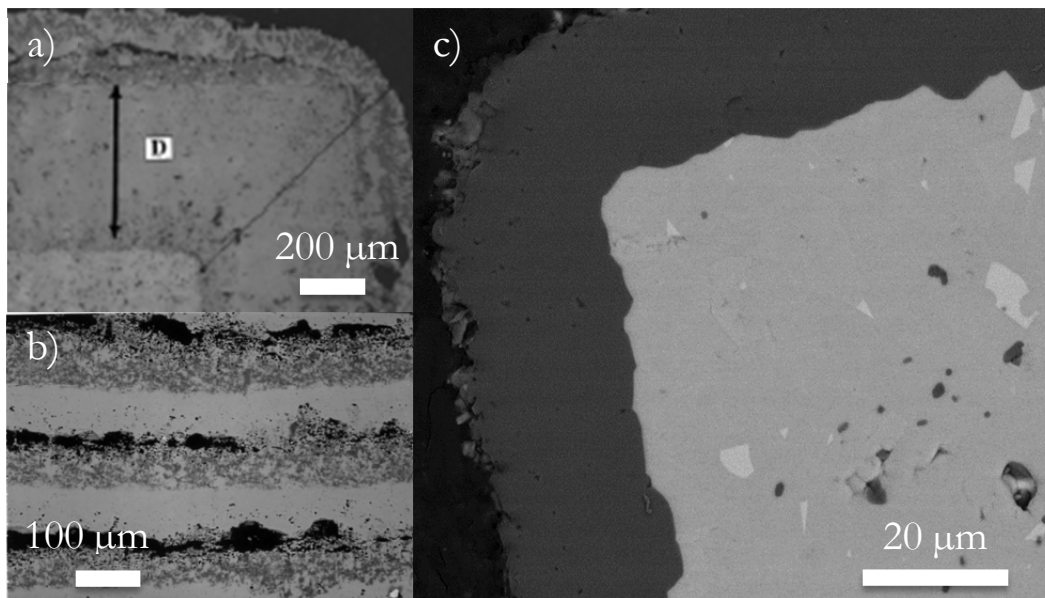
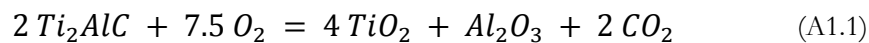


Figure A1.1 a) Oxidation of the  $Ti_{n+1}AlX_n$  phases results in the formation of a rutile based solid solution with approximate chemistry of  $(Ti_{1-y}Al_y)O_{2-y/2}$ , where  $y \approx 0.05$  and alumina,  $Al_2O_3$ . b) At longer times, kinetic demixing results in the formation of layers of  $TiO_2$ ,  $Al_2O_3$  and pores [39]. c) SEM micrograph of  $Ti_2AlC$  oxidized in air at  $1200\text{ }^\circ\text{C}$  for 2873 h showing a  $\approx 21\text{ }\mu\text{m}$  thick, coherent and fully dense  $Al_2O_3$  layer which conforms to the corners of the sample.

The oxidation kinetics were initially found to be parabolic, but at longer times tended towards linear, implying that the layers were not protective over the long run. Using Wagner's formalism it was further concluded that the rate-limiting step was the inward diffusion of oxygen and the outward diffusion of titanium through the  $TiO_2$  layer that forms. In other words the oxidation reaction was presumed to be [39]:



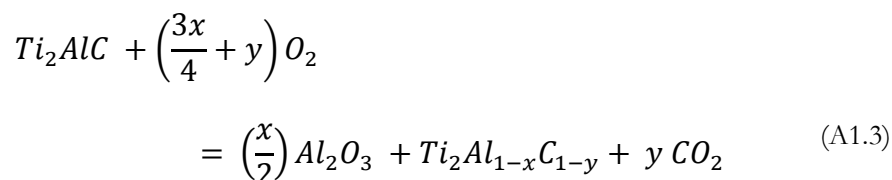
The C was presumed to diffuse through the rutile layer and oxidize. As discussed below, when the oxide that forms is  $TiO_2$  the oxidation resistance is poor. Fortunately, in many cases, the oxide that forms is  $Al_2O_3$ , in which case the oxidation resistance is excellent. In the remainder of this paper, the discussion will deal exclusively with oxidation that results in the formation of dense protective  $Al_2O_3$  layers.

### A1.2.1 Ti<sub>2</sub>AlC

Following the initial work in 2001, there have been many studies that have explored the oxidation behavior of Ti<sub>2</sub>AlC. In 2003, Wang and Zhou quantified the oxidation kinetics of Ti<sub>2</sub>AlC as cubic by heating it in air for 20 h in the 1000 °C to 1300 °C temperature range [42]. In other words, they concluded that the oxidation kinetics were best described by:

$$\left(\frac{\Delta w}{A}\right)^3 = k_c t \quad (\text{A1.2})$$

where  $\Delta w$  is the weight gain,  $A$ , is the surface area exposed to the atmosphere,  $t$  is time and  $k_c$  is the cubic reaction rate constant. In this case, the overall simplified reaction is assumed to be:



where  $x < 0.5$ .

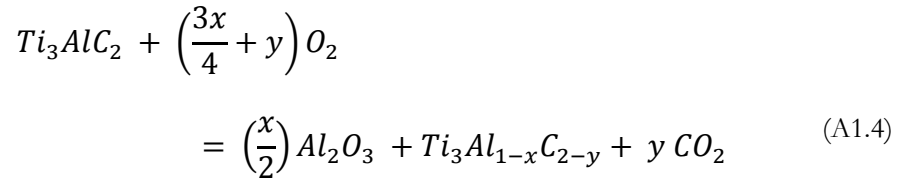
Here again, the C is presumed to diffuse through the Al<sub>2</sub>O<sub>3</sub> layer and oxidize. A typical microstructure of a Ti<sub>2</sub>AlC sample oxidized for almost 3000 h at 1200 °C is shown in Figure A1.1c. Note that the reaction layer is comprised of almost pure Al<sub>2</sub>O<sub>3</sub> and that it conforms to the samples' corners.

In 2004, Sundberg *et al.* reported parabolic oxidation kinetics for Ti<sub>2</sub>AlC up to 1400 °C in air [131]. In 2007, Byeon *et al.* reported that the oxidation kinetics were *cubic* in isothermal and cyclical oxidation tests at 1000, 1200, and 1400 °C [132]. Contrary to their previously published work in which it was claimed that the kinetics were cubic [42], in a recent review article, Wang and Zhou reported that Ti<sub>2</sub>AlC exhibited parabolic behavior [133]. In 2011 Cui *et al.* reported parabolic rates for Ti<sub>2</sub>AlC up to 1400 °C [46]. In 2012, Yang *et al.*

reported cubic kinetics for  $Ti_2AlC$  at 1200 °C [124]. Basu *et al.* also reported cubic oxidation kinetics for  $Ti_2AlC$  in both air and steam in the 1000 °C to 1300 °C temperature range [47].

### A1.2.2 $Ti_3AlC_2$

The oxidation behavior of  $Ti_3AlC_2$  has been less widely studied. In 2003, Wang and Zhou reported that the kinetics were parabolic [41]. Qian *et al.* reported the oxidation kinetic to be parabolic, in the 1000-1300 °C range [134]. Lee *et al.* [135] reported that the oxidation kinetics were temperamental; some samples formed predominantly  $TiO_2$  layers, others formed  $Al_2O_3$  layers in which case the oxidation reaction is presumably:

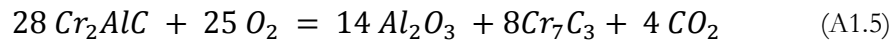


where  $x < 0.5$ .

Needless to add, the samples that formed an  $Al_2O_3$  layer were quite oxidation resistant. As noted above, when the oxide layers formed were  $TiO_2$ -based the resulting oxidation resistance was poor.

### A1.2.3 $Cr_2AlC$

In 2007, Lin *et al.* reported that the oxidation kinetics for  $Cr_2AlC$  in the 800-1300 °C range were parabolic [136]. The overall oxidation reaction was surmised to be:



In this case a continuous  $Cr_7C_3$  sub-layer formed between the protective alumina layer and the  $Cr_2AlC$  substrate (Figure A1.2). As discussed below, the presence of this sub-layer has important implications and ramifications.

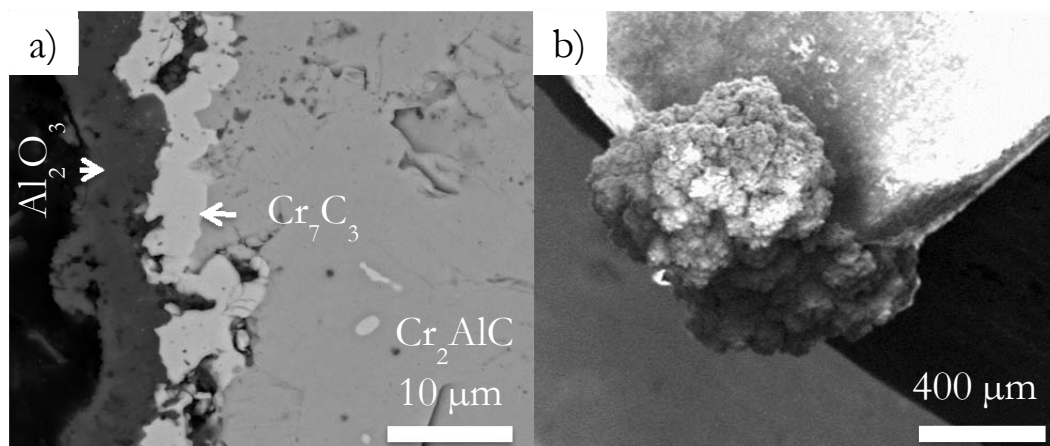


Figure A1.2 SEM micrograph of a) cross-sectioned  $\text{Cr}_2\text{AlC}$  sample oxidized at 1200 °C. The outer layer is a Cr-containing  $\text{Al}_2\text{O}_3$  and the inner layer is  $\text{Cr}_7\text{C}_3$ ; b) of sample oxidized at 1100 °C for 35 h clearly showing  $\text{Cr}_2\text{O}_3$  nodules (Gupta, unpublished results). This is the only MAX phase to show the formation of a carbide layer beneath the oxide layers formed during oxidation.

At 1300 °C, the  $\text{Al}_2\text{O}_3$  layer has a tendency to spall off and the oxidation resistance is compromised [43]. In 2008, Lee *et al.* further showed that the cyclic oxidation resistance of  $\text{Cr}_2\text{AlC}$  in air to be excellent at 1000 C, good at 1100 C, intermediate at 1200 C, but poor at 1300 °C [44]. Hajas *et al.* in 2011 reported parabolic oxidation kinetics for  $\text{Cr}_2\text{AlC}$  thin films in the 1230 to 1410 °C range [137]. Most recently, in 2012, Li *et al.* explored the effect of grain size on oxidation kinetics of  $\text{Cr}_2\text{AlC}$ : coarse-grained (CG) samples exhibited cubic oxidation kinetics at 1100 and 1200 °C, whereas fine-grained (FG) samples were less than parabolic at 1100 °C, and cubic at 1200 °C [138]. Also in 2012, Lee *et al.* showed that at 1200 °C, after a period of about 10 h during which there was an increase in weight, beyond that time the samples lost weight more or less linearly [139].

### A1.3 Parabolic, Cubic or Power law Kinetics

---

The brief review of the literature of the oxidation of  $Ti_2AlC$ ,  $Ti_3AlC_2$  and  $Cr_2AlC$  makes it amply clear that most agree on one fact, viz. the formation of an alumina layer is critical with endowing these compounds with their excellent oxidation resistance. When rutile forms instead, the oxidation resistance is greatly diminished. Where there is quite a bit of disagreement, however, is whether the kinetics are cubic or parabolic. This distinction is of outmost importance, because if the kinetics are indeed parabolic, then the long term prognosis is not good. However, if the kinetics are slower than parabolic, e.g. cubic or even better, then the oxidation resistance would be good enough for practical applications. This is a crucial point that needs to be established beyond a reasonable doubt since many, following the lead of Wang and Zhou, also assumed parabolic oxidation kinetics. The same conclusion was reached in a recent review article [133] despite the fact that Byeon *et al.* [132] and more recently Basu *et al.* [47] clearly showed the kinetics to be cubic. More problematic is that most of the studies on the oxidation of  $Cr_2AlC$  to date claim parabolic oxidation kinetics, including a recent review article on this compound [43, 44, 133, 136, 140].

In the remainder of this paper we emphatically make the case that the oxidation kinetics are better described as cubic, and quite comparable for the three compounds. The latter conclusion should not be surprising given that a dense, cohesive  $Al_2O_3$ -rich layer forms in all cases. We make our case using a two-pronged approach. The first is to re-plot some of the results of the early papers in which the authors maintained that the oxidation kinetics were parabolic and show that they can be better described by cubic kinetics (i.e. Eq. A1.2). The second is to report on the longest oxidation experiment carried out to date on  $Ti_2AlC$  at 1200 °C that clearly show the oxidation kinetics to be cubic or near cubic. Before proceeding further, we note that typically three laws have been used to describe the

oxidation kinetics of alumina formation in literature: parabolic, cubic, and power law given by, respectively:

$$\Delta x^2 = K' \left( \frac{t}{t_0} \right) \quad (\text{A1.6})$$

$$\Delta x^3 = K' \left( \frac{t}{t_0} \right) \quad (\text{A1.7})$$

$$\Delta x = K' \left( \frac{t}{t_0} \right)^n \quad (\text{A1.8})$$

where  $\Delta x$  is oxide scale thickness ( $\mu\text{m}$ ),  $t_0 = 1$  s,  $K'$  is a constant, and  $n$  is the power law scale growth exponent. In the following sections we critically assess which law best fits the oxidation of  $\text{Ti}_3\text{AlC}_2$ ,  $\text{Ti}_2\text{AlC}$  and  $\text{Cr}_2\text{AlC}$ .

### A1.3.1 $\text{Ti}_2\text{AlC}$ and $\text{Ti}_3\text{AlC}_2$

When the results of Wang and Zhou reported in Ref. [41] for  $\text{Ti}_3\text{AlC}_2$  are re-plotted as  $(\Delta w/A)^3$  vs.  $t$  (Figure A1.3a) least squares fits of the data resulted in  $R^2$  values that were quite high ( $> 0.998$ ). The  $R^2$  value for the parabolic plot given by the authors (Fig. 2 in Ref. [41]) is around 0.98. In other words, their own results fit a cubic law better than a parabolic one. It thus makes more sense to assume the kinetics to be cubic.

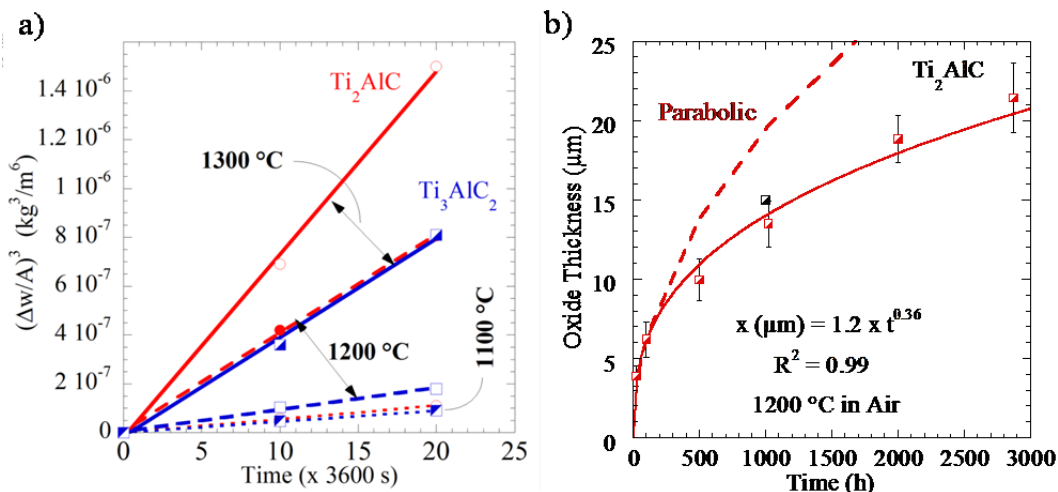


Figure A1.3 a) Replotted results from the 2003 Wang and Zhou papers on the oxidation of  $\text{Ti}_3\text{AlC}_2$  and  $\text{Ti}_2\text{AlC}$  [41, 42] showing a linear fit when  $(\Delta w/A)^3$  is plotted vs.  $t$ . Least squares fit of the 1300 °C plot results in an  $R^2$  value of 0.998, compared to 0.98 for the parabolic fit reported in the original articles. The compounds and graphs are color coded for clarity. b) Oxide scale thickness ( $x$ ) versus time for  $\text{Ti}_2\text{AlC}$  held at 1200 °C for >2800 h. A power fit of the results shown yields a time exponent of 0.36, viz. cubic kinetics. Dashed line shows the  $\Delta x$  based on a parabolic rate constant fitted to the first 100 h of oxidation.

Also plotted in Figure A1.3a are the results by the same authors reported in Ref. [42] for  $\text{Ti}_2\text{AlC}$ . This side-by-side comparison makes it clear that the kinetics for both compounds are not only both cubic, but as importantly, of the same order of magnitude. At 1100 °C, the oxidation kinetics for both ternary phases are nearly identical as they should be if in *both* cases, a dense alumina layer forms. Given the latter it is highly unlikely that the kinetics would be parabolic in one case ( $\text{Ti}_3\text{AlC}_2$ ) and cubic ( $\text{Ti}_2\text{AlC}$ ) in the other. This conclusion is further confirmed when the post-oxidation microstructures are compared. After 20 h oxidation at 1300 °C, the  $\text{Al}_2\text{O}_3$  layer thickness is  $\approx 25 \mu\text{m}$  in  $\text{Ti}_2\text{AlC}$  and  $\approx 14 \mu\text{m}$  in  $\text{Ti}_3\text{AlC}_2$ . After 20 h at 1200 °C, the oxide layer thicknesses - at  $\approx 5 \mu\text{m}$  - are almost identical for both compounds [41, 42].

Furthermore, Byeon *et al.* showed that when commercially available  $\text{Ti}_2\text{AlC}$  polycrystalline samples were heated in air, a continuous, adherent  $\alpha\text{-Al}_2\text{O}_3$  formed [132]. They also concluded that the oxidation kinetics were cubic [132]. The thickness of the layer was  $\approx 15$



$\mu\text{m}$  after 25 h of isothermal oxidation at 1400 °C. Roughly the same thickness was observed after 1,000 one hour cycles from ambient temperature to 1200 °C. In both cases, the layer remained adherent and protective (Figure A1.4a).

Similarly, recent results by Basu *et al.* [47] on the oxidation of commercially available  $\text{Ti}_2\text{AlC}$  samples, also showed that: i) the oxidation kinetics up to 120 h were *cubic*; ii) there is little difference between oxidation in air and in a 100 % steam environment up to 1300 °C; iii) the activation energy was about 270 kJ/mol; iv) the oxidation results a continuous and stable layer of  $\alpha\text{-Al}_2\text{O}_3$ , along with a thin surface layer of rutile in both environments. The thin  $\text{TiO}_2$  layer, however, volatilizes by forming gaseous  $\text{TiO}(\text{OH})_2$  in the presence of water vapor at temperatures  $>1200$  °C.

To help resolve this question, we conducted an isothermal oxidation experiment on  $\text{Ti}_2\text{AlC}$  at 1200°C for  $> 2800$  h. Samples were prepared by pouring pre-reacted  $\text{Ti}_2\text{AlC}$  powders (Kanthal, Sweden) in a graphite die that was in turn placed in a hot press and hot pressed, HPed, for 4 h at 1300 °C under a load corresponding to a stress of  $\approx 30$  MPa and a vacuum of  $10^{-2}$  torr. The resulting fully dense samples were electro-discharged machined, EDM, into smaller blocks and rinsed in dilute hydrochloric acid prior to testing.

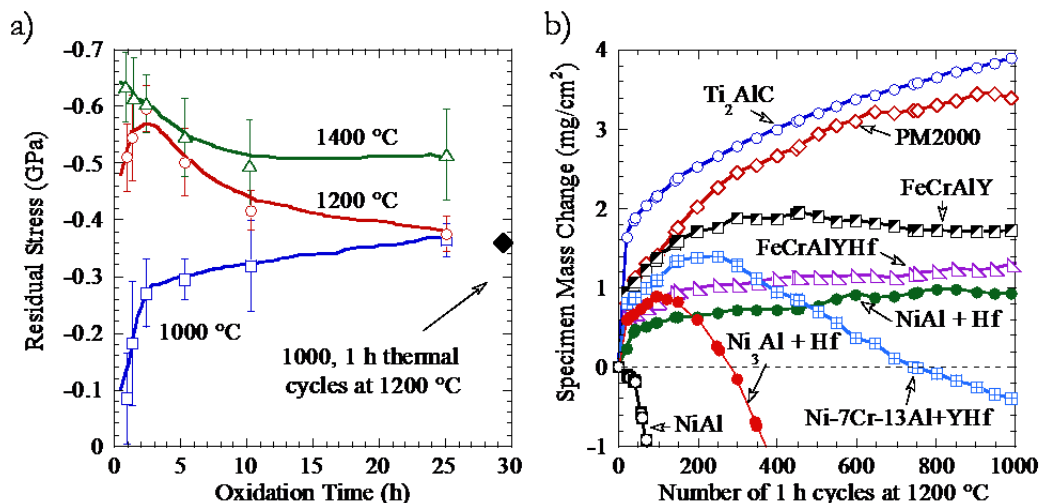


Figure A1.4 a) Magnitude of compressive residual stress within the Al<sub>2</sub>O<sub>3</sub> scale determined from luminescence-shifts as a function of time of isothermal oxidation at 1000, 1200 and 1400 °C [132]. The residual stresses are compressive, a function of time and temperature, and of the order of 500 MPa which is considered low [132]. b) Oxidation kinetics of Ti<sub>2</sub>AlC are compared with other more established/commercial oxidation resistant alloys. Note that if the very first oxidation cycle is omitted from the Ti<sub>2</sub>AlC results, its oxidation kinetics are comparable to PM2000 [132].

The initial dimensions and weights were recorded. Samples were then loaded into a 1200 °C box furnace and held at temperature for 25, 100, 500, 1000, 2000, and 2873 h. After almost 3000 h, the resulting microstructure (Figure A1.1c) clearly shows the formation of a thin cohesive Al<sub>2</sub>O<sub>3</sub> layer. After holding at 1200 °C for up to 2873 h, the oxide layer reached a thickness of about 21 μm (Figure A1.1c). Grain size was measured using the line intercept method on fractured surfaces (see Figure A1.9). About 200 grains per sample were measured.

When  $\Delta x^3$  is plotted vs.  $t$  a straight line (not shown) is obtained. Least squares fit of the results resulted in an  $R^2 > 0.988$ . To further confirm the cubic kinetics, a power law fit (Eq. 8) of the results (Figure A1.3b) resulted in the following relationship:

$$\Delta x (\mu m) = 1.2 \left( \frac{t}{t_0} \right)^{0.36} \quad R^2 = 0.99 \quad (\text{A1.9})$$

where  $t_0 = 1$  s. At 14  $\mu\text{m}$ , the  $\text{Al}_2\text{O}_3$  layer thickness observed after 1000 h is in very good agreement to the 15  $\mu\text{m}$  found after 1000, 1 h cycles to 1200 °C conducted by Byeon *et al.*[132], shown in Figure A1.3b as a black square. Based on these results and previous work, it is reasonable to conclude that the oxidation kinetics of  $\text{Ti}_2\text{AlC}$  are indeed near cubic. Table A1.1 summarizes the  $k_c$  values obtained from the various studies on  $\text{Ti}_2\text{AlC}$ ,  $\text{Ti}_3\text{AlC}_2$  and  $\text{Cr}_2\text{AlC}$ .

What is noteworthy and of great practical importance is the fact that even after this extended time at 1200 °C, no cracks were observed anywhere, not even at the corners (Figure A1.1c). One of the main reasons why the oxidation resistance of  $\text{Ti}_2\text{AlC}$  is as good as it is, and so resistant to thermal cycling, is the excellent match in thermal expansions between it and the  $\alpha\text{-Al}_2\text{O}_3$  protective layer that forms. Photoluminescence of the  $\alpha\text{-Al}_2\text{O}_3$  scale indicated that the residual stresses formed in that layer were compressive, a function of time and temperature and of the order of 500 MPa (Figure A1.4a) [132]. Such residual stresses are considered low, and partially explain the high spallation-resistance of the  $\alpha\text{-Al}_2\text{O}_3$  scale (Figure A1.4b).

Table A1.1 Summary of  $k_c$  ( $\text{kg}^3\text{m}^{-6}\text{s}^{-1}$ ) values for the oxidation of  $\text{Ti}_2\text{AlC}$ ,  $\text{Ti}_3\text{AlC}_2$  and  $\text{Cr}_2\text{AlC}$ .

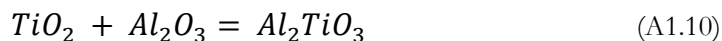
Phase	1000 °C	1100 °C	1200 °C	1300 °C	1400 °C	Comments and Ref.
$\text{Ti}_2\text{AlC}^*$	$2.3 \times 10^{-13}$	$1.5 \times 10^{-12}$	$1.1 \times 10^{-11}$	$2.1 \times 10^{-11}$		[42]
$\text{Ti}_2\text{AlC}$	$3.3 \times 10^{-13}$	$1.9 \times 10^{-12}$	$1.0 \times 10^{-11}$	$5.1 \times 10^{-11}$		Air [47]
$\text{Ti}_2\text{AlC}$	$5.6 \times 10^{-13}$	$2.0 \times 10^{-12}$	$1.2 \times 10^{-11}$	$6.0 \times 10^{-11}$		100 % $\text{H}_2\text{O}$ [47]
$\text{Ti}_3\text{AlC}_2$		$1.3 \times 10^{-12} \ddagger$	$2.6 \times 10^{-12} \ddagger$	$1.1 \times 10^{-11} \ddagger$	$6.1 \times 10^{-10} \ddagger$	[41]
$\text{Cr}_2\text{AlC}$			$3.8 \times 10^{-12} \ddagger$	$3.2 \times 10^{-11} \ddagger$		[136]
$\text{Cr}_2\text{AlC}$ CG		$2.8 \times 10^{-13} \ddagger$	$9.7 \times 10^{-12} \ddagger$			[138]
$\text{Cr}_2\text{AlC}$ FG		$7.5 \times 10^{-13} \ddagger$	$1.47 \times 10^{-11} \ddagger$			[138]
$\text{Cr}_2\text{AlC}$		$4.4 \times 10^{-13} \ddagger$				[139]

\* In [42], the results listed in their Table 1 are wrong. The correct values, based on the results they show in their Fig. 1c, are listed here and are the correct ones.

‡ These values are calculated from the weight gain results reported in the original papers. In the original papers,  $k_c$  was either not provided or incorrectly reported as parabolic.

Figure A1.4b compares the oxidation kinetics of  $\text{Ti}_2\text{AlC}$  with other more established/commercial oxidation resistant alloys [132]. We note in passing that commercially available Fe- and Ni-based  $\text{Al}_2\text{O}_3$ -forming alloys have relatively high CTE's and typically require reactive element additions to improve their spallation resistance [141]. Also note that if the very first oxidation cycle is omitted from the  $\text{Ti}_2\text{AlC}$  results, its oxidation kinetics are comparable to PM2000 (Figure A1.4b).

After heating  $\text{Ti}_2\text{AlC}$  to 1200 °C, and cooling to room temperature, Cui *et al.* identified twins and stacking faults bounded by partial dislocations by TEM in surface  $\text{TiO}_2$  grains [46]. These defects most probably formed as a result of the thermal stresses generated due to thermal expansion mismatches during cooling. Cui *et al.* also confirmed the formation of  $\text{Al}_2\text{TiO}_5$  above 1400 °C following the reaction:



This  $\text{Al}_2\text{TiO}_5$  layer was correlated with the formation of cracks upon cooling. These cracks were ascribed to thermal expansion mismatches, and as importantly to the high anisotropy of thermal expansion of  $\text{Al}_2\text{TiO}_5$ . This compound has a thermal expansion of  $10.9 \times 10^{-6} \text{ K}^{-1}$  along the a-axis,  $20.5 \times 10^{-6} \text{ K}^{-1}$  along b and  $-2.7 \times 10^{-6} \text{ K}^{-1}$  along c. The formation of  $\text{Al}_2\text{TiO}_5$  should thus be avoided as much as possible.

Using transmission electron microscopy, Lin *et al.* explored the microstructures of  $\text{Ti}_3\text{AlC}_2$  and  $\text{Ti}_2\text{AlC}$  samples after oxidation in air for 10 h at 1200 °C [142]. An enrichment of Ti in the  $\text{Al}_2\text{O}_3$  grain boundaries and Ti-rich precipitates in the  $\text{Al}_2\text{O}_3$  scales were identified. They also showed that Al depletion at the oxide/substrate interface was *minimal*, indirectly confirming that the diffusivity of Al in the carbides is quite fast at these temperatures. These results again emphasize the close similarities of the oxidation behavior observed in both  $\text{Ti}_3\text{AlC}_2$  and  $\text{Ti}_2\text{AlC}$ .

### A1.3.2 Crack Healing

Before discussing the oxidation of  $\text{Cr}_2\text{AlC}$ , it is important to review a remarkable property of  $\text{Ti}_2\text{AlC}$  and  $\text{Ti}_3\text{AlC}_2$ , namely their crack healing ability [45, 143]. Crack healing of  $\text{Ti}_3\text{AlC}_2$  was investigated by oxidizing partially pre-cracked samples. A crack near a notch was introduced into the sample by tensile deformation. After oxidation at 1100 °C in air for 2 h, the crack was completely healed, with oxidation products consisting primarily of  $\alpha\text{-Al}_2\text{O}_3$ , as well as some rutile  $\text{TiO}_2$  (Figure A1.5a to d). A schematic of the process is shown in Figure A1.5e. The indentation modulus and hardness of the crack-healed zone were slightly higher than those of the original  $\text{Ti}_3\text{AlC}_2$  base material. The preferential oxidation of Al atoms in  $\text{Ti}_3\text{AlC}_2$  grains on the crack surface resulted in the predominance of  $\alpha\text{-Al}_2\text{O}_3$  particles forming in a crack less than 1  $\mu\text{m}$  wide.

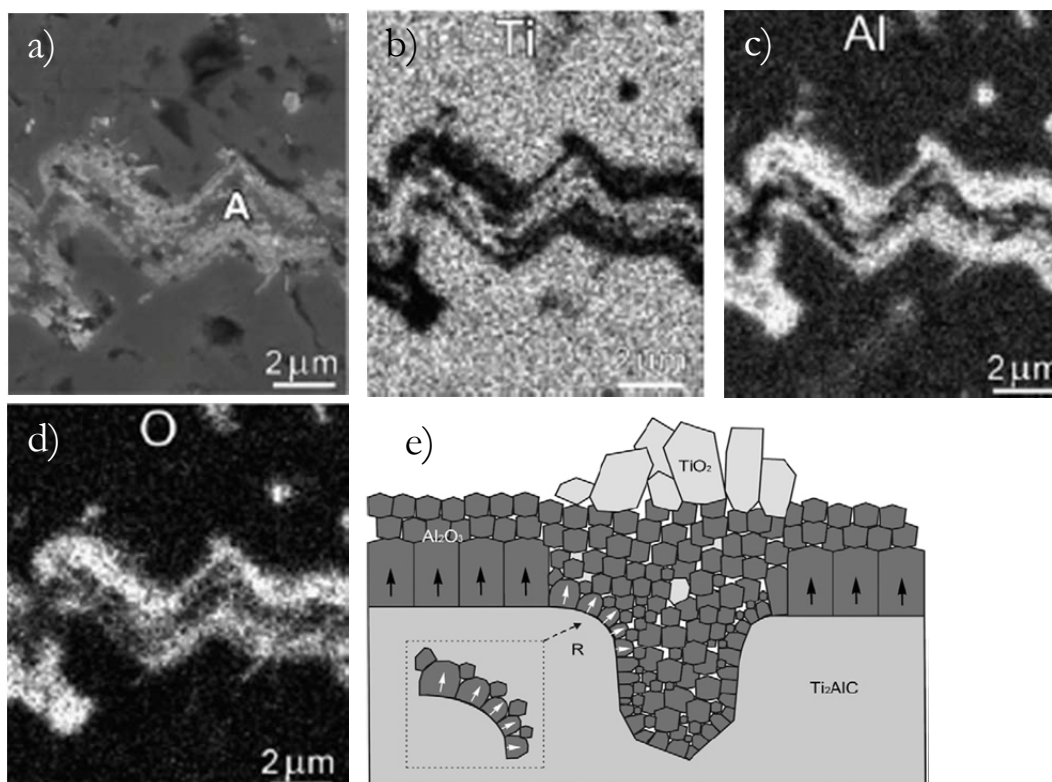


Figure A1.5 After oxidation at 1100 °C in air for 2 h, crack healing of  $\text{Ti}_3\text{AlC}_2$  is seen via SEM micrographs a) showing the formation of primarily  $\alpha\text{-Al}_2\text{O}_3$ , as well as some rutile  $\text{TiO}_2$ ; Energy dispersive x-ray spectroscopy (EDS) element maps of the crack region show concentrations of b) Ti, c) Al, and d) O as the alumina forms in the crack. A schematic of the process is shown in e) [45].

In 2011, the same group [143] revisited the oxidation of  $\text{Ti}_2\text{AlC}$  and carefully examined the morphology of the various oxide layers that form both on flat and curved surfaces or cracks. They found that after oxidation at 1200 °C for 16 to 100 h, the  $\alpha\text{-Al}_2\text{O}_3$  particles that formed on flat surfaces were small ( $\approx 1 \mu\text{m}$ ), densely packed and columnar. Those that formed in the cracks or cavities, on the other hand, were more equiaxed and less densely packed. The rutile grains, on the other hand, exhibit a broad size distribution, ranging from sub-micrometer to 10  $\mu\text{m}$ . The authors also confirmed the presence of small  $\text{TiO}_2$  particles at the  $\alpha\text{-Al}_2\text{O}_3$  grain boundaries first reported by Lin *et al.* [142].

Even more recently, the same group [125] showed that  $\text{Ti}_2\text{AlC}$  was capable of repeatedly repairing damage events. When the authors introduced Knoop indentations on the tensile

side of  $\text{Ti}_2\text{AlC}$  flexural bars, the flexural strength dropped from  $211 \pm 15$  MPa to  $152 \pm 20$  MPa. Heating the indented bars, in air for two hours, resulted in an increase in the flexural strengths to  $224 \pm 50$  MPa, a value that was slightly *higher* on average than the virgin samples, albeit with larger scatter. Even more impressively, after successively extending the same crack seven times and healing it between each fracture event, the fracture toughness dropped from  $\approx 6.5$   $\text{MPa}\sqrt{\text{m}}$ , to about  $3$   $\text{MPa}\sqrt{\text{m}}$ . It is important to note here that by the end of the 7<sup>th</sup> cracking iteration the filled crack was of the order of 1 mm (Figure A1.6a). As in their previous work, Li *et al.* showed that the main healing mechanism at high temperature is the filling of the cracks by the formation of well adhering  $\text{Al}_2\text{O}_3$  layers and some  $\text{TiO}_2$  (Figure A1.6b to e). The authors write in their abstract: “Self-healing ceramics have been studied for over 40 years to obtain some performance recovery and to prevent material failure during service, but so far only materials with the capability of single healing event per damage site have been realized.” They then proceed to show how  $\text{Ti}_2\text{AlC}$  is capable of multiple healing events.

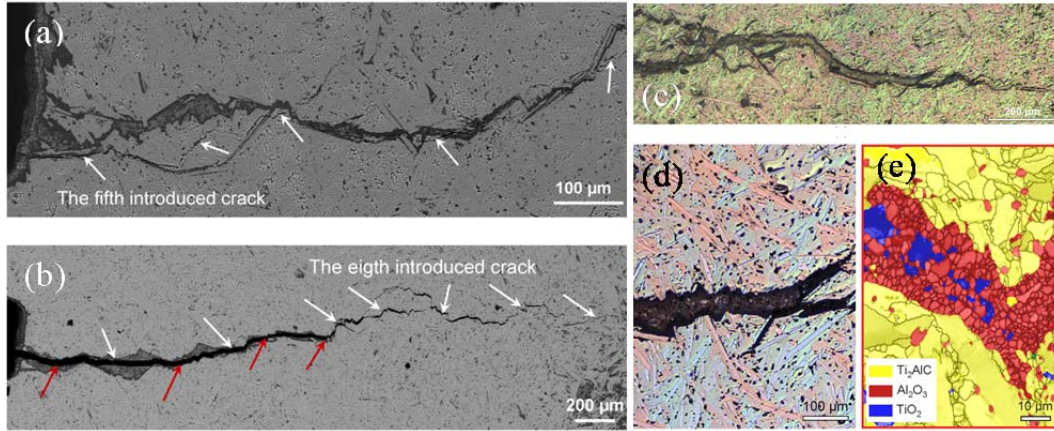


Figure A1.6 Images of fracture and crack-healing in  $\text{Ti}_2\text{AlC}$ ; (a) Crack path after four cycles of healing at  $1200\text{ }^\circ\text{C}$  for 2 h, and subsequent fracture. (b) Crack path after seven cycles of healing, and subsequent fracture. The red arrows indicate the location of remnant crack parts. (c) OM image of a crack fractured eight times before annealing in air at  $1200\text{ }^\circ\text{C}$  for 100 h showing the complete filling of the crack. (d) Enlarged OM image taken from (c). Two opposite fracture surfaces were covered by the same  $\text{Al}_2\text{O}_3$  layer (black) and the gap between the two surfaces was fully filled by a mixture of  $\text{Al}_2\text{O}_3$  (black) and  $\text{TiO}_2$  (white particles). (e) SEM image of the healed-damage zone obtained using electron backscatter diffraction [125].

### A1.3.3 $\text{Cr}_2\text{AlC}$

As noted above, the situation for  $\text{Cr}_2\text{AlC}$  is even more muddled, since most papers claim parabolic kinetics [43, 44, 136, 137, 140], when as shown below they are far from parabolic. Figure A1.7a re-plots the results of Lin *et al.* [136] together with two power fits (solid lines), assuming cubic kinetics (dotted lines) and the parabolic rate constants reported by the authors (dashed lines). The power fits result in the following relationships at  $1200\text{ }^\circ\text{C}$  and  $1300\text{ }^\circ\text{C}$ , respectively.

$$\Delta w \text{ (kg/m}^2\text{)} = 1.4 \times 10^{-4} \left(\frac{t}{t_0}\right)^{0.34} \quad R^2 = 0.986 \quad (\text{A1.11})$$

$$\Delta w \text{ (kg/m}^2\text{)} = 8.8 \times 10^{-4} \left(\frac{t}{t_0}\right)^{0.23} \quad R^2 = 0.977 \quad (\text{A1.12})$$



When the same exercise was carried out on some recent long term oxidation (up to one year) results by Lee *et al.* [139] reproduced in Figure A1.7b, the following relationships - shown by the solid lines in Figure A1.7b - at 700 °C, 800 °C and 1000 °C, respectively, were obtained:

$$\Delta x (\mu\text{m}) = 0.009 \left(\frac{t}{t_0}\right)^{0.24} \quad R^2 = 0.91 \quad (\text{A1.13})$$

$$\Delta x (\mu\text{m}) = 0.001 \left(\frac{t}{t_0}\right)^{0.46} \quad R^2 = 0.98 \quad (\text{A1.14})$$

$$\Delta x (\mu\text{m}) = 0.24 \left(\frac{t}{t_0}\right)^{0.18} \quad R^2 = 0.99 \quad (\text{A1.15})$$

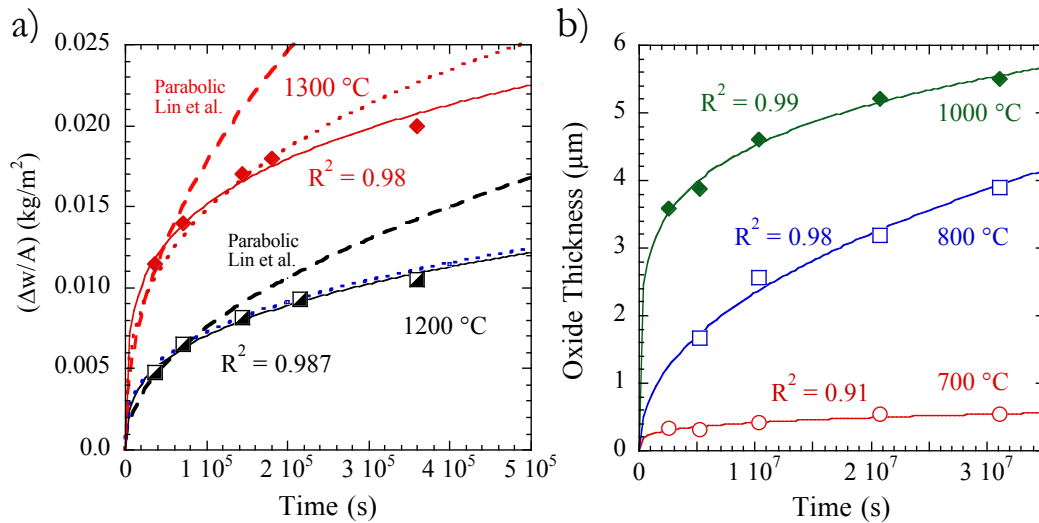


Figure A1.7 a) Re-plots of the results of Lin *et al.* [136] together with two power fits (solid lines), assuming cubic kinetics (dotted lines) and the parabolic rate constants reported by Lin *et al.* (dashed lines) are shown. Cubic power fits result in time exponents of 0.34 and 0.25 for 1200 °C and 1300 °C, respectively. b) The same exercise in a) - carried out on data by Lee *et al.* [139] - results in power fits shown by the solid lines with time exponent values of 0.24, 0.46 and 0.18 at 700 °C, 800 °C and 1000 °C, respectively. With the possible exception of 800 °C, the oxidation kinetics of  $\text{Cr}_2\text{AlC}$  are certainly not parabolic, and in most cases even better than cubic.

Taken *in toto* these results make it amply clear that, with the possible exception of oxidation at 800 °C, the oxidation kinetics of Cr<sub>2</sub>AlC are certainly not parabolic, and for the most part, not even cubic. These results are noteworthy because they confirm that at 700 °C, 1000 °C and 1300 °C the oxidation kinetics are significantly *slower than cubic*. In other words, the time exponents are significantly less than 1/3. At 1200 °C they are close to cubic. The results at 800 °C are anomalous, and reflect either enhanced oxidation kinetics at 800 °C for reasons that are unclear and/or experimental uncertainty. If the first point at 800 °C is ignored, the exponent value drops to about 0.38, which is probably more realistic. This comment notwithstanding, more work at 800 °C is needed to better understand the nature of this possible anomaly.

In the final analysis, the oxidation kinetics of Cr<sub>2</sub>AlC, for the most, part cannot be fit adequately with a simple model for the simple reason that the kinetics are initially relatively fast, but then slowly decrease with time to the point where the oxide layers almost stop getting thicker. The best example of this state of affairs can be found in the results shown in Figure A1.7b. After 30 days of oxidation at 1000 °C, the oxide thickness was 3.5 μm; in the next 330 days, however, the oxide thickness increased by less than 2 μm.

Lastly, when all the results shown in Table A1.1 are plotted on an Arrhenian plot (Figure A1.8), it is clear that the absolute values of the cubic rate constants are comparable in the 1100 °C to 1200 °C. However, at  $507 \pm 90$  kJ/mol, the activation energy for the oxidation of Cr<sub>2</sub>AlC is roughly double the  $250 \pm 30$  kJ/mol of the Ti<sub>2</sub>AlC and Ti<sub>3</sub>AlC<sub>2</sub>. Why the activation energies are different is not clear at this time.

Note that the results listed in Table A1.1 all assumed cubic kinetics, when in some cases, as discussed above, the kinetics may not have been exactly cubic. The values listed in Table A1.1 are nevertheless useful because it is only by comparing them can the oxidation kinetics of the various materials be compared. However, for practical purposes where predictions of

oxide thickness values at long times need to be made, the power law fits – with maybe the omission of the first 10 or so hours - are to be used instead.

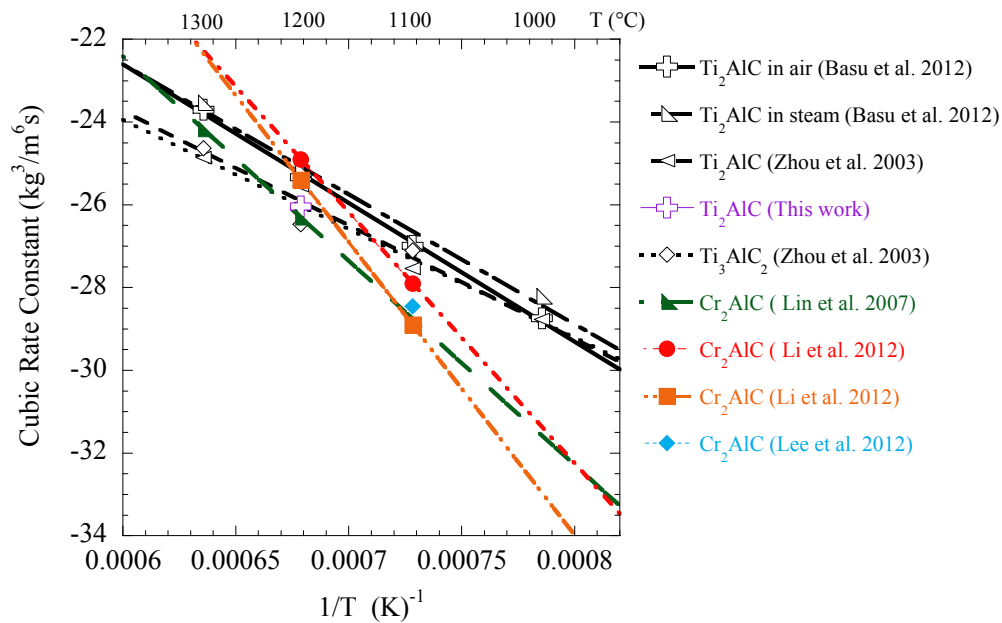


Figure A1.8 Arrhenian plot of cubic rate constants for  $\text{Al}_2\text{O}_3$ -forming MAX phases,  $\text{Ti}_2\text{AlC}$ ,  $\text{Ti}_3\text{AlC}_2$  and  $\text{Cr}_2\text{AlC}$  listed in Table A1.1.

#### A1.3.4 Implications of the presence of $\text{Cr}_7\text{C}_3$ layer after the oxidation of $\text{Cr}_2\text{AlC}$

Of more than 20 MAX phases whose oxidation response in air have been studied [37, 144–151], only one –  $\text{Cr}_2\text{AlC}$  – forms a carbide layer. This observation indirectly implies that for this compound C is *not* diffusing out as fast as the Al, which results in its accumulation at the substrate/oxide interface. This in turn implies that the alumina that forms on  $\text{Cr}_2\text{AlC}$  must be somewhat different from the one that forms on  $\text{Ti}_2\text{AlC}$ . Further evidence for the conclusion that the  $\text{Al}_2\text{O}_3$  oxide layer that forms on  $\text{Cr}_2\text{AlC}$  is different than the one that forms on  $\text{Ti}_2\text{AlC}$  can be found in the over two orders of magnitude better corrosion resistance of  $\text{Cr}_2\text{AlC}$  to oxidation in the presence of  $\text{Na}_2\text{SO}_4$ , compared to  $\text{Ti}_2\text{AlC}$  or  $\text{Ti}_3\text{AlC}_2$

[136]. Lastly, a perusal of the results listed in Table A1.1 and shown in Figure A1.8 makes it clear that at all temperatures  $< 1200$  °C,  $\text{Cr}_2\text{AlC}$  has better oxidation resistance. Why this is the case is unclear at this time, but the dissolution of small amounts of  $\text{Cr}_2\text{O}_3$  in the  $\text{Al}_2\text{O}_3$  layer that forms when  $\text{Cr}_2\text{AlC}$  is oxidized [43, 136, 137, 139, 140] could play a role. Another factor may be the presence of small  $\text{TiO}_2$  particles at the grain boundaries of the alumina that forms on  $\text{Ti}_2\text{AlC}$  [39, 42, 47, 124, 125, 132, 142].

Note that the behavior of  $\text{Cr}_2\text{AlC}$  cannot be traced to the stability of  $\text{Cr}_7\text{C}_3$  relative to  $\text{TiC}$  since the latter is significantly more stable. It is also unlikely that the anomalous behavior is associated with a low diffusivity of Al in  $\text{Cr}_2\text{AlC}$  since there is no reason to believe that the diffusivity of Al in  $\text{Cr}_2\text{AlC}$  is much different than it is in  $\text{Ti}_2\text{AlC}$ , which as discussed above is fast enough to prevent any depletion of Al at the oxide/ $\text{Ti}_2\text{AlC}$  interface.

The presence of  $\text{Cr}_7\text{C}_3$ , however, is quite problematic for the simple reason that if for any reason the protective alumina layer is breached, the oxidation of the underlying carbide at high temperature would, more likely than not, be catastrophic (see Figure A1.2b). When this is combined with the fact at  $1200$  °C, scale cracking and spalling is observed and at  $1300$  °C, the oxidation resistance deteriorates quickly as a function of cycling owing to the formation of voids and scale spallation [44], it follows that despite its excellent oxidation resistance, it is unlikely that  $\text{Cr}_2\text{AlC}$  can be used at temperatures much higher than  $1100$  °C or even  $1000$  °C. Note the propensity for spallation can be traced to the relatively high thermal expansion of this compound ( $\approx 12.8 \times 10^{-6} \text{ K}^{-1}$  [152]) relative to that of the protective alumina layer that forms.

## A1.4 Comparison to FeCrAl alloys

---

It is well documented that grain size coarsening leads to a decrease in oxide scale thickness growth rates in FeCrAl alloys, where inward oxygen diffusion dominates [153-158]. Naumenko *et al.* have shown a near cubic rate power law dependence by correlating oxide grain growth with the scale thickness, with a time dependence exponent ranging from 0.35 to 0.37 in FeCrAlY [154]. Liu *et al.* [155] developed a mathematical model to explain the dependence of scale thickness on oxide grain coarsening, which was seen to follow a  $t^{1/3}$  dependence in the scale layer in FeAlCrY, in good agreement with previous work by Whittle *et al.* [156]. Quadakkers *et al.* have criticized the use of parabolic rate calculations for determining the oxidation kinetics of  $\alpha$ -Al<sub>2</sub>O<sub>3</sub> in FeCrAl alloys, showing instead that they are better described by near cubic time dependencies with a power law fit [153]. Smeltzer *et al.* showed that the decrease in grain boundary diffusion paths over time limit the inward diffusion of oxygen during oxidation [159]. As the area fraction of short circuit paths decreases, there is an overall decrease in oxide scale growth rates. Unsurprisingly, as discussed in the next section, the alumina layers formed herein are similar to those seen in other alumina forming materials (Figure A1.9).

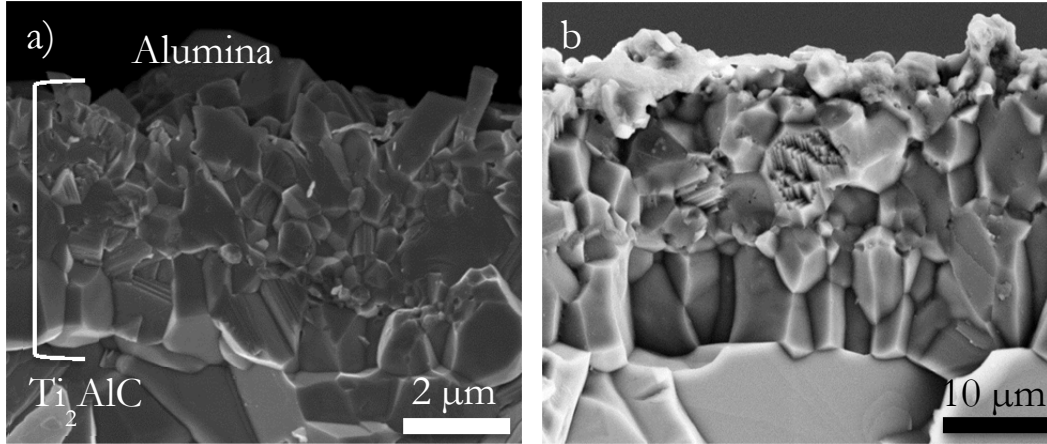


Figure A1.9 SEM micrographs of the fracture surface of  $Ti_2AlC$  after a) 25 h and b) 2873 h at 1200 °C in air. The oxide scale is seen to increase in grain size linearly towards the MAX phase interface.

### A1.5 Modelling of the Oxidation Kinetics

In general, the scale thickening rate can be written as [160]:

$$\frac{dx}{dt} = D_{eff} \frac{\Delta\mu}{RT} \cdot \frac{1}{x} \quad (A1.16)$$

where  $D_{eff}$ , is the effective diffusion coefficient;  $\Delta\mu$ , the oxygen potential difference between the scale/gas and scale/metal interfaces and  $R$  and  $T$  have their usual meaning.

If one assumes that the oxidation kinetics are controlled by grain boundary diffusion of oxygen, then [161]:

$$D_{eff} = D_{GB} \frac{2\delta_{GB}}{r_G} \quad (A1.17)$$

where  $D_{GB}$  is the oxygen grain-boundary diffusion coefficient;  $\delta_{GB}$ , the grain-boundary width; and  $r_G$ , the oxide grain size.

In general, grain coarsening kinetics can be described by [162]:

$$d^m = d_0^m + Kt \quad (\text{A1.18})$$

where  $K$  is a constant,  $m$  is the grain growth exponent and  $d_0$  the initial grain size. Combining Eqs. A1.16, A1.17, and A1.18, it can be shown that at longer times [155]:

$$x^2 \approx K' \left( \frac{t}{t_0} \right)^{(m-1)/m} \quad (\text{A1.19})$$

where  $x$  is the scale thickness and  $K'$  is a constant. It follows that if the assumptions made above are correct, then the following relationship applies:

$$n \approx (m - 1)/2m \quad (\text{A1.20})$$

To test this idea we measured the grain sizes of the alumina films that formed on the  $\text{Ti}_2\text{AlC}$  sample that was oxidized for almost 3000 h. The results are shown in Figure A1.10a. Based on the least squares fit of the results,  $m \approx 3.23$ . According to Eq. 20,  $n \approx 0.345$ , which, coincidentally or not, is in excellent agreement with the value of 0.36 derived from the results shown in Figure A1.3b. Plotting  $d^{3.23}$  vs.  $t$  (Figure A1.10b) results in a straight line fit, with intercept  $d_0 = 0.93 \mu\text{m}$ , further validating the assumption - that  $d_0$  can be ignored at longer times - made in deriving Eq. (A1.19). Whether this agreement is fortuitous or not must await the results of further work at different temperatures and different alumina forming MAX phases.

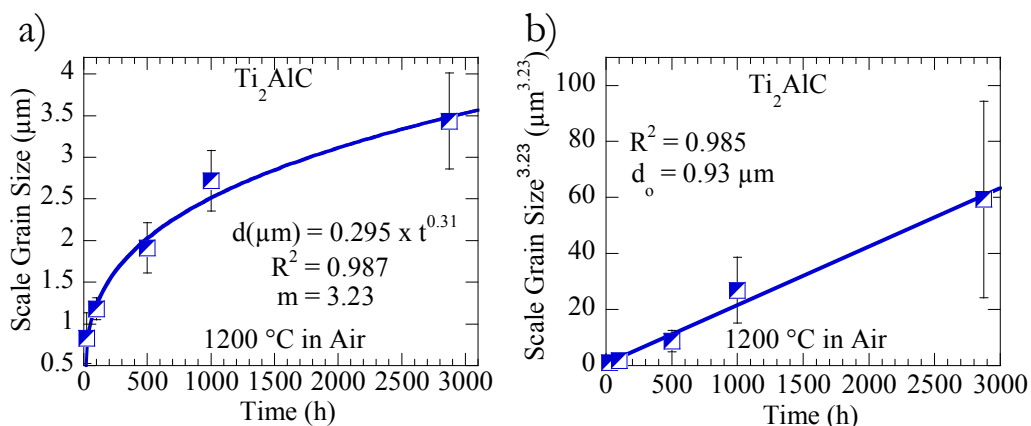


Figure A1.10 a) Oxide scale grain coarsening kinetics plotted with a power law fit. b) A least squares fit of  $d^m$  vs.  $t$  results in a straight line, where the intercept is equal to  $d_o^m$ . At  $0.93\ \mu\text{m}$ ,  $d_o$  is sufficiently small to assume that at long times it can be ignored in Eq. A1.19 [155].

## A1.6 Summary and Conclusions

The oxidation resistances, in air, of the MAX phases,  $\text{Ti}_2\text{AlC}$ ,  $\text{Ti}_3\text{AlC}_2$  and  $\text{Cr}_2\text{AlC}$  are excellent because, in most cases, a dense, spall resistant, protective  $\text{Al}_2\text{O}_3$  layer forms. Of the three, and despite the fact that the oxidation kinetics of  $\text{Cr}_2\text{AlC}$  at temperatures  $< 1200\text{ }^\circ\text{C}$  are slower than those of  $\text{Ti}_2\text{AlC}$  (Figure A1.8), for practical applications  $\text{Ti}_2\text{AlC}$  is by far the most attractive for several reasons that include: a) the higher concentration of Al as compared to  $\text{Ti}_3\text{AlC}_2$ , which is important because it increases the activity of Al at the substrate/oxide interface thus increasing the probability of the formation of the all-important alumina layer; b) the excellent match between the thermal expansions of  $\text{Ti}_2\text{AlC}$  and alumina, which in turn minimizes thermal residual stresses and concomitant propensity of spallation; c) lower density and, d) crack healing. Lastly, the fact that the raw materials for this MAX phase are some of the lowest costing of all MAX phases cannot be underestimated.



The formation of  $\text{Cr}_7\text{C}_3$  upon the oxidation of  $\text{Cr}_2\text{AlC}$  is unique to this compound and implies that the alumina layer that forms is less pervious to C than the one that forms on  $\text{Ti}_2\text{AlC}$ ,  $\text{Ti}_3\text{AlC}_2$  and other MAX phases. The reason for this somewhat surprising result is unclear at this time.

At most temperatures, the oxidation kinetics are better described as cubic than parabolic. This comment notwithstanding, even cubic kinetics are an approximation. The best strategy to predict the time dependence of the alumina layer thickness is to fit the results to a power law fit. Lastly, by measuring the grain sizes of the alumina scale, we present evidence that the rate-limiting step is oxygen diffusion down the alumina scale grain boundaries. The agreement with power law equations derived using oxygen grain boundary diffusion assumptions is shown to be quite good. Further studies at different temperatures with other alumina forming MAX phases are indicated at this time to further confirm these conclusions.

### **Acknowledgements**

This research is supported by DOE's Office of Nuclear Energy University Program (DOE/NEUP).

## A2 TENSILE CREEP OF $Ti_2AlC$ IN AIR IN THE 1000- 1150 °C TEMPERATURE RANGE

---

In the secondary regime of the tensile creep of  $Ti_2AlC$ , made with commercial powders with a grain size of  $14\pm 8$   $\mu m$ , the minimum creep rate is given by a power law, with a stress exponent of  $2.5\pm 0.3$ , and activation energy of  $362\pm 88$  kJ/mol. Dislocation creep - with possibly grain boundary sliding - are presumed to be the dominant creep mechanism(s). The high failure strains ( $>15\%$ ) are attributed to substantial grain kinking near the fracture surface and concomitant damage tolerance.

**Key Words:**  $Ti_2AlC$ , tensile creep, high temperature, power law creep, rupture.

## A2.1 Manuscript

---

The  $M_{n+1}AX_n$  (MAX) phases are a class of layered, machinable, transition ternary metal carbides and/or nitrides, where M is an early transition metal, A is a group 13 to 16 element, and X is C and/or N. These compounds are classified as thermodynamically stable nanolaminates having relatively high fracture toughness (8-12 MPa $\sqrt{m}$ ), and yet are machinable, lightweight, and relatively soft [28, 30-32, 163]. Some also undergo a brittle to ductile transition above 1000 °C.

Creep, in most crystalline solids, occurs by a variety of mechanisms in three stages: a primary stage, where the strain rate decreases with time, a secondary or quasi-steady state, where the strain rate reaches a steady state or a minimum, and lastly, a tertiary stage. Surprisingly given their potential as high temperature structural materials there have been very few creep studies on the MAX phases. As far as we are aware, the only two papers dealing with the tensile creep of a MAX phase are those by Radovic *et al.* on the creep of  $Ti_3SiC_2$  [56, 164]. In those papers, it was shown that the minimum creep rate,  $\dot{\epsilon}_{min}$ , is well represented by a power law relation given by [165, 166]:

$$\dot{\epsilon}_{min} = \dot{\epsilon}_0 A \left( \frac{\sigma}{\sigma_0} \right)^n \exp\left(\frac{-Q}{RT}\right) \quad (A2.1)$$

where  $\sigma$ ,  $A$ ,  $n$  and  $Q$  are, respectively, the uniaxial applied stress, a stress-independent constant, stress exponent and activation energy for creep;  $\dot{\epsilon}_{min} = 1 \text{ s}^{-1}$  and  $\sigma_0 = 1 \text{ MPa}$ .  $R$  and  $T$  have their usual meaning.

Radovic *et al.* concluded that the main creep mechanism was dislocation creep, with a  $Q$  of  $\sim 460$ , for both fine (FG) and coarse (CG) grained microstructures [56, 164]. At  $n = 2.0$  for the CG and  $n = 1.5$  for FG, the stress exponents were comparable. The creep response was

found to depend on the generation and dissipation of large internal stresses during loading. Stresses were dissipated *via* delamination, cavitation, and kinking [56, 164]. Up to 4 % plastic strain was accommodated without the formation of observable cracks or voids. Between 4 % and failure, the strains were accommodated by cracks and voids. None of the failed samples exhibited necking. Zhen *et al.* reported similar damage mechanisms for the compressive creep of  $\text{Ti}_3\text{SiC}_2$ , and showed that at temperatures above 1000 °C, kink bands and dislocation arrays interact in such a way as to form deformation cells, effectively subgrains [58, 59]. Bao *et al.* found subcritical crack growth to be the dominating failure mechanism in bending creep of  $\text{Ti}_3\text{AlC}_2$  [57].

Using electron backscatter diffraction and transmission electron microscopy, TEM, of post-creep samples, Barcelo *et al.* [167], presented evidence for three deformation mechanisms in individual grains, namely: (i) basal dislocation glide, to form dislocation arrays/stacking faults, (ii) formation of dislocation walls of opposite sign that result in kinking of individual grains and, (iii) formation of mobile dislocation walls, MDW, or low angle grain boundaries, of the same sign that result in grain bending [167]. They also showed that the deformation was not uniform, with evidence showing completely undamaged grains next to heavily kinked grains, a characteristic of solids in which deformation is occurring with less than 5 independent slip systems. This response is expected for all MAX phases, especially in CG microstructures.

Several studies have shown that  $\text{Ti}_2\text{AlC}$  performs significantly better than  $\text{Ti}_3\text{SiC}_2$  in oxidizing environments up to 1300 °C [40, 42, 131, 132]. The latter exhibits parabolic law oxidation, which transitions to linear above 925°C and exposure times longer than 30 h, forming silica and rutile layers [40]. In contrast, a dense inner layer of coherent alumina,  $\alpha\text{-Al}_2\text{O}_3$ , with a discontinuous rutile,  $\text{TiO}_2$ , outer layer forms on  $\text{Ti}_2\text{AlC}$ . Wang *et al.* reported that the oxidation of  $\text{Ti}_2\text{AlC}$  obeyed a cubic law, with cubic rate constants,  $k_c$ , increasing

from  $2.4 \times 10^{-12}$  to  $2.1 \times 10^{-11}$   $\text{kg}^3/\text{m}^6/\text{s}$ , as the temperature increased from 1000 to 1300 °C [42]. Sundberg *et al.* also reported excellent oxidation resistance for  $\text{Ti}_2\text{AlC}$  made from  $\text{Ti}_2\text{AlC}$  pre-reacted powders. The protective  $\text{Al}_2\text{O}_3$  layer formed maintained excellent adhesion, even through 8000 thermal cycles to 1350 °C [42, 131]. Beyon *et al.* showed that the presence of 3 oxidation phases results in the variation between parabolic and cubic rate laws seen in previous work:  $\text{Al}_2\text{O}_3$ ,  $\text{TiO}_2$ , and  $\text{Al}_2\text{TiO}_5$  seen at 1400 °C after 10 h [132]. Beyon *et al.* also showed that the residual stresses in the  $\text{Al}_2\text{O}_3$  layers were relatively low because of the excellent match between the thermal expansion coefficients of  $\text{Ti}_2\text{AlC}$  and  $\text{Al}_2\text{O}_3$ .

Herein, we report on the tensile creep of polycrystalline  $\text{Ti}_2\text{AlC}$  samples with a grain size of  $14 \pm 8$   $\mu\text{m}$ , in the 1000 - 1150 °C temperature, and the 10 MPa to 40 MPa stress, ranges, respectively. Whenever possible the results are compared with previous work on the creep of  $\text{Ti}_3\text{SiC}_2$  [56, 164].

The processing details are described elsewhere [33, 168]. The samples were prepared by pouring pre-reacted  $\text{Ti}_2\text{AlC}$  powders (Kanthal, Hallstahammar, Sweden) in a graphite die that was then placed in a hot press and hot pressed, HPed, for 4 h at 1300 °C under a load corresponding to a stress of  $\approx 30$  MPa and a vacuum of  $10^{-2}$  torr. The resulting samples were fully dense, predominantly single-phase, with randomly aligned plate-like grains. The length,  $d_l$ , and width,  $d_w$ , of the grains were measured using an optical microscope (OM) and the line intercept method. The average grain size was calculated as the geometric mean value

of the grain lengths and widths, *viz.*  $\sqrt[3]{d_l^2 \cdot d_w}$ .

Details of the tensile creep measurements can be found elsewhere [56, 164, 168, 169]. Electro-discharge machined dog-bone specimens SR51 (prismatic gage section:  $2 \times 2.5 \times 12$   $\text{mm}^3$ ) [168] were tested, with a final surface preparation of 600 grit polish along the loading

direction to remove surface defects and contamination from sample preparation. The strain rate measurements were made using a laser-extensometry system (1100 series, Zygo Corp, Middlefield, CT) [170]. Initial loads, corresponding to a stress of 1 MPa, were applied to the samples prior to heating for alignment purposes. All samples were then heated to the testing temperatures (1000 to 1150 °C) in  $\approx 1.5$  h, and held at that temperature for 2 h before the loads were applied. Most samples were loaded with step load configurations over a range of loads corresponding to stresses that varied between 10-40 MPa, due to limited sample quantities.

The fracture surfaces were examined using a scanning electron microscope, SEM (Carl Zeiss Supra 50VP, Germany). Cross-sections were taken from the gauge area, and select surfaces that were parallel to the applied load were ground and polished for optical microscopy, and SEM analysis. Some of the polished samples were etched using a 1:1:1 by volume 0.5M HF:0.7M HNO<sub>3</sub>:H<sub>2</sub>O solution in order to better expose the grains [171].

The HPed samples were predominantly single phase and fully dense (Figure A2.1a). The average grain size was  $14 \pm 8$   $\mu\text{m}$ . The average aspect ratio ( $d_l/d_w$ ) was 4, indicating that the grains, like most MAX phases, are more plate-like than equiaxed (Figure A2.1a-b). The size distribution is somewhat bimodal because of the presence of small grains ( $\sim 8$   $\mu\text{m}$ ) entrapped between larger grains ( $\sim 19$   $\mu\text{m}$ ). The post creep microstructure in the grip section (Fig. 1b) was found to be identical to the as-received samples (Figure A2.1a).

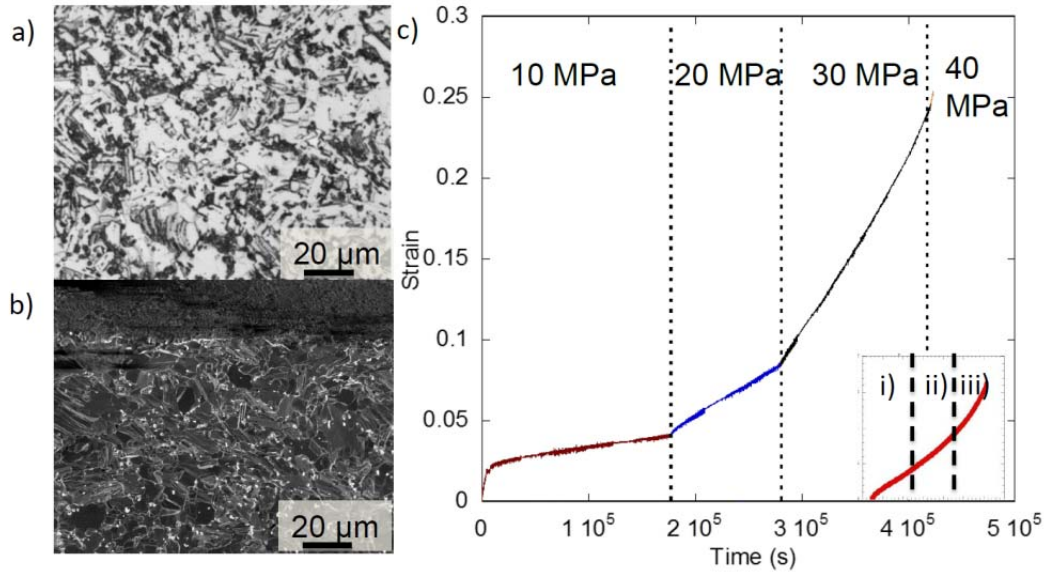


Figure A2.1 a) OM micrographs of as-received microstructure are compared to b) SEM micrographs of the grip section post creep, showing minimal difference in grain size. c) plots the effect of time,  $t$ , and  $\sigma$  on the minimum tensile strains,  $\epsilon_{min}$ , at 1050 °C for step loads of. Inset in Fig. 1c shows a typical strain vs. time plot for a sample that was loaded to a load corresponding to a stress of 30 MPa at 1050 °C.

Figure A2.1c plots the effect of time,  $t$ , and  $\sigma$  on  $\dot{\epsilon}_{min}$  at 1050 °C. Inset in Figure A2.1c shows a typical strain vs. time plot for a sample that was loaded to a load corresponding to a stress of 30 MPa at 1050 °C. As for  $Ti_3SiC_2$  [56, 164], three regimes are distinguishable:

- An initial transient regime, labeled i in inset of Figure A2.1c, where  $\dot{\epsilon}$  decreases with  $t$ .
- A secondary creep regime, labeled ii in inset of Figure A2.1c, in which  $\dot{\epsilon}$  is more or less constant with time. In this regime, the creep rate reaches  $\dot{\epsilon}_{min}$ .
- A tertiary creep regime, labeled iii in inset of Figure A2.1c, in which  $\dot{\epsilon}$  increases until failure.

A ln-ln plot of  $\dot{\epsilon}_{min}$  vs.  $\sigma$  as a function of stress is shown in Figure A2.2a. An Arrhenius plot of  $\dot{\epsilon}_{min}$  is shown in Figure A2.2b. Bilinear regression analysis of the results shown in

Figure A2.2a and b was carried out, assuming Eq. 1 was operative [165, 166]. The analysis, on the logarithmic form of Eq. A2.1, resulted in the following relationship:

$$\dot{\epsilon}_{min}(s^{-1}) = \dot{\epsilon}_0 \exp(12.5) \left(\frac{\sigma}{\sigma_0}\right)^{2.5 \pm 0.3} \exp\left(\frac{-362 \pm 88 \text{ kJ/mol}}{RT}\right) \quad (\text{A2.2})$$

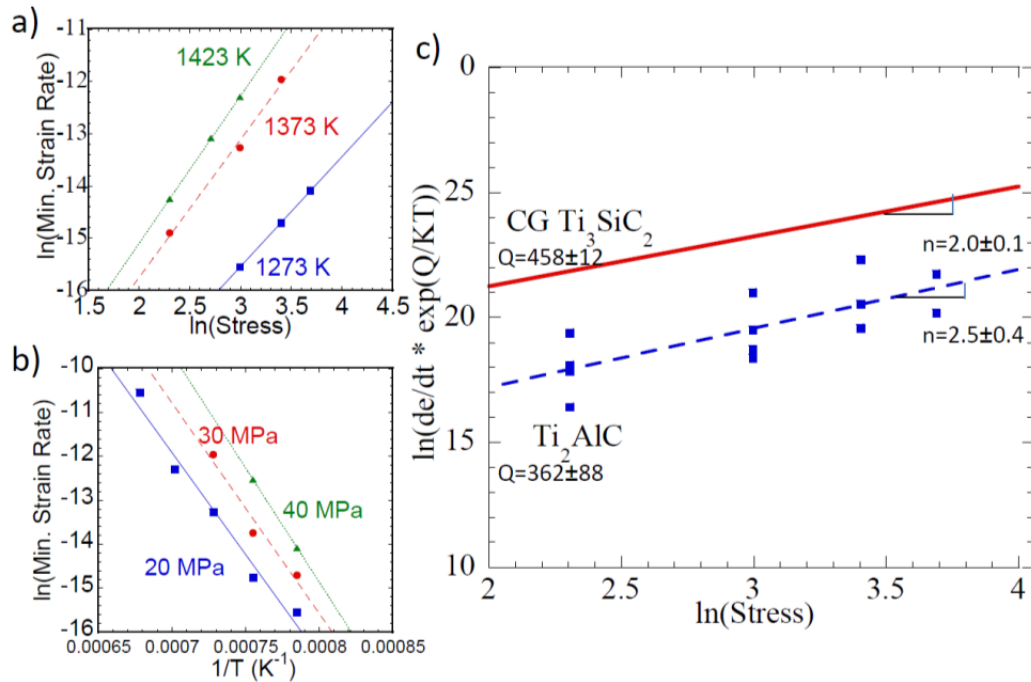


Figure A2.2 a) Ln-ln plot of  $\dot{\epsilon}_{min}$  vs. stress as a function of T; b) Arrhenius plots of min. strain rate as a function of stress; c) Ln-ln plot of min. strain rate vs. stress assuming Q of 362 kJ/mol for  $Ti_2AlC$  compared to  $Ti_3SiC_2$  [56, 164]. Results of bilinear regression as a function of stress and temperature are shown as lines in each plot, the slopes of which reveal Q, n and  $\sigma$  for the creep power law (Eq. A2.2)

Figure A2.2c plots this relationship, as a dashed line. At 30 MPa, the strains to failure,  $\epsilon_f$ , are  $\approx 16\%$  at  $1100^\circ\text{C}$ , and  $\approx 24\%$  at  $1000^\circ\text{C}$ . The maximum  $\epsilon_f$  was 27%, for a sample held at  $1100^\circ\text{C}$  that was step loaded to loads corresponding to stresses of 10, 20, and 30 MPa.

Sections parallel to the loading direction of step loaded samples held at  $1150^\circ\text{C}$  (Figure A2.3) show significant crack formation and damage accumulation. This SEM micrograph is



representative of all samples tested. Deformation occurs without necking in the gauge area (Figure A2.3). Crack formation is almost perfectly perpendicular to the vertical loading direction. All samples formed a protective  $\text{Al}_2\text{O}_3$  layer - some having a discontinuous  $\text{TiO}_2$  outer layer - with thicknesses that depended on temperature and time (see inset in Figure A2.3). As noted above, that creep failure occurred without evidence of necking is again in agreement with the  $\text{Ti}_3\text{SiC}_2$  results [164].

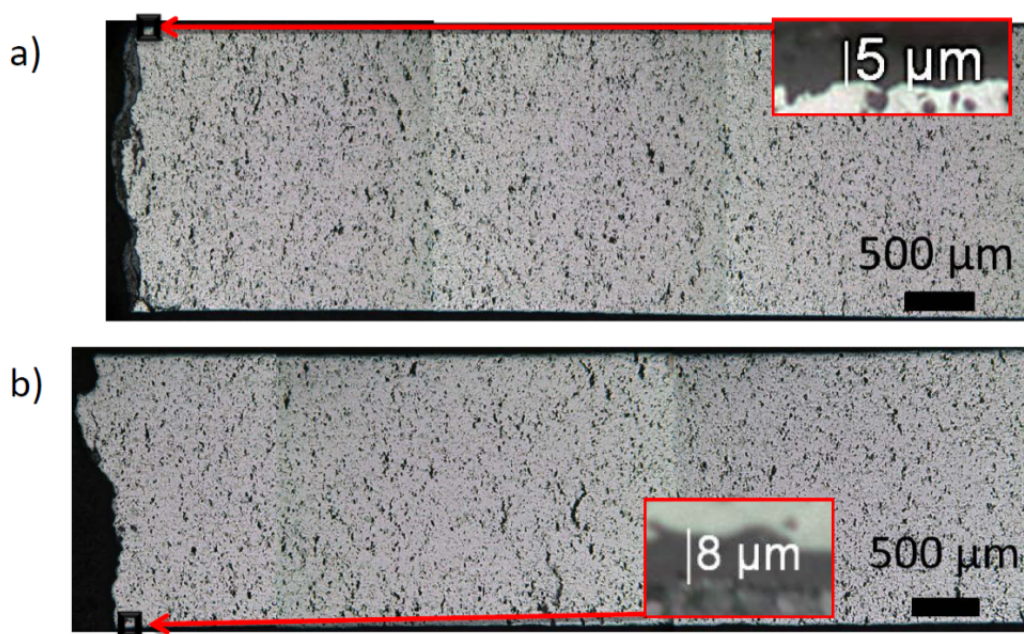


Figure A2.3 Composite OM micrographs showing cross-sections of step loaded  $\text{Ti}_2\text{AlC}$  at a)  $1100^\circ\text{C}$  loaded at 10-20-30 MPa for 55h to a final strain of 27% and b)  $1150^\circ\text{C}$  loaded at 5-10-15-20 MPa for 86h to a final strain of 26%. Samples do not exhibit necking, and insets show the formation of protective  $\text{Al}_2\text{O}_3$  for each sample.

At  $8.5 \pm 1.3 \mu\text{m}$ , the thickest  $\text{Al}_2\text{O}_3$  layer observed was found on the sample held at  $1150^\circ\text{C}$  for 86 h. The sample also showed a sporadic, discontinuous covering of  $7.5 \pm 2.7 \mu\text{m}$  thick  $\text{TiO}_2$ . The oxide layers were significantly thinner than the  $\text{SiO}_2/\text{TiO}_2$  layers seen for  $\text{Ti}_3\text{SiC}_2$  [164]. The protective  $\text{Al}_2\text{O}_3$  layer formed as shown in previous oxidation studies of  $\text{Ti}_2\text{AlC}$ .

Note that these layers do not influence the measured values of the minimum strain rate for the same reasons discussed in Appendix A in Ref. [164].

When the fractured surface of a sample held at 1100°C and 30 MPa for 3 h to a  $\epsilon_f$  of 16 % was examined in the SEM (Figure A2.4) it was found to be covered with grains that were heavily kinked (Figure A2.4). At  $1.7 \pm 3 \mu\text{m}$ , the grain size of the fractured surface was significantly smaller than the initial  $14 \pm 8 \mu\text{m}$  grain size (Figure A2.4b, c). This observation is new and the extent of kinking is somewhat surprising, but consistent with the idea that in the MAX phases the major deformation mechanism at high temperatures are dislocation pileups and kink band formation [28]. The development of subgrains is also consistent with the deformation by kinking found during the compressive creep of  $\text{Ti}_3\text{SiC}_2$  [59].

Not surprisingly, the overall creep response of  $\text{Ti}_2\text{AlC}$  is quite similar to that of  $\text{Ti}_3\text{SiC}_2$  [56, 164]. At  $362 \pm 88 \text{ kJ/mol}$ ,  $Q$  for  $\text{Ti}_2\text{AlC}$  is roughly 75% that reported for  $\text{Ti}_3\text{SiC}_2$ . At  $2.5 \pm 0.4$ ,  $n$  for  $\text{Ti}_2\text{AlC}$  is comparable to  $\text{Ti}_3\text{SiC}_2$ . At 30 MPa, the strains to failure,  $\epsilon_f$ , are  $\approx 16\%$  at 1100°C, and  $\approx 24\%$  at 1000°C. Zhen *et al.* reported an order of magnitude increase in creep rates for  $\text{Ti}_3\text{SiC}_2$  samples composed of sintered, commercially available pre-reacted powders [59]. It is therefore presumed that improved creep resistance will be achievable with the use of elemental powders for sample fabrication of  $\text{Ti}_2\text{AlC}$ , as opposed to the commercial powders used herein.

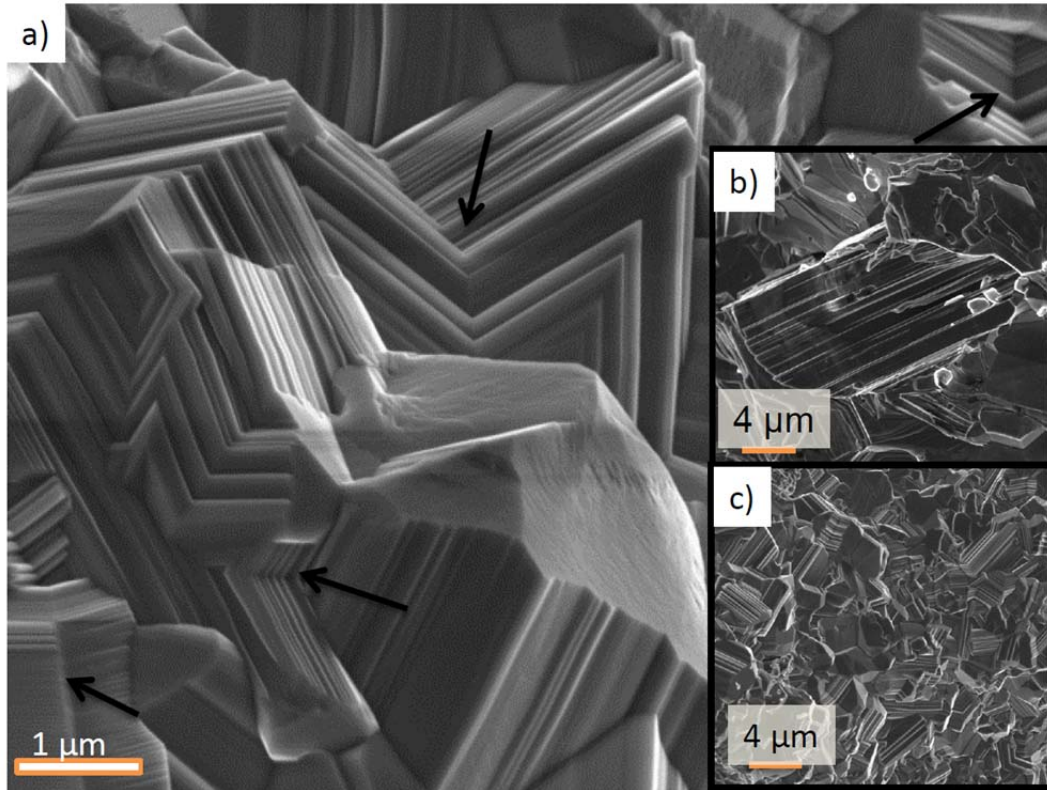


Figure A2.4 SEM micrograph of, a) fracture surface of  $\text{Ti}_2\text{AlC}$  sample held at  $1100\text{ }^\circ\text{C}$  and  $30\text{ MPa}$  for  $3\text{ h}$  to a final strain of  $16\%$ . The distinctive layered structure can be seen, as well as stepped grain boundaries. Kinks (referred by black arrows) are readily apparent at the fracture surface. Ruptured grains stick out of the fracture plane. A difference in grain size between b) grip section and c) fracture surface can be seen.

The rate controlling mechanism for steady state creep of the MAX phases is believed to be a combination of dislocation creep and grain boundary sliding [56, 164]. Results shown here offer additional evidence to this conjecture. Since  $\dot{\epsilon}_{min}$  can be described by a single power law (Eq. A2.2; Figure A2.2 and Figure A2.3) it is fair to assume that the same thermally activated rate-controlling mechanisms operate over the entire range of testing temperatures and stresses. As the pre-reacted  $\text{Ti}_2\text{AlC}$  microstructure investigated herein consists of large grains with many small grains filling in the spaces between (Figure A2.1a), grain boundary sliding cannot be discounted as a contributing mechanism. Results confirm a combination of creep and grain boundary sliding, as shown by the stepped grain surface seen in Figure A2.4. Kinking occurs through the movement of mobile dislocation walls, *viz.* low angle

grain boundaries and delaminations along dislocation pileups. It follows that the strongest evidence that dislocations play a role during creep is extensive kinking seen on the fracture surface of a crept sample (Figure A2.4). It is unclear at this time whether the continuous grain refinement affects  $\dot{\epsilon}_{min}$ ; further testing is required. But given the weak dependence of creep on grain size [56, 164], it is reasonable to assume that such an effect would be small here. Further work with varying grain sizes is needed, however.

In summary, the tensile creep of  $Ti_2AlC$  over a range of testing temperatures (1000–1150°C) and stresses (10–40 MPa) is comparable to that of  $Ti_3SiC_2$ . At 2.5, the stress exponent for  $Ti_2AlC$  is slightly higher than those found for CG and FG  $Ti_3SiC_2$  samples. At 363 kJ/mol, the activation energy, on the other hand, was found to be about 25 % lower than that for  $Ti_3SiC_2$ . At 26%, the maximum rupture strain is more than double that reported for  $Ti_3SiC_2$  [164]. The samples also developed a dense, coherent, and quite protective  $Al_2O_3$  layer. Substantial kinking on the post-creep fractured surface is strong evidence that dislocations play an important role in the creep process.

### 8.3. Acknowledgments

This work was supported DOE's Nuclear Energy University Programs (CFP-09-790). We thank Mark Shiber (Drexel University, PA) for helping us during the specimen preparation. We also appreciate the use of Drexel University Centralized Research Facility equipment. Help provided by William Luecke (NIST, MD) is also greatly appreciated.

## V I T A

### Education

Drexel University: Philadelphia, Pennsylvania  
**Ph.D. in Materials Science and Engineering** Sept 2009- Sept 2015

Drexel University: Philadelphia, Pennsylvania  
**B.S. in Materials Science and Engineering** Sept 2004- June 2009

### Research and Collaborative Projects

**Graduate Research Assistant**, Drexel University: Philadelphia, PA 2009-2015  
**Visiting Graduate Researcher**, SRNL: Aiken, SC 2011, 2012

### Honors and Awards

The Joseph and Shirley Carleone Endowed Fellowship, Drexel (2015). Alpha Sigma Mu Honor Society, Drexel (2010-2015). 1st place prize, ASM International Metallography Contest Drexel (2012)

### Presentations

#### Invited Talks:

D. J. Tallman, L. He, E. N. Hoffman, B. Garcia-Diaz, G. Kohse, R. L. Sindelar, M. W. Barsoum. NSUF User's Week, INL, Idaho Falls, ID June 2015

D. J. Tallman, E. N. Hoffman, E. N. Caspi, G. Kohse, R. L. Sindelar, M. W. Barsoum. ICACC, Daytona Beach, FL, January 2013.

#### Other Presentations in:

ICACC (Daytona Beach, FL, 2015), CIMTEC (Montecatini Terme, Italy, 2014), TMS (San Diego, CA, 2014), ICACC (Daytona Beach, FL, 2014), MRS (Boston, MA, 2013), ANS Winter Meeting (Washington, D.C., 2013), FCRD Advanced Fuels Campaign, LANL (Los Alamos, NM, 2012), TMS (Orlando, FL, 2012), TMS (San Diego, CA, 2011)

### Publications

12. C. Hu, C. Li, J. Halim, S. Kota, D. J. Tallman, M. W. Barsoum. *J. Am. Ceram. Soc.* 2015
11. D. J. Tallman, L. He, B. Garcia-Diaz, E. N. Hoffman, G. Kohse, R. L. Sindelar, M. W. Barsoum. *J. Nucl. Mater.* (Accepted) 2015
10. M-Q Zhao, M. Sedran, Z. Ling, M. R. Lukatskaya, O. Mashtalir, M. Ghidui, B. Dyatkin, D. J. Tallman, Thierry Djenizian, M. W. Barsoum, Y. Gogotsi. *Angew. Chem.* (2015)
9. D. J. Tallman, J. Yang, L. Pan, B. Anasori, M. W. Barsoum. *J. Nucl. Mater.* **460** (2015) 122-129.
8. D. J. Tallman, E. N. Hoffman, E. N. Caspi, B. Garcia-Diaz, G. Kohse, R. L. Sindelar, M. W. Barsoum. *Acta Mater.* **85** (2015) 132-143
7. M. K. Patel, D. J. Tallman, J. A. Valdez, J. Aguiar, O. Anderoglu, M. Tang, J. Griggs, F. Engang, Y. Wang, M. W. Barsoum. *Scripta Mater.* **77** (2014) 1-4.
6. D. J. Tallman, B. Anasori, M. W. Barsoum. *Mater. Res. Lett.* **1** (2013) 115-125.
5. D. J. Tallman, M. Naguib, B. Anasori, M. W. Barsoum. *Scripta Mater.* **66** (2012) 805-808.
4. E. N. Hoffman, D. W. Vinson, R. L. Sindelar, D. J. Tallman, G. Kohse, M. W. Barsoum. *Nucl. Eng. Des.* **244** (2012) 17-24.
3. M. Naguib, V. Presser, D. J. Tallman, J. Lu, L. Hultman, Y. Gogotsi, M. W. Barsoum. *J. Am. Ceram. Soc.* **94** (2011) 4556-4561.
2. M. Naguib, V. Presser, N. Lane, D. J. Tallman, Y. Gogotsi, J. Lu, L. Hultman, M. W. Barsoum. *RSC Advances.* **1** (2011) 1493-1499.
1. E. N Hoffman, M. W. Barsoum, R. L. Sindelar, D. J. Tallman. *Trans. Am. Nucl. Soc.* **102** (2010) 702-703.